CHEMICAL REVIEWS

pubs.acs.org/CR Review

Beyond the Average: Spatial and Temporal Fluctuations in Oxide Glass-Forming Systems

Katelyn A. Kirchner, Daniel R. Cassar, Edgar D. Zanotto, Madoka Ono, Seong H. Kim, Karan Doss, Mikkel L. Bødker, Morten M. Smedskjaer, Shinji Kohara, Longwen Tang, Mathieu Bauchy, Collin J. Wilkinson, Yongjian Yang, Rebecca S. Welch, Matthew Mancini, and John C. Mauro*

Cite This: https://doi.org/10.1021/acs.chemrev.1c00974 Read Online

ACCESS | Metrics & More | Article Recommendations

ABSTRACT: Atomic structure dictates the performance of all materials systems; the characteristic of disordered materials is the significance of spatial and temporal fluctuations on composition−structure−property−performance relationships. Glass has a disordered atomic arrangement, which induces localized distributions in physical properties that are conventionally defined by average values. Quantifying these statistical distributions (including variances, fluctuations, and heterogeneities) is necessary to describe the complexity of glass-forming systems. Only recently have rigorous theories been developed to predict heterogeneities to manipulate and optimize glass properties. This article provides a comprehensive review of experimental, computational, and theoretical approaches to characterize and demonstrate the effects of short-, medium-, and long-range statistical fluctuations on physical properties (e.g., thermodynamic, kinetic, mechanical, and optical) and processes (e.g., relaxation, crystallization, and phase separation), focusing primarily on commercially relevant oxide glasses. Rigorous investigations of fluctuations enable researchers to improve the fundamental understanding of the chemistry and physics governing glass-forming systems and optimize structure−property−performance relationships for next-generation technological applications of glass, including damage-resistant electronic displays, safer pharmaceutical vials to store and transport vaccines, and lower-attenuation fiber optics. We invite the reader to join us in exploring what can be discovered by going beyond the average.

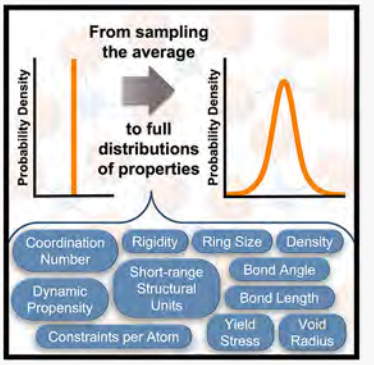

CONTENTS

Received: November 21, 2021

1. INTRODUCTION

Glasses are a vital component of the modern world due to their unique combination of material properties, including high optical transparency, chemical durability, and strength.[1] New breakthroughs in the fundamental understanding of glass chemistry and physics are needed to address global challenges for which glass materials play a crucial role, in areas including information technology (e.g., next-generation displays, augmented reality, memory storage, and optical data transfer), transportation and architecture (e.g., automotive interiors, energy-efficient glazing, and acoustic damping materials), energy (e.g., wind energy, photobioreactors, photovoltaics, solid-state batteries, solar thermal, and nuclear waste immobilization), and healthcare (e.g., pharmaceutical packaging, antimicrobial glass surfaces, and bioactive glasses).[1−3] The impact of glass on our world has been tremendous, but the fundamental processes that govern its behavior are not completely understood.[4,5] Two main complexities that obfuscate research efforts are that the glassy atomic structure is disordered and evolves with time.

Deviations in microscopic structural features directly impact the macroscopic properties and performance of a glass for each of the applications listed above. For example, consider the role of glass applications in information technology, such as optical communication and quantum cryptography. Glass optical fibers transmit data around the globe and deliver high-bandwidth, light-speed connectivity necessary for today's information-driven world.[6] To meet the increasing demand for reliable high-speed data transfer, the optical attenuation (i.e., power lost or dissipated) over the length of a glass optical fiber must be minimized. Attenuation in low-loss optical fibers is dominated by Rayleigh scattering, which is in turn governed by atomic density fluctuations in the glass fiber.[6−8] Increased localized density fluctuations scatter more light, thereby dissipating more power within the optical fiber.[6−8] Localized atomic-scale fluctuations similarly impact crystal nucleation, phase separation, relaxation modes, compaction, and crack propagation in glass products, as discussed in sections 6−10 of this review.

The deviations of the atomic structure from the average, in space and time, are referred to as spatial and temporal fluctuations, respectively. To date, most studies omit spatial and temporal fluctuations and instead evaluate glass performance solely based on the mean-field description of structural features.[9−14] In practice, glasses with similar average values can behave differently, and statistical distributions of microscopic features play a pivotal role in uncovering the phenomena that govern the differences in the observed properties and performance of glass-forming systems. Underscoring the criticality of fluctuations in disordered systems, the 2021 Nobel Prize in Physics was awarded to Giorgio Parisi "for the discovery of the interplay of disorder and fluctuations in physical systems from atomic to planetary scales."[15−17] Critical work, and reviews of such work, have been conducted by the theoretical statistical physics community, who are responsible for recent advances related to the fundamental physical nature of model glassy systems, including spin glasses, binary Lennard-Jones systems, hard disks or spheres, jammed systems, quantum fluctuations, etc.[18−27] However, a comprehensive

https://doi.org/10.1021/acs.chemrev.1c00974
Chem. Rev. XXXX, XXX, XXX−XXX

review of the physical chemistry of spatial and temporal fluctuations of structural glass materials (e.g., oxide, metallic, and chalcogenide glasses) is currently missing. The following paper takes a first step toward filling this gap by examining the impact of fluctuations, while focusing on oxide glass-forming systems with commercial applications.

This article provides a comprehensive review of various experimental and computational techniques to characterize and evaluate the effect of spatial and temporal fluctuations on physical properties and processes that are critical for commercially relevant glass systems (primarily oxide glasses) and applications. This article begins by mathematically defining fluctuations, and then explains the community's current understanding for the thermodynamic and kinetic origins of fluctuations in glass-forming systems, followed by an introduction to experimental and computational techniques that characterize and model fluctuations. Next, this review provides an analysis of recent work investigating how fluctuations impact glass relaxation, crystallization, phase separation, mechanical properties, and optical properties. Readers less familiar with glass structure and terminology are invited to start with section 1.1 and the List of Key Terms provided at the end of this review. Readers with a thorough background in the mathematical, kinetic, and thermodynamic origins of fluctuations and standard experimental and computational techniques within the structural glass science field are invited to jump to sections 6−10 for applications of fluctuations linked to structure−property−performance relationships. The scope of this paper focuses on the nonequilibrium glassy state; however, especially when discussing relaxation (section 6) and nucleation (section 7), the equilibrium supercooled liquid state is highlighted to address the importance of the parent liquid state and thermal history during glass synthesis in dictating the formation of spatial and temporal fluctuations in the glassy state.

Understanding the impact of fluctuations on properties and processes will not only enable researchers to improve fundamental knowledge of the chemistry and physics governing disordered systems but also aid in the design of new glasses with optimized or unusual properties and performance, wherein fluctuations can be leveraged as an additional degree of freedom (besides the mean-field structure). In this review article, we explore the consequences of statistical fluctuations in glass-forming systems and invite the scientific community to join us in exploring beyond the average.

1.1. Glassy Atomic Structure

While fluctuations (i.e., deviations from the average) occur in all material systems, their impact on structure−property−performance relationships is especially critical for structural glasses. One example of fluctuations in a nonglassy system is the variation of solute concentration within a solvent. Locally, some of the solute ions might be closer together and some might be farther apart, but neither region is exactly at the average bulk concentration. The distinction is that, in the solution, ions are freely mobile, whereas in glass the atoms are considered "frozen" into the disordered arrangement; hence, the spatial fluctuations are semipermanent. Glass not only lacks long-range ordered structures, but it is also a nonequilibrium material that appears like a solid on a short time scale but continuously relaxes toward the liquid state on a longer time scale.[1,28]

Depending on the temperature and pressure, the time scale of interest for temporal fluctuations ranges from seconds, minutes, hours, to millennia and above.[1] Glass structure exhibits fluctuations on three length scales: short (∼first nearest neighbors), medium (∼second or third nearest neighbors), and long (a few nanometers and above). Figure 1 is a two-dinemsional (2D) schematic contrasting the

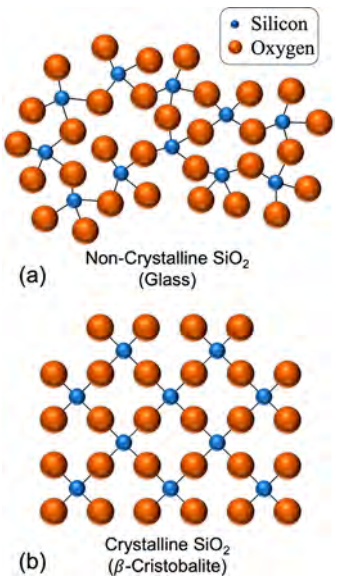

Figure 1. Two-dimensional schematics of (a) noncrystalline SiO_2, i.e., the glassy atomic structure, and (b) crystalline SiO_2, i.e., the β-cristobalite atomic structure, where the blue smaller circles are silicon atoms and the orange larger circles are oxygen atoms. Both structures contain short-range order of 2-fold coordinated oxygen atoms and 4-fold coordinated silicon atoms and fairly similar average Si−O bond lengths. The crystalline structure (b) has uniform silicon rings and long-range periodicity, whereas the glassy SiO_2 structure (a) shows a distribution of 3−7-membered silicon rings and lacks a long-range pattern.

disordered atomic structure of glassy SiO_2 to that of the ordered, crystalline SiO_2 (β-cristobalite). The β-cristobalite structure shown in Figure 1b exemplifies how crystalline materials possess atomic order on all three length scales. In contrast, glass (shown for silica glass in Figure 1a) possesses short-range order (where the Si atoms are mostly 4-fold coordinated and O atoms are mostly 2-fold coordinated), limited medium-range order (a distribution of ring structures often ranging from ∼3 to 10 members, in terms of the number of Si atoms they comprise), and no long-range periodicity.[1] Over the three length scales, the noncrystalline structure of glassy networks induces various distributions of spatially and temporally fluctuating features (e.g., bond lengths, bond angles, coordination numbers, polyhedral connectivity, density, and elasticity), unique from the crystalline counterparts of the same material.

Common structural glass compositional families include oxide glasses that contain oxygen (e.g., silicates, borates, phosphates, aluminates), chalcogenide glasses with chemistries predominately containing chalcogen elements (e.g., S, Se, Te), and metallic glasses with chemistries predominantly containing metallic atoms. Considering both commodity and specialty glass applications, 95% of the commercial tonnage of glass consists of oxide glasses, with silica-based glasses being the

https://doi.org/10.1021/acs.chemrev.1c00974
Chem. Rev. XXXX, XXX, XXX−XXX

largest percentage by far.[1] Therefore, while the theories discussed in this review article apply to all glass-forming systems, the provided examples primarily focus on oxide glasses.

The short-range structure of oxide glasses refers to distributions in the cation−anion pairs. In oxide glasses, the cations are traditionally classified as being network formers, network modifiers, or network intermediates. Network-forming cations, such as Si, P, and B, form strong covalent bonds with oxygen to form the backbone of the glass network, while network-modifying cations, such as alkali and alkaline earth ions, modify the network by forming weaker ionic bonds with oxygen. Network intermediates act as either network formers or modifiers, depending on their chemical environment in the glass-forming system.[1,29−31] In oxide glasses, oxygen is the only anion. Each oxygen can either be a bridging oxygen (BO) bonded to two (or potentially three) network formers or a nonbridging oxygen (NBO) bonded to one network former. Each modifier ion has multiple ways to alter the structure and resulting material properties, as shown in Figure 2 for a sodium borosilicate glass. The introduction of the modifier Na_2O is shown to modify the borosilicate network by either decreasing the number of BOs by breaking a Si−O−Si bond (Figure 2b) or converting trigonal boron to an effective 4-fold coordination, which increases the number of BOs (Figure 2c). Statistical mechanics can quantify the probability of a modifier occupying each available site in the structure, and for the sodium borosilicate example, there is a nonzero probability associated with a given Na^+ ion breaking the Si−O−Si bond or converting boron to an effective 4-fold coordination (see section 5.2).

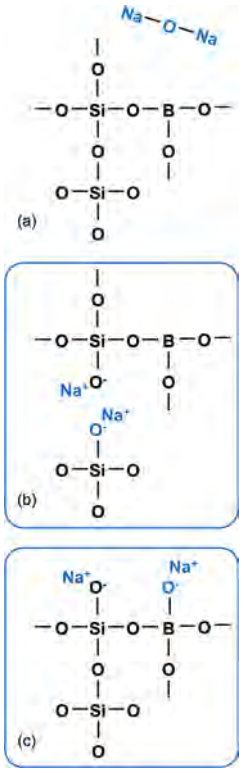

Figure 2. Examples of how modifier ions can affect network-former sites in a sodium borosilicate system. (a) Na_2O introduced to a borosilicate glass network. The two Na^+ ions in an Na_2O molecule can (b) break an O−Si bond and form two NBOs or (c) charge-compensate a boron, converting the boron from 3-fold coordination to effective 4-fold coordination.

Note that the site occupations illustrated in Figure 2, parts b and c, change the bonding structure and therefore the properties of the glass-forming system, such as the rigidity of the network. Rigidity is a unitless scaling factor that defines the flexibility of a bond length or angle, where a rigid bond length or angle acts as an interatomic constraint that confines the atomic position. Highly rigid bond lengths or angles are characterized by small standard deviations of bond length and bond angle, respectively, as shown for bond A and angle α of Figure 3. Conversely, flexible or broken constraints are characterized by broad standard deviations in bond length and/or angle, as shown for bond B and angle β in Figure 3. As rigid bonds/angles are broken, the network's rigidity and the total number of constraints decrease.

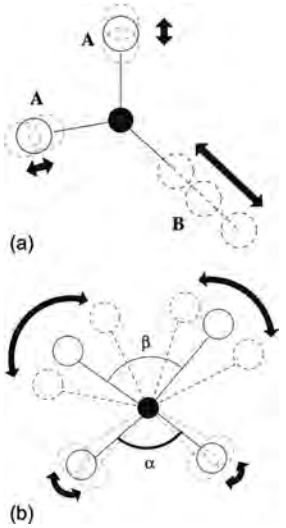

Figure 3. Schematic of rigid and flexible (a) bonds and (b) angles for an arbitrary atom (black circle) that is bonded to three or four other atoms (white circles). The dotted white circles indicate the magnitude of radial or angular excursions around the mean. Small standard deviations of bond length (A) or bond angle (α) represent a rigid bond/angle. Large standard deviations of bond length (B) or bond angle (β) represent a flexible bond/angle. Reprinted with permission from ref 32. Copyright 2011 Elsevier B.V.

In silicate, germanate, and phosphate glasses, the short-range structural units are the Si, Ge, and P tetrahedral units, respectively, and, for borate glasses, it is the B trigonal unit. The short-range structural units in oxide glasses are called Q^n units, where n is the number of BOs bonded to the network-forming atom. The potential short-range structural units in silicate glasses are shown in Figure 4. Note that, for some network formers, such as boron and phosphorus, the unoccupied Q^n speciation is Q^3 rather than Q^4, due to boron being 3-fold coordinated and phosphorus having an electron pair. The finite options of Q^n species creates uniform short-range order; however, each Q^n species will have a distribution of bond lengths and bond angles. Additionally, coordination number may change with composition (further discussed in sections 4−10). These Q^n species can then bond together to form varying ring sizes, where the length of the ring is labeled based on the number of network-former atoms within a closed loop. For example, Figure 1a shows seven-, three-, and five-

https://doi.org/10.1021/acs.chemrev.1c00974
Chem. Rev. XXXX, XXX, XXX−XXX

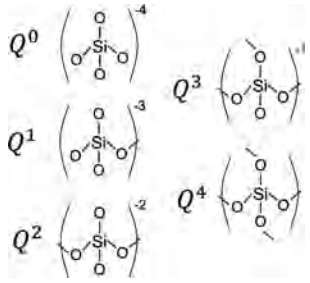

Figure 4. Five potential Q^n species of SiO_2, where n is the number of BOs bonded to the central Si atom.

membered rings. Note, not all studies on glass-forming systems implement the Q^n notation because it was originally designed for tetrahedral units. In this paper, the Q^n notation is used to categorize different coordination numbers of network formers because it is a convenient and common means of unifying the structural unit notation.

2. MATHEMATICAL DESCRIPTION OF FLUCTUATIONS

Before analyzing the impact of fluctuations on glass properties and processes, the term fluctuations need to be defined precisely and mathematically. A fluctuation is a deviation of the local value (for spatial fluctuations) or instantaneous value (for temporal fluctuations) of a property from its mean value. Capturing the fluctuations of a property entails calculating the full distribution of that property, which can be done with an understanding of the mathematical moments of a distribution.

2.1. Moments of a Distribution

The statistics of any distribution are quantified using mathematical moments, where the i^{th} order raw moment of a given function $f(x)$ is defined as

$$\mu_i = \int_{-\infty}^{\infty} x^i f(x)\, dx \tag{1}$$

The first-order ($i = 1$) raw moment of a function is its *mean*, i.e., average value, given by

$$\mu_1 = \int_{-\infty}^{\infty} x f(x)\, dx = \langle f(x) \rangle \tag{2}$$

The higher-order moments ($i > 1$) are typically defined as central moments about the mean, with the general form being

$$\mu_i = \int_{-\infty}^{\infty} (x - \mu_1)^i f(x)\, dx \tag{3}$$

As an example, consider the second-order central moment (i.e., $i = 2$), which is called the *variance* of the function and is given by

$$\mu_2 = \int_{-\infty}^{\infty} (x - \mu_1)^2 f(x)\, dx = \langle [f(x) - \langle f(x) \rangle]^2 \rangle \tag{4}$$

The higher-order moments beyond the second-order central moment (i.e., skewness, kurtosis, hyperskewness, hypertailedness) mathematically capture the asymmetry and tailedness of a distribution. Since many material property distributions are often assumed to follow a normal (i.e., Gaussian) function that has zero skewness, this review article will focus primarily on the second-order central moment. Therefore, when referring to the magnitude of "fluctuations" or "heterogeneities", we typically discuss the variance or standard deviation of the property distribution. The *standard deviation* of a function is the square root of the second-order central moment (i.e., variance) given by

$$\sigma = \sqrt{\mu_2} = \sqrt{\langle [f(x) - \langle f(x) \rangle]^2 \rangle} \tag{5}$$

2.2. Time and Ensemble Averages

There are two domains of fluctuations to consider: time and ensemble. To differentiate the two, consider the analogy of driving. A road trip from Philadelphia, Pennsylvania, U.S.A. to New York City, New York, U.S.A. is ~90 miles, and the trip takes ~1.5 h by car. On the basis of the average mileage, the car could be assumed to drive 60 mph during the entire trip; however, in reality the car may have been driving 40 mph on residential streets, and at other times the car may have been driving 80 mph on the highway. This scenario reflects time domain fluctuations, i.e., how a property (the speed of a car) varies with time. If instead the scenario is the distribution of the speeds of many cars driving on the same road, this would be considered as an ensemble domain, i.e., how the speed of a car varies compared to the other cars. Note that a time average of some property A is denoted as $\bar{A}$, while the ensemble average of that same property is denoted as $\langle A \rangle$.

Considering the ensemble average case, fluctuations are defined as

$$\delta A = A - \langle A \rangle \tag{6}$$

Rather than the change in property A, fluctuations can also be expressed using the variance as discussed in eq 4. The variance in property A is hence given by

$$\sigma_A^2 = \langle (\delta A)^2 \rangle = \langle (A - \langle A \rangle)^2 \rangle \tag{7}$$

$$\sigma_A^2 = \langle A^2 \rangle - \langle A \rangle^2 \tag{8}$$

or equivalently

$$\sigma_A^2 = \sum_j p_j A_j^2 - \langle A \rangle^2 \tag{9}$$

where p_j is the probability of obtaining property value A_j. The distinction between time and ensemble domains plays a critical role in glass-forming systems because glasses are characterized by broken ergodicity, which will be discussed in the next section.

2.3. Statistics of Nonergodic Systems

An ergodic system is one that has the same behavior averaged over time as averaged over the ensemble of all the system's states in its phase space.[33] Mathematically, ergodicity is achieved when the time average of a property equals its ensemble average:

$$\bar{A} = \langle A \rangle \tag{10}$$

The ergodic hypothesis states that a system will become ergodic in the limit of infinite time; in other words, ergodicity is restored in the limit of infinite observation time for any system within a given phase space and finite temperature and pressure.[33,34]

To elucidate the concept of ergodicity, recall the driving analogy from section 2.2. Consider the set of all cars driving on the same road, where the road has a universal speed limit. The average speed is measured by driving a car for a long time across the entire road (i.e., time average) or, equivalently, by having many people drive their cars on different parts of the

https://doi.org/10.1021/acs.chemrev.1c00974
Chem. Rev. XXXX, XXX, XXX−XXX

road (i.e., ensemble average). When ergodicity is valid, these two scenarios will lead to the same measured average speed. However, ergodicity will break down if at least one path becomes less accessible, e.g., a car accident or road work that slows down or restricts access to a portion of the road. In this scenario, the time average is *not* equal to the ensemble average, so the condition of ergodicity does not hold. In fact, a traffic jam is a specific example of a more general "jamming transition," which involves a transition from an ergodic to a nonergodic system, i.e., a breakdown of ergodicity.[21,35,36]

A breakdown of ergodicity results from having an internal relaxation time scale much longer than the external observation time scale, which causes the system to be unable to explore the complete phase space of the material. In glass-forming systems, a breakdown of ergodicity occurs as the atoms are frozen in place during the glass transition, i.e., as the system is cooled from the metastable equilibrium supercooled liquid state to the nonequilibrium vitreous, rigid state (further discussed in section 3). Glass relaxation is a unifying process by which ergodicity is spontaneously restored in the limit of long time (further discussed in section 6).

To model the physics of broken ergodicity, a statistical mechanical framework developed by Palmer[37] is often employed, which partitions the complex nonergodic system into a set of disjoint, internally ergodic regions, called components or metabasins. Each metabasin Γ_α consists of a set of atomic microstates where the probability of transitioning between metabasins is assumed to be negligible. In other words, if a system is in a particular metabasin Γ_α at time t, there is an insignificant probability of the system leaving that metabasin over the observation time $t + t_{obs}$. However, all microstates within a metabasin are mutually accessible on a time scale much shorter than $t + t_{obs}$, i.e., internal ergodicity holds within each Γ_α. The complete phase space Γ of the nonergodic system is the union of the set of confined, internally ergodic metabasins Γ_α:

$$\Gamma = \bigcup_{\alpha} \Gamma_\alpha \tag{11}$$

Mauro et al.[38] extended the Palmer approach to enable direct calculation of entropy loss, account for transition rates between microstates, and, hence, create a generalized statistical mechanical framework for continuously broken ergodicity applicable to the glass transition. The metabasin statistical approach to represent broken ergodic systems is critical for modeling glass-forming systems and will be further discussed in section 5.3.[34]

2.4. Spatial and Temporal Fluctuations

Spatial fluctuations refer to how the properties vary in different regions of the material, which encompass fluctuations in structure and network topology (i.e., the atomic connectivity). Temporal fluctuations refer to how the instantaneous value of a property changes with time. Spatiotemporal fluctuations are fluctuations in both space and time.

Even though an average value may provide adequate estimations, a comprehensive review of spatial and temporal fluctuations within the time and ensemble domain can promote the fundamental physical chemical understanding of glass-forming systems. Following the driving analogy of section 2.2, if time and ensemble domain averages omit the detail necessary to describe something as simple as a road trip, scientists could similarly benefit from going beyond average values to fully describe something as complex as glass structure−property−performance relationships. Now that the term fluctuation has been defined for the context of this article, the next question to address is why a high degree of spatial and temporal fluctuations is present in glass-forming systems.

3. KINETIC AND THERMODYNAMIC ORIGIN OF FLUCTUATIONS IN GLASS-FORMING SYSTEMS

The kinetic and thermodynamic origins of spatial and temporal fluctuations relate to the nonequilibrium nature of glass. Thermodynamics determines the driving force for the transition from the nonequilibrium glassy state to the lower-free energy, metastable equilibrium, supercooled liquid state.[34] Kinetics sets the rate and intermediate steps required for the transition to occur.[34] Spatial and temporal fluctuations in glass-forming systems are historically difficult to characterize; however, their presence in glass-forming systems induce kinetic and thermodynamic fluctuations, which can be modeled using molecular dynamics, Monte Carlo, and statistical mechanics (see sections 5.1 and 5.2). This section discusses the driving forces for why spatial and temporal fluctuations occur in glass-forming systems and introduces kinetic and thermodynamic equations, which will be utilized in sections 5.1 and 5.2.

A key characteristic that distinguishes glasses from amorphous solids is that glasses exhibit a glass transition, i.e., a continuous, kinetic transition between the supercooled liquid and glassy states.[1] This kinetic transition is shown in the volume−temperature (V−T) diagram (Figure 5).[39] The system is in the equilibrium liquid state at the maximum volume and temperature. As the system is quenched (i.e., as temperature decreases), the system reaches the melting temperature T_m, where the system can undergo a first-order thermodynamic phase transition into the equilibrium crystal state. If the system is quenched faster than the rate at which the atoms kinetically rearrange into the equilibrium crystalline

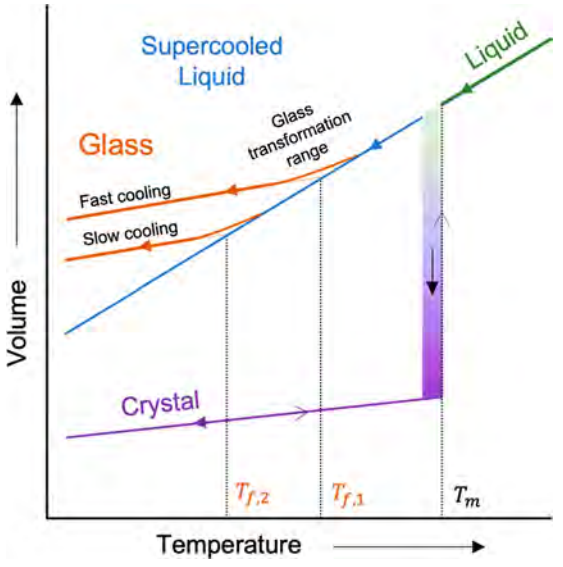

Figure 5. Volume−temperature diagram, which plots the comparative volumes of a system in its liquid, supercooled liquid, glass, and crystal states at various temperatures. T_m is the melting temperature (which only depends on the liquid composition), and T_f is the fictive temperature (which depends on the liquid composition and cooling rate).

https://doi.org/10.1021/acs.chemrev.1c00974
Chem. Rev. XXXX, XXX, XXX−XXX

state, the system enters the metastable equilibrium supercooled liquid state without crystallizing. The room-temperature volume (and therefore density and material properties) of a glass depends on the fictive temperature T_f at which the glass deviates from the supercooled liquid state.[1,40] A slower quench rate results in a lower T_f, which allows the atoms to have more time to rearrange, and usually results in a more compact atomic structure (i.e., lower volume, denser) room-temperature glass, with properties that approach those of the supercooled liquid. With more time for the atoms to reorganize, especially at elevated temperatures, the glass will relax toward the metastable equilibrium supercooled liquid state.

A rate of 10 K/min is used to define the calorimetric glass transition temperature T_g (often defined by its corresponding viscosity of $\sim 10^{12}$ Pa·s for inorganic glasses),[41] which is a constant for a given glass composition, while T_f varies depending on the thermal history (i.e., quench rate) imposed during processing. In Figure 5, a glass refers to the nonequilibrium state at temperatures below T_f, a glass-forming liquid refers to the equilibrium liquid state above T_f, and a glass-forming system refers to the system at all temperatures.

The kinetic theory of glass formation states that any liquid can be vitrified (i.e., formed into a glass) if it is cooled sufficiently fast to avoid crystallization.[1] The kinetic driving force for a transition to occur is the activation energy and time required for an atom to rearrange, which could involve breaking or reforming bonds. The thermodynamic driving force is the net change in free energy, e.g., Gibbs free energy ΔG, which at constant temperature is given by

$$\Delta G = \Delta H - T\Delta S \tag{12}$$

Here ΔH is the change in enthalpy, T is the absolute temperature, and ΔS is the change in entropy. As seen in eq 12, the change in enthalpy and entropy dictates whether a transition will be spontaneous ($\Delta G < 0$) or nonspontaneous ($\Delta G > 0$). When ΔH and ΔS have the same signs, a competition forms to dictate the spontaneity of a reaction. The competition between the enthalpic and entropic factors induces distributions in the probability of site occupation (see sections 5.2 and 5.3), and therefore the formation of spatial fluctuations.

3.1. Kinetic-Derived Properties

Kinetically driven properties of specific interest for glass-forming systems, and where temporal fluctuations are most critical, include glass relaxation, crystallization, and phase separation (see sections 6–8). Each of these kinetic properties is influenced by the constraints of the glass's nonequilibrium, noncrystalline, and nonergodic nature, and the common underlying driving factor centers around entropy production. As established by the second law of thermodynamics, the entropy of an isolated system increases with time. However, as with every law of macroscopic physics, systems are subject to fluctuations, that is, there is a nonzero probability to observe negative entropy production in physicochemical systems.[42] The fluctuation theorem quantifies statistical fluctuations in entropy production for equilibrium and nonequilibrium systems. Derivations from the fluctuation theorem have led to theorems such as Green–Kubo relations which are often used to define the kinetics of glass-forming systems within modeling approaches such as molecular dynamics (MD) (further discussed in section 5.1).

The mathematical framework of Green–Kubo relations and calculation of transport phenomena in glass-forming systems begins with an understanding of time correlation functions, which define the correlation between two properties (A and B) in time:[43]

$$C_{AB}(t) = \langle \delta A(t)\delta B(0)\rangle \tag{13}$$

A high correlation C_{AB} indicates that properties A and B exhibit highly correlated fluctuations, and a value of $C_{AB} = 0$ means that the properties are completely uncorrelated.[34] If A and B are the same property ($A = B$), eq 13 represents the autocorrelation function, which defines the correlation of a property with itself over time. Properties that vary quickly have a low autocorrelation function, since they quickly lose the memory of their past states. Equation 13 is of interest in this review because macroscopic properties can be calculated using the integrals of the correlation functions, and experimentally measured spectra can be related to the Fourier transforms.[34,43] For example, MD investigations of glassy kinetics are often based on Green–Kubo relations, which involve the infinite time integral of an autocorrelation function at equilibrium for an arbitrary transport coefficient γ:

$$\gamma = \int_0^\infty \langle \dot{A}(t)\dot{A}(0)\rangle \, \mathrm{d}t \tag{14}$$

where $\dot{A}$ is the time derivative of property A. Each γ is calculated using the corresponding Einstein relation:[43]

$$2\gamma t = \langle (A(t) - A(0))^2 \rangle \tag{15}$$

This approach of implementing time correlation functions has been used to derive equations for transport properties such as diffusivity, shear viscosity, volume viscosity, and thermal conductivity,[43−45] and, most relevant for the purposes of this review article, dynamical heterogeneities, which are regions of slower or faster kinetics caused by chemical or structural fluctuations in condensed systems. Green–Kubo relations have also been used to uncover interesting nonmonotonic relaxation behaviors of the various property standard deviations such as density fluctuations (see section 5.1).[43,44]

Green–Kubo and Einstein relations for the transport coefficients in a nonequilibrium steady state are derived using the fluctuation theorem, specifically by assuming that the probability distribution of the time-averaged dissipative flux is Gaussian. The Green–Kubo equation is based on the fluctuation–dissipation theorem, a linear response theory.[46,47] Work by Searles and Evans[46] has shown that the Green–Kubo relations are not valid in the nonlinear regime when a system is driven far from equilibrium, which has called into question the validity of these assumptions when modeling glass-forming systems.[47] Similarly work by Malek Mansour and Baras[42] has shown that the underlying fluctuation theorem exhibits limitations in its ability to describe dynamic properties correctly within nonequilibrium systems. Sections 4–10 of this article review the glass community's recent advances in characterizing and modeling temporal fluctuations of kinetic properties and processes; however, future work is required to further develop the underlying theorems for applicability toward structural glass-forming systems. For example, common computational techniques, such as molecular dynamics, still implement Green–Kubo relations which assume a Gaussian time-averaged dissipative flux, even though dynamical heterogeneities in glass-forming systems manifest as nonmonotonic, non-Gaussian probability distributions.

https://doi.org/10.1021/acs.chemrev.1c00974
Chem. Rev. XXXX, XXX, XXX−XXX

Table 1. Thermodynamic Properties Derived from the Fundamental Equation in Eq 16

definition of variables		derived properties	
C_V = isochoric heat capacity		$C_V = \left(\frac{d\bar{U}}{dT}\right)_{N,V}$	$\beta_T = -\frac{1}{V}\left(\frac{\partial^2\bar{G}}{\partial P^2}\right)_{T,N}$
C_p = isobaric heat capacity α = thermal expansion coefficient β_T = isothermal compressibility β_S = adiabatic compressibility α_{ij} = thermal strain		$C_p = \left(\frac{d\bar{H}}{dT}\right)_{N,p}$	$\beta_S = -\frac{1}{V}\left(\frac{\partial^2\bar{H}}{\partial P^2}\right)_{S,N}$
S = entropy	T = temperature	$\alpha = \frac{1}{V}\left(\frac{\partial^2\bar{G}}{\partial T \partial P}\right)_N$	
V = volume	H = enthalpy		
P = pressure	U = internal energy	$\alpha_{i,j} = -\frac{\partial^2\bar{G}}{\partial T \partial \sigma_{ij}} = \left(\frac{\partial \overline{\varepsilon_{ij}}}{\partial T}\right)_{\sigma,E,H}$	
σ_{ij} = stress	μ = chemical potential		
ε_{ij} = strain	N = no. of moles		

3.2. Thermodynamic-Derived Properties

Properties such as heat capacity, thermal expansion coefficient, and compressibility can be calculated from quantified fluctuations in thermodynamic parameters. This section mathematically defines such relations that are used to link microscopic fluctuations to macroscopic properties (see sections 5.1.3 and 5.2.4).

Thermodynamic parameters (internal energy U, temperature T, entropy S, pressure P, volume V, chemical potential μ, and amount of species N) are related through the fundamental equation of thermodynamics:

$$dU = TdS - pdV + \mu dN \tag{16}$$

The first and second derivatives of the fundamental equation relate all thermal, mechanical, electrical, and magnetic thermodynamic properties.[48] A few example manipulations of averaged thermodynamic parameters are shown in Table 1, where each equation shown can be calculated from quantified microscopic fluctuations. Below is an example derivation for how the known microscopic fluctuations in internal energy, enthalpy, and volume mathematically define the bulk heat capacity and thermal expansion coefficient for any system.

Thermodynamic variables fluctuate, even at equilibrium. Suppose the internal energy of the system U is the only fluctuating variable (i.e., all other extensive parameters are held constant). The deviation of $U - \bar{U}$ is a fluctuating variable of average value zero. Recall from section 2 that the variance of U in the time domain is given by

$$d\sigma_U{}^2 = \overline{(U - \bar{U})^2} = \overline{(U^2)} - (\bar{U})^2 = \sum_j p_j U_j^2 - (\bar{U})^2 \tag{17}$$

where p_j is given by

$$p_j = \frac{1}{Z}\exp\left(-\frac{U_j}{k_B T}\right) \tag{18}$$

k_B is Boltzmann's constant, T is the absolute temperature, and Z is the partition function to normalize the summation of all p_j values to unity. Note that eq 18 assumes that all states are accessible, and therefore, eq 18 only applies to glass-forming liquids or within a metabasin where internal ergodicity is achieved. Manipulating eq 17 and applying the product rule to the derivative simplifies as

$$\sum_j p_j U_j^2 = k_B T^2 \frac{\partial \bar{U}}{\partial T} + \bar{U}^2 \tag{19}$$

Combining eq 17 and eq 19 then gives

$$\sigma_U{}^2 = \sum_i p_i U_i^2 - \bar{U}^2 = k_B T^2 \frac{\partial \bar{U}}{\partial T} \tag{20}$$

Following Table 1, the isochoric heat capacity is given by

$$C_V = \left(\frac{d\bar{U}}{dT}\right)_{N,V} \tag{21}$$

Substituting eq 21 into eq 20 reveals that the variance of the energy fluctuations is directly proportional to the isochoric heat capacity:

$$\sigma_U{}^2 = \langle(\delta U)^2\rangle_{NVT} = k_B T^2 C_V \tag{22}$$

A variety of thermodynamic properties can be calculated from the underlying microscopic fluctuations in this way. For example, if the same derivation shown in eqs 16−20 is repeated for fluctuations of enthalpy instead of internal energy, a direct relationship between the variance of the enthalpy fluctuations and the isobaric heat capacity C_P is revealed:

$$\sigma_H{}^2 = \langle(\delta H)^2\rangle_{NPT} = k_B T^2 C_P \tag{23}$$

Similarly, the volumetric thermal expansion coefficient is uncovered through a cross-correlation of volume and enthalpy fluctuations:

$$\langle \delta V \delta H\rangle_{NPT} = k_B T^2 V \alpha \tag{24}$$

Recall that glass is a nonergodic system, meaning that the time average does not equal the ensemble average of a thermodynamic property. Palmer's approach to account for broken ergodicity is to consider that the individual microstates are grouped together into metabasins satisfying the conditions of internal ergodicity and confinement (see section 2.3).[34,37] Take the energy fluctuations again as the example. Within a given metabasin α, the variance of energy fluctuations is given by

$$(\sigma_U{}^2)_\alpha = k_B T^2 \frac{\partial \overline{U_\alpha}}{\partial T} \tag{25}$$

https://doi.org/10.1021/acs.chemrev.1c00974
Chem. Rev. XXXX, XXX, XXX−XXX

Considering p_α as the probability of the system being confined to metabasin α, then the expected value of C_V is an ensemble average over all metabasins, given by

$$\langle C_V \rangle = \frac{1}{k_B T^2}\langle {\sigma_U}^2 \rangle = \frac{1}{k_B T^2}\sum_\alpha p_\alpha ({\sigma_U}^2)_\alpha \tag{26}$$

and similarly

$$\langle C_P \rangle = \frac{1}{k_B T^2}\langle {\sigma_H}^2 \rangle = \frac{1}{k_B T^2}\sum_\alpha P_\alpha ({\sigma_H}^2)_\alpha \tag{27}$$

For more detailed derivations of equations linking microscopic fluctuations to bulk thermodynamic properties, refer to ref 34, and for discussions of techniques that model thermodynamic fluctuations, refer to sections 5.1 and 5.2.

4. CHARACTERIZATION TECHNIQUES

Experimental techniques capable of precise and quantitative measurements of structural and topological fluctuations are critical for characterization of spatial and temporal fluctuations in glass. This section introduces experimental techniques which characterize structural and topological fluctuations. Short- and medium-range order structural units in glass-forming systems are often characterized with spectroscopic and diffraction techniques such as nuclear magnetic resonance (NMR), X-ray, neutron, and electron diffraction, vibrational spectroscopy, and small-angle scattering (SAS). Various features of spatial fluctuations can thereby be characterized, such as Q^n speciation from NMR, bonding fluctuations from diffraction or vibrational spectroscopy techniques, ring size analysis from Raman spectra, and density fluctuations from SAS.

In glass-forming systems, distributions in microscopic features can induce fluctuations in macroscopic properties. For example, atomic voids create density fluctuations and thereby induce refractive index variations which lead to Rayleigh scattering. Due to the complex nature of characterizing medium-range structure, spatial fluctuations are often studied indirectly through property analysis, such as atomic density and refractive index measurements. Positron annihilation lifetime spectroscopy (PALS) directly characterizes the size of voids to link to density fluctuations and Rayleigh scattering in glass-forming systems.

A myriad of experimental techniques, such as dynamic light scattering,[49] have been used to characterize nonexponential and non-Arrhenius behaviors in glass. Further discussion into these and additional methods to characterize spatiotemporal fluctuations for specific properties are introduced in sections 6−10. The experimental techniques discussed in this section have not been newly developed specifically for spatiotemporal fluctuations in glass-forming system, and therefore, the standard operating procedures and mechanisms of the processes are not within the scope of this review article. In metallic glasses or crystals, spatial fluctuations at small length scales can be imaged with high-resolution transmission electron microscopy techniques, but the same methods do not work well for nonconducting glass materials, such as oxide glasses.[50] Therefore, electron microscopy techniques will also not be discussed.

4.1. Nuclear Magnetic Resonance: Q^n Speciation Analysis

With solid-state NMR, the effects of atomic coordination, bond length, bond angle, and Q^n speciation distributions in glasses can be observed. NMR spectroscopy probes differences in magnetic field shielding imposed by surrounding atoms on the quantum mechanical transition of nuclear spin states under resonant electromagnetic irradiation.[51,52] Magic angle spinning (MAS) NMR spectroscopy spins the sample at an angle of 54.74° with respect to the magnetic field direction to produce higher resolution NMR spectra for solid-state materials. Through various pulse sequences and spectral editing, MAS NMR can detect structural information on the first and second coordination of network-forming elements; however, deconvolution of the peaks is often complicated.[53,54] For glassy materials, the MAS NMR spectral features are quite broad, indicative of the broad distributions of nonuniform atomic arrangements around the atoms being probed.[55] In contrast, in crystalline solids, the surrounding atom positions are governed by uniform packing structure, allowing the MAS NMR spectra to produce very sharp peaks with distinct chemical shifts, each of which correspond to specific structural units.

The NMR spectral features for aluminosilicate glasses are defined using Q^n_m notation for tetrahedral Si units, where n is the number of bridging oxygens per structural unit, similar to the Q^n speciation notation introduced in section 1.1. The subscript m is the number of bonded AlO_4 units ($0 \le m \le n \le 4$).[55] As an example, the ^{29}Si MAS NMR spectra of anorthite $CaAl_2Si_2O_8$ glass and the corresponding crystalline compound are compared in Figure 6.[55] The ^{29}Si MAS spectrum (Figure 6b) of the crystalline phase extends over 10 ppm, with eight sites of similar chemical environment of Q^4_4. In contrast, the spectrum for the glass phase (Figure 6a) is broad and featureless, spanning more than 20 ppm with different Q^n_m chemical configurations of the SiO_4 tetrahedron.[55]

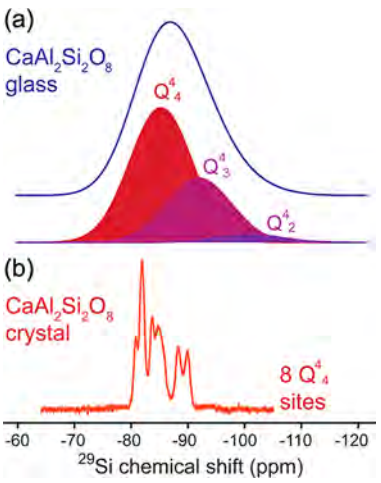

Figure 6. ^{29}Si MAS NMR spectra of (a) glass and (b) crystalline phases of anorthite $CaAlSi_2O_8$. The crystalline phase shows eight Q^4_4 sites, and the broad glass peak is deconvoluted into Q^4_4, Q^4_3, and Q^4_2 structural motifs. Reprinted with permission from ref 55. Copyright 2013 American Chemical Society.

In glass-forming systems, the exact values of the chemical shifts vary depending on the angle of Si−O−T (where T denotes the Q^n-connected tetrahedron) and the type of the T element.[55−57] In ^{29}Si MAS NMR, typical chemical shifts of silicon species in silicate glasses are roughly ∼110 ppm for Q^4, ∼90 ppm for Q^3, ∼80 ppm for Q^2, and ∼70 ppm for Q^1 species with respect to the tetramethylsilane reference.[58,59] In ^{27}Al MAS NMR, the chemical shift is referenced with respect to 1

https://doi.org/10.1021/acs.chemrev.1c00974
Chem. Rev. XXXX, XXX, XXX−XXX

M $Al^{3+}(aq)$, and typical values for AlO_4 groups are ~70−80 ppm for aluminate, ~60−70 ppm for aluminosilicate, and ~35−45 ppm for aluminophosphate. Note that the precise values vary depending on the number of Al, Si, P, and B neighbors in the second coordination shell of Al.[60] If the Al coordination increases, then the peak position shifts toward a smaller chemical shift side, with the six coordination at nearly 0 ppm. Due to quadrupolar contributions in ^{27}Al NMR, deconvolution of the peak to different coordination species is often complicated and not as straightforward as the Q^n speciation of Si.[61] Typical chemical shifts for $B^{[3]}$ and $B^{[4]}$ are around 15 and 1 ppm, respectively, with respect to the $NaBH_4$ reference.[62] This band broadening in glass, compared to that of crystalline phases, reflects the broad distribution of structural disorders in bond length and angle.[63] The bond length and angle distributions can also be deduced from the ^{17}O NMR analysis.[64,65]

4.2. Diffraction Experiments: Bonding Fluctuations

The interatomic distance distributions can be directly obtained from X-ray, electron, and neutron diffraction, where X-ray and electron diffraction are more sensitive to larger atomic number elements and neutron diffraction is more sensitive to lighter elements.[54,66] These techniques measure the total structure factor in the reciprocal space, the inverse Fourier transform of which reveals the pair distribution function (PDF) in real space. Total structure factor is $S(k)$, where the scattering vector magnitude (i.e., momentum transfer magnitude) k defines reciprocal space distance and is given by

$$k = (4\pi/\lambda)\sin\theta \tag{28}$$

In eq 28, 2θ is the scattering angle and λ is the X-ray, electron, or neutron wavelength. The corresponding real space information is contained in the reduced PDF $G(r)$, where r is the atomic distance in real space.[54,66] The PDF provides the structural disorder or interatomic distance distribution which can be extracted from the peak width. The PDF $g(r)$, the total correlation function $T(r)$, and the radial distribution function RDF(r) are defined as follows:

$$g(r) = \frac{G(r)}{4\pi r\rho} + 1 \tag{29}$$

$$T(r) = G(r) + 4\pi r\rho = 4\pi r\rho g(r) \tag{30}$$

and

$$\mathrm{RDF}(r) = rG(r) + 4\pi r^2\rho = rT(r) \tag{31}$$

where ρ is the atomic number density. The smallest distance peak directly corresponds to the bond length of the main constituent of the glass network.[67,68] Consequently, these real-space functions make it possible to obtain distribution widths, interatomic distances, and coordination numbers in glass systems.

The choice of using X-ray, electron, or neutron diffraction is determined by what element is targeted to be probed. Figure 7 exemplifies this concept by comparing neutron and X-ray total correlation functions $T(r)$ for glassy SiO_2; peaks of lighter elements like the oxygen−oxygen correlation are more easily detected using neutrons, while peaks of heavier elements like the cation-related correlation are more easily detected by X-rays.[66,69] By combining X-ray, electron, and neutron diffraction, results can show sensitivity to elements with a diversity of atomic numbers.

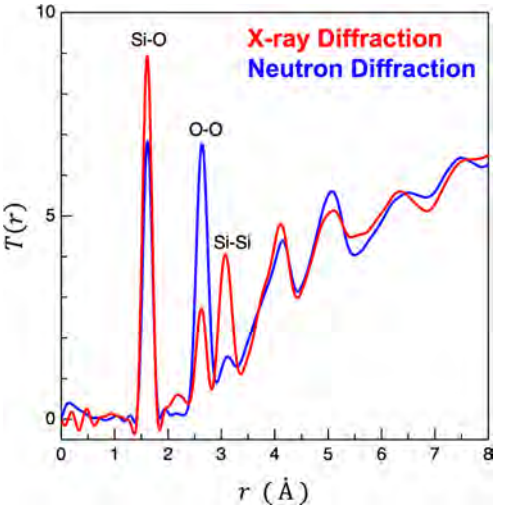

Figure 7. Neutron (blue) and X-ray (red) total correlation functions $T(r)$ for glassy SiO_2 glass. Fourier transforms of the $S(k)$ were performed with k_{max} = 30 $Å^{-1}$. A Lorch function was used as the modification function. Data from refs 66 and 69.

Figure 7 also exemplifies the limited medium-range order and lack of long-range order in glass-forming systems, which manifest as spatial fluctuations in such glass systems. Notice the broad, low-intensity peaks at 4.15 and 4.9−5.1 Å. In crystalline quartz, these peaks are as strong and well-defined as the 3.1 Å peak of the two Si atoms connected via two covalent bonds.[70] The peak at 4.15 Å corresponds to the distance between atoms connected through three covalent bonds (for example, from the Si atom to the O atom in the adjacent SiO_4 tetrahedron), and the peak at 4.9−5.1 Å corresponds to the distances between atoms connected through four covalent bonds. This comparison reveals that there are some degrees of partial medium-range order in the glass network beyond the length scale of the first and second coordination shells, and such diffraction experiments can be conducted to quantify bonding fluctuations. However, it is difficult to deconvolute using experimental techniques.[70] To explore spatial fluctuations for a glassy network in the medium range, it is often necessary to employ combined experimental and computational approaches. With that being said, several analytical approaches have recently been reported which can also infer the ring size distribution from neutron diffraction.[71,72]

Atomistic simulations allow visualization of structure based on experimental diffraction data (further discussed in section 5.1). For example, in work by Onodera et al.,[69] experimental diffraction data was used in conjunction with a combined reverse Monte Carlo (RMC) and MD simulation to reveal the mixed alkali effect in sodium potassium silicate glass. The diffraction data was used to set the constraints for the coordination number of silicon, bond angle distribution of O−Si−O, and partial pair-distribution functions within the first coordination shell, and Q^n distributions were assigned to avoid physically unreasonable configurations.[69] Confirmation of the short-range modeling predictions in real space are shown in Figure 8, where high-energy neutron diffraction data (Figure 8a) and X-ray diffraction data (Figure 8b) are shown in black curves, and the colored curves are RMC−MD computational results. With a validated atomistic model, further explorations

https://doi.org/10.1021/acs.chemrev.1c00974
Chem. Rev. XXXX, XXX, XXX−XXX

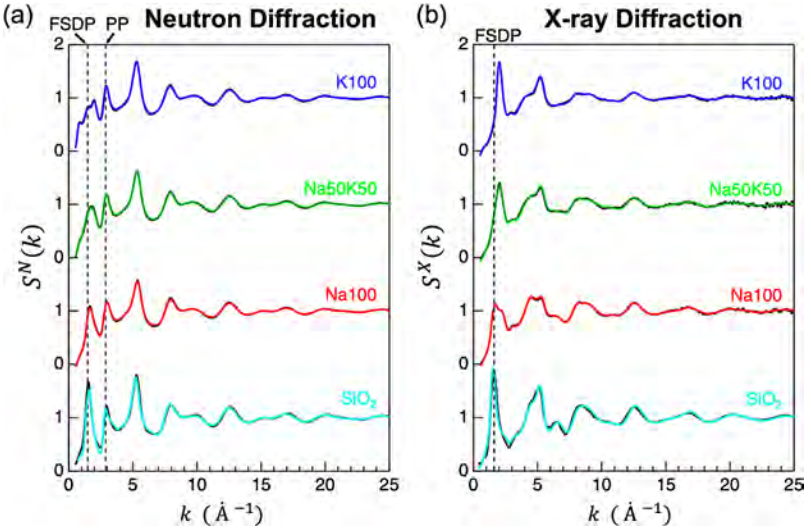

Figure 8. Comparison of experimental spectra (black curves) and computationally predicted spectra (colored curves) in reciprocal k-space for sodium potassium silicate glasses $22.7R_2O-77.3SiO_2$, where the modifier R is 100% K ions (K100), 100% Na ions (Na100), or 50% Na and 50% K ions (Na50K50). Spectra of the 0% modifier ion composition is included for reference and labeled as pure SiO_2. The (a) neutron total structure factor $S^N(k)$ and (b) X-ray total structure factor $S^X(k)$ are compared. The colored superimposed spectra are predicted results from the RMC−MD simulation. The first sharp diffraction peak (FSDP) and the second principal peak (PP) are shown as vertical dashed lines. Note that the $S^N(k)$ exhibits both the FSDF and PP because PP is the oxygen-related correlation, which is easily detected by neutrons. Adapted with permission from ref 69. Copyright 2019 Onodera et al. http://creativecommons.org/licenses/by/4.0/.

in clusters, voids, and ring distributions are obtainable (further discussed in section 5.1). Both Figures 7 and 8 therefore showcase experimental diffraction data which can be collected to quantify spatial fluctuations such as bonding fluctuations and employed to validate computational predictions.

4.2.1. Angstrom-Beam Electron Diffraction Measurement: Two-Phase Fluctuations. X-ray diffraction can observe average structure; however, the goal of this review is to target structural fluctuations. In this pursuit, angstrom-beam electron diffraction (ABED) proves especially beneficial since ABED enables direct measurement of two-phase fluctuations. Hirata et al.[73,74] developed ABED to investigate the local structure of disordered SiO. Their work has since devolved a combined experimental−computational heterostructure model of the disproportionated SiO with diffraction intensity profiles from ABED, X-ray diffraction, and computer simulations.[73−75] Figure 9 shows a schematic of the ABED experimental setup, where the yellow color indicates nanoregions structurally different from the blue regions. The electron probes the local atomic structure across the sample to character diffraction patterns of various nanoregions and the interfaces between nanoregions. With this setup, ABED can capture multi-phase structural fluctuations in disordered materials.

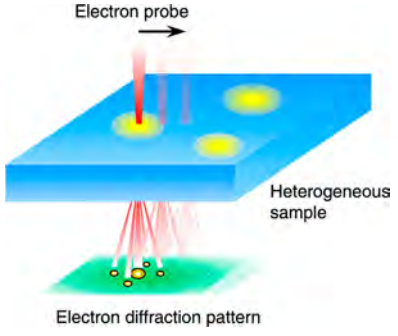

Figure 9. Schematic illustration of the ABED measurements of SiO with nanoscale structural heterogeneity. The nanoregions indicated in yellow are structurally different from the regions indicated in blue. Reprinted with permission from ref 75. Copyright 2016 Hirata et al. http://creativecommons.org/licenses/by/4.0/.

Figure 10 shows typical ABED patterns taken from (Figure 10a) bright, (Figure 10b) interface, and (Figure 10c) dark regions of glass SiO local structures and the corresponding structure factors $S(k)$ of (Figure 10d) SiO_2 (yellow), SiO (red), Si (black), and the summation of a-Si and a-SiO_2 (blue). The $S(k)$ of SiO seems to be intermediate between those of SiO_2 and Si; however, the averaged data (blue) of SiO_2 and Si is not consistent with that of SiO. This behavior is consistent with previous reports;[76] particularly, the first peak in the averaged data has a two-peak structure, which is very different from that observed at $k \sim 1.8$ Å^{-1} of SiO. The excellent agreement between the averaged data and SiO at the high-k part demonstrates that the short-range order of SiO is similar to those of SiO_4 and $SiSi_4$ tetrahedra in SiO_2 and Si. Results from this ABED study confirmed that SiO is not a simple composite of Si and SiO_2, but rather, SiO may have an interfacial region between the SiO_2 and Si domains.

4.3. Vibrational Spectroscopy: Bonding and Ring Size Distribution

Vibrational spectroscopy techniques of spectral reflectance infrared (SR-IR) spectroscopy and Raman spectroscopy characterize energy exchanges between molecules and electromagnetic radiation, which can be used to probe structural disorders in glass networks. Similar to NMR and diffraction techniques, vibrational spectra of glass materials exhibit broad absorption bands, while crystalline silicate materials give very sharp and well-resolved vibrational bands.[77−80] The shift and broadness of the vibrational bands, compared to the vibrational spectra of crystalline counterparts, are mainly due to the broad distribution of local structural disorders; however, the spectral

https://doi.org/10.1021/acs.chemrev.1c00974
Chem. Rev. XXXX, XXX, XXX−XXX

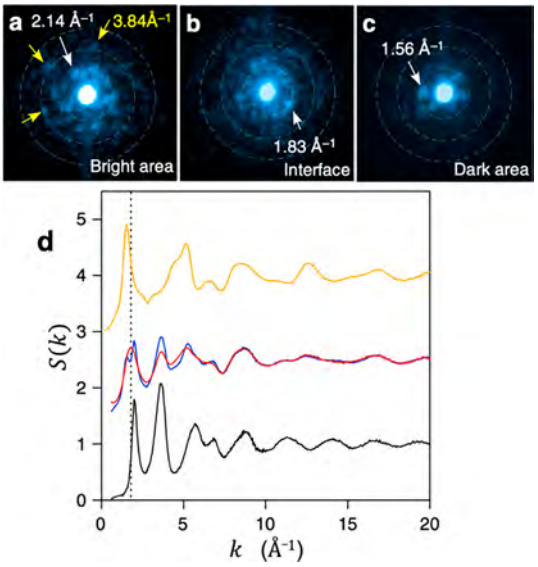

Figure 10. ABED experiments and X-ray diffraction of SiO. Experimental ABED from SiO glass local structures. ABED patterns are taken from the (a) bright, (b) interface, and (c) dark regions, respectively. The white dashed rings represent k values of ∼1.8, 3.6, and 5.2 Å^{-1}, respectively, which correspond to those of the first three peaks in the X-ray total structure factors $S(k)$ of SiO shown in panel d. In panel d the total structure factors $S(k)$ are shown for SiO_2 (yellow), SiO (red), Si (black), and the average of a-Si and a-SiO_2 (blue). The dashed line is a guide to the eyes. Adapted with permission from ref 75. Copyright 2016 Hirata et al. http://creativecommons.org/licenses/by/4.0/.

interpretation principle is not as rigorously established as that of the NMR and PDF analyses.[81]

Recent studies by Kim and co-workers[81−83] have found an empirical correlation between the position of the Si−O−Si stretch band in IR spectra and the Si−O bond length distribution for simple silica and silicate glasses. Figure 11 shows the SR-IR spectra for a series of sodium silicate glasses $[Na_2O]_x[Al_2O_3]_2[SiO_2]_{98-x}$, where x = 7, 12, 17, and 22, with fused quartz included for reference.[81] Since the force constant of the Si−O stretch vibration is extremely high, a small change

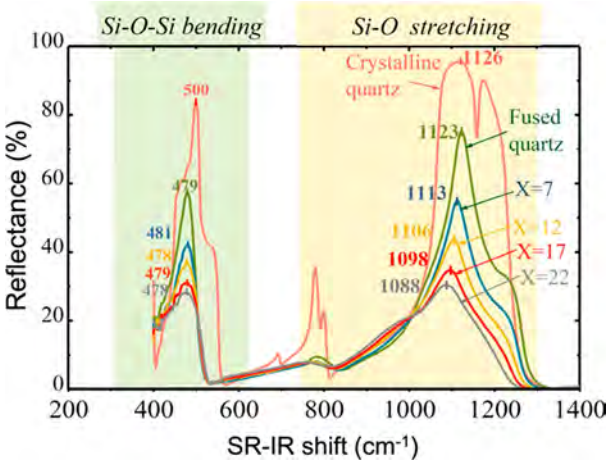

Figure 11. SR-IR spectra for a series of sodium silicate glasses $[Na_2O]_x[Al_2O_3]_2[SiO_2]_{98-x}$, where x = 7, 12, 17, and 22, with crystalline and fused quartz plotted for reference. Adapted with permission from ref 81. Copyright 2020 American Ceramic Society.

in the bond length (even less than 0.01 Å) can be manifested as a large change in the spectral peak position. Consequently, this work concluded that the Si−O−Si stretch band can be used as a probe to estimate changes in the Si−O bond length distribution.

Unlike NMR and diffraction techniques, which have very low absorption or scattering cross sections (and hence require large samples), the high absorptivity of vibrational modes allows vibrational spectroscopy to be coupled with a topographic imaging technique for spectral analysis of small areas. Figure 12 shows example results where a silica glass was subjected to nanoindentation and then imaged with scattering scanning near-field optical microscopy in the mid-IR region near the Si−O−Si stretching mode.[84] Within the indentation imprint (i.e., the plastically deformed region), the main band intensity is quite low compared to the never-touched outside region. Even in the elastic contact region where there is no induced change made (for example, the outside region adjacent to the triangle mark in Figure 12), the Si−O−Si stretching mode is found to be altered. This work indicates that, although the glass surface appears topographically homogeneous, there could be subsurface structural modification in the region that has been contacted with a foreign object. The locations with such subsurface structural changes appear to be more susceptible to aqueous corrosion, thereby affecting the material's mechanical and chemical properties.[85−87]

Unlike IR spectroscopy, which focuses on bonds and angular vibrations, Raman spectroscopy probes vibrational modes of covalently bonded atoms, where certain bending vibration bands can be attributed to different sizes of rings to uncover ring size fluctuations in glass-forming systems. Note that the SR-IR spectra in Figure 11 show relatively small changes in the bending vibration regions. Raman spectra exhibit larger variances depending on the glass composition and processing conditions, which is why Raman spectroscopy is typically preferred for ring investigations. Figure 13 provides example Raman spectra for the same sodium aluminosilicate system as that in Figure 11.[81] Through comparison with computational results, the Raman peaks at ∼430, ∼495, and ∼600 cm^{-1} have been attributed to six-, four-, three-membered rings, respectively.[77,88] Current ring-size analysis capabilities are limited to small ring sizes, such as three-, four-, and six-membered rings, since they are easier to identify especially in structures produced via computer simulations. Larger rings are somewhat ambiguous since their shapes are highly irregular and the interior spaces defined by those rings are not necessarily empty.

Rings have been visualized in transmission electron microscopy images of 2D silica;[89] however, there is no spectroscopic or diffraction technique that is particularly sensitive to specific sizes of such rings, making it experimentally difficult to confirm the presence or exact distribution of larger rings in bulk glass. Similar to diffraction experiments of glass structural fluctuations, when investigating ring structures, a combined experimental−computational plan is often implemented (see section 5). Recent investigations have uncovered an intriguing phenomenon that the relative intensities of bands in Raman spectra do not match the ring size distributions determined from MD simulations.[81] Such results have stirred questions about the validity of the interpretation or assignment of the Raman bands in the bending vibration region to ring size.[90] Further investigations

https://doi.org/10.1021/acs.chemrev.1c00974
Chem. Rev. XXXX, XXX, XXX−XXX

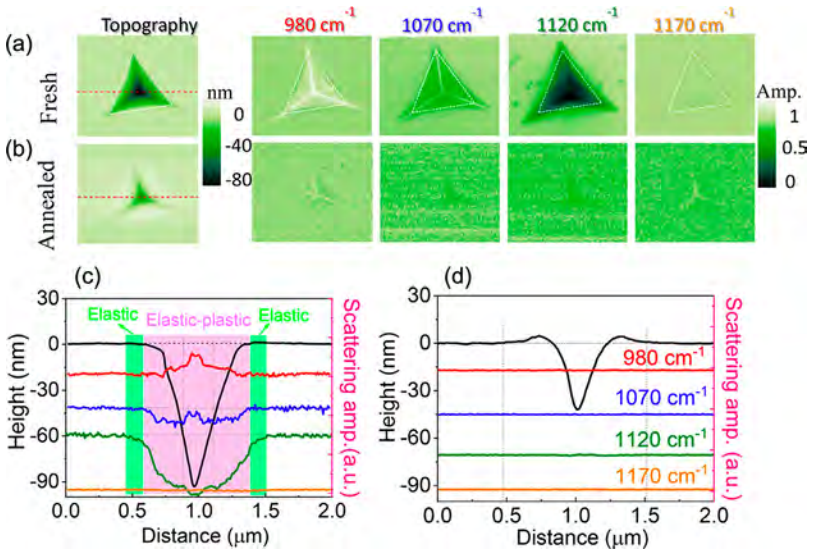

Figure 12. (a) Topography and scattered IR intensity images of (a) fresh and (b) sub-T_g annealed nanoindentation marks made with a Berkovich tip at an applied load of 5 mN on silica glass. The topography and IR images are 2 μm × 2 μm in the $x-y$ directions. The white triangles are the guidelines added to show the three facet edges of the nanoindentation mark identified in the topography image. The plots in panels c and d compare the cross-sectional line profiles of the topography and IR images of the fresh and annealed nanoindentation marks, respectively, at the location marked with red lines in panel a. Reprinted with permission from ref 84. Copyright 2021 Acta Materialia Inc.

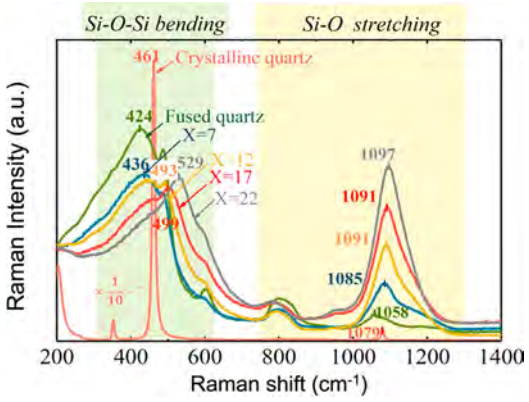

Figure 13. Raman spectra for a series of sodium silicate glasses $[Na_2O]_x[Al_2O_3]_2[SiO_2]_{98-x}$, where x = 7, 12, 17, and 22, with crystalline and fused quartz plotted for reference. Adapted with permission from ref 81. Copyright 2020 The American Ceramic Society.

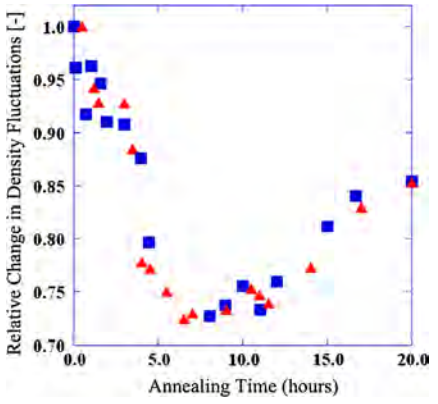

Figure 14. *In situ* SAXS measurements of the temporal evolution of density fluctuations during isothermal relaxation at 868 K for Corning Inc. code 7059 glass. The blue and red markers show results from two identically setup runs. Adapted with permission from ref 7. Copyright 2009 American Physical Society.

surrounding this question are needed before conclusions can be drawn.

4.4. Small-Angle Scattering: Density Fluctuations

Small-angle scattering includes small-angle X-ray scattering (SAXS) and small-angle neutron scattering (SANS), both of which quantify nanoscale density differences by analyzing the elastic scattering of X-rays or neutrons at small angles. SAS techniques are consequently used to characterize nanoparticle size distributions, pore sizes, void sizes, and density. Figure 14 plots the temporal evolution of density fluctuations from *in situ* SAXS measurements of Corning 7059 boroaluminosilicate glass during isothermal relaxation at 868 K. The magnitude of density fluctuations initially decreases, overshoots the equilibrium value, and then increases to equilibrium following a nonmonotonic relaxation function. This result questions the previously assumed monotonic relaxation of glass-forming systems and is attributed to density-driven dynamical heterogeneities, where the relaxation time varies with the localized molar volume in the system. For further discussions and explanations for why this effect is observed see section 6 on glass relaxation.[7]

4.5. Rayleigh Scattering: Density and Refractive Index Fluctuations

As addressed in section 1, Rayleigh scattering occurs due to density fluctuations. Therefore, another approach to capture density fluctuations is through Rayleigh scattering intensity measurements. The light scattering coefficient is expressed as[91]

$$\alpha_R = \frac{8\pi^3}{3\lambda^4}\frac{n^8 p^2}{\rho^2}\langle|\Delta\rho|^2\rangle V \tag{32}$$

where $\langle|\Delta\rho|^2\rangle$ is the mean square of the density fluctuations, λ is the wavelength of the incident light, ρ is the mean density, n is the refractive index, and p is the photoelastic constant. Therefore, Rayleigh scattering intensity measurements directly

https://doi.org/10.1021/acs.chemrev.1c00974
Chem. Rev. XXXX, XXX, XXX−XXX

determine the amount of density fluctuations. A convenient method to measure Rayleigh scattering in silica glass is to obtain the cumulative loss by measuring transmitted light through a fiber medium. The optical loss of a fiber can be measured by the cutback method. In this method, the initial transmitted light by utilizing Beer–Lambert's law is given by

$$I = I_0 \exp(-\alpha D) \tag{33}$$

where α is the loss coefficient, D is the length of the fiber, and I_0 is the intensity of the incident radiation. Then, the fiber is cut into $D - \delta$ (δ is usually more than a meter long). The transmitted light intensity will then be given by

$$I = I_0 \exp(-\alpha(D - \delta)) \tag{34}$$

Figure 15 shows an example of optical loss (i.e., attenuation) versus wavelength for a conventional silica glass fiber. More

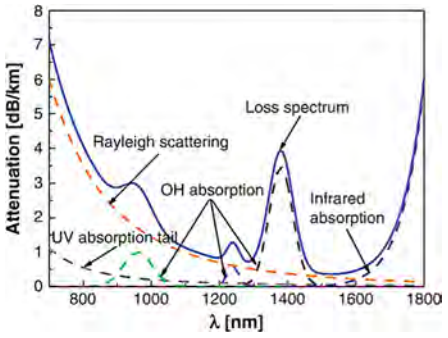

Figure 15. Optical loss of a conventional silica glass fiber. The loss spectrum is constructed of more than 80% Rayleigh scattering, with remaining small contributions of UV absorption tail and OH absorption. The OH absorption can be reduced by using dehydrated SiO_2 as the fiber preform. Data were obtained from ref 92.

than 80% of the loss against light with wavelengths shorter than 1.7 μm obeys eq 32, indicating Rayleigh scattering is taking place.

If a fiber form is not obtainable, direct observations of the scattered light at 90° angle are typically done.[93] By this method, the difference in density fluctuation of silica glass is directly compared to that of α-quartz for reference.[94] For some materials, the cavity ring down spectroscopy (CRDS) approach might be used. In this method, the sample is placed in an optical cavity formed by highly reflective mirrors and the optical loss is determined by the change in lifetime of the cavity.

4.6. Positron Annihilation Spectroscopy: Void Size, Density, and Refractive Index Fluctuations

For silica glass, the total volume of empty space accounts for more than 60% of the structure, based on assumed ionic radii of each atom.[95] Thus, information on the voids should be important to understand the density fluctuation. PALS is a nondestructive spectroscopy that can directly observe voids in glasses.[96,97] The operating principle is that a positron will be annihilated through interactions with electrons, which releases detectable γ rays. A positron is the opposite particle of an electron . Positronium (Ps) is a bound state of a positron and electron (Figure 16). The positroniums of interest for void studies are the ones that localize in subnanovoid in glasses (labeled as τ_3) and have a long lifetime; they disappear when the positron in a positronium meets an electron at the edge of the void, a phenomenon referred to as "pick-off annihilation".

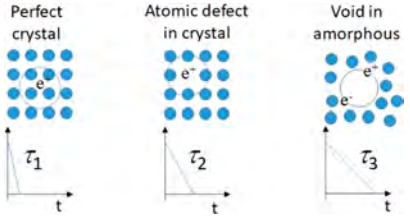

Figure 16. Schematics of the lifetime component of the positron lifetime profiles and their corresponding atomic arrangement. Here, blue circles show atoms, e^+ is a positron, and e^- is an electron. A positron pairs with an electron and forms a positronium. The dotted circle shows the free radius of the positron in vacuum. When the material is a perfect crystal, the positron disappears within the time constant of τ_1 (approximately 125 ps). If there is an atomic defect in the crystal, the positronium lives longer (τ_2 approximately up to 0.5 ns). For noncrystalline materials like glass, positroniums live longer in voids for τ_3's of approximately 1–3 ns. In the PALS measurement, these three components are detected together.

Thus, the lifetime of the τ_3 position is used as an indicator of the size of the voids.[98]

Using PALS, Ono et al.[99] investigated the effect of fictive temperature T_f on void size in silica glass. As shown in Figure 17, lifetime (and thereby void diameter) increased with

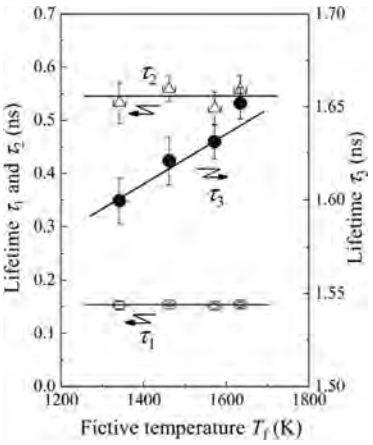

Figure 17. Fictive temperature dependence of positron lifetime parameters τ_1, τ_2, and τ_3. τ_1 is the lifetime of a parapositronium (a single state of positronium) or a free positron that did not form a pair with an electron. τ_2 is the annihilation of positrons trapped in defects. τ_3 is the pick-off annihilation of orthopositronium that is trapped in a void. Reprinted with permission from ref 99. Copyright 2012 American Institute of Physics.

increasing T_f. The results indicate that, as T_f increases, voids expand, but the number of voids remains constant. As discussed in section 3 when introducing the $V-T$ diagram, glass is typically known to densify when it is quenched from higher temperatures. If the void size also increases, then the dense regions of atoms must be densifying, and consequently, the spatial density fluctuations must also significantly increase. Void space can be regarded as having a refractive index the same as that of vacuum. Thus, the large density fluctuations must have a strong relationship with the refractive index fluctuations, which in turn induce the Rayleigh scattering phenomenon. Under ambient pressure, the PALS-observed void radius R_V can explain Rayleigh scattering with appropriate values of the number of scattering particles N and relative refractive index n, given by

https://doi.org/10.1021/acs.chemrev.1c00974
Chem. Rev. XXXX, XXX, XXX–XXX

$$\alpha_R = \frac{2}{3}\pi^5 N\left(\frac{n^2-1}{n^2+2}\right)^2 \frac{(2R_V)^6}{\lambda^4} \quad (35)$$

Hence, the void radius R_V can be considered as a representative parameter to quantify spatial fluctuations in glass-forming systems related to Rayleigh scattering phenomena.

5. MODELING TECHNIQUES

Experimental techniques can provide indirect signatures of the structure of glasses with high precision (as discussed in section 4), but at a high cost of time and equipment. Computational approaches, on the other hand, provide direct access to the structure itself, with the downside of requiring simplifying assumptions about atomic interactions or time and length scales.[100,101] Models are not only validated against experimental data, they are critical predictive tools that enable the artificial manipulation of properties at a very fundamental level and the observation of macroscopic properties sometimes unobtainable with experiments themselves.[102]

Challenges when developing computational techniques for studying spatiotemporal fluctuations in glass-forming systems include the applicability of models over relevant time and length scales, the ability to discern physically meaningful fluctuations from calculation noise, and the ever-present challenges of glassy systems being nonequilibrium, noncrystalline, and nonergodic materials. This section introduces five widely used modeling techniques which can capture spatial and temporal fluctuations in glass-forming systems: molecular dynamics (MD), statistical mechanical models, energy landscapes, topological constraint theory (TCT), and machine learning (ML). Monte Carlo (MC) and density functional theory (DFT) are addressed in tandem with other techniques, and models specific to particular properties will be introduced in sections 6−10. In this section, only implementation techniques specific for spatiotemporal fluctuation investigations of glass-forming systems will be discussed. For further details of the computational techniques in general, we refer the reader to other review articles.[1,43,103−109]

Atomistic simulations are useful for exploring fluctuations in structure, topology, and thermodynamic properties, i.e., distributions in coordination number, bond angle, local constraints, density, pressure, enthalpy, etc. MD, which is based on solving Newton's equations of motion to quantify the time evolution of spatial fluctuations, is a useful tool for providing structural input for other types of modeling approaches. Metropolis Monte Carlo (MMC) (discussed in section 5.1.4) is a stochastic approach to explore similar atomic and thermodynamic fluctuations to MD, but with more limited applicability to glass fluctuations studies. DFT simulations incorporate electron densities and offer more accurate descriptions of mean-field atomic structure than either MD or MC; however, the computational cost and restricted length and time scales make DFT infeasible for investigating fluctuations in many glass-forming systems.[110−114] Since DFT is therefore poorly suited for fluctuation studies in glass, it will not be discussed in detail in this review article.

A typical approach to capture spatiotemporal fluctuations is to calculate the relative probability of a mixture of atoms arranging into a given atomic configuration. Statistical mechanical models and energy landscape approaches can be used to calculate such occupation probabilities. Energy landscapes capture spatial and temporal fluctuations through mapping the configurational phase space of a given system and incorporating deterministic or stochastic sampling techniques, such as master equations or kinetic Monte Carlo (kMC) (discussed in section 5.3). Statistical mechanical models can quantify distributions in structural units, network connectivity, and thermodynamic properties. Statistical mechanical models can also provide useful information for TCT models, which link structural fluctuations with topological fluctuations to uncover further structure−property relationships.[115] Recent advances in computational algorithms and hardware enable incorporation of data analytics to aid in the statistical investigation of spatiotemporal fluctuations and material discovery.

5.1. Molecular Dynamics

MD is a method for modeling materials at the atomistic scale using interatomic potentials to calculate the potential energy as a function of particle coordinates. This section introduces MD, discusses its capabilities for quantifying distributions in structural features, dynamical heterogeneities, and thermodynamic fluctuations, and provides prospective on a comparative atomic simulation technique, MC.

MD simulates short- and medium-range structural distributions, dynamical heterogeneities, and thermodynamic fluctuations by implementing time integration to solve Newton's equations of motion.[103] In classical MD simulations, the atoms in a system interact with each other via a force field or interatomic potential which is a simplified mathematical representation of the short-range atomic bonding interactions, van der Waals interactions, and/or (for charged systems) long-range Coulombic interactions. An interatomic potential can be derived from *ab initio* data (e.g., calculated from DFT) and/or experimentally measured properties (e.g., density, elastic modulus, heat of fusion, structural features).[103] The trajectory of each atom, including the position and velocity, is obtained by integrating Newton's equations of motion using a proper integration time step on the order of one femtosecond (1 fs = 10^{-15} s), which is less than the typical fastest atomic vibration in the system (10^{-13}−10^{-12} s).[43,103] Experimental time scales of interest for glass-forming systems can extend to seconds, hours, or years; therefore, the major limitation of MD is the restricted time scale. The limited length scales are also a concern if the fluctuations of interest are large compared to the MD system size.[43,103]

5.1.1. Spatial Fluctuations. Recall that glass has short-range, limited medium-range, and no long-range structural order. Consequently, the length scale of intrigue for fluctuation studies is the limited medium-range order (i.e., distributions in bond angles, rings, and voids). While MD simulation on glass-forming systems can capture distributions in coordination number (CN),[116−118] site speciation,[119] bond angles,[65,120] local bond constraints,[121] ring structures,[71,72,122−129] and analyses of voids/cavities, and clusters,[130,131] the examples discussed in this section focus on bond angle, ring, and void investigations. Figure 18 depicts MD results from Wiles et al.,[132] who simulated pressure effects on the structure of tectosilicate calcium aluminosilicate (t-CAS) glasses having the chemical formula $(1-x)(CaO + Al_2O_3)x(SiO_2)$, where x = 0.50, 0.70, 0.85, and 0.90. Figure 18 shows the O−Si^V−O bond angle probability distribution before (atmospheric pressure), during loading, and during unloading of a 15 GPa hydrostatic compression. Even though this study found that the Si^V bond

https://doi.org/10.1021/acs.chemrev.1c00974
Chem. Rev. XXXX, XXX, XXX−XXX

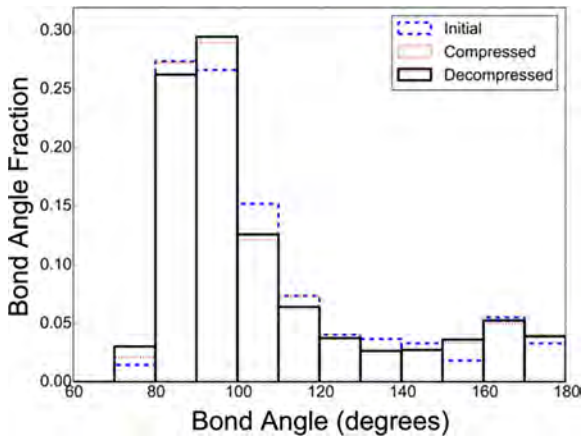

Figure 18. Distribution of O−Si^{V}−O angles in calcium aluminosilicate glass, before (initial) compression, after compression, and after decompression of a 15 GPa hydrostatic compression. Adapted with permission from ref 132. Copyright 2020 Elsevier B.V.

angle distribution in t-CAS glasses is not significantly affected by pressure, the distribution of bond angles is still of interest. The Si^{V} angle is often assumed to equal the tetrahedral angle of 109.5°. While the mean in Figure 18 does cluster around 109.5°, the O−Si^{V}−O angles within the system range between 70° and 0.180°.

Modeling the bond angle distribution can help determine the rigidity of a glass from a topological perspective. Fluctuations in the local bond constraints exist in glasses if there is a variation of coordination number, site speciation, or bond angle. Work by Bauchy and Micoulaut[32] has linked bond angle fluctuations to topological understanding for sodium disilicate glass ($Na_2O{\cdot}2SiO_2$). Figure 19 plots the standard

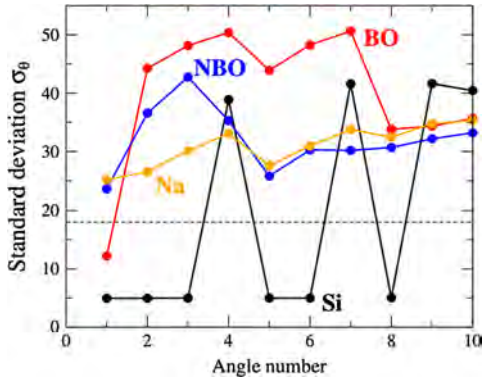

Figure 19. Bond angle standard deviation σ_θ for four types of angles in a sodium disilicate glass: the angle centered around a Si atom (black), Na atom (yellow), bridging oxygen (BO) (red), and nonbridging oxygen (NBO) (blue). The dotted black line divides the seven lowest standard deviation angles to approximate intact (below) and broken (above) angular constraints. Reprinted with permission from ref 32. Copyright 2011 Elsevier B.V.

deviation of bond angle θ, σ_θ, as a function of an arbitrary bond angle number, for the centered partial bond angles surrounding the Si, Na, BO, and NBO atoms. Recall from section 1.1 that a constraint is a rigid bond or angle, and a low standard deviation infers high rigidity in the bond distance or angle. In Figure 19, the atoms with low standard deviation (i.e., small fluctuations and high rigidity) that contribute most to the constraints of the system are the six Si-centered angles (leading to five independent angular constraints) and one BO angle. As temperature increases, Bauchy and Micoulaut[32] observed an increase in the thermal energy of the system resulting in a broadening of the bond constraint distributions and a decrease in the degree of rigidity of a given bond constraint.[32] This work shows that the standard deviation of the radial and angular bond over time and space from MD simulations can be used to determine the number of constraints broken by thermal activation. Local bond constraints have also been shown to be responsible for ductile deformation of silicate glass.[121]

Similar to bond angle distribution, MD is also used to map fluctuations in ring size.[133] There are various descriptions of what constitutes a ring, therefore leading to inconsistent modeling results depending on the definition assumed. Figure 20 compares ring size distributions in silica glass as defined by

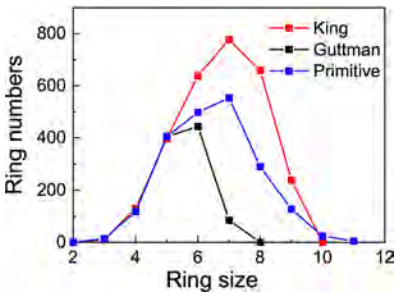

Figure 20. Number of rings with a given ring size in silica glass, where a ring is defined by either the King (red), Guttman (black), or primitive (blue) definition. Reprinted with permission from ref 71. Copyright 2021 American Association for the Advancement of Science.

the King,[127] Guttman,[126] and primitive definitions.[129] King[127] defines a ring as the shortest path between two of the nearest neighbors of a given node. For silica, this refers to two oxygen atoms that are connected to a central silicon atom. The Guttman[126] definition counts only the silicon atoms and defines the length of ring based on the number of silicon atoms needed to complete the shortest loop. The primitive definition, introduced by Goetzke and Klein,[129] is where a ring is one that cannot be decomposed into two smaller rings. In Figure 20, all three definitions match for ring sizes less than five members, but deviations begin for six or more membered rings. A critical step in the advancement of ring size distribution studies is to determine a universal understanding of what constitutes a ring within a glass-forming system.[71]

Using the available definitions of rings, fluctuations have been linked to topological and macroscopic property understanding using MD simulations. Work by Onodera et al.[134] combined MD and RMC modeling to compare primitive ring statistics in SiO_2 crystals and glass. In this work, Onodera et al.[134] also recorded the pair of radii at which a ring in a specific location appears (birth) or disappears (death) to make links between ring distributions and consequent density fluctuations. Work by Du et al.[135] used MD to investigate ring distributions in hydrated silicate glasses. Results suggest that the propensity for passivation is intrinsically governed by the reorganization of the medium-range order structure and, specifically, the formation of small silicate rings that hinder water mobility. Once again, this is an example where the incorporation of modeling techniques like MD allowed scientists not only to quantify ring size distributions but also to predict the effect of

https://doi.org/10.1021/acs.chemrev.1c00974
Chem. Rev. XXXX, XXX, XXX−XXX

those distributions on the consequent properties and performance of glass.

MD capabilities also extend to exploring distributions of cluster analysis and void radius size (shown in Figure 21).

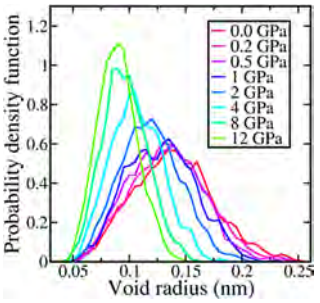

Figure 21. MD results of void radius distributions in pressure-quenched silica glass, with varying applied pressures. Adapted with permission from ref 137. Copyright 2020 Yang et al. http://creativecommons.org/licenses/by/4.0/.

Fluctuations in the glass structure can be well-depicted by the different types of the clusters comprising the materials that are found in both MD simulations[117,136] and, more recently, experiments.[73,130] Figure 21 shows the work by Yang et al.[137] who explored pressure effects on voids in silica glass using MD simulations. As the pressure increases, the void radius decreases, and the distribution narrows.

5.1.2. Isoconfigurational Ensemble MD to Capture Dynamical Heterogeneities. Recent developments in implementation approaches, such as the development of the isoconfigurational ensemble technique, have extended MD capabilities to investigate dynamical heterogeneities. The isoconfigurational ensemble is an MD-based approach developed by Widmer-Cooper et al., which offers unique capabilities for quantifying dynamic fluctuations in glass-forming systems.[138,139] The isoconfigurational ensemble approach calculates distributions of atomic displacement by varying each atom's initial velocity vector. Like standard MD, an initial configuration is known, and the initial atomic velocities are calculated from a Maxwell−Boltzmann distribution at the specified temperature. With the isoconfigurational ensemble approach, many molecular dynamics simulations are performed, each with unique, randomized initial atomic velocities recalculated at the same temperature to maintain the same average kinetic energy. Each MD simulation begins with an identical initial configuration and propagates the system for the same period of time while recording the mean square displacement (MSD) of each atom. Dynamic propensity is defined as the average of the MSD values for each atom during the constant time interval over all the MD simulations, where a higher propensity indicates a higher mobility of the atom.[34,140]

The isoconfigurational ensemble approach has shown definitively that different local environments in atomic structures lead to faster or slower relaxing regions, thus proving a structural origin for dynamical heterogeneities.[138−141] For example, Vargheese et al.[141] applied the isoconfigurational ensemble approach to a series of calcium aluminosilicate systems with varying ratios of $[CaO]/[Al_2O_3]$. Given the large disparity in dynamic propensity among the four elements in the system (Ca, O, Al, Si), normalized dynamic propensities were reported to visualize the mobility of the structure more clearly. The process of normalizing the propensity values involves grouping each atom by its atom type. Each atom's propensity is then normalized against its element's minimum, average, and maximum value, where a value of 0 is the minimum, 0.5 is the average, and 1.0 is the maximum propensity found for that given atom type. Figure 22

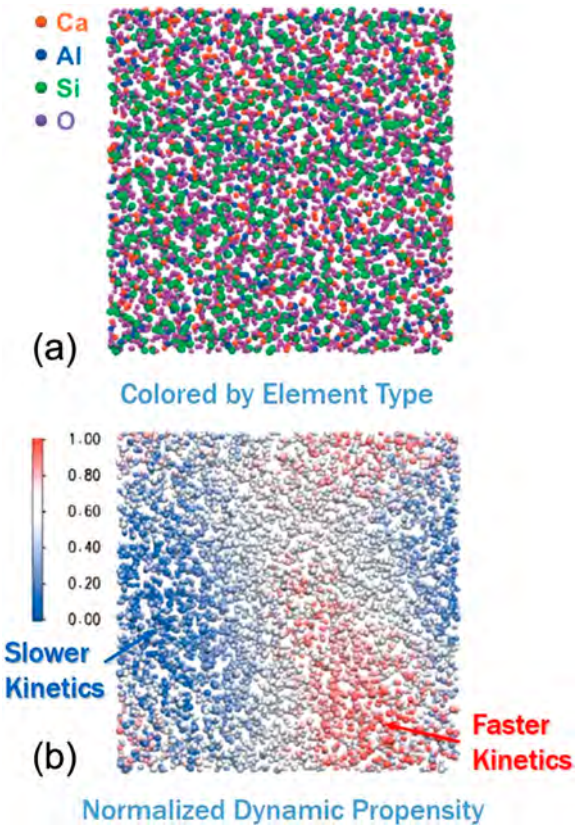

Figure 22. MD initial atomic configuration of $30CaO{\cdot}10Al_2O{\cdot}60SiO_2$ (mol %) where the atoms are colored by (a) atom type and (b) normalized dynamic propensity, where <0.5 is below average propensity and >0.5 is above average propensity based on the atom type. Reprinted with permission from ref 141. Copyright 2010 American Institute of Physics.

shows two images of the initial atomic configuration that was repeated for all the MD simulations of $30CaO{\cdot}10Al_2O{\cdot}60SiO_2$ (mol %). In Figure 22a, the atoms are colored according to atom type, and in Figure 22b the atoms are colored according to their normalized dynamic propensity. In Figure 22b, the regions with higher dynamic propensity (shown in red) have faster kinetics and greater mobility. Vargheese et al.[141] found that the regions with faster kinetics also have greater localized concentration of calcium, concluding that the dynamical heterogeneities are a direct result of chemical fluctuations.

The isoconfigurational ensemble enables the investigation of distributions of dynamic propensities for different element types, which correlate with fluctuations in the initial configuration (e.g., localized chemical fluctuations, density fluctuations, bonding fluctuations), where localized structural features lead to faster or slower kinetics for those atoms. Note that the isoconfigurational ensemble is only applicable to explore dynamical heterogeneities and has the same time and length scale limitations as MD.

https://doi.org/10.1021/acs.chemrev.1c00974
Chem. Rev. XXXX, XXX, XXX−XXX

5.1.3. Kinetic and Thermodynamic Fluctuations. For fluctuation studies in glass-forming systems, MD is also a useful tool to provide structural input (such as fluctuations in enthalpy, volume, Q^n speciation) for theoretical models. To calculate kinetic properties, MD uses time-dependent fluctuations to integrate correlation functions (see section 3.1). With Green−Kubo relations, MD has been used to calculate transport properties such as diffusivity, thermal conductivity, and dynamical heterogeneities.[43−45,142] MD also captures fluctuations in thermodynamic parameters such as enthalpy and volume, allowing these atomic simulations to calculate thermodynamic fluctuations using the methods discussed in section 3.2.[43]

5.1.4. Metropolis Monte Carlo. Metropolis Monte Carlo (MMC) is an alternative approach that can access similar structural and thermodynamic fluctuations to MD.[43] MMC is based on having accurate interatomic potentials to calculate the potential energy as a function of particle coordinates.[34] MMC is a type of Monte Carlo simulation specifically designed to explore atomistic systems. The simulation starts with a random initial configuration. One atom is randomly selected and displaced, and then the energy difference between the two states is computed to calculate whether to accept or reject the proposed displacement following a Boltzmann acceptance criterion. The trial displacements are repeated until a minimum free energy configuration is converged. Like MD, MMC is another successful technique for calculating the standard deviation of properties like volume, enthalpy, rigidity, bond length, bond angle, and ring size in glass-forming systems.[43,143−146] MMC is not the only type of Monte Carlo simulation technique; section 5.3.2 introduces kinetic Monte Carlo and its capability to sample energy landscapes stochastically.

Compared to MD, which primarily samples low-energy states close to equilibrium, MMC equally samples low energy states and high energy excited states. Consequently, MMC is more effective for accessing different ensembles and primarily useful for sampling rare events such as nucleation. MMC automatically incorporates the entropic contributions of site speciation since a more highly degenerate site will be randomly selected more often; therefore, if given enough trial moves, the algorithm will find the global free energy minima. Since the minimum global free energy in a glass-forming system is the crystal state (see section 3), MMC can be especially useful for nucleation studies of glass-forming systems.

While MD solves Newton's laws of motion using force calculations, MMC employs potential energy calculations, hence omitting the need for force calculations. MD software tools have simplified such calculations by implementing derivative look-up tables; nonetheless, MMC often remains more computationally efficient for analyzing static properties, such as structure, density, and chemistry fluctuations.[34] A limitation of MMC is that it lacks a time step, therefore prohibiting its use for time-dependent phenomena. To incorporate time, MD or kMC (see section 5.3.2) is needed. MD is generally more prevalent in the field, since more tools are currently available for MD. Consequently, the results covered in this section focus on MD rather than MC.

5.2. Statistical Mechanical Models

Given a closed system, the number of mechanically stable atomic arrangements is finite. Statistical mechanics is a probabilistic approach that connects the probabilities of each possible atomic microstate of a system with its macroscopic properties. This section presents one type of statistical approach for quantifying the distributions of structural units in a glass-forming system. Section 5.3 presents an energy landscape technique for describing the statistical mechanics of a system. In both sections 5.2 and 5.3, the probability distributions associated with different atomic configurations will be used to calculate the standard deviations of structural and, therefore, property distributions.

Statistical mechanical models are often employed to correlate topology to glass properties[147] and explore previously unexplained structural phenomena.[148] The statistical mechanical approach employs probability theory to describe structural fluctuations by analyzing the entropic and enthalpic contributions that govern the overall structure and bonding of a glass network.[105,115,119,149−154] Oxide glasses consist of network-former and network-modifier species. When modifiers are introduced into a glassy network, they can occupy different sites associated with the various network-forming species in the glass. The same modifier ion alters macroscopic properties differently depending on what site it occupies, as discussed in section 1.1. The probability of a modifier associating with a particular network-former site can be calculated from the underlying statistical mechanics. The details of this approach are the focus of this section.

Statistical mechanics is a very broad field. This section introduces two mathematical derivations of statistical mechanical models (stochastic sampling and probabilistic method) which calculate the probability of site occupation for glass-forming systems. These models can also be used to capture time-dependent relaxation;[45,155] however, the approach for implementing statistical theory must be addressed carefully due to the nonequilibrium and nonergodic nature of glass.[38,156−159] Most often the equations discussed in this section are used to study the metastable supercooled liquid state, where the fluctuations can be considered in equilibrium, using a partition function that excludes the crystalline state. Below the glass transition temperature, the fictive temperature T_f must be substituted for the absolute temperature T as an approximation of the nonequilibrium structure. Above the glass transition temperature, the structure is an equilibrium liquid state; therefore, the equations presented for glass-forming systems also apply to any liquid.

The statistical modeling approach discussed in sections 5.2.1 and 5.2.2 is used to study structural fluctuations because it describes the inherent disorder in glass-forming systems and calculates the macroscopic properties associated with a suitable ensemble of microscopic states.[106,143,160−169] Diffraction experiments and atomistic simulations (e.g., MD) have provided information regarding the statistics of glass structure (such as the probability distributions of atomic positions, the time evolution of the material,[170−172] and energies associated with bond constraints); however, these simulations are restricted by time and length scale limitations. Thus, they are too computationally intensive to be applied for thorough compositional studies.[143,144,173,174] *Ab initio* simulations offer more accurate descriptions but at a higher computational cost, making them infeasible for large systems or long time scales.[110−114] Mauro et al.[105,151] developed a statistical mechanical model based on a noncentral hypergeometric distribution of site occupancies to circumvent the time and length scale limitations of traditional atomic scale simulations.

https://doi.org/10.1021/acs.chemrev.1c00974
Chem. Rev. XXXX, XXX, XXX−XXX

5.2.1. Statistics of Glass Structural Units. The key feature of the statistical mechanics approach introduced in this section is that the distribution of structural units in oxide glasses can be described using a hypergeometric distribution.[151] Hypergeometric distributions are used to describe the probabilities of a series of events, considering the history of previous events.[7] The "events" in this case are modifier ions choosing which site to occupy. Recall the borosilicate example in Figure 2 in section 1.1, where each Na^+ ion had two potential occupations: break an O−Si−O bond or convert boron to become effectively 4-fold coordinated.

There are entropic and enthalpic factors that dictate the probability of a given Na^+ modifier ion occupying either network-forming site. If the interaction between a modifier and a network-former species could be assumed to be completely entropically controlled (e.g., no difference in the enthalpic preference for a Na^+ modifier ion to interact with Si or B network formers), the hypergeometric distribution would explain the distribution of structural units as a function of modifier concentration. However, in a real glass system, the modifier−former interactions are also affected by enthalpic contributions, with the system approaching a minimum potential energy. The enthalpic driving force for a modifier−former interaction is captured by using a type of noncentral hypergeometric distribution, where each possible event is corrected by a weighting factor specific to that event. Such a distribution is described mathematically by the Wallenius-type noncentral hypergeometric distribution:[7,8]

$$p_{i,m} = \frac{(I_i - \lambda_{i,m-1})w_i}{\sum_{j=1}^{M}\sum_{m=0}^{m-1}(I_j - \lambda_{j,m-1})w_i} \tag{36}$$

where $p_{i,m}$ is the probability of occupying network-forming species i with modifier ion m. I_i is the initial number of network-forming species of type i, $\lambda_{i,m-1}$ is the number of type i species already occupied before modifier m, M is the total number of modifier ions, and w_i is a correction weighting factor for the enthalpic penalty of occupying species type i. The expression of w_i is uncovered in the following derivation. The numerator in eq 36 is the number of species of type i available before the given occupation multiplied by the weighting factor of species i, and the denominator in eq 36 is a partition function, which sums all potential occupations of networking-forming sites to ensure the summation of all $p_{i,m}$ equals one.

To define a physical meaning to the weighting factors, we recall that the noncentral hypergeometric distribution is derived from the Boltzmann distribution function.[121] In statistical mechanics, this noncentral function describes the probability for a system to be in each state as a function of the system's temperature and the energy of that state

$$p_\alpha = \frac{\exp\left(-\frac{U_\alpha}{k_B T}\right)}{\sum_{\beta=1}^{\Gamma}\exp\left(-\frac{U_\beta}{k_B T}\right)} \tag{37}$$

where p_α is the probability of state α, k_B is Boltzmann's constant, T is the temperature of the system, U_α is the total energy of state α, and Γ is the total number of states, which in our scenario is equal to the total number of modifiers M. Work by Mauro[151] proposed to use the Boltzmann distribution to describe the modifier−former interactions in mixed former oxide glasses. With the model by Mauro,[151] the probabilities of states p_α are defined to be interactions between modifier ions and network-former sites i, and consequently, U_i becomes the free energy of this interaction, which can be described by entropic S and enthalpic H contributions:

$$p_i = \frac{\exp\left(-\frac{(H_i - S_i T)}{k_B T}\right)}{\sum_{j=1}^{M}\exp\left(-\frac{(H_j - S_j T)}{k_B T}\right)} \tag{38}$$

Next, we introduce the statistical entropy of the system as

$$S_i = k_B \ln g_i \tag{39}$$

where g_i is the degeneracy of the microstate i, i.e., the number of microstates consistent with a given macrostate for species i. Consequently

$$p_i = \frac{\exp\left(-\frac{H_i}{k_B T} + \ln g_i\right)}{\sum_{j=1}^{M}\exp\left(-\frac{H_j}{k_B T} + \ln g_j\right)} \tag{40}$$

which can be rewritten as

$$p_i = \frac{g_i \exp\left(-\frac{H_i}{k_B T}\right)}{\sum_{j=1}^{M} g_j \exp\left(-\frac{H_j}{k_B T}\right)} \tag{41}$$

The number of microstates consistent with the macrostate of species i divided by the total number of microstates consistent with the macrostate of the oxide glass will be the same as the relative fraction of species i divided by the total number of species. Since the fraction of a given structural species i in the glass changes with composition, g_i is equal to the number of available species i, which from eq 36 we found to be

$$g_{i,m} = I_i - \lambda_{i,m-1} \tag{42}$$

When calculating the probability of an interaction of species i with modifier m, the number of available (i.e., previously unoccupied) species i is given by the previous modifier occupation (i.e., $m - 1$). The final equation for the occupational probability of species i with modifier m is given by

$$p_{i,m} = \frac{(I_i - \lambda_{i,m-1})\exp\left(-\frac{H_i}{k_B T}\right)}{\sum_{j=1}^{M}(I_j - \lambda_{j,m-1})\exp\left(-\frac{H_j}{k_B T}\right)} \tag{43}$$

The probability distribution function in eq 43 is a noncentral hypergeometric distribution function, where the relative enthalpy H_i values set the enthalpic contribution and T is assumed to be equal to the fictive temperature T_f for $T < T_f$, since the structure is assumed to be frozen at the fictive temperature. The enthalpic weighting factor in eq 36 is therefore given by the Boltzmann weighting factor:

$$w_i = \exp\left(-\frac{H_i}{k_B T}\right) \tag{44}$$

5.2.2. Probabilistic Modeling Approach. While eq 43 provides a computationally efficient means to calculate the approximate spatiotemporal fluctuations, the exact distribution of fluctuations can be obtained by explicitly calculating the combinations and permutations of which of the available sites will be occupied. Each modifier ion will occupy a site within

https://doi.org/10.1021/acs.chemrev.1c00974
Chem. Rev. XXXX, XXX, XXX−XXX

the glass network, and which sites become occupied controls the final structure of the network. This probabilistic sampling approach calculates the probability of each possible atomic configuration forming without the use of stochastic means.

Each occupation of a network-former site will have a specific degeneracy based on the number of combinations of modifiers and network formers. For a system with a total number of M modifier ions and F network-former sites, m is the number of modifiers selected to occupy f network-former sites. Therefore, for occupation of sites, m of M modifier ions are selected (of M choose m) to occupy a specific network-former site (of F choose f), resulting in the degeneracy of site type F being

$$g_f = \binom{M}{m}\binom{F}{f} = \frac{M!}{m!(M-m)!}\frac{F!}{f!(F-f)!} \tag{45}$$

Each network-former site is distinguishable, while each modifier is considered indistinguishable.[153] Consequently, the individual modifiers do not contribute to a microstate's degeneracy or the system's entropy,[175] i.e.:

$$\binom{M}{m} = 1 \tag{46}$$

and

$$g_f = \frac{F!}{f!(F-f)!} \tag{47}$$

The degeneracy of the system is the product of each type of network-former site's degeneracy. If the system considers of two types of network-former sites, A and B, the total degeneracy of microstate i will be given by[153]

$$g_i = g_A g_B = \frac{A_T!}{a!(A_T-a)!}\frac{B_T!}{b!(B_T-b)!} \tag{48}$$

where A_T is the total number of A sites, a of which became occupied by a modifier ion, and B_T is the total number of B sites, b of which became occupied by a modifier ion.

Each event will have an associated enthalpy change due to the transition from an unoccupied to an occupied state. The enthalpic expense of changing configurations from an A unoccupied site to an A occupied site (i.e., occupying one A site) is H_A. Therefore, the probability of an A site occupation occurring is given by the Boltzmann probability

$$p_A = \frac{1}{Z_A} g_A \exp\left(-\frac{aH_A}{k_B T}\right) \tag{49}$$

Similarly, occupying one B site requires H_B causing the probability of creating the b sites to be

$$p_B = \frac{1}{Z_B} g_B \exp\left(-\frac{bH_B}{k_B T}\right) \tag{50}$$

where Z_A and Z_B are partition functions. The system's configurational enthalpy is the summation of the enthalpy required to occupy each site. For the system with two unique network-former sites A and B and one modifier type, H_{system} is then given by

$$H_{systen} = aH_A + bH_B \tag{51}$$

The total normalized probability of microstate i (out of all possible microstates Γ) forming can be therefore given by

$$p_i = \frac{p_A p_B}{\sum_\Gamma p_\Gamma} = \frac{g_i \exp\left(-\frac{(a_i H_A + b_i H_B)}{k_B T}\right)}{\sum_\Gamma g_\Gamma \exp\left(-\frac{(a_\Gamma H_A + b_\Gamma H_B)}{k_B T}\right)} \tag{52}$$

5.2.3. Structural Fluctuations. In glass systems, statistical mechanics has been used to describe distributions in site occupation, calculate the average concentration of structural units as a function of glass composition,[176−178] predict thermodynamic properties, and provide insights for structure−property−performance relationships. Required inputs for this technique are composition, temperature, and enthalpies of formation for each potential occupation site in the system. The limiting factor for statistical mechanics is the knowledge of the relevant bond energetics. *Ab initio* simulations can calculate the enthalpy formation values. Additionally, Bødker et al.[154] found that the model of eq 43 can be fit to experimentally obtained structural data of binary oxide glass systems to obtain H_i values specific to each modifier−structural unit pair. These enthalpy parameters can then be used to calculate the structural distribution in more complex glasses based on knowledge of all the contributing enthalpy values, without any additional fitting. Besides the average structure, recent studies have found that the approach is also well-suited to calculate and explore structural fluctuations in glass-forming liquids by computing the probability distribution function of modifier−former interactions.[115,119,152,153] By iterating over eq 43, a standard deviation to the mean probability can be obtained as a measure of the degree of structural fluctuations.

Figure 23a shows the calculated probability distributions for different interaction enthalpies for a modifier ion to interact with a site named B in a theoretical glass containing equal amounts of sites A and B.[115] The standard deviation for the probability density increases as ΔH decreases, where $\Delta H = H_A - H_B$. In other words, as the interactions become entropically more favorable, the propensity for structural fluctuations increases, which is obtained by either smaller ΔH values or by increasing the temperature, showing that the structural fluctuations are affected by the thermal history of the glass. Figure 23b shows results for a similar composition system, showing that, as long as the stochastic approach has enough runs to converge, it equals the results of the approach in section 5.2.2.

The benefit of the statistical mechanics approaches outlined in this section is that the full distribution of properties can be explored. Figure 24 plots the distribution in the number of constraints n_c as a function of temperature T and modifier concentration x calculated using the technique introduced in section 5.2.1 and topological constraint theory (introduced in section 5.4) for the example of a glass-forming system composition with two types of network-forming sites A and B, and one type of modifier. Figure 24 depicts the dependency of modifier concentration [M] on the distribution of constraints when the enthalpy difference between networking sites A and B equals zero (Figure 24a) and does not equal zero (Figure 24b). Figure 24a visualizes the concept that multiple glass-forming systems can have the same mean property value but different standard deviations, which aids in material design. For an application such as smart phone cover screens, a minimum standard deviation is ideal to prevent cracks from propagating; however, for applications that need to promote atomic rearrangement, systems with more broad distributions are ideal. By quantifying beyond just average property values,

https://doi.org/10.1021/acs.chemrev.1c00974
Chem. Rev. XXXX, XXX, XXX−XXX

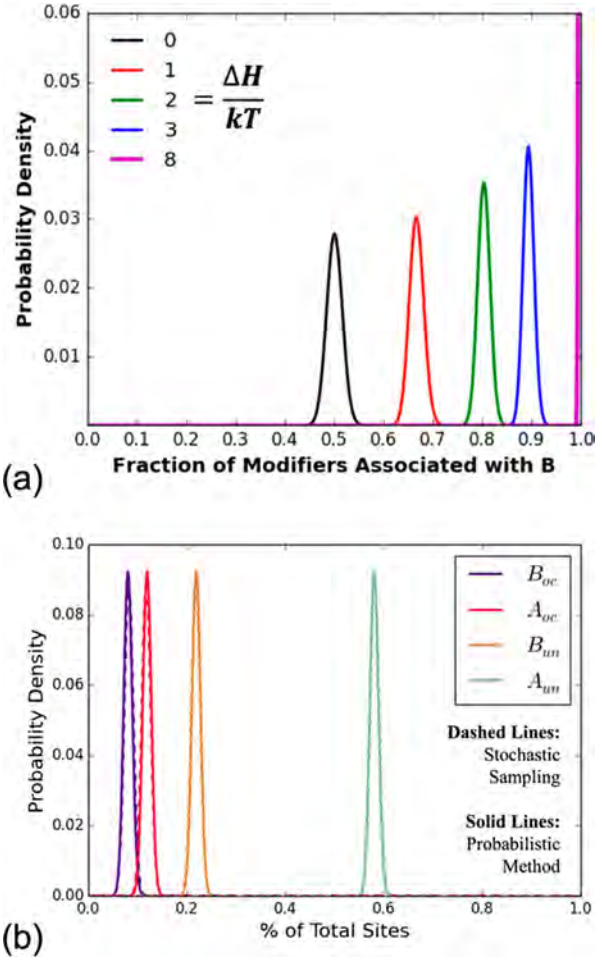

Figure 23. (a) Calculated distribution of modifiers associated with site B in a theoretical glass containing equal amounts of sites A and B. The distributions are calculated for five different values of $\Delta H/k_BT$ = 0, 1, 2, 3, 8 (unitless). As $\Delta H/k_BT \rightarrow 0$, the distribution follows a central hypergeometric distribution, while as $\Delta H/k_BT \rightarrow \infty$, it collapses to a Dirac δ function. Reprinted with permission from ref 115. Copyright 2018 Elsevier B.V. (b) The same type of compositional system but instead plotted as the distribution of occupied (oc) and unoccupied (un) network-forming sites. Each of the four distributions has superimposed dashed (stochastic sampling results) and solid (probabilistic method) lines plotting the two sets of results. Reprinted with permission from ref 153. Copyright 2020 Elsevier B.V.

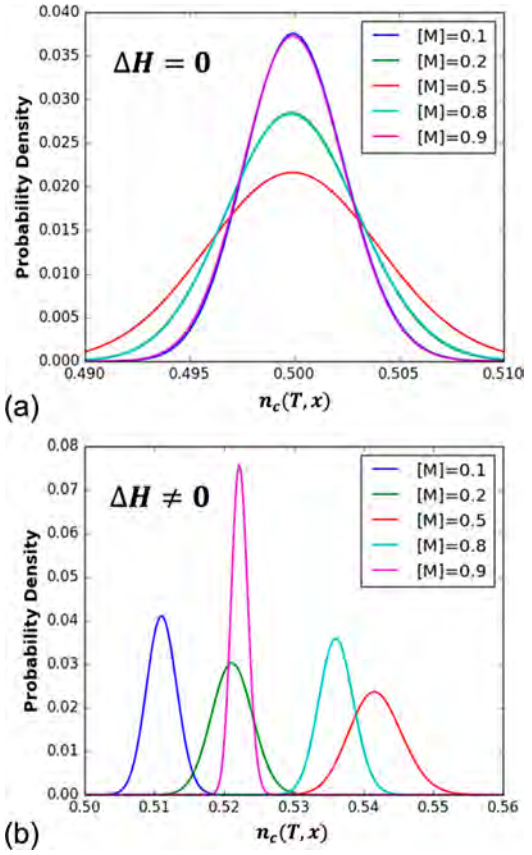

Figure 24. Effect of modifier concentration on the number of constraints $n_c(T, x)$ for a glass-forming system composed of two types of network-forming sites A and B and one type of modifier when (a) the enthalpy difference between A and B is negligible and when (b) the enthalpy difference between A and B is non-negligible, where $\Delta H = H_A - H_B$. Both figures adapted with permission from ref 115. Copyright 2018 Elsevier B.V.

systems can be more finely tuned to meet the property requirements of specific applications.

The statistical mechanical models introduced in this section have also been applied to real glass-forming systems to calculate structural properties like Q^n speciation.[119] Figure 25 illustrates the predicted Q^n speciation based on eq 43 as applied to $ZnO{\cdot}P_2O_5$ glasses. While Figure 23 illustrates a theoretical case for ΔH values, Figure 25a is an example of how ΔH values are obtained in a real glass system ($ZnO{\cdot}P_2O_5$) by fitting eq 43 to experimental data. The experimental data are obtained from NMR spectroscopy and shown as symbols.[119,179−181] These represent the average Q^n speciation for a given composition. The width of the calculated lines represents the standard deviation for the structural distribution, which is shown in Figure 25b as a function of ZnO concentration. Parts a and b of Figure 25 thus reveal the impact of the competition between entropy and enthalpy on site occupancy and the propensity for fluctuations around the average speciation values. For low concentrations of modifier ions, i.e., low x values in the figures, the enthalpy terms in eq 43 dominate the speciation. The contribution of entropy becomes more dominant as the population of Q^3 sites decreases and the magnitude of fluctuations increases. Q^1 and Q^0 species have more nonbridging oxygens, form less connected phosphate chains, and reduce the rigidity of the network. With less rigidity, atoms can more easily rearrange, enabling the maximum propensity for fluctuations in Q^n at the composition around x = 0.67.

5.2.4. Thermodynamic Fluctuations. The probabilistic sampling technique for statistical mechanics in section 5.2.2 directly calculates the explicit degeneracy and probability of each site being occupied. With an accurate representation of the possible microstates and their respective probabilities, we can calculate the system's configurational enthalpy H_{system}, configurational entropy S_{config}, and configurational Gibbs free energy G.[153] The Gibbs entropy S_G is a function of the probability of each individual microstate P_i, given by

$$S_G = -k_B \sum_i P_i \ln(P_i) \tag{53}$$

Note that P_i is the probability of an individual microstate (e.g., the occupation of one site A), while p_i is the probability of a set of microstates forming (e.g., the occupation of a number of A

https://doi.org/10.1021/acs.chemrev.1c00974
Chem. Rev. XXXX, XXX, XXX−XXX

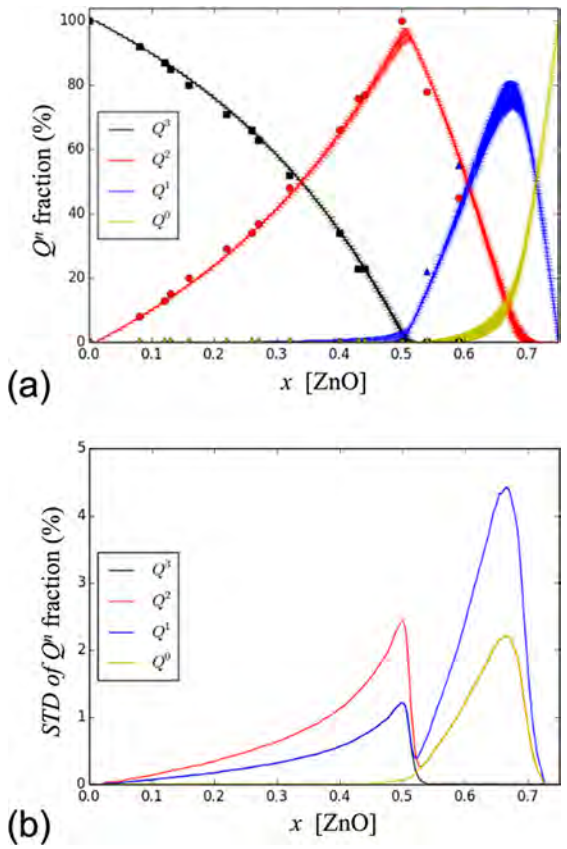

Figure 25. (a) Q^n speciation as a function of modifier concentration for ZnO phosphate glasses. Error bars represent the standard deviation of the Q^n species. The symbols represent experimental NMR data, which validates the predicted mean Q^n fractions (refs 19−21). (b) Standard deviation (STD) of Q^n species for ZnO. Both figures reprinted with permision from ref 119. Copyright 2019 American Chemical Society.

sites and b number of B sites). For each configuration i, the degeneracy of each state multiplied by the individual microstate probability determines the total probability of the set of degenerate microstates given by

$$p_i = \mathrm{P}_i g_i \tag{54}$$

Equation 53 written in terms of degenerate microstate probabilities is then given by

$$S_G = -k_B \sum_{i}^{\text{all states}} \frac{p_i}{g_i} \ln\left(\frac{p_i}{g_i}\right) \tag{55}$$

$\ln(p_i/g_i)$ is a constant over a configuration, meaning that eq 55 can be rewritten as

$$\ln\left(\frac{p_i}{g_i}\right) \sum_{i}^{\text{degenerate states}} \frac{p_i}{g_i} = p_i \ln\left(\frac{p_i}{g_i}\right) \tag{56}$$

Therefore, the configurational entropy becomes

$$S_G = -k_B \sum_{i}^{\text{all configurations}} p_i \ln\left(\frac{p_i}{g_i}\right) \tag{57}$$

and

$$S_{\text{config}} = -k_B \sum_i (p_i \ln(p_i) - p_i \ln(g_i)) \tag{58}$$

With eqs 51 and 58 the configurational Gibbs free energy can be calculated as such

$$G = H_{\text{system}} - TS_{\text{config}} \tag{59}$$

Therefore, this statistical mechanical approach has the capability to capture both structural and thermodynamic fluctuations.

As introduced in section 1, localized fluctuations in glass-forming systems affect many properties and practical applications such as Rayleigh scattering as a function of density fluctuations for low-loss optical fibers, high-performance displays, nucleation and phase separation, and mechanical properties such as fracture behavior.[7,8,121,176,178,182] The statistical mechanics-based model reviewed in this section offers a prediction of the degree of structural fluctuations as a function of both glass composition and thermal history. Additional research is needed to independently verify the predictions of fluctuations (such as those in Figure 25), for example, by comparing the structural results from multiple quenches of the same glass-forming composition with either low or high propensity for fluctuations. The knowledge offered by the model would then become a valuable tool when rationally designing glass compositions for applications affected by localized fluctuations as well as a tool to inform any subsequent measures of the network connectivity, such as presented in section 5.4. As such, the structural fluctuations can be directly translated into topological fluctuations that in turn control a wide range of properties.

5.3. Potential Energy Landscapes

A potential energy landscape is a map of a system's potential energy U as a function of all possible position coordinates of the particles, given by

$$U = U(\mathbf{r}_1, \mathbf{r}_2, \cdots, \mathbf{r}_N) > N\lambda \tag{60}$$

where N is the number of interacting particles in the system, $\mathbf{r}_1$,$\mathbf{r}_2$, ..., $\mathbf{r}_N$ are the position vectors of each particle, and λ is a constant denoting the potential energy per particle for the lowest energy state. Local minima in potential energy, called inherent structures, represent mechanically stable arrangements of the system. A condensed material of N particles has a continuous $(3N)$-dimensional potential energy landscape; a one-dimensional pictograph of a potential energy landscape is provided in Figure 26a. The continuous landscape is divided into a discrete set of basins, where each basin represents a region of configurational phase space that leads to the formation of the corresponding inherent structure. As seen in Figure 26a, each basin corresponds to one inherent structure. The probability of the system occupying a given basin defines the statistics of the formation of each atomic configuration, and the evolution of the occupation probabilities (in time and space) dictates the presence of configurational spatiotemporal fluctuations. This section introduces potential energy landscapes (and enthalpy landscapes) to discuss two sampling techniques to evaluate spatiotemporal fluctuations in glass-forming systems.

Within the landscape framework, the activation barrier heights govern the kinetic propensity of the system to transition among the various atomic configurations and the basin enthalpies and degeneracies determine the thermody-

https://doi.org/10.1021/acs.chemrev.1c00974
Chem. Rev. XXXX, XXX, XXX−XXX

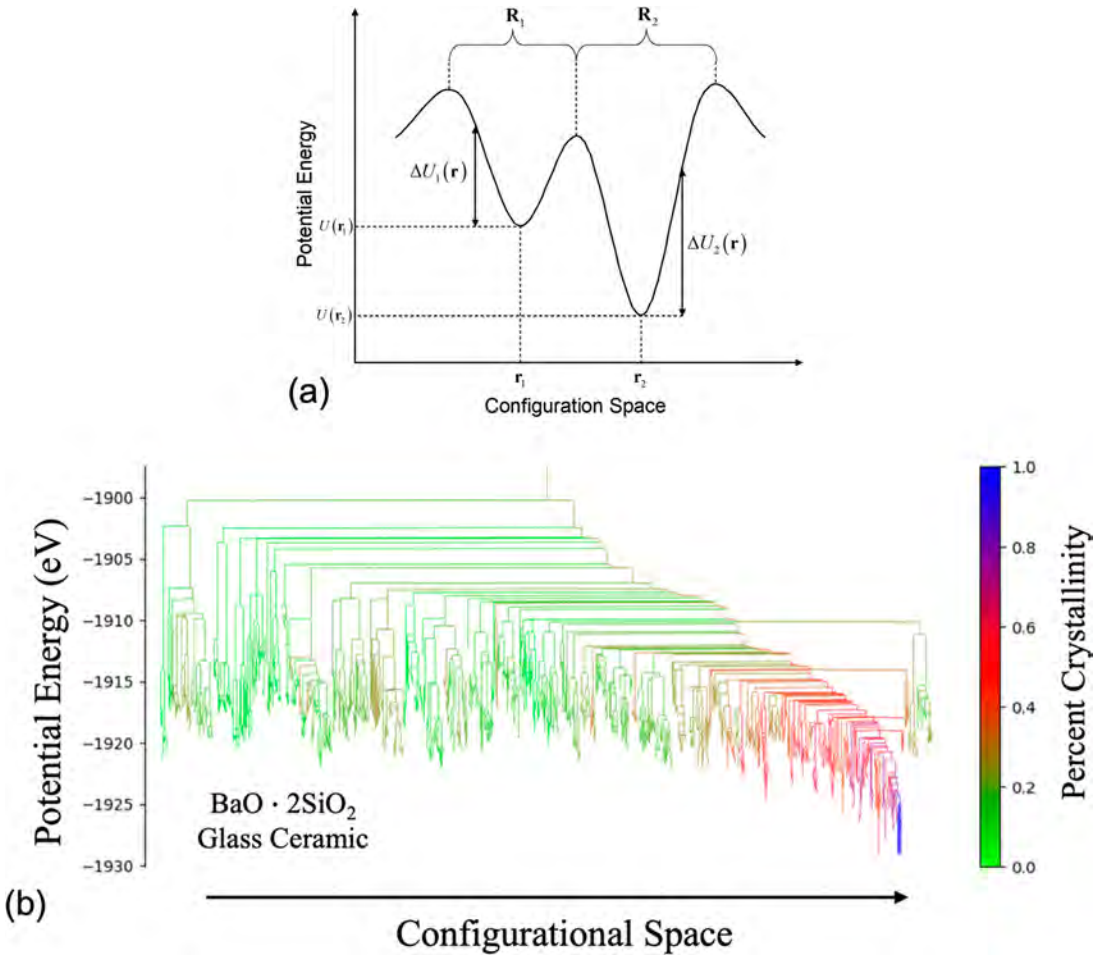

Figure 26. (a) Schematic of a potential energy landscape for a system with two basins (i.e., two inherent structures) where r_1 and r_2 represent inherent structures and R_1 and R_2 are the regions corresponding with basin 1 and basin 2. (b) Potential energy landscape of barium disilicate glass-ceramic calculated using ExplorerPy, where the colors represent the percent crystallinity of the sample, the x-axis is the phases position in arbirary configurational space, and the length of the vertical lines represents the change in potential energy (eV) required to overcome the energetic barrier to transition between basins. Both figures reprinted with permission from ref 34. Copyright 2020 Elsevier Inc.

namically stable configurations. Since the calculation of creating potential energy landscapes is not specific to spatiotemporal fluctuations or glass-forming systems, refer to ref 34 for details of the mathematics behind the model. ExplorerPy[183] is a python-based open-source software package which interfaces with molecular dynamics to calculate the inherent structures and transition points for a given system. Figure 26b shows an example potential energy landscape calculated using ExplorerPy for a barium disilicate glass-ceramic. This visualization of a landscape is called a disconnectivity graph, where the x-axis plots the available atomic arrangements in configurational phase space and the y-axis quantifies the potential energy of each inherent structure.[34] The length of each vertical line represents the potential energy required to transition between two given basins.

While potential energy landscapes are suitable for modeling systems under isochoric conditions (constant volume V), many real systems exist under isobaric conditions (constant pressure P), which require the use of enthalpy landscapes, and a zero-temperature enthalpy H landscape can be given by

$$H = U(\mathbf{r}_1, \mathbf{r}_2, \cdots, \mathbf{r}_N) + PV \tag{61}$$

where the y-axis of a disconnectivity graph becomes enthalpy instead of potential energy, and volume is included as a coordinate, making the enthalpy landscape $(3N+1)$-dimensional. Both landscape forms are solved using the same mathematical and computational approaches. For the remainder of this section, when the text refers to potential energy landscapes or enthalpy landscapes, note that the information discussed applies to both.

While the energy and enthalpy landscapes themselves are independent of time, the way the system samples the landscape evolves with the full thermal history of the system. There are two conventional techniques to calculate the time evolution of the basin occupational probabilities within a landscape to capture the configurational fluctuations. The first is a deterministic method which involves solving a set of master equations, and the second is a stochastic method based on kinetic Monte Carlo.

5.3.1. Deterministic Sampling: Master Equations. The occupational probability of each basin i is given by p_i. Recall from section 5.2 that the occupational probability of available equilibrium atomic arrangements is given by eq 41. The same statistical mechanics equation applies to equilibrium occupational probabilities for landscapes. Note that, in equilibrium, all atomic configurations are accessible, allowing eq 41 to omit

https://doi.org/10.1021/acs.chemrev.1c00974
Chem. Rev. XXXX, XXX, XXX−XXX

considering the effect of transition rates between basins. Once the glass-forming system transitions into the vitreous glassy state, some atomic configurations will be kinetically inaccessible, reducing those basin's occupational probabilities to zero. To represent the rate of change of occupation probabilities in nonequilibrium systems, the equations must consider the evolution of transition rates between basins. This is solved using master equations.

Master equations are a set of Ω coupled differential equations, which solve the evolution of the basin occupation probabilities over time, where Ω is the number of basins.[34,104,184−188] The probability of occupying basin i is the rate to transition into basin i from any other basin (K_{ji}) minus the rate of transitioning out of basin i into any other basin (K_{ij}), weighted by the probability of originally being in a given basin:

$$\frac{\mathrm{d}p_i(t)}{\mathrm{d}t} = \sum_{j\neq i}^{\Omega} K_{ji}[T(t)]p_j(t) - K_{ij}[T(t)]p_i(t) \tag{62}$$

The transition rate between basins is given by the enthalpy or potential energy activation barrier of the transition ΔH, the probability of originally being in basin i, and the frequency of attempts to transition (given by vibrational frequency ν_{ij}):

$$K_{ij}[T(t)] = \nu_{ij} \exp\left(-\frac{\Delta H(i \rightarrow j)}{k_B T(t)}\right) \tag{63}$$

The rate of change of occupational probabilities of basin i is therefore given by

$$\frac{\mathrm{d}p_i}{\mathrm{d}t} = \sum_{j\neq i}\left(p_j\nu_{ji}\exp\left[-\frac{H^*(j \rightarrow i)}{kT}\right] - p_i\nu_{ij}\exp\left[-\frac{H^*(i \rightarrow j)}{kT}\right]\right) \tag{64}$$

The occupation probabilities for the nonequilibrium vitreous glassy state are therefore calculated by determining equilibrium probabilities from eq 41, and then solving for the rate of change of probability based on the amount of elapsed time t using eq 64. The same equations apply to potential energy landscapes by substituting ΔH as ΔU.

As temperature, composition, and time change, so do the most dominant atomic configurations, and therefore all associated properties. Note that eq 64 is time-dependent allowing this approach to capture both spatial and temporal fluctuations. The benefit of this deterministic approach is that exact occupational probabilities are known, allowing the full distribution of fluctuations to be quantified. The downside is the computational cost of solving the master equation for transitions between all atomic configurations.

5.3.2. Stochastic Sampling: Kinetic Monte Carlo. An alternative method to explore occupational probabilities in energy landscapes is using kinetic Monte Carlo (kMC). kMC is a stochastic technique where the system jumps among individual microstates, such that the full set of inherent structures and the transitions between all basins do not need to be known. Instead, possible transitions are randomly selected from the current configuration, and the process repeats itself multiple times to calculate the time evolution of the system. The kMC approach can be applied multiple times with different random seeds to calculate fluctuations in the ensemble domain.[34,43]

Note that MMC (discussed in section 5.1.4) is designed for atomic studies but lacks a time step, making it incapable of predicting the real timeline in which the structural changes occur. In MMC, when an atom is randomly selected and displaced, it is the energy difference between the two states that sets the transition probability. kMC is a form of MC that allows for a time step, therefore enabling dynamics to be explored. With kMC, the transition probability is calculated considering the energy difference between the two states as well as the barriers to realize a new state. kMC is under-utilized in the glass community because (i) the computational cost for finding the barriers is extremely high, (ii) traditionally there has been a lack of convenient software (recently, Henkelman and co-workers[189−192] have produced a plethora of easy-to-use tools), and (iii) comparison of results is challenging due to the difficulty in finding barriers.

kMC can access long time scales, and the landscapes do not need to be mapped beforehand (unlike the master equations approach) since the transition points are calculated at each step. However, calculating the transition points so often is computationally expensive, and the kMC approach is therefore much slower. Another downside to the kMC stochastic approach is that the system only occupies one point in phase space, so it does not capture the full distribution of possible configurations unless kMC is run multiple times. The master equation approach from section 5.3.1 obtains the full set of occupational probabilities over time so the full configurational fluctuations are immediately obtained. Also, arbitrary time scales can be achieved by taking advantage of broken ergodicity. However, the relevant configurations in the enthalpy or energy landscapes must be fully mapped prior to applying the master equation approach.

5.3.3. Spatiotemporal Fluctuation Investigations. Energy and enthalpy landscapes are models that account for composition and thermal history to offer predictive calculations of macroscopic properties in glass-forming systems.[109] Sampling of landscapes is a newly developing field that has already shown promise in predicting glass transition behavior, relaxation, viscosity, nucleation and growth rates, and thermodynamic properties such as configurational entropy, enthalpy, and Gibbs free energy.[183,193] Figure 27 shows results by Mauro and Loucks,[109] who computed molar volume and enthalpy distributions of selenium glass using the deterministic master equations sampling approach. The distribution in both properties is shown as the gray-scale-normalized probability density along the z-axis. These landscape techniques have also been shown to be reproducible and experimentally validated. Mauro and Loucks[109] validated their calculations against thermal expansion coefficient and heat capacity data using their distribution analysis of selenium glass enthalpy and molar volume. At 300 K, upon reheating at a rate of 3 K/min, the computed linear expansion coefficient was found to be 45.3 ppm/K and the experimental value was 44.5 ppm/K ± 3%. Similarly, Grosse et al.[194] reported an experimental heat capacity of 26.4 J/(mol K); Mauro and Loucks computed a heat capacity of 27.1 J/(mol K), hence validating the ability for the landscape approach to capture thermodynamic fluctuations and properties. Since the landscape approach calculates the full distribution of occupation probabilities, and hence property fluctuations, like the statistical mechanical models introduced in section 5.2, the next application for fluctuation studies seems open-ended and appears to be a field worthy of further investigation.

https://doi.org/10.1021/acs.chemrev.1c00974
Chem. Rev. XXXX, XXX, XXX−XXX

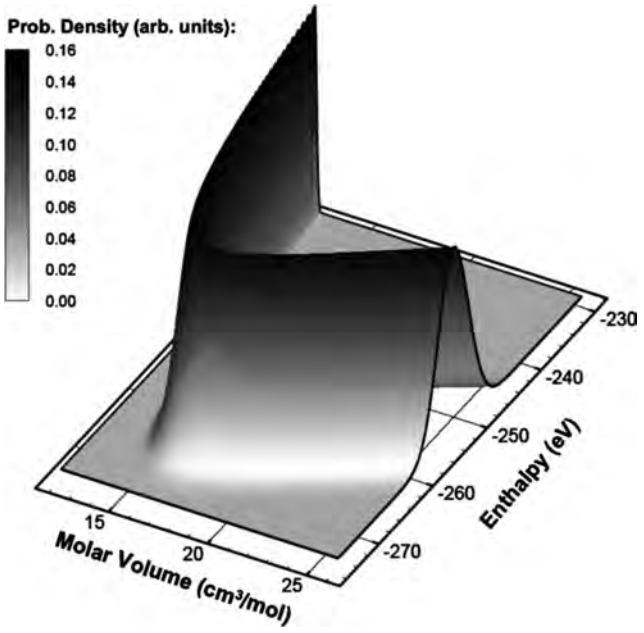

Figure 27. Three-dimensional plot of the distribution (shown as the normalized probability density in arbitrary units) of inherent structure enthalpies and molar volumes for a 64-atom selenium system, solved using the master equation landscape sampling technique. Reprinted with permission from ref 109. Copyright 2007 American Physical Society.

5.4. Topological Constraint Theory

With the structural fluctuation understanding from MD simulations, statistical mechanical models, and mapping energy landscapes, conventional mean-field models can be extended to explore fluctuations, as exemplified with topological constraint theory (TCT). TCT, also known as rigidity theory, is a mathematical technique to elucidate topological understanding from structural information, which has been widely used to predict the composition and temperature dependence of glass properties such as the glass transition temperature, fragility, viscosity, hardness, crystallization, phase separation, crack propagation, dissolution rate, and glass relaxation.[106,143,166,195−213] As a proof of concept, Figure 28 plots the experimental validation of the TCT ("model") predictions for the composition dependence of the glass transition temperature of a sodium borate glass.[196,214−218] Further discussions of applications of TCT, specifically in the context of exploring the implications of structural fluctuations in glass-forming systems, are discussed in section 5.4.4.

TCT is based on the pioneering works of Phillips,[160,219] Thorpe,[213,219−221] Gupta,[167,222,223] and Cooper[222,224] who first proposed treating glass as a network of constraints, analogous to mechanical trusses. The number of interatomic constraints n_c (i.e., the number of rigid bonds and angles per atom that confine the atomic position) is compared to the available translational degrees of freedom f.[225] If $\langle n_c \rangle < f$ the system is underconstrained ("flexible" or "floppy") and the atoms can easily rearrange into the minimal energy configuration of the crystalline state. If $\langle n_c \rangle > f$ the system is overconstrained ("stressed-rigid"), which also drives the system to crystallization to eliminate the additional stress. If $\langle n_c \rangle = f$ the system is isostatic, which is the ideal glass-forming condition and means the atoms have lost all translational degrees of freedom. Following an energy landscape point of view, each topological

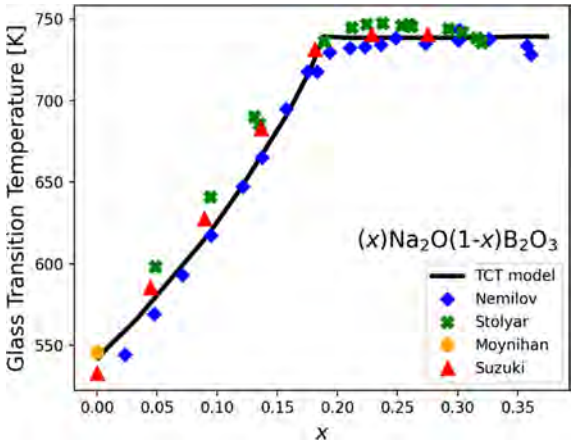

Figure 28. Temperature-dependent constraint theory provides an analytical prediction of the composition dependence of the glass transition temperature T_g in the sodium borate system $x\mathrm{Na_2O}(1-x)\mathrm{B_2O_3}$. The solid black lines show the TCT model predictions, and the data points are experimental data taken from Nemilov (ref 214), Stolyar et al. (ref 215), Moynihan (ref 216), and Suzuki et al. (ref 217). Figure adapted with permission from ref 196. Copyright 2009 American Institute of Physics.

constraint creates an energy minimum (i.e., a basin) inside the energy landscape, while internal degrees of freedom ($f - \langle n_c \rangle$) lead to the formation of channels between these energy minima.[108] The channels allow for atomic reorganizations to occur with low energy barriers. Consequently, it is easier for glass networks with small $\langle n_c \rangle$ to adapt to external stimuli than for those with large $\langle n_c \rangle$. Note that the remainder of this review article will consider systems in three-dimensional space, i.e., where $f = 3$.

TCT was originally proposed as a mean-field technique, and consequently, in literature n_c is typically defined as the *average* number of constraints per atom.[160,167,213,219−225] With the progression of statical mechanical approaches, TCT has developed the capability to quantify distributions of n_c, which is the focus of this discussion. Thereby, in the context of this review article, $\langle n_c \rangle$ refers to the *average* number of atomistic constraints, while n_c refers to the *distribution* of the number of atomistic constraints, and fluctuations in n_c arise solely from the fluctuations in glass structure.

Mathematically, the average number of constraints per atom is the sum of each atom's radial and angular constraints. Since each bond is shared between two atoms, the radial constraints for each atom are given by $\langle r \rangle/2$ where $\langle r \rangle$ is the average atomic coordination number. For an atom with two neighbors (i.e., when $\langle r \rangle = 2$), there is one angle that needs to be defined. Each new bond requires two additional independent angles, so the number of angular constraints is given by $2\langle r \rangle - 3$. The average number of constraints per atom for all atoms in the system is hence given by[1]

$$\langle n_c \rangle = \frac{\langle r \rangle}{2} + (2\langle r \rangle - 3) \tag{65}$$

Setting $\langle n_c \rangle = 3$ defines an isostatic network, and so $\langle r \rangle = 2.4$ is the corresponding ideal atomic coordination number, which is called the rigidity percolation threshold (obtained by solving eq 65 for $\langle n_c \rangle = 3$). Gupta and Mauro[166,196] extended this theory by implementing a probability function for constraint rigidity that accounts for thermal effects and varying strengths of different types of bonds. The next two sections introduce

https://doi.org/10.1021/acs.chemrev.1c00974
Chem. Rev. XXXX, XXX, XXX−XXX

two implementation techniques to calculate the distribution of n_c.

5.4.1. Temperature-Dependent Constraint Model. On the basis of the work of Gupta and Mauro,[166,196] $n_c(T, x)$ is considered to be separable, following the double summation[166]

$$n_c(T, x) = \sum_i N_i(x) \sum_c \varpi_{i,c} q_c(T) \tag{66}$$

where the first sum is over the network-former species i and the second sum is over the various types of constraints c. $N_i(x)$ is the mole fraction of network species i in composition x (typically implemented as the distribution of short-range order species which were introduced in section 1.1), $\varpi_{i,c}$ is the number of constraints type c associated with the species type i, T is the absolute temperature of the system, and $q_c(T)$ is the temperature-dependent rigidity of constraint type c. The microscopic rigidity $q_c(T)$ defines a specific type of angle's or bond's resistance to bending, stretching, twisting, breaking, or other deformations. The temperature and composition dependence of each constraint's rigidity impacting the network's total number of rigid constraints per atom (often referred to as network rigidity) is $n_c(T, x)$, which is captured in eq 66.

Rigidity, $q_c(T)$, is a unitless scaling factor that ranges from 0 (fully flexible) to 1 (fully rigid). The rigidity for each constraint c is an independent function of temperature T given by[156,166]

$$q_c(T) = \left[1 - \exp\left(-\frac{F_c^*}{k_B T}\right)\right]^{\nu t_{obs}} \tag{67}$$

where ν is the vibrational attempt frequency, t_{obs} is the observation time, and νt_{obs} can typically be approximated as 1000.[196] F_c^* is the activation free energy for breaking constraint c, given by[166]

$$F_c^* = -k_B T_c \ln(1 - 2^{-1/\nu t_{obs}}) \tag{68}$$

T_c is the onset temperature for constraint c, which defines the temperature at which the probability of breaking the constraint is exactly 50%, i.e., $q_c(T) = 0.5$.

Equation 67 is derived by considering the probability of an atom remaining trapped in a free energy well, as represented in Figure 29. An atom needs only to escape once; if the escape is

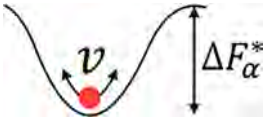

Figure 29. Rigidity modeled as an atom in a free energy well. ν is the vibrational attempt frequency, and F_c^* is the activation free energy for breaking the constraint c. If the particle successfully escapes the well during the observation time t_{obs}, the constraint is broken and considered flexible. Reprinted with permission from ref 153. Copyright 2020 Elsevier B.V.

successful, then the constraint is broken. In eq 67, $1 - \exp(-F_c^*/k_B T)$ is the probability of *not* escaping in a single attempt, and the exponent νt_{obs} accounts for the total number of escape attempts, i.e., the total number of vibrations within the observation time period.

If the probability of a constraint breaking is zero, i.e., $q_c(T) = 1$, then the constraint is fully rigid. When $q_c(T) = 0$, the constraint is fully flexible. Values of $q_c(T)$ between 0 and 1 indicate a degree of partial rigidity, meaning a fraction of the constraints equal to $q_c(T)$ are rigid, while the remaining fraction $(1 - q_c(T))$ are flexible. Figure 30 shows a plot of eq

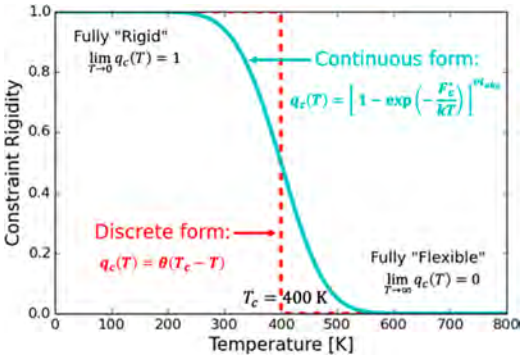

Figure 30. Rigidity of constraint c, $q_c(T)$, plotted as a function of temperature using the discrete form (shown in red) and continuous form (shown in blue), about an onset temperature T_c = 400 K. The discrete function is a unit step function about the onset temperature T_c. The continuous form is a function of the free energy to break constraint c F_c^*, Boltzmann's constant k (referred to as k_B in this review article), vibration frequency ν, and the observation time t_{obs}. Note that both the continuous and discrete forms of the TCT model are effective means to calculate the number of rigid constraints per atom within a disordered structure (refs 115, 119, 162, and 226). Inspired by figures in ref 106.

67 to visualize the temperature dependency of rigidity about the onset temperature T_c. As $T \to 0$, there is zero thermal energy available to break the constraints, so all constraints are fully rigid ($q_c(T) \to 1$). As $T \to \infty$, thermal energy becomes large enough to enable all constraints to break easily ($q_c(T) \to 0$); hence, the constraint is considered flexible.

An important challenge is to determine the $q_c(T)$ function or at least the constraint onset temperature. In the early studies, the onset temperatures associated with each particular type of constraint were unknown and estimated either from experimental glass transition temperature data or considered as fitting parameters.[195,227,228] Later, in the work of Bauchy and Micoulaut,[32] MD simulations were used to estimate the onset of constraint rigidity by considering the partial bond angle distributions as discussed in section 5.1. Onset temperatures are time-scale-dependent (and therefore also cooling-rate-dependent), so to be consistent with experimental time scales, the onset temperature values determined by MD are then rescaled by the MD activation free energies curve.[229]

5.4.2. Discrete Temperature-Dependent Constraint Model. Given the sharp cutoff of rigidity being 0 (fully flexible) or 1 (fully rigid) seen in Figure 30, a simplifying approach for implementing TCT is to employ the discrete model. In this case, the current temperature of the system dictates if a type of constraint is to be counted, i.e., if $T < T_c$, constraint c is considered fully rigid, i.e., $q_c(T) = 1$. There is a finite number of bonds and angles in the system; therefore, there is a finite amount of each type of constraint. With an understanding of the short-order structural units present in the system, the total number of rigid constraints per atom in the system is the sum of each type of constraint i that is considered rigid:[230]

$$n_c(x) = \sum_i n_{c,i}(x) \tag{69}$$

https://doi.org/10.1021/acs.chemrev.1c00974
Chem. Rev. XXXX, XXX, XXX−XXX

The equations that define each $n_{c,i}(x)$ and the number of constraints within each short-range order species will vary based on the glass-forming system. Table 2 lists some common

Table 2. Examples of the Discrete Temperature-Dependent TCT Model Being Implemented for Several Glass-Forming Oxide Systems

glass-forming system	reference number
silicate	229, 231, 232
borate	196, 227
phosphate	169, 230, 233
germanate	234
tellurite	235
aluminosilicate	236
borosilicate	228
phosphosilicate	237, 238
borophosphate	197, 201
boroaluminosilicate	202

oxide glass families and references to derive their respective constraint counting equations. Typically, there are six types of constraints to consider: in order of decreasing onset temperature, they are α, β, γ, δ, ε, and ς. In an oxide system where NF is a network former and NM is a network modifier, α represents the O−NF−O angular constraint. There are two linear constraints to consider; β is the NF−O bond constraint, and γ is the NM−O bond constraint. The remaining three types of constraints are angular: the NF−O−NF δ angular constraint occurring at each bridging oxygen, the NF−O−NM ε constraint incorporating the nonbridging oxygens, and the O−NM−O ς angular constraint. In a glass-forming system, each short-range order species will have a defined number of these angles and bonds based on the presence of bridging oxygens and nonbridging oxygens (see section 1.1).

Note that, for this discrete approach, the calculations for the composition dependence of network rigidity additionally require scaling factors relating the fraction of the short-range order species per network-former atom and per modifier ion. The temperature dependence is captured by considering which constraints are rigid or floppy based on the amount of thermal energy available in the system. It should also be noted that, while the discrete model works well for predicting properties such as hardness or dissolution rate at a fixed temperature, the full temperature dependence of constraint rigidity is needed for predicting properties such as the liquid fragility index, which is a temperature-derivative property.[196]

5.4.3. Pressure-Dependent Constraint Model. As of the publication of this review article, extending TCT to incorporate pressure dependence is less studied than that of composition or temperature dependence. Nevertheless, rigidity induced by pressure has been obtained in simple network formers from MD simulations.[239] Additionally, recent work by Bauchy and Micoulaut[240] has established an approach using MD and TCT to capture the pressure dependence of network rigidity. Pressure tends to increase connectivity, which, in turn, tends to increase the rigidity of the network. With changing pressure, the short-range structural units have the potential to transition. For example, silicate systems under pressure can experience a tetrahedral to octahedral conversion of the silicon environment,[199,241] and in borate systems, pressure induces the transition of 3-fold to 4-fold coordinated boron. Network rigidity is dependent on the short-range structural units and atomic coordination observed at a specific pressure; therefore, the pressure dependence of the number of constraints per atom can be modeled. However, additional work is still needed to understand how pressure affects the constraint rigidity at a specific temperature.

5.4.4. Implications of Exploring Property Fluctuations with TCT. A consequence of a disordered structure is the presence of localized fluctuations in atomic coordination, which impact how an atomic region behaves on the macroscopic scale. For example, even if the system achieves $\langle n_c \rangle = 3$, localized underconstrained and overconstrained regions provide ideal paths for rapid crack propagation (exemplified in section 9). Similarly, in a localized overconstrained region, the additional rigidity induces localized stresses, and elimination of these stresses can be achieved through imposing crystalline order or inducing phase separation, which results in the formation of glass-ceramics (refer to sections 7 and 8).[225,242] Fluctuations in localized constraints also define the variance in observed Rayleigh scattering, which dictates the power attenuation in glass optical fibers (refer to section 10). In general, network topology is responsible for critical behaviors in several thermal, mechanical, and optical properties, and hence, TCT enables direct calculation of macroscopic properties in glass-forming systems.[106,143,166,195−210,212,213] Work exemplifying such TCT fluctuation-property predictions are thoroughly discussed in sections 6−10; therefore to reduce redundancy, the next section will instead focus on unexplained phenomena that are able to be explored since the development of the fluctuations-based TCT approach.

5.4.5. Adaptable Network Topology and the Intermediate Phase. The extension of TCT to explore distributions in constraints has broadened the understanding of glass macroscopic properties, but it has also enabled scientists to explore the physics of atomic rearrangements more thoroughly. When TCT was originally proposed by Phillips and Thorpe,[219] the isostatic state was predicted to be achieved at a single composition, i.e., at the rigidity percolation threshold, which is represented in Figure 31a. However, in 1999 experiments by Boolchand and co-workers[243−245] revealed a finite width of compositions maintaining the minimum enthalpy state of the isostatic condition; this finite-width region has since been termed the intermediate phase. An example of experimental results highlighting the intermediate phase is given in Figure 31b, which shows modulated differential scanning calorimetry (MDSC) results for a Ge_xSe_{1-x} chalcogenide glass system. The width of a system's intermediate phase is called the reversibility window. Reversibility windows for several oxide and chalcogenide glass-forming systems exhibiting adaptable network topologies are given in Figure 32.

A challenge when studying the intermediate phase is the apparent irreproducibility of some of the experiments, causing the physical origins and very existence of the phase to be controversial. Evidence of the intermediate phase has been found through numerical studies,[248] analysis of finite cluster sizes,[123] MDSC,[243−245,249,250] and Raman scattering,[244,249−252] but some results also attribute the observed finite widths as possible experimental artifacts,[253−256] for example, regarding the interpretation of the nonreversing enthalpy obtained by MDSC.[257] While the existence of the intermediate phase and the underlying mechanisms are thus still a point of debate, the studies typically agree on the central role of fluctua-

https://doi.org/10.1021/acs.chemrev.1c00974
Chem. Rev. XXXX, XXX, XXX−XXX

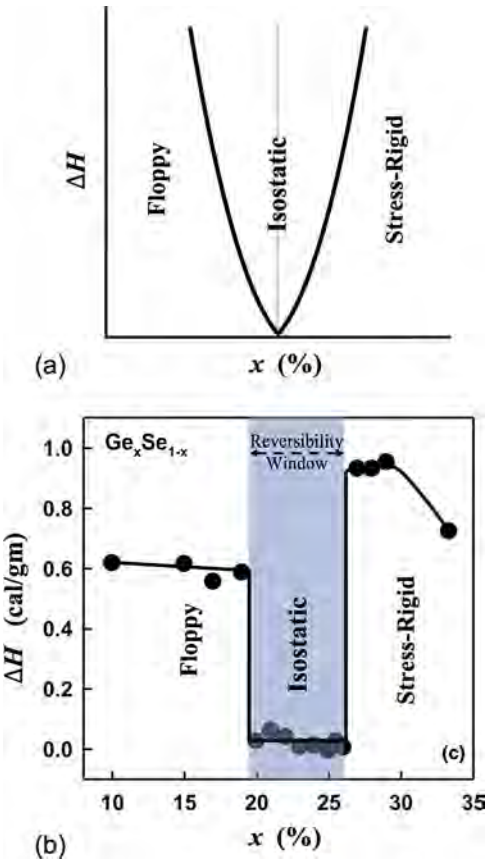

Figure 31. Visual representation of (a) the Phillips−Thorpe single isostatic composition theory and (b) the Boolchand intermediate phase theory. Panel b plots enthalpy ΔH as a function of composition x for Ge_xSe_{1-x} from MDSC experiments. The global minimum in enthalpy corresponds to the isostatic condition, $\langle n_c \rangle = 3$. Panel b reprinted with permission from ref 246. Copyright 2012 The American Ceramic Society and Wiley Periodicals, Inc.

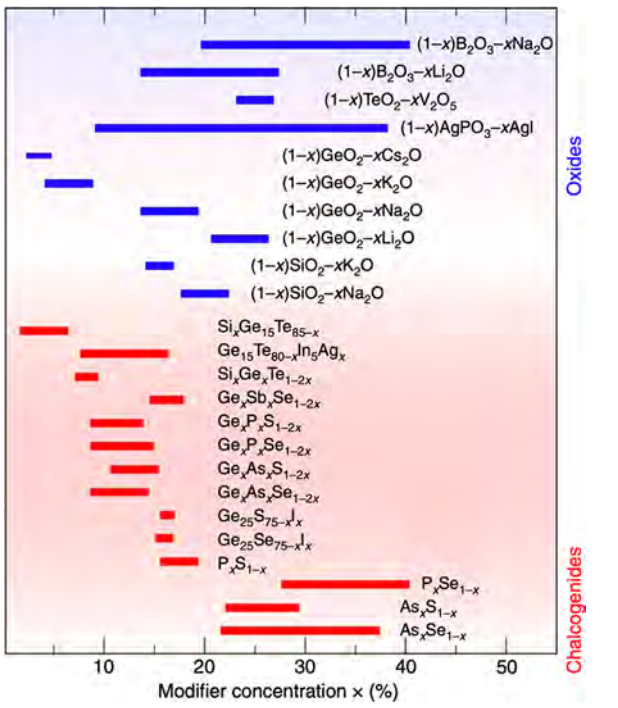

Figure 32. Observed reversibility window from MDSC experiments for various oxide (shown in blue) and chalcogenide (shown in red) glass systems, where the magnitude of a glass sytem's reversibility window is given as the length of the corresponding horitzontal line. Adapted with permission from ref 247. Copyright 2015 Macmillan Publishers Ltd.

tions.[36,165,248,258−260] More specifically, it is proposed that structural fluctuations in the system enable the atoms to self-organize into a stress-free state while still maintaining a noncrystalline structure of the glass. These structural rearrangements relieve additional stresses, driving the system back toward a lower free energy state and hence maintain the isostatic condition of $\langle n_c \rangle = 3$. While causation has yet to be theoretically or experimentally confirmed, a correlation between increased fluctuations in network rigidity and the increased width of the reversibility window has been modeled by Kirchner et al.[152] Also, work by Yan[261] has attributed the increase in entropy as the driving factor for the increased structural disorder when the glass system is close to the rigidity percolation threshold.

5.5. Machine Learning

Unveiling the structural origin of dynamic or mechanical fluctuations in glasses is a complex task as it requires pinpointing the key influential structural features that govern fluctuations within the complex disordered structures of glasses, which is essentially a "needle in a haystack" problem.[262] To identify the structural features that govern dynamical/mechanical fluctuations in glasses, one option is to adopt intuition- or physics-based metrics (e.g., excess entropy,[263] free volume,[264] structure symmetry[265]). Although these approaches are physically sound, the applicability of these local metrics can be highly system-specific.[266,267] As a promising alternative route, the key influential structural features that govern dynamical/mechanical fluctuations in glasses can be identified by machine learning (ML), wherein a ML local structural quantity is built to exhibit a maximum correlation with local dynamical/mechanical behaviors. Since such a ML approach does not require any preexisting physical knowledge or intuition, it has the potential to offer a more generic framework to identify structure−property relationships in different glassy systems. In the following sections, we review several developing ML techniques that can pinpoint influential structural features within the disordered structure of glasses.

5.5.1. Machine Learning Methods to Model Correlations of Spatiotemporal Fluctuations. Here we introduce several supervised and unsupervised ML techniques currently under development for feature identification of spatiotemporal fluctuations in disordered materials:

(1) The softness approach
(2) Graph neural networks (GNNs)
(3) Alternative approaches, including nonparametric models and unsupervised approaches

First is the pioneering "softness" machine-learned metric, which has found much success in recent years.[268−273] Cubuk et al.[274] first introduced this method where they define a microstructural quantity, termed "softness", based on a supervised ML model. To determine the "softness" of a particle, a set of structural functions are defined to identify particles that are prone to rearrange their positions with their atomic neighbor. A particle with higher softness means the particle shows an enhanced spatial correlation with the regions undergoing large rearrangements.

https://doi.org/10.1021/acs.chemrev.1c00974
Chem. Rev. XXXX, XXX, XXX−XXX

In the softness approach, the atoms are first divided into two groups (e.g., mobile and immobile). In practice, for each atom i, the output y_i is labeled as 0 or 1 according to whether the displacement of this atom is lower or higher than a threshold value (which typically corresponds to the magnitude of atomic vibrations). A binary classification model is then trained to map selected structural features F that characterize the local structure around each atom i to its mobile or immobile state y_i. In detail, the output predicted by the model y_i^{P} (i.e., a number between 0 or 1) for atom i can be expressed as a function of the local structure around atom i:

$$y_i^{\mathrm{P}} = \Gamma(\mathbf{w}, F(\mathbf{X}_i)) \tag{70}$$

where $\mathbf{X}_i$ is a vector that contains the coordinates of the atoms that are located in the neighborhood of atom i, F is a function that transforms these coordinates $\mathbf{X}_i$ into some structural features (e.g., radial and order parameters, see below), $\mathbf{w}$ is a vector that assigns a distinct weight to each of the features $F(\mathbf{X}_i)$, and Γ is a function (specific to the ML model, e.g., sigmoid for logistic regression) that transforms the weighted local structural features F to the output of the model. Note that the accuracy of the model highly relies on the selection of the features F. A convenient choice is to define these features as a series of radial and angular order parameters:[274]

$$G_i(r) = \sum_j \exp\left(-\frac{(r_{ij} - r)^2}{\delta^2}\right) \tag{71}$$

and

$$\Psi_i(\xi, \lambda, \zeta) = \sum_j \sum_k e^{-(r_{ij}^2 + r_{ik}^2 + r_{jk}^2)/\xi^2} (1 + \lambda \cos \theta_{ijk})^{\zeta} \tag{72}$$

where r_{ij} is the distance between atoms i and j, θ_{ijk} is the angle formed by a central atom i and two neighbors j and k, r is a series of target radial distances, and δ, ξ, λ, and ζ are constants. These order parameters offer a general description of the local radial and angular environment of each atom i. For instance, the radial order parameter $G_i(r)$ captures the local density of neighbors that are located at a distance r from the central atom i, as averaged over a typical shell with a width δ. A visualization of $G_i(r)$ is provided in Figure 33, parts a and b. Note that the selection of the structural features F and the transformation function Γ largely determine the interpretability of the machine learning model, which often acts as a "black-box" model when the structural features F are not intuitive or the transformation function Γ is highly complex. Using intuitive input features is likely key to uncover useful insight into the hidden structural origin of fluctuations in glasses (see refs 271 and 275 for more details).

After building the classification model, the weight vector $\mathbf{w}$ is optimized by fitting the model to a training set, that is, a series of "ground-truth" input features F and associated immobile/mobile labels y_i for a collection of atoms: $\{(\mathbf{X}_1,y_1),(\mathbf{X}_2,y_2),\cdots(\mathbf{X}_M,y_M)\}$. In practice, various classification algorithms can be used, e.g., support vector machines (SVM),[276] XGBOOST,[277] logistic regression,[278] etc. In the case of linear SVM or logistic regression, the decision boundary hyperplane that separates mobile ($y_i = 1$) from immobile ($y_i = 0$) atoms within the feature space F can be expressed as

$$\mathbf{w}\cdot F - b = 0 \tag{73}$$

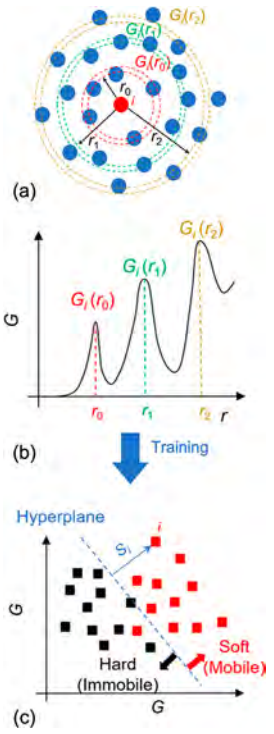

Figure 33. (a) Illustration of the definition of the radial density $G_i(r)$ of neighbors around atom i. (b) Evolution of $G_i(r)$ as the function of the distance r. The $G_i(r)$ metrics are used to construct the feature space. (c) Illustration of the softness S_i, i.e., the orthogonal distance of each atom i from the decision boundary hyperplane in the feature space.

where b is a bias coefficient. Beyond simply predicting the mobile versus immobile state of the atoms, this approach can be used to define the softness S_i of each atom, which is a real number that is correlated to their displacement. For each atom i, the softness metric is defined as the orthogonal distance of each atom from the decision boundary hyperplane in the high-dimensional feature space, as depicted in Figure 33c:

$$S_i = \mathbf{w}\cdot F(\mathbf{X}_i) - b \tag{74}$$

An atom is then labeled as "soft" if $S_i > 0$, and otherwise, marked as "hard." Although the softness approach is relatively simple as compared to other more complex models, the machine-learned softness metric has been shown to accurately predict atoms' mobility under different temperatures[268,269,279] in various disordered systems (e.g., metallic glass,[270] gels,[271] Lennard-Jones liquids,[269] etc.).

The second ML technique is graph neural network. To increase the accuracy of classification models, one option is to include more complex structural descriptors within the list of input structural features.[275,280] However, feature selection (i.e., selecting influential features while filtering out irrelevant features) is a complex task that, in addition to being potentially system-specific, requires some level of intuition. To address this difficulty, a model based on a GNN has recently been proposed.[281] In the same fashion as convolutional neural networks are ideal models to describe photos since they can automatically construct low- and high-level features to describe images (e.g., contours, shapes, etc.), GNNs are a natural approach to treat networks.[282] In brief, GNNs use as inputs a graph structure, that is, an ensemble of nodes (the atoms) that are connected to each other via edges (the interatomic bonds).

https://doi.org/10.1021/acs.chemrev.1c00974
Chem. Rev. XXXX, XXX, XXX−XXX

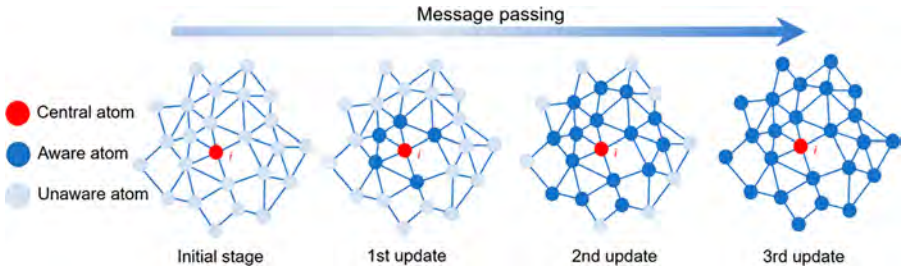

Figure 34. Illustration of the message propagation in GNNs. During the updating process, the atoms gradually become aware of the information offered by the other nodes (neighboring atoms) and edges (interatomic bonds) that are directly or indirectly connected through the networks.

As such, GNN models do not rely on any handcrafted, human-defined arbitrary choice of input structural features. Rather, GNN models can identify on its own what are the influential topological features (e.g., coordination number, angles, ring size, etc.) that govern the dynamics of atoms. GNNs then rely on a message-passing scheme, wherein each node and edge gradually shares information with neighboring nodes, as visualized in Figure 34. By bypassing the need for human-defined structural features, this approach has been noted to offer an improved accuracy as compared with previous models.[281]

An alternative solution to avoid human-defined structural features consists of adopting nonparametric structural functions that do not rely on any fixed analytical form and, rather, are trainable during the learning process. Unlike the parametric models that rely on fixed analytical formula, nonparametric models can construct the formula solely based on the training process and, importantly, do not rely on any assumption regarding the complexity of the model (i.e., the number of fitting parameters). To achieve this, the structure functions can be represented as a set of basis functions (e.g., Gaussian basis functions[283]).

All three ML approaches described above rely on supervised learning, that is, wherein the model is exposed to the knowledge of the output label of each atom (i.e., mobile or immobile) during its training. However, such supervised approaches are not always practical when the number of labeled data is low. As an alternative route, a recent study has shown that, in the absence of any information regarding the dynamics of the atoms, an unsupervised machine learning approach can automatically identify some structural predictor metrics that are correlated with the mobility of atoms.[284] This can be achieved by using a clustering analysis, which can group atoms into clusters of atoms that exhibit some similarity in their local environment, without the need for any knowledge of their dynamics (see Figure 35).

5.5.2. Structural Fluctuations and Dynamical Heterogeneities. By leveraging recent increases in computing power and artificial intelligence algorithms, ML-based structural predictors have gradually faced increased popularity over the recent years. Although the interpretability of a machine-learned structural predictor often remains limited as compared with physical-based metrics, such ML approaches have already demonstrated a tremendous potential to uncover previously hidden relationships between structural and dynamical fluctuations in glasses.

The softness approach has been shown to successfully identify the structural origin of the thermally- or stress-induced heterogeneous atomic mobility in disordered materials[269,271] and identify local structural fluctuations that are correlated to

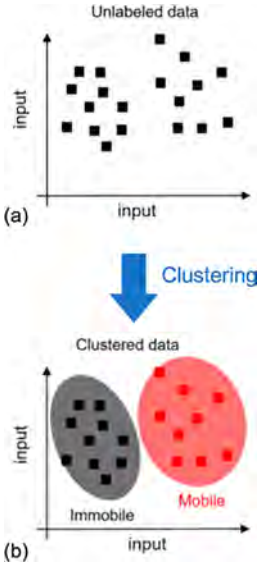

Figure 35. (a) Illustration of the clustering unsupervised approach, wherein (b) atoms sharing common characteristics are grouped into clusters (with no a priori knowledge of their mobile or immobile state).

the tendency for crystallization,[285] local energy barriers,[275] plasticity,[286] fracture toughness, and flexibility.[270] The softness approach has also been used to characterize fluctuations in short- and medium-range structural units.[280] Figure 36a shows results by Fan et al.,[270] who used the softness approach to characterize volume and structural flexibility distributions in Cu−Zr metallic glass, where a high correlation was found between these two property fluctuations. In this work, flexibility refers to the distribution of a property within the system and input stimuli. In Figure 36a, the color scales with density (where dark is the maximum density). As seen in Figure 36b, similar linear correlations were found between structural fluctuations of Cu atoms in $Cu_{50}Zn_{50}$ and volume flexibility V_{flex}, boson peak intensity I_{BP}, shear modulus G, and fictive temperature T_f.

The ML softness approach can also predict dynamical properties.[268,269] These works typically rely on SVMs[276] and use physical intuition to precompute heuristic features for each particle. The softness approach can predict whether particles will rearrange after a certain period of time. However, for long-time dynamics, GNNs[282,287,288] are preferable because (1) they do not treat each input feature as independent and (2) instead of requiring human-defined features, GNNs leverage the power of deep networks for feature discovery.[289] Work by Bapst et al.[281] created a GNN model to explore such dynamical heterogeneities. Figure 37 is the model prediction of the linear

https://doi.org/10.1021/acs.chemrev.1c00974
Chem. Rev. XXXX, XXX, XXX−XXX

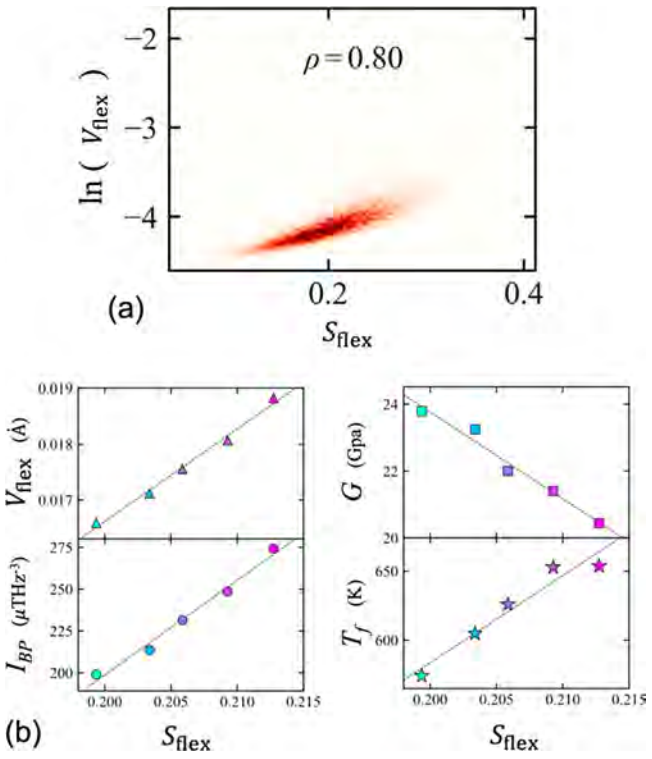

Figure 36. Property correlations with structural fluctuations in $Cu_{50}Zr_{50}$ metallic glass, calculated using the softness approach. (a) Correlation between structural flexibility S_{flex} of Cu and volume flexibility V_{flex}, where the term flexibility refers to the distribution of a property within the system and input stimuli. The color scale plots density (where dark is the maximum density). The Pearson correlation coefficient ρ ranges between 0 and 1 to define the error between the predicted and true value of y_i. (b) Linear correlations found between the structural flexibility S_{flex} of Cu and volume flexibility V_{flex}, boson peak intensity I_{BP}, shear modulus G, and fictive temperature T_f. Adapted with permission from ref 270. Copyright 2020 Elsevier Ltd.

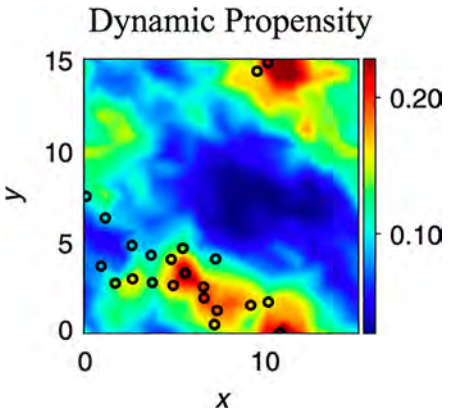

Figure 37. Two-dimensional slice of the simulation box showing a color map of particle dynamic propensity in the x and y directions. The results were calculated using a GNN. Black circles are the 10% most mobile particles. Reprinted with permission from ref 281. Copyright 2020 Bapst et al. under exclusive licence to Springer Nature Limited.

interpolation of the distribution of dynamic propensity, shown as a two-dimensional slice of the simulation box, where the 10% most mobile particles are depicted as black circles.

There has also been recent progress in the area of physics-informed ML for identification of governing dynamics and predictions, as applied to complex systems data. For example, deep learning[290] and Gaussian process approaches can incorporate physical understanding into the model architecture or cost functions to develop highly interpretable predictive models. Also, leveraging deep autoencoders seems to be a promising approach to identify coordinate transforms that linearize nonlinear dynamics and learn salient features governing the dynamics. These models also make future state predictions. The development of such ML techniques will expand their applicability to explore the physical chemistry of spatial and temporal fluctuations in glass-forming systems.

As of now, the potential of such ML approaches nevertheless remains limited by (i) their limited interpretability (which makes it challenging to uncover some new physics), (ii) the limited/sparse nature of typical data sets (which limits the potential of deep learning approaches), and (iii) the lack of standard data sets that could be used as a benchmark to meaningfully compare the performance of various ML approaches (in the same fashion as the ImageNet data set has greatly accelerated the development of new state-of-the-art approaches in deep learning applied to image analysis). Some of these challenges could be addressed by developing novel closed-loop integrations between atomistic simulations and ML, wherein simulations are performed "on-the-fly" to expand the training data set in the regions of the data sets corresponding to the highest model uncertainty, yield ground-truth outputs for previously unlabeled data points, offer insights into potential physically meaningful input features, or validate in real time the predictions of ML models following an active learning fashion. In turn, ML has the potential to greatly accelerate atomistic simulations (e.g., via the development of machine-learned empirical force fields), which could facilitate the modeling of fluctuations associated with large length scales or extended time scales, which are presently out of reach by conventional atomistic simulations.

6. GLASS RELAXATION

The process of relaxation in glasses and supercooled liquids is one of the oldest problems in chemical physics; however, the chemical and structural origins of relaxation remain elusive.[291−294] The rich phenomenology exhibited by glassy systems, in general, has garnered immense attention in terms of fundamental research from several disciplines,[295−300] and demystifying the fundamentals of the glassy state has an immediate impact on the design of high-performance glasses.[301] The properties of a glass are strongly influenced by its temperature or pressure history,[302−305] which are coupled with how the glass relaxes as it is being cooled through the glass transition. For example, suppressing volume relaxation (compaction) is crucial for high-performance display glasses that serve as substrates for high-resolution displays with small pixel sizes,[306,307] the ion-exchange temperature used to chemically strengthen glass is limited by stress relaxation in the glass,[301] and attenuation in optical fibers is related to Rayleigh scattering which is a nontrivial function of density fluctuations, which are governed by thermal history.[308] A complete and well-accepted theory of glassy dynamics will aid in determining glass chemistry and processing paths to achieve a target set of desired material properties.

Much of the focus over the last few decades has been on the characterization of the heterogeneous nature of liquids and

https://doi.org/10.1021/acs.chemrev.1c00974
Chem. Rev. XXXX, XXX, XXX−XXX

glasses. Dynamical heterogeneities are a key component in modern descriptions of glassy dynamics.[309] This section discusses theoretical, experimental, and computational advances regarding the role of spatiotemporal fluctuations in relaxation behavior with the intent of bridging the gap between engineering high-performance glasses and the sometimes more esoteric theoretical models of glassy dynamics.

6.1. Nonexponential Relaxation and Temporal Evolution of Fluctuations

Before discussing dynamical heterogeneities, it is important to understand the impact of time evolution and relaxation in glass-forming systems. Two salient properties exhibited by glass-forming systems are nonexponential relaxation and non-Arrhenius temperature dependence of the relaxation time scale. Nonexponential relaxation was originally observed by Kohlrausch[310] in 1854 while studying the relaxation of residual charge in a Leyden jar. Since then it is known that a wide range of glass-forming systems exhibit a departure from the exponential relaxation behavior,[1,293,311,312] conforming to the empirical Kohlrausch stretched exponential function $\phi(t)$[310,313]

$$\phi(t) = \exp\left(-\left(\frac{t}{\tau_k}\right)^{\beta^*}\right) \tag{75}$$

where t is time, τ_k is the characteristic relaxation time, and β^* is the dimensionless stretching exponent. The origin of stretched exponential relaxation in glass is ascribed to the presence of a broad distribution of simple exponential relaxation functions originating from heterogeneous dynamics. The width of this distribution is proportional to $1/\beta^*$ and serves as a measure of the departure from exponential behavior. Dynamical heterogeneities and expressions for the distribution of relaxation times will be discussed in depth in the subsequent section 6.2.

A myriad of experimental techniques such as dielectric spectroscopy,[314,315] quasi-elastic light scattering,[316] Brillouin spectroscopy,[317] dynamic light scattering,[318−320] specific heat spectroscopy,[318] and mechanical spectroscopy[319,320] have been used to characterize the nonexponential and non-Arrhenius behavior in glass. The parameters in eq 75 are fit to experimental data measured in the time domain through the decay of fluctuations of some property $P(t)$ that varies with time, from its equilibrium value $P(\infty)$:

$$\phi(t) = \frac{P(t) - P(\infty)}{P(0) - P(\infty)} \tag{76}$$

The parameters may also be determined in the frequency domain by fitting spectroscopy data to the Fourier transform of the stretched exponential function,[313] which was found to be related to the symmetric Lévy stable distribution.[321] Assuming that the stretched exponential function is a differential distribution of time, the average relaxation time for nonexponential relaxation is defined as the integral of eq 75:[311]

$$\langle\tau\rangle = \tau_k \Gamma\left(1 + \frac{1}{\beta^*}\right) \tag{77}$$

where Γ is the Euler gamma function.

The liquid fragility index, defined from the mean relaxation time as[322,323]

$$m \equiv \left.\frac{\mathrm{d}(\log\langle\tau\rangle)}{\mathrm{d}(T_g/T)}\right|_{T=T_g} \tag{78}$$

is a measure of the departure from Arrhenius behavior. A common industrially relevant property that is used to measure the temperature dependence of the relaxation time scale is the shear viscosity, and the fragility is often defined as the slope of the base-10 logarithm of viscosity versus T_g/T curve computed at T_g; this graph is known as the Angell plot.[322] The importance of understanding the temperature and composition dependence of viscosity and its relation to nonexponential relaxation cannot be understated.[324,325] While in-depth discussions about shear viscosity are outside of the scope of this review (because viscosity relates to the time-scale of relaxation rather than temporal fluctuations) we are motivated by its relevance to discuss its association with spatiotemporal fluctuations.

The Adam−Gibbs model, which purports the existence of cooperatively rearranging regions (CRRs) in which ensembles of molecules or monomers can rearrange themselves independently of their surroundings, is a popular model used to describe the temperature scaling of viscosity. A modification of this model incorporating coupling between the CRRs was proposed by Ngai et al.,[326,327] and it has been used to derive a stretched exponential response. Böhmer et al. originally proposed the existence of an inverse correlation between the liquid fragility and β^* measured at T_g; however, this has been a subject of debate because of the large scatter in the data.[315,328,329] The existence of this correlation has the interesting physical consequence that the temperature dependence of spatial fluctuations in relaxation times contributes to the fragility of the glass-forming system. The temperature dependence of the heterogeneous dynamics is reflected in the temperature dependence of β^* for which a model has recently been proposed by Wilkinson et al.[330]

The microscopic origin of stretched exponential relaxation in glasses has been intensively studied theoretically and experimentally. The dimensionless stretching exponent β^* is thought to be inversely related to the broadness of the distribution of relaxation times, and theoretical models have attempted to quantifiably relate it to microscopic origins. For example, Phillips,[331] based on Grassberger and Procaccia's[332] interpretation of the diffusion trap problem, hypothesized that the stretching exponent is a function of the fractional dimension of the diffusion process involving the diffusion of "excitations" toward randomly distributed static "traps". Quantitatively, this is expressed as

$$\beta^* = \frac{fd}{fd + 2} \tag{79}$$

where d is the dimensionality of the space in which diffusion is taking place and f is the fraction of activated relaxation pathways. Phillips,[331] based on a thorough literature survey of relaxation data, also proposed "magic" values for β^* at low temperatures which were reported to be 3/5 for stress relaxation (d = 3 and f = 1) and 3/7 for structural relaxation (d = 3 and f = 0.5). This result has been experimentally supported[333,334] and points to fundamentally different mechanisms governing the two relaxation phenomena as they appear to correspond to different effective dimensionalities. Modeling stretched exponential relaxation in such a manner

https://doi.org/10.1021/acs.chemrev.1c00974
Chem. Rev. XXXX, XXX, XXX−XXX

implies that the general mechanism underpinning relaxation involves the relaxation of the faster degrees of freedom before the slower ones relax.

It has been argued that simple relaxation experiments involving two-point correlation functions do not reveal substantial information about heterogeneous dynamics;[335] however, the analysis of the temporal evolution of fluctuations in properties such as density corroborate well with the aforementioned theoretical result. Studies on the variation in density and enthalpy fluctuations (in the sub-T_g regime) as glassy selenium relaxes have revealed that the fluctuations evolve nonmonotonically.[336,337] As illustrated in Figure 38a,

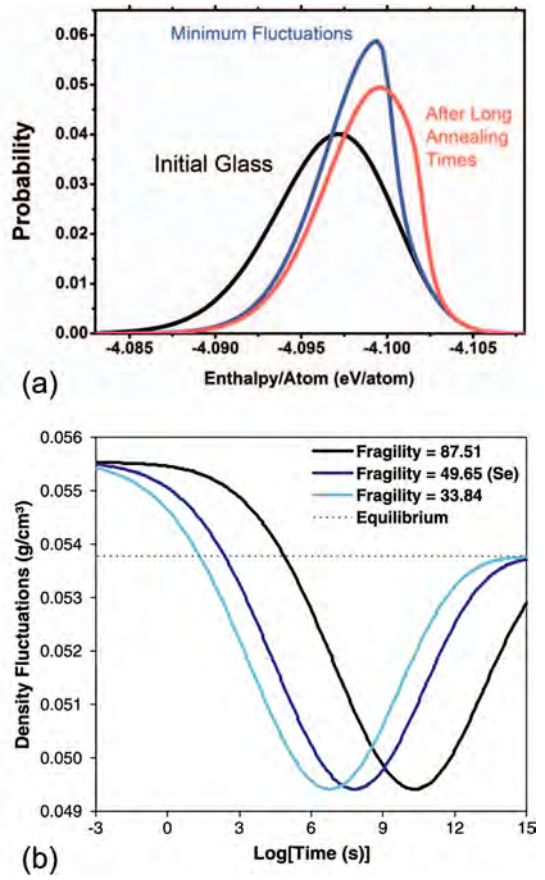

Figure 38. (a) Computed distribution of enthalpy fluctuations. Reprinted with permission from ref 337. Copyright 2013 AIP Publishing LLC. (b) The impact of fragility on the nonmonotonic evolution of density fluctuations. Reprinted with permission from ref 338. Copyright 2011 Elsevier B.V.

the distribution of fluctuations initially narrows due to the relaxation of the faster changing degrees of freedom and is followed by a broadening of the distribution as the sample equilibrates due to the relaxation of the slower changing degrees of freedom. A subsequent computational study[338] involving enthalpy landscape techniques considered the impact of fragility on the evolution of fluctuations. It was revealed that the fragility had no impact on the magnitude of the minimum in density fluctuations but an increase in fragility extended the time needed for the fluctuations to undergo a crossover, as seen in Figure 38b.

6.2. Heterogeneous Dynamics

It is well-established that supercooled liquids and glasses exhibit nonexponential relaxations, which are ascribed to their intrinsic heterogeneities. The microscopic underpinnings of the stretched exponential correlation function can be ascribed to two scenarios:[339] (a) the dynamics are spatially homogeneous and the correlation function for each site within a sample decays as a stretched exponential, and (b) the dynamics are spatially heterogeneous and the correlation function for each site within a sample decays as a simple exponential. However, there is a broad spatial distribution of relaxation times at temperatures for which $\beta^* \ll 1$, and the superposition of exponential decays generates a stretched exponential decay for the ensemble-averaged correlation function. These scenarios have been illustrated in Figure 39a. A general mathematical description of these two scenarios is

$$\phi(t) = \int_0^\infty g(\tau)\, \exp(-(t/\tau)^{\beta^*_{\text{intr}}})\, \mathrm{d}\tau \tag{80}$$

where $g(\tau)$ is the probability density function for the relaxation times τ and $\beta^*_{\text{intr}} \geq \beta^*$ is the dimensionless stretching exponent of the intrinsic nonexponential decays.

On the basis of eq 80, Richert and Richert[340] have elucidated the properties of $g(\tau)$ and introduced the following expression for the probability distribution:

$$g(\tau) = \frac{\beta^*_{\text{intr}}}{\tau} \sum_{n=1}^{\infty} \frac{(-1)^n}{n!} \frac{(\tau/\tau_k)^{n\beta^*}}{\Gamma(-n\beta^*/\beta^*_{\text{intr}})} \tag{81}$$

We find that, in the purely homogeneous case, $\beta^*_{\text{intr}} = \beta^*$ and $g(\tau) = \delta(\tau - \tau_k)$, where $\delta(x)$ is the Dirac δ function. In the purely heterogeneous case, $\beta^*_{\text{intr}} = 1$ and the dispersion in the correlation function arises solely from $g(\tau)$. For the intermediate case where $0 < \beta^* < 1$ and $\beta^* \leq \beta^*_{\text{intr}} \leq 1$, Böhmer et al.[341] have established a continuous scale (denoted η) that linearly interpolates between 0 for the purely homogeneous case and 1 for the purely heterogeneous case, where

$$\eta = \frac{\beta^*_{\text{intr}} - \beta^*}{1 - \beta^*} \tag{82}$$

Experimental results for organic glass-forming systems[342−344] seem to suggest that low molecular weight glass formers tend to exhibit pure heterogeneity while polymers tend to exhibit homogeneous contributions to the overall correlation function.[335] An alternative integral expression related to the Lévy stable distribution[345] has been presented recently by Doss and Mauro[346] based on earlier results by Montroll and Bendler[321] and Jurlewicz and Weron[347] for the $\beta^*_{\text{intr}} = 1$ scenario. The probability distributions for the purely heterogeneous case and intermediate cases have been plotted in Figure 39b. Here, we highlight the fact that all the distributions appear to be power laws (straight line regions on a log−log plot) over approximately many decades of relaxation time, implying the presence of a temporal scale invariance symmetry.

While this power-law behavior may appear to be a mere mathematical requirement, many theoretical models rooted in physical processes that exhibit stretched exponential correlation functions appear to follow this trend. Some examples are (i) the Förster direct-transfer model,[348] a parallel channel relaxation model that arose from studies of excitation transfers

https://doi.org/10.1021/acs.chemrev.1c00974
Chem. Rev. XXXX, XXX, XXX−XXX

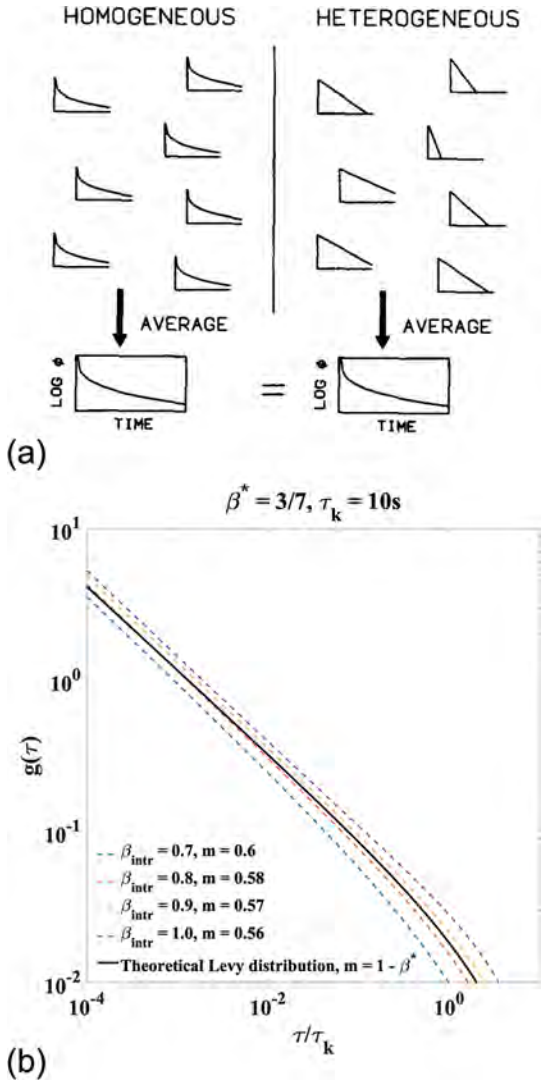

Figure 39. (a) Spatially homogeneous vs heterogeneous dynamics result in an ensemble-averaged nonexponential decay. Reprinted with permission from ref 339. Copyright 1993 Elsevier B.V. (b) Distributions of relaxation times for the purely heterogeneous scenario given by the theoretical distribution in Doss and Mauro (ref 346) (solid bold line) and intermediate cases (dashed lines) where $\beta^*_{intr} \neq \beta^* = 3/7$. A comparison of the Levy stable distribution with the expression in eq 82 for $\beta^*_{intr} = 1$ reveals small differences in the density values which could be attributed to numerical errors from performing the summation. The slopes (m) of the straight-line regions are similar (~0.57) for both probability densities.

from donor to static defects in condensed media, (ii) the hierarchically constrained dynamics model proposed by Palmer et al.,[349] a serial relaxation model that supposes that relaxation occurs in stages wherein the faster degrees of freedom must relax first (thereby imposing a constraint on the slower degrees of freedom), and (iii) the defect-diffusion model proposed by Glarum[350] which suggests that migrating defects trigger the relaxation of frozen dipoles in amorphous materials.

Unlike the more abstract diffusion trap model, the aforementioned models are rooted in a physical mechanism that describes the dynamics of a system relaxing in response to a certain excitation. These models also introduce a more palatable interpretation of the stretching exponent β^* relative to the more abstract notion of a "fraction of relaxation pathways" discussed in the Phillips diffusion trap model. Klafter and Shlesinger[351] summarize that the unifying feature within these different physical models is the generation of a scale-invariant distribution (power-law distribution) of relaxation times, whose exponent is related to β^*.

If the spatial distribution of relaxation times appears to possess scale-invariance symmetry, does this have implications for the underlying structure of the liquid or glass? While there have been no direct links between the underlying structure and temporal scale invariance,[352] studies focused on characterizing the shape and size of CRRs in glass-forming liquids have reported that the heterogeneities are fractal,[353,354] alluding to the presence of scale invariance in the geometry of these heterogeneities. The relationship between the length scale of dynamical heterogeneities and length scale of CRRs is not known.

Dynamical heterogeneities manifest themselves as a non-Gaussian probability distribution of particle displacements in colloidal systems wherein the length scale of heterogeneities is experimentally accessible.[355,356] Heterogeneities are on the order of nanometers in network glasses and organic systems,[354,357] making experimental characterization of their mechanisms challenging. To this end, site-specific dynamics of oxygen atoms have been investigated in a network potassium silicate liquid using ^{17}O NMR spectroscopy wherein it was found that NBO sites lead to significantly shorter relaxation modes compared to the time scale of shear stress relaxation.[358] A common theme among NMR, photobleaching dielectric, and magnetic hole burning experiments is that sites that are associated with a subset of relaxation times are selectively modified or observed.[309]

Considering the difficulty associated with experimentally probing mechanisms underpinning dynamical heterogeneities in a wide range of glass-forming systems, atomic-scale simulations have proven to be a resourceful alternative. The investigation of dynamical heterogeneities has been carried out most notably on binary Lennard-Jones systems[359−365] and real systems such as water,[366,367] silica,[364,365,368,369] propylene carbonate, and salol. The introduction of the MD isoconfigurational ensemble (see section 5.1.2) established a link between dynamical heterogeneities and the underlying structure of a liquid. This technique was used by Vargheese et al.[357] to study the origin of dynamical heterogeneities in peraluminous and peralkaline aluminosilicate liquids, which revealed a clear correlation between concentration fluctuations and dynamical heterogeneities. It was found that regions of high dynamic propensity had higher concentrations of aluminum and calcium while regions of low dynamic propensity were rich in silica. While the isoconfigurational ensemble technique has been very resourceful in aiding our understanding of heterogeneous dynamics, new first-principles and data-driven techniques must be developed to isolate salient structural units and relaxation modes to cement the connection between heterogeneous dynamics and nonexponential relaxation.

7. CRYSTALLIZATION

When a liquid is supercooled below its melting or liquidus temperature, one or more crystalline phases will tend to form to reach thermodynamic equilibrium. This process takes place in two steps: (i) the formation of critical crystalline clusters (nucleation), which result directly from thermal or compositional fluctuations, and (ii) the increase in volume of these clusters (growth). Crystal nucleation and growth lead to

https://doi.org/10.1021/acs.chemrev.1c00974
Chem. Rev. XXXX, XXX, XXX−XXX

crystallization, which is a ubiquitous process in nature (e.g., snow and mineral formation) and in technology (e.g., metal solidification and production of glass-ceramics). Crystallization counteracts vitrification, the temporary freezing of a supercooled liquid into a glass.[39] Upon heating, crystal nucleation and growth often result in devitrification. Understanding crystallization is imperative because the prevention of crystal nucleation and growth upon supercooling a liquid—or upon heating certain gels—leads to a glass. Also controlling the nucleation and growth steps can lead to the formation of glass-ceramics.

In both vitrification and ceramming (controlled crystallization of glasses to produce a glass-ceramic), crystallization plays a pivotal role. Hence, reliable models are needed for understanding, controlling, or predicting nucleation and crystallization kinetics. Thus, knowledge about the possible crystallization pathways allows us to formulate kinetic criteria. Several monographs and review papers provide detailed information on these processes and materials.[3,370−372]

In addition to their practical relevance, glass-forming liquids serve as remarkable experimental models of metastable highly viscous systems, in which crystallization and liquid−liquid phase separation (see section 8) processes can be quickly initiated, accelerated, or delayed. These processes can thus be studied conveniently under different conditions on laboratory time scales. For this reason, glass-forming liquids have served as platforms for testing crystal nucleation and growth theories, providing a deeper insight into different phase formation processes. In this section, we present some key concepts of crystal nucleation in glass-forming liquids with emphasis on fluctuations and the effects of dynamical heterogeneities and structural relaxation.

7.1. Formation of a Stable Crystalline Nucleus

The physical nature of nucleation phenomena in general, and crystal nucleation in supercooled liquids, was first established and described by Gibbs in the early 1900s.[373,374] His basic idea is illustrated by the following approximation for the change of the Gibbs free energy during the formation of a spherical crystal cluster (also called a nucleus):

$$\Delta G = N\Delta\mu + \gamma A \tag{83}$$

with the difference of the chemical potential given by

$$\Delta\mu = \mu_{cr} - \mu_{liq} \tag{84}$$

the surface area given by

$$A = 4\pi r^2 \tag{85}$$

and the number of particles (atoms, molecules, or more generally the basic structural units of the crystalline phase) given by

$$N = \frac{4\pi}{3} c_\alpha r^3 \tag{86}$$

where γ is the interfacial energy, μ_{liq} is the chemical potential of the liquid phase, μ_{cr} is the chemical potential of the crystalline phase, r is the radius of the nuclei, and c_α is the particle number density in the crystal cluster. An intrinsic assumption of eq 83 is that any elastic strain arising during nucleation is rapidly released by viscous flow. The equation is therefore only valid for the case of polymorphic or congruent crystallization, when the supercooled liquid and crystal consist of the same chemical components. Also, it is assumed that the properties of the crystal clusters are size-independent. Qualitatively, the situation does not change in general cases of incongruent crystallization, when the crystal and liquid phases have different compositions.

According to thermodynamic evolution criteria, at constant pressure, P, and temperature, T, spontaneous macroscopic processes are tied to a decrease in the Gibbs free energy of the system. If $\Delta\mu$ is positive, then ΔG is a monotonically increasing function of the cluster size for any positive value of r; crystal clusters of any size will disappear over time. If $\Delta\mu$ is negative, then ΔG has a maximum at a positive value of r called the critical radius (r_c), shown in Figure 40a; the probability of a crystal cluster to dissolve back into the ambient phase decreases as r increases, becoming highly improbable for clusters with $r > r_c$.

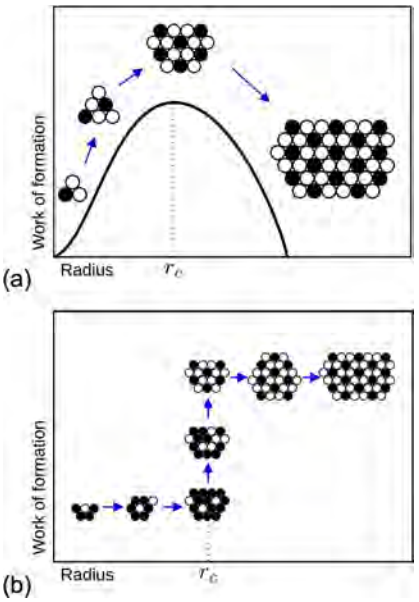

Figure 40. Classical nucleation model and a possible generalization: (a) with only one parameter, radius, describing the state of the cluster; (b) alternative scenario of crystallization in multicomponent liquids. The figure was inspired by the schematics of ref 375.

As demonstrated in Figure 40a, the critical cluster size is defined by the maximum of ΔG. Systems showing such behavior are denoted as metastable. Metastable states are stable with respect to small fluctuations (generating clusters with sizes $r < r_c$) but unstable with respect to larger fluctuations (leading to clusters with sizes $r > r_c$). Thus, supercritical crystal clusters capable of deterministic growth must exceed a critical size. It is this criticality that determines the crucial impact of these embryos (subcritical) and nuclei (supercritical) on the nucleation processes.

Taking the chemical potential difference and the specific interfacial energy as constant (i.e., the capillarity approximation), one can derive the critical cluster size and the value of ΔG_c at the critical size by solving

$$\Delta G_c \equiv \Delta G(r_c) = 0 \tag{87}$$

These parameters are given by

$$r_c = \frac{2\gamma}{c_\alpha \Delta\mu} \tag{88}$$

and

https://doi.org/10.1021/acs.chemrev.1c00974
Chem. Rev. XXXX, XXX, XXX−XXX

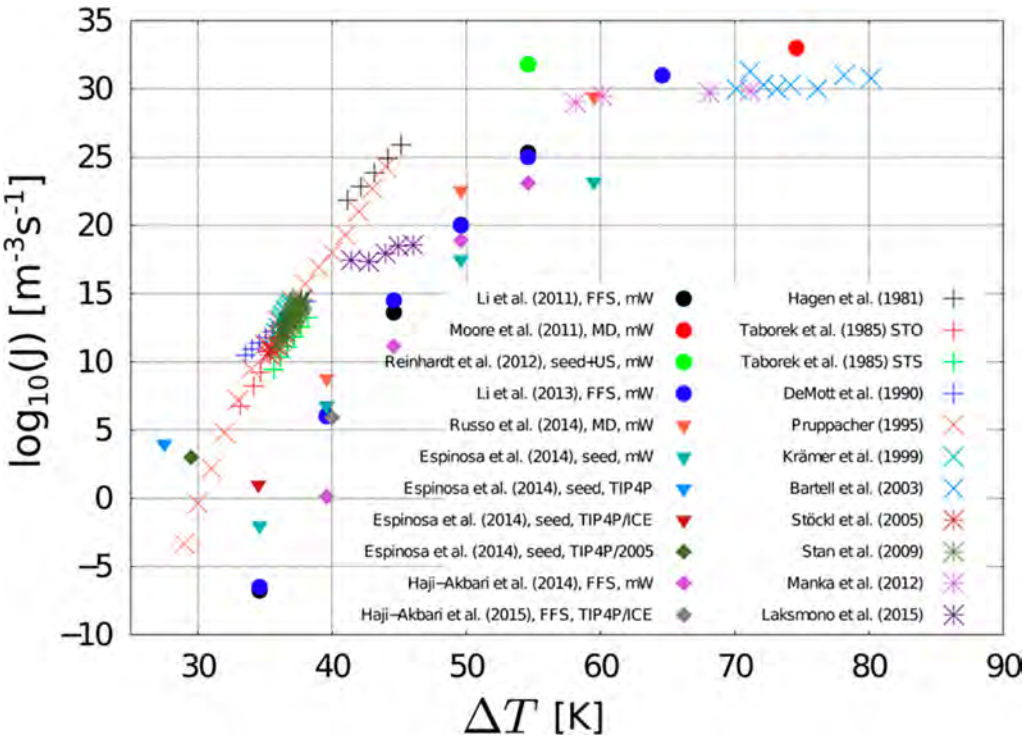

Figure 41. Homogeneous nucleation rates for water. The *x*-axis shows the supercooling with respect to the melting points of different water models and 273.15 K for any experiment. Nucleation rates obtained with computational approaches since 2011 are shown as solid symbols, whereas the experimental rates obtained since 1981 are shown as crossed symbols. For each computational study, the approach and the water force field used are specified. All the references are given in Sosso et al. (ref 107). Reprinted with permission from ref 107. Copyright 2016 American Chemical Society.

$$\Delta G_c = \frac{1}{3}\gamma A_c = \frac{16\pi}{3}\frac{\gamma^3}{(c_\alpha \Delta\mu)^2} \tag{89}$$

with the critical area given by

$$A_c = 4\pi r_c^2 \tag{90}$$

Figure 40b shows an alternative picture of phase formation.[371] In this case, the composition of the crystal cluster changes until a nearly constant size is reached; only after completion of this process are the kinetics governed by the growth of clusters with a constant composition. In several multicomponent systems,[4] the latter path of evolution (Figure 40b)—and not the classical picture (Figure 40a)—dominates nucleation.

A more realistic model of cluster formation is obtained by considering that not only the size but also the composition of the cluster (described by the number of particles n_i of two components) may change. In this case, the critical cluster corresponds to a saddle point of the Gibbs free energy surface. We note that, in certain cases, the evolution of the new phase may not proceed via the saddle point but via a ridge trajectory if such a trajectory is kinetically favored. This type of behavior may be expected to occur in crystallization occurring at deep supercooling because of the disordered and nonstoichiometric nature of the crystals that precipitate in the early stages.

Embryos and critical clusters form by stochastic thermal fluctuations. According to fundamental assumptions of statistical physics, the probability of such fluctuations can be expressed as a function of the minimum work of a reversible thermodynamic process. The minimum work to form a critical cluster is $W_c = \Delta G_c$, where ΔG_c is given by eq 88. When the crystal nuclei form evenly within a pure liquid, the nucleation is said to be homogeneous. However, nucleation can be readily catalyzed by certain solid impurities embedded in the volume or present on surfaces of glasses. Heterogeneous nucleation usually dominates at small supercooling (i.e., small departure from equilibrium, small $T_m - T$) because of the lower work of critical cluster formation than that of homogeneous nucleation. At high supercooling, however, homogeneous nucleation dominates due to the much larger number of sites (all "molecules" of the system). Frequently, fluctuations lead to several different stable or metastable phases that may be formed in the supercooled liquid. In such cases, the most favorable stable phase is formed via several stages in which different metastable phases are formed first; this phenomenon is known as Ostwald's rule of stages.

Two of the most celebrated theories to model crystal nucleation are classical nucleation theory (CNT) and diffuse interface theory (DIT). The first considers that the interface between the nucleus and the ambient phase is sharp, while the latter considers that this interface could extend to several molecular layers.[376] By employing fitting procedures, the DIT theory proved to be consistent with the nucleation data on a variety of substances, including liquid metals, the inorganic glasses $Li_2O{\cdot}2SiO_2$, $BaO{\cdot}2SiO_2$, $Na_2O{\cdot}2CaO{\cdot}3SiO_2$, and the metallic glass $Fe_{40}Ni_{40}P_{14}B_6$.[377,378] CNT has been at stake for several decades. In section 7.2 we briefly describe the current state of the art and demonstrate that CNT describes quite well the experimental nucleation rate data for different substances.

7.2. Modeling Crystal Nucleation

As crystal nucleation in supercooled liquids (SCLs) may involve extremely small time and length scales, computer simulations can provide unique insights into the microscopic

https://doi.org/10.1021/acs.chemrev.1c00974
Chem. Rev. XXXX, XXX, XXX−XXX

aspects of crystallization. In a very extensive review article, Sosso et al.[107] compiled and described selected molecular dynamics simulations that have unraveled crucial aspects of crystal nucleation in liquids. They summarized the theoretical framework of CNT and the state-of-the-art computational methods and showed that MD simulations have provided key insights into diverse nucleation scenarios.

For instance, Sosso et al.[107] revealed that studies on colloidal particles provided evidence for two-step nucleation mechanisms, and the investigation of Lennard-Jones liquids yielded valuable insights into the effects of confinement. Also, the investigation of realistic systems has provided results related to problems of great relevance. For example, the influence of different solvents on the early stages of urea crystallization has important consequences in the fertilizer industry, and the molecular details of clathrate nucleation could help to rationalize and prevent hydrate formation in oil or natural gas pipelines. In more detail, Sosso et al.[107] reviewed different substances, in order of increasing complexity. They started with colloids and Lennard-Jones liquids. These systems are described by simple interatomic potentials that allow large-scale MD simulations, and thus many aspects of CNT could be investigated and nucleation rates calculated. In special cases, the latter were directly compared to experimental results. These simple liquids demonstrated that understanding the intricacies of crystal nucleation is still far from satisfactory, even within these toy models.

Figure 41 reproduces a collection of nucleation kinetics for water. In general, most simulated nucleation rates (more or less) agree with each other and overlap, whereas most experimental points lie over 10 orders of magnitude above them. However, for a larger degree of supercooling, $\Delta T > 60$ K, the simulations and experiments agree satisfactorily. The possible reasons for agreement and discrepancies are detailed in the original reference.[107] As suggested by Sosso et al.,[107] by improving existing interatomic potentials and enhancing sampling methods, we could move toward accurate investigations of systems of practical interest, thus bringing simulations a step closer to experiments.

In 2006, Evteev et al.[379] provided a very illustrative isothermal time−temperature−transformation (TTT) diagram (Figure 42) for the initiation of homogeneous nucleation. It was constructed by an MD model of fast-quenched supercooled liquid iron near the glass transition temperature. This diagram was compared with the theoretical curve calculated using information obtained by analyzing the kinetics of the initial stage of nucleation and growth of supercritical nuclei at several temperatures. They found a close agreement of the theoretical curve with simulated data at temperatures higher than T_g and substantial disagreement with data below T_g, where crystallization is necessarily preceded by the formation of an icosahedral percolation cluster. The authors concluded that this result demonstrates the substantive influence of fluctuations that form an icosahedral substructure on the nucleation rates.

Recently, Separdar et al.[380] were able to deeply supercool zinc selenide (ZnSe) by fast quenching and determine spontaneous homogeneous steady-state nucleation rates, J_{MD}, by MD simulations using the mean lifetime method. At moderate supercoolings, where the nucleation rates are much smaller, they used the seeding method to compute the nucleation rates by the CNT formalism, J_{CNT}, using the physical properties obtained by MD simulations: the melting

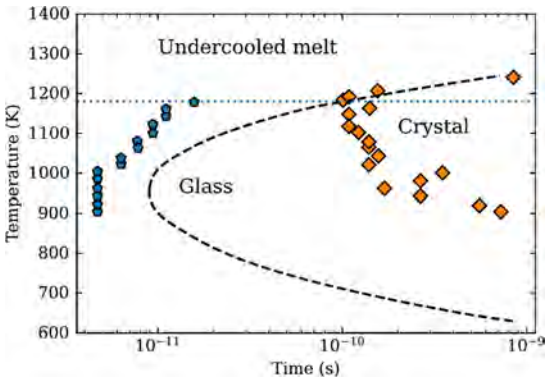

Figure 42. TTT diagram of the beginning of homogeneous nucleation (time to form the first critical nucleus) for supercooled iron liquid (rhombs). The dashed curve was calculated using CNT assuming steady-state conditions. The blue pentagons refer to the formation of stable icosahedral clusters in the glass. For temperatures above $T_g \sim 1180$ K (dashed horizontal line), stable icosahedral percolation clusters do not form. Data obtained from ref 379.

temperature, the number of atoms per unit volume in the liquid, the melting enthalpy, the diffusion coefficient, and the critical nucleus size, combined with two theoretical expressions for the thermodynamic driving force. The interfacial free energy calculated by the CNT expression using the MD simulation data, via both the seeding method and the mean lifetime method, show a weak positive temperature dependence, which agrees with the prediction of DIT. The extrapolated values of γ, from the spontaneous nucleation regime to the seeded nucleation region, cover the range of values of γ calculated via the seeding method and the CNT formalism. Finally, the values of J_{CNT} extrapolated from moderate to deep supercoolings—without the use of any fitting parameter—are in good agreement with the J_{MD}. These results comparing simulated with calculated nucleation rates are visualized in Figure 43 and corroborate the validity of the CNT for this substance.

The work of Tipeev et al.[381] on the Ge system is one of very few that compared simulations with experimental nucleation rates. They carried out comprehensive MD simulations of the nucleation kinetics of supercooled germanium using the Stillinger−Weber potential covering a moderate supercooling range of $T/T_m = 0.70-0.86$. The seeding method was used to determine the number of particles in the critical crystal nuclei at each degree of supercooling. The transport coefficient at the liquid−nucleus interface and the melting point were also obtained by simulation. Using the parameters resulting directly from the simulations, and experimental values of the thermodynamic driving force, the predictions of the CNT embraced the experimental nucleation rates (Figure 44). Therefore, without using any fitting parameters, the calculated nucleation rates agreed with the experimental $J(T)$ curve for Ge, reinforcing the validity of the CNT.

Finally, recent original work proposed by Wilkinson et al.[193] employs an energy landscape approach to account for the thermodynamic and kinetic features of nucleation. It is a new method to compute nucleation rates, where parametrization of all CNT variables is made independently. Figure 45 shows the resulting predicted nucleation curve for barium disilicate. Given the extreme sensitivity of the nucleation kinetics to minor variations in diffusivity, and the interfacial and volumetric free energy, the nucleation curve is reasonably

https://doi.org/10.1021/acs.chemrev.1c00974
Chem. Rev. XXXX, XXX, XXX−XXX

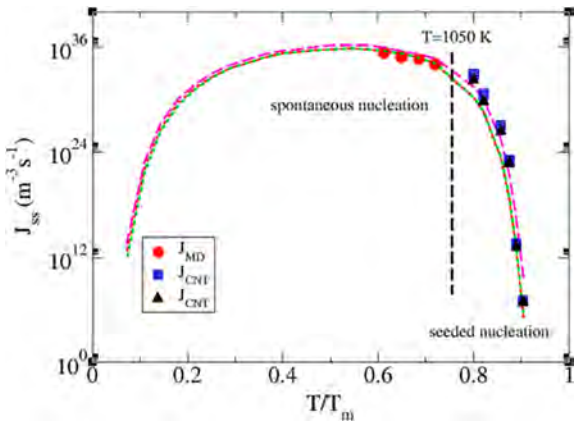

Figure 43. Homogeneous nucleation rates vs reduced temperature in ZnSe. The red circles refer to the spontaneous steady-state nucleation rates evaluated by $J_{MD} = 1/(\tau_1 V)$, where V is the volume of the system and τ_1 is the time of formation of the first critical nucleus as obtained by MD. directly obtained from the simulation. The black triangles are the nucleation rates calculated by the CNT equation using MD data. The blue squares were calculated from MD results with a unique expression for $\Delta\mu$. The red and green dashed lines refer to the J_{MD} extrapolated from the spontaneous nucleation regime to the seeded nucleation regime by substituting D, ρ_i, $\Delta\mu$, and the average value of γ. The pink line refers to extrapolated J_{MD} from the spontaneous regime to the seeded nucleation regime by substituting D, $\Delta\mu$, λ, and the temperature dependence of γ, into the CNT equation. Reprinted with permission from ref 380. Copyright 2020 Elsevier B.V.

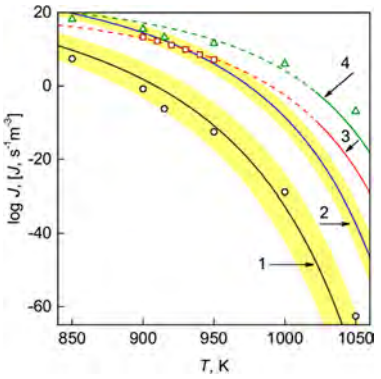

Figure 44. Temperature dependence of the steady-state nucleation rates $J(T)$ of supercooled Ge. Line 1 refers to $\gamma = 0.23(1)$ J/m^2, line 2 refers to $\gamma = 0.201(5)$ J/m^2, line 3 refers to $\gamma = 0.244$ J/m^2, and line 4 refers to $\gamma = 0.23$ J/m^2. The blue circles are calculated using CNT and MD data (with a calculated driving force value), the green triangles are calculated using MD and CNT (without the use of any fitting parameters, i.e., an experimental value of the driving force), and the brown squares are experimental data. The dashed continuations of lines 3 and 4 correspond to a linear extrapolation of the experimental $\Delta\mu(T)$. The estimated uncertainty of $J(T)$ is shown in yellow. Reprinted with permission from ref 381. Copyright 2020 American Chemical Society.

predicted. Despite the shortcoming that the predicted nucleation rates are not in perfect agreement with experimental values, this energy landscape model can provide additional insights into the physics of nucleation and on the validity of CNT and other theoretical models, without the constraints of using fitting parameters, paving the road for further studies.

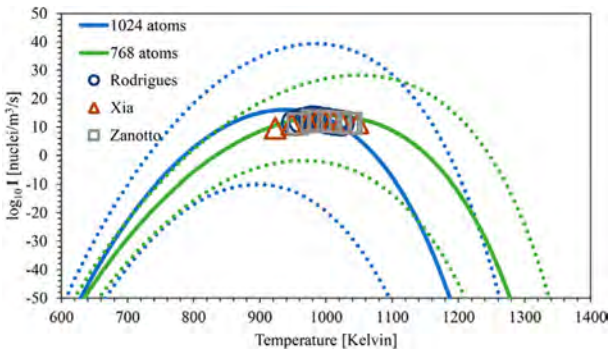

Figure 45. Nucleation curve for barium disilicate as predicted using the energy landscape model. The data referenced can be found in refs 382−384. Reprinted with permission from ref 193. Copyright 2021 Acta Materialia Inc.

7.3. Spatial Fluctuations: Relaxation Effect on Crystal Nucleation

In the application of CNT and all other theoretical models of crystallization of glass-forming liquids, it is assumed that nucleation proceeds only after the supercooled liquid or the glass has completed the structural relaxation process driven by fluctuations toward the metastable equilibrium SCL state. Recently, Schmelzer et al.[385] provided a theoretical treatment of a different situation, when nucleation proceeds concomitantly with structural relaxation. They propose expressions for the thermodynamic driving force and the surface tension in an evolving nonequilibrium liquid as deviations of structural order parameters from their metastable equilibrium values. Relaxation results in changes of the structural order parameters with time; hence, the thermodynamic driving force and surface tension and other basic characteristics of nucleation, such as the work of critical cluster formation and the steady-state nucleation rate, also become time-dependent. They have shown that this scenario may be realized at temperatures close and below the T_g only if the effective diffusivity controlling nucleation and the viscosity (controlling the α-relaxation process) decouple. Analytical estimates were illustrated and confirmed by numerical computations for a model system. The modified theory was applied to the interpretation of experimental data for lithium silicate, used as an example. They confirmed that, only when the characteristic times of structural relaxation are similar or longer than the characteristic times of crystal nucleation (which are only significant for temperatures well below the T_g), elastic stresses evolving in nucleation may significantly affect this process.

One of the most important assumptions of CNT and DIT is that they neglect structural relaxation by assuming that crystal nucleation proceeds in a relaxed, metastable, supercooled liquid. Considering this assumption, the thermodynamic driving force, diffusion coefficient, and interfacial free energy should be constant for a given substance at any temperature. In a recent paper, in an attempt to validate the theoretical framework of Schmelzer at al.,[385] Fokin et al.[386] carried out experiments of a lithium disilicate glass for extended times (up to about 2200 h at 703 K) at several temperatures below the laboratory T_g = 726 K. Their results show that crystal nucleation starts concomitantly with glass relaxation toward the SCL, which strongly affects the nucleation kinetics, taking over 500 h to reach the ultimate steady-state regime at 703 K. Interestingly, this very long relaxation process proceeds much

https://doi.org/10.1021/acs.chemrev.1c00974
Chem. Rev. XXXX, XXX, XXX−XXX

slower than the well-known α-relaxation determining, e.g., the temporal evolution of the glass density, which takes only ~20 h at this same temperature. The structural relaxation process decreases the work of critical nucleus formation leading to a continuous increase of the nucleation rate. This time-dependent nucleation rate mainly reflects the long structural relaxation mode of the glass and is not related to the classical transient nucleation, which has been exclusively employed so far in the interpretation of nucleation kinetics below T_g by most researchers. Their experimental results and analyses prove the effect of glass relaxation (which is related to fluctuations) on crystal nucleation and also confirm the recent results of Cassar et al.[387] and Xia et al.[388] that the alleged "breakdown" of the CNT at temperatures close and below T_g results from improper use of non-steady-state nucleation rates.

7.4. Dynamical Heterogeneity Effect on Nucleation

The cumulative understanding of dynamical heterogeneities provides an approach to understand the slowdown of SCL dynamics during vitrification as the temperature decreases.[389−391] Furthermore, attention has been given to investigate the relationship between structural relaxation and dynamical heterogeneity in glass-forming liquids.[392,393]

Nanosized crystalline clusters or embryos statistically appear and disappear within a supercooled liquid and only become sustainable when a critical size is reached. However, despite the extraordinary relevance of crystal nucleation, due to the extremely small size scales and either very long or very short time scales, experimental assessment of such small clusters is very challenging, and comprehension of some microscopic details of nucleation remains intangible. All nucleation theories assume that SCLs are structurally and chemically uniform; however, we now know that this is not true. Relevant questions then arise: What is the effect of dynamical heterogeneities on crystal nucleation? In which regions of the supercooled liquid does nucleation occur?[394−397] We address these relevant issues in the next paragraphs.

The microscopic connection between the dynamical heterogeneity and crystal nucleation was not known until recently. Water crystallization is the most omnipresent phase transition on earth; hence, significant effort has been focused on understanding the macro- and microscopic details of ice nucleation.[398] From a structural perspective, some investigations highlighted differences between very mobile and very immobile regions within the liquid.[399] Regarding bond-orientational order, Russo and Tanaka[400] have observed a higher degree of tetrahedrality in less mobile regions and five-membered rings acting as locally preferential structures.[400] However, it has been under debate whether the immobile or mobile regions could be favored domains for nucleation. Fitzner et al.[396] filled this important gap with computer simulations to infer in which regions of the SCL ice nucleation happens preferentially. They have shown the evolution of the coarse-grained immobility and crystallinity fields from a particular trajectory. In the prenucleation stage, there is the absence of crystalline order in the large immobile domains. However, during nucleation, an ice nucleus forms and grows within the immobile domain.

The same authors reported simulation results that allowed them to sample many nucleation events at high temperatures. Simulation details are given in the original article.[396] Fitzner et al.[396] have also analyzed the distribution of primitive rings in the regions of extreme mobility, denominated as MI and MM. The MI regions have a ring distribution with a sharp peak around 6 ± 1 members, whereas the distribution for the MM domains is much broader. Moreover, the percentage of fully H-bonded rings is much higher in the MI region. In particular, an abundance of six one-membered hydrogen-bonded rings can be considered as the critical structural characteristic of the MI domains in the liquid. If regarded in isolation, most of the six-membered rings in the MI domains are seen as icelike, which is the sign of the relative orientation between rings that is different from the crystal and therefore the missing component in forming ice. Since this was observed in the MI region, which shows a reduced diffusivity, the authors suggested that the mechanism of the initial formation of icelike clusters is collective. This is consistent with a picture of ring reorientation rather than single-particle attachments through diffusive motion. In conclusion, Fitzner et al.[396] have clearly shown that ice nuclei are formed in immobile regions of the SCL water. Additionally, the ring distribution is the structural hallmark of dynamical heterogeneities.

In an independent study, Puosi and Pasturel[397] inferred by MD simulations the mechanism underlying crystal nucleation in supercooled Cu_5Zr metal, which shows crystalline and noncrystalline (local) order based on icosahedral symmetry. Figure 46 shows the crossover temperature T_s where the supercooled liquid no longer follows the Stokes−Einstein

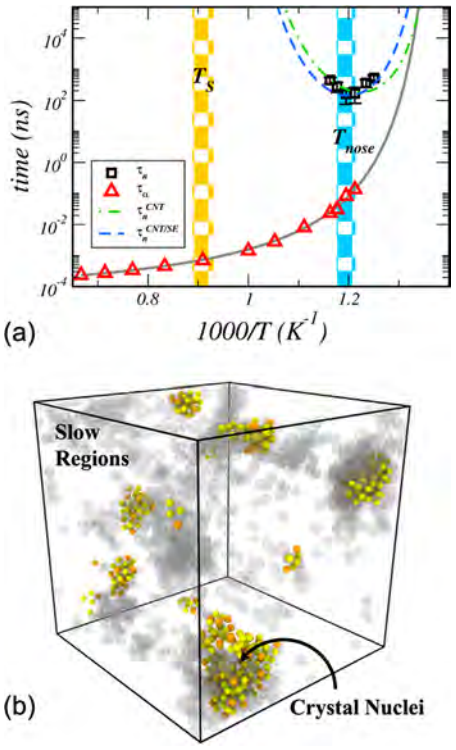

Figure 46. (a) Average nucleation time (squares), τ_n (also known as $\langle t_1 \rangle$), and relaxation time (triangles), τ_α, vs inverse of temperature for Cu atoms. The solid line is a fit of relaxation data by the Vogel−Fulcher−Tammann (VFT) viscosity equation. The dash-dotted and dashed lines show the CNT predictions of the nucleation time. The shaded regions mark the onset temperature, T_S, and the temperature T_{max} (with their uncertainty). (b) Colored particles are crystal nuclei; gray particles are slow regions of dynamical heterogeneities for selected configurations at T = 837 K, close to T_{max}, and t = 160 ns. Reprinted with permission from ref 397. Copyright 2019 Acta Materialia Inc.

https://doi.org/10.1021/acs.chemrev.1c00974
Chem. Rev. XXXX, XXX, XXX−XXX

relation. This temperature coincides with the emergence of spatially heterogeneous dynamics. This coincidence is very relevant to physics and materials science.

These authors showed that the origin of these phenomena is related to an increase of icosahedral symmetry in the SCL on the cooling path toward the glass transition. Homogeneous, spontaneous crystal nucleation could be detected by MD near the glass transition temperature and occurs in domains of high icosahedral symmetry. The underlying nucleation mechanism was thus linked to the slow regions of dynamical heterogeneities. The crystallization pathways were described as follows: (i) formation of heterogeneities in the supercooled liquid start below T_s, and (ii) slow regions of dynamical heterogeneities, having a high degree of icosahedral symmetry, act as nucleation ancestors (Figure 46b). These findings corroborate Fitzner's[396] conclusions for ice nucleation and allowed them to quantify how the nonuniform nature of supercooled liquids influences the nucleation theory.

The above-discussed research works on recent MD simulations show that homogeneous nucleation in Cu_5Zr and H_2O happen in the largest, most immobile regions that arise from heterogeneous dynamics in supercooled liquids. It would be educational and relevant to test these novel findings with other substances.

7.5. Growth of Stable Crystalline Nuclei

Crystal growth is the next step after a stable crystalline nucleus is formed within a supercooled liquid, as discussed in section 7.1. When a crystalline cluster is sufficiently large, crystal growth becomes deterministic and averages out the effects of fluctuations.[401] However, it is still possible to connect the early stages of crystal growth to fluctuations, as will be discussed in this section.

After a crystalline embryo overcomes a certain temperature-, pressure-, and composition-dependent critical size r^*, it becomes a stable crystal nucleus resistant to dissolving back into the ambient phase; the greater the size above the critical value, the lower the probability for it to dissolve back. If a system is below its liquidus temperature, increasing the volume of any stable crystalline nucleus leads to a reduction in the free energy of the system. Strictly speaking, any noncrystalline substance with one or more supercritical crystalline nuclei cannot be considered metastable and should be considered an unstable phase fated to crystallize (assuming, of course, that no other chemical transformation happens between its current and fated states). This notion is of particular interest here, as the system's free energy can be lowered through crystal growth. One possible growth mechanism is by effective attachments of molecular units mediated by fluctuations in the crystalline–ambient interface, without the need to access states of higher energy. Note that, as expected, not all fluctuations will lead to attachments.

In the crystal growth process, the crystalline phase increases its volume at the expense of the ambient phase. In the initial stages of crystal growth, right after a supercritical nucleus is formed, the crystal growth velocity depends on the curvature of the nucleus boundary. Assuming a spherical isotropic cluster in isobaric conditions, Kelton and Greer arrived at the following equation for the growth velocity of supercritical nuclei using classical nucleation theory kinetic rate equations:[402,403]

$$\frac{\partial r}{\partial t} = \frac{16D}{\lambda^2}\sqrt[3]{\frac{3V}{4\pi}}\sinh\left(-\frac{V}{2k_BT}\left[\Delta G_V + \frac{2\gamma}{r}\right]\right) \quad (91)$$

Here, r is the radius of the crystalline cluster, t is the time, D is the diffusion coefficient governing crystal growth, λ is the average jump distance, V is the molecular volume, ΔG_V is the change in the Gibbs free energy per unit volume due to crystallization ($\Delta G_V = \Delta G_{cr} - \Delta G_{liq}$), where the subscripts cr and liq refer to the crystalline and liquid phases, respectively), and γ is the interfacial energy. Equation 91 is an approximation; its accuracy is lower when the size of the nucleus is close to critical.

Alexandrov and Malygin[404] advanced a rigorous physical description of the effect of fluctuations in the crystal growth stage of a melt. In their formulation, they assumed a melt absent of crystals that is instantaneously cooled by an amount $\Delta\theta_0$ below the liquidus temperature at a time $t = 0$. Considering that the system undergoes homogeneous crystal nucleation, the particle-radius density distribution function, f, can be related to the crystal growth rate, g, via a Fokker–Planck kinetic equation:

$$\frac{\partial f}{\partial t} + \frac{\partial}{\partial r}(gf) = \frac{\partial}{\partial r}\left(D_\rho\frac{\partial f}{\partial r}\right) \quad (92)$$

D_ρ is a function representing the rate of fluctuations that must be determined by statistical physics or can be assumed proportional to the crystal growth rate, as considered by Alexandrov and Malygin.[404] Equation 92 requires that $t > 0$ and $r > r^*$, with the initial condition of $f = 0$ when $t = 0$ (i.e., no crystals present at the start of the experiment). Solutions to the differential eq 92 were advanced by Alexandrov and Malygin[404] after considering some thermal and kinetic assumptions. A simulation for a typical metallic liquid is shown in Figure 47.

The crystal growth velocity of sufficiently large crystal clusters ($r \gg r^*$) becomes independent of the curvature of the cluster (see Figure 48). Crystal growth is deterministic at this

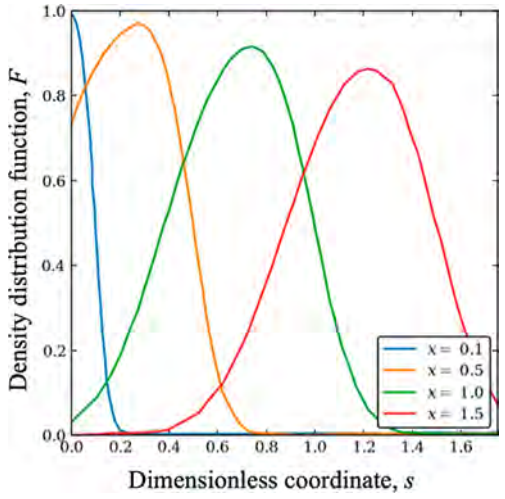

Figure 47. Density distribution ($F = fg/I_0$, where I_0 is the crystal nucleation rate of the supercooled liquid) of crystalline clusters [$s = r(I_0/g)^{0.25}$] at different dimensionless modified times x for a typical metallic melt. Data collected from Alexandrov and Malygin (ref 404); the simulation details and an in-depth description of the reduced variables are discussed therein.

https://doi.org/10.1021/acs.chemrev.1c00974
Chem. Rev. XXXX, XXX, XXX–XXX

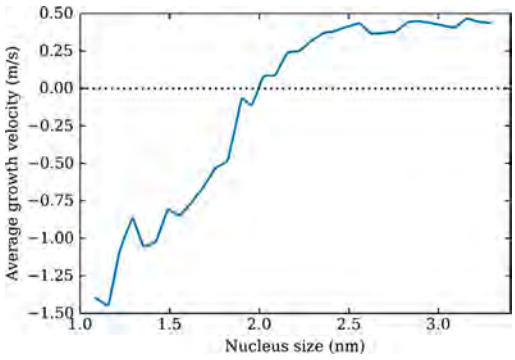

Figure 48. Average crystal growth velocity vs size of crystalline nucleus for germanium simulated via molecular dynamics at 2000 K (1/2 T_m).[405] The zero growth velocity happens for the critical nucleus size. The velocity approaches a size-independent value as the nucleus grows. Data obtained from ref 405.

scale, averaging out any effect of fluctuations.[401] In this scale, the similarity between the crystal cluster composition and the ambient phase is critical for the kinetics of the process. The following two paragraphs discuss this topic within the theoretical framework of the classical crystal growth models.

When the crystalline phase composition is equal or sufficiently similar to the ambient phase, crystal growth is governed by attachment and detachment of the atoms or molecular units that are readily available at the boundary; this process is termed "interface controlled", "kinetically limited", or "ballistic" growth. Interface controlled growth of a sufficiently large crystal is usually linear (within the same crystallographic direction) with respect to time in isobaric conditions if the latent heat of crystallization is promptly dissipated; crystal growth catalyzed by latent crystallization heat is discussed elsewhere.[406−408]

Alternatively, when the crystalline phase is chemically different from the ambient phase, crystal growth can only happen by long-range diffusion of the necessary atomic or molecular building blocks, a situation called "diffusion-controlled" or "diffusion-limited" growth.[409] Diffusion-controlled growth can be linear with respect to time (e.g., dendritic growth) or have a fractional dependence with time;[409] either way, the long-range diffusion required for this mechanism is mediated by compositional fluctuations and will depend on the diffusing entity, the diffusion environment, and thermal energy. The modeling of diffusion is discussed in depth by Crank.[410]

Impurities or stoichiometric deviations from the congruent melt composition can cause compositional striations due to crystal growth rate fluctuations.[411] Some causes for this growth fluctuation are vibrations, melt and ambient temperature control, thermal convection in the melt, and crystal rotation. Under a carefully controlled experiment, only the last two contribute to growth fluctuations. For instance, Carruthers et al.[411] reported that for lithium niobate, under typical conditions, rotational striations are spaced 4−6 μm apart while thermal convection striations are spaced 20−40 μm apart. These fluctuations cause optical inhomogeneity and can be detected by measuring birefringence.

It is well-established that all materials can vitrify when subjected to sufficiently fast cooling from the liquid state. Thus, novel materials, such as thin metallic and chalcogenide glasses with unusual properties, have been obtained successfully by very fast quenching. Also, controlled, catalyzed internal crystallization of specific glasses has led to a variety of advanced glass-ceramics that are manufactured commercially. Deeper insights into glass crystallization processes, such as precise predictions of nucleation and growth rates and critical cooling rates for glass formation, based solely on materials properties, will depend critically on new developments in nucleation theories and computer simulation techniques.

Despite the many advances achieved in understanding crystal nucleation in SCL and glasses, the role of fluctuations and other problems remain open. Among the most important, we remark the following: (i) knowledge of the bulk (structure, composition, density) and surface properties of the critical nuclei and sub- and supercritical crystals as a function of their size; (ii) a theoretical description of the temperature dependence of the crystal nucleus/liquid interfacial energy; (iii) the nature of the effective diffusing entities and related coefficients that control crystal nucleation (viscosity, crystal growth velocity, nucleation time lag); (iv) a deeper understanding of the relationship, if any, between the molecular structure of glass-forming melts, fluctuations, and the nucleation mechanism;[412] (v) the precise relation between the sizes of supercritical nuclei and the sizes of cooperatively rearranging regions of the domains of heterogeneous dynamics in viscous liquids;[413] such work could contribute to generalize or not the crossover predicted by Stevenson and Wolynes;[395] (vi) further research along the lines originally described by Wilkinson et al.[193] using improved energy landscape models and larger system sizes.

The analyzed problems connecting the crystal nucleation phenomenon to fluctuations in supercooled liquids—dynamical heterogeneities, relaxation, and liquid−liquid phase separation (section 8)—simultaneously shed light and raise new questions on the physics of nucleation. The solution to these problems, and others not mentioned here, could significantly deepen the understanding of this intricate process and, ultimately, aid in the development of novel glasses and glass-ceramics having exotic, unusual compositions and combinations of properties, which serve as a great incitement for supercooled liquid and glass crystallization being a very active research topic.

8. PHASE SEPARATION

The phenomenon of liquid−liquid phase separation (LLPS)—also termed liquid phase separation, amorphous phase separation, glass-in-glass phase separation or liquid immiscibility—refers to immiscible liquids. It is pervasive in glass-forming systems. LLPS stems from thermal and compositional fluctuations in a liquid or supercooled liquid, which result in two widely distinct transformation mechanisms: nucleation and growth and spinodal decomposition. In the later stages of transformation, when the chemical compositions of the liquid phases reach the binodal boundaries (to be described later), both mechanisms lead to coarsening, and the largest droplets/fluctuations grow at the expense of the smallest, decreasing their total number and interfacial area with time.

Spontaneous LLPS is usually unwanted in glass manufacturing because it leads to loss of transparency. It modifies the physical and chemical properties of glass-forming liquids, making it difficult to mold glass articles, and deteriorates the optical transparency and the quality of the final glass.[414] However, for certain applications, the production of heterogeneous glassy materials containing phases of a different nature and morphology can be considered an advantage, such as in

https://doi.org/10.1021/acs.chemrev.1c00974
Chem. Rev. XXXX, XXX, XXX−XXX

the field of glass-ceramics or opal glasses. It is frequently suggested that prior LLPS can be a key step in the production of glass-ceramics with copious internal crystallization. The range of phase-separated glasses and the diversity of their compositions and physical properties cover a variety of commercial applications, including the well-known Vycor and opal glass and, more recently, porous glass membranes.[415]

The size, distribution, and morphology of the separated phases can be well-described by kinetic laws. The first models were based on diffusion processes[416] and are still relevant. Other models based on structural considerations have also been developed.[417] Nevertheless, relatively scarce experimental evidence is available to validate these concepts. New methodological developments associated with structural (NMR, electron paramagnetic resonance, and micro-Raman) and microstructural (SEM, high-resolution TEM, and SAS) characterization methods open new perspectives toward the understanding of these mechanisms. Other techniques, such as *in situ* high-temperature experimental methods (environmental SEM, X-ray microtomography, and Raman microspectroscopy) are particularly suitable for determining the mechanisms and extent of the immiscibility ranges, such as phase separation temperature, stability range, and quantity of separated phases. Computer simulations have also been used to model simpler systems and will most probably play an important role with the advent of faster computers.[417]

A detailed description of the thermodynamics of phase separation and equations to describe the different types of LLPS mechanisms and kinetics have been dealt with in many articles and recently summarized in a textbook.[417] Here, we will present a summary of the process, an overall picture of LLPS, and its effects on crystal nucleation, which is another fluctuation-controlled phenomenon covered in section 7.

As an example, Figure 49 shows the phase diagram of the $BaO-SiO_2$ system, with the metastable miscibility gap. The gap contains two regions: the spinodal, where LLPS occurs by continuous growth of compositional fluctuations, and the binodal, where LLPS takes place by nucleation and growth of liquid droplets having compositions that widely differ from that of the starting SCL. Recall that nucleation is also fluctuation-driven. The spinodal region is centered within the miscibility gap. In Figure 49, the miscibility gap is located at a critical point of 1460 ± 50 °C and 10 ± 1 mol % BaO.

LLPS can take place above or below the liquidus temperature, T_L; the latter is metastable and shown in Figure 49. This matter was intensively discussed by the oxide glass community in the 1970s and 1980s, which resulted in many articles and monographs[414] on the subject. More recently, the chalcogenide glass and metallic glass communities reported that LLPS also takes place in some systems and significantly affects several properties, including the glass-forming ability.[418] This fact is particularly relevant because these two communities are eagerly searching for new formulations having good glass-forming ability.

8.1. Thermodynamic Fluctuations Driving Liquid Phase Separation

The birth of two immiscible liquids in a homogeneous binary system is associated with a positive value of the mixing enthalpy, ΔH_m. In general, a slightly positive enthalpy of mixing may still result in a stable solution, where the Gibbs free energy of mixing remains negative over the full composition range. However, higher values of ΔH_m may encourage regions

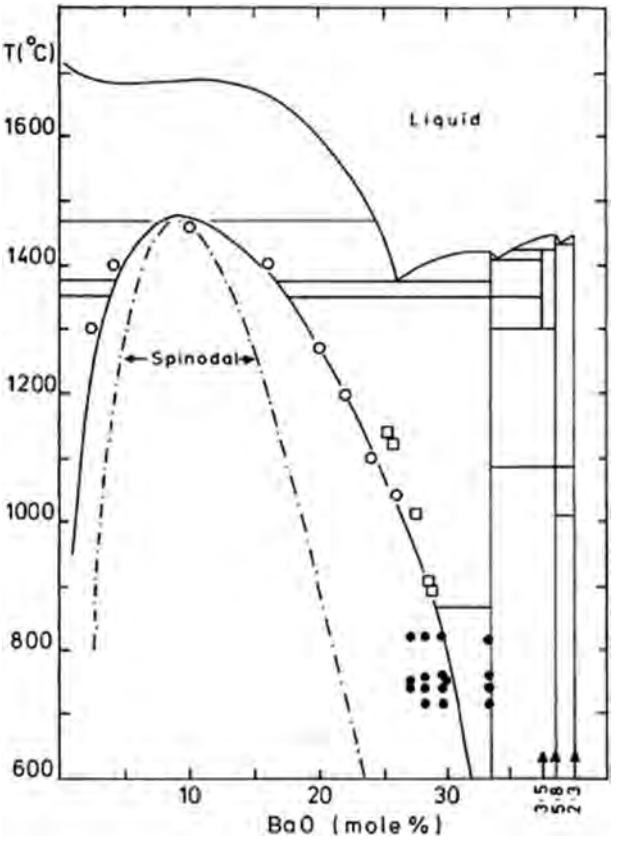

Figure 49. Phase diagram of the $BaO-SiO_2$ system showing the metastable miscibility gap. The solid line refers to the binodal boundary, and the dash-dotted line represents the spinodal. The experimental points for the binodal were determined by (○) Seward et al. (ref 419) and (□) Ramsden (ref 420) The black dots refer to thermal treatments used by (●) Zanotto (ref 421) for compositions inside and outside the gap. Reprinted with permission from ref 421. Copyright 2020 Elsevier Ltd.

where fluctuations leading to phase separation are thermodynamically favorable. For example, as shown in Figure 50a, the entropy term predominates at high temperatures, and the free energy has only a single minimum; at lower temperatures, the entropy term decreases and changes the shape of the Gibbs free energy curve, as shown in Figure 50b.

The Gibbs free energy variation associated with phase separation depends on the temperature. Minimization of the free energy of the system during this process is initiated by thermal[422] or chemical[423] fluctuations, which are responsible for the appearance of different phases in the supercooled liquid. Figure 51 shows a miscibility gap in a binary phase diagram with two liquids of different compositions separated by a binodal curve that defines the compositional region of miscibility versus temperature. Above a critical (or consolute) temperature, T_{Cb}, the free energy of mixing exhibits only a single minimum. Temperatures below T_{Cb} result in a change in the Gibbs free energy that exhibits two minima leading to phase separation. At a temperature T_1, the equilibrium compositions of the liquid phases A_1 and B_1 arising from an original solution M (composition $X_A < X_M < X_B$) are determined by the two points on the Gibbs free energy curve having the same tangent, which represents the maximum driving force for the precipitation of the two phases. Their equilibrium compositions and quantities vary with the

https://doi.org/10.1021/acs.chemrev.1c00974
Chem. Rev. XXXX, XXX, XXX−XXX

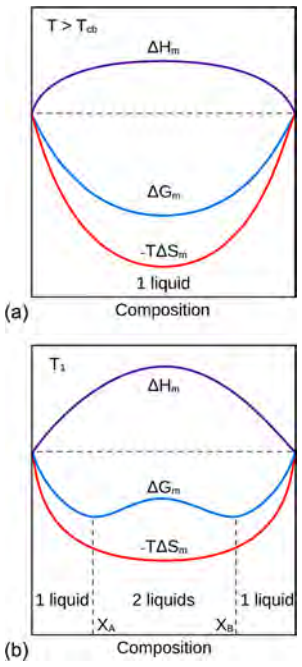

Figure 50. Variation of ΔG_m vs temperature-dependent entropy: (a) for a high temperature ($T > T_{Cb}$) where the entropy term is maximum; (b) for $\Delta H_m \gg 0$ at low temperatures (T_1) where the entropy is minimum.

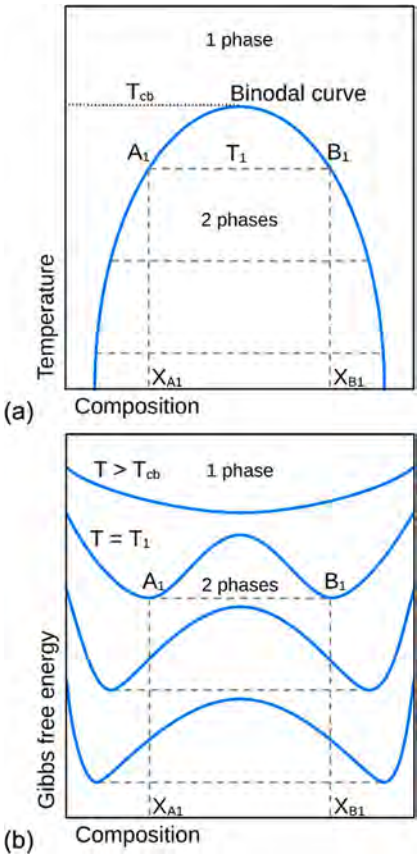

Figure 51. (a) Schematic representation of a coexistence (binodal) curve on a phase diagram and (b) the associated Gibbs free energy variation as a function of temperature.

temperature until the glass transition or crystallization takes place. The phase diagram shows that, as the temperature rises, the immiscibility range diminishes and finally disappears at the critical temperature T_{Cb}.

The mechanism of phase separation depends on the parent glass composition and temperature. A description of the Gibbs free energy variation during the process can distinguish between regions where phase separation occurs in different ways (Figure 52). The conditions of phase stability in terms of

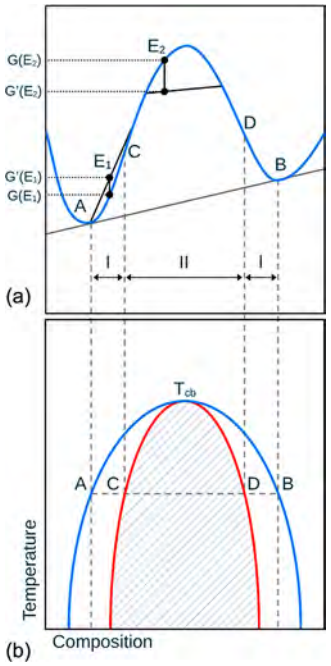

Figure 52. Gibbs free energy variation around composition E_1 in the nucleation and growth region (area I, metastable) and around composition E_2 in the regions of spinodal decomposition (area II, unstable).

the first and second derivative of the free energy with respect to composition were defined by Gibbs,[373,424] who stressed the special significance of the inflection points on the free energy curves (Figure 52). Phase separation occurs in the composition region between two minima (points A and B where $\partial G/\partial X = 0$). The metastable binodal regions AC and DB have a positive curvature ($\partial^2 G/\partial X^2 > 0$), whereas the unstable spinodal region has a negative curvature ($\partial^2 G/\partial X^2 < 0$).

Take a composition E_1 in the binodal region of Figure 52 at constant temperature and pressure. The Gibbs free energy at point E_1, $G(E_1)$, increases for a small composition fluctuation and reaches G' (small fluctuation around E_1) > $G(E_1)$. Thus, in the binodal area, the system is stable with respect to small fluctuations, and phase separation can only occur if a larger composition fluctuation takes place. This leads to LLPS via nucleation and growth. Considering composition E_2 in the spinodal region of Figure 52, any small fluctuation decreases the free overall energy; thus, the system is unstable against any minute compositional fluctuation and spontaneously evolves toward its equilibrium state without any activation barrier. This process refers to LLPS via spinodal decomposition. Future study is needed before being able to correlate computational studies on concentration[141] with experimental and computational phase separation studies (for the same composition and ideally in the unstable spinodal region) to comment on

https://doi.org/10.1021/acs.chemrev.1c00974
Chem. Rev. XXXX, XXX, XXX−XXX

potential microscopic instabilities driving the phase separation process.

The inflection points C and D ($\partial^2 G/\partial X^2 = 0$) in Figure 52 are the spinodal points and the minima A and B ($\partial G/\partial X = 0$) are the binodal points. In the isobaric temperature/composition space, the loci of the spinodal points define the spinodal curve, and similarly, the binodal points define the binodal curve. The spinodal curve is always contained within the binodal. They have one tangent point called the critical or consolute temperature, T_{Cb}, which corresponds to the highest temperature for which LLPS is observed within the considered binodal/spinodal domain. The inflection points C and D become one, and the Gibbs free energy of mixing has a single minimum with respect to the composition.

In the binodal region, LLPS occurs by nucleation and growth, resulting in a nano- or microstructure with globular separated particles dispersed in a residual liquid matrix (Figure 53a). These particles are separated from the matrix by a relatively sharp interface (compared to the spinodal structures), and their composition does not change over time, whereas the composition of the residual glass matrix moves toward the binodal with heat treatment time. After it reaches the binodal, it no longer changes, and the coarsening mechanism takes over. The kinetics of liquid phase separation by nucleation and growth can be described by the nucleation theories discussed in section 7; a thermodynamic barrier must be overcome before the nucleation process becomes operative.

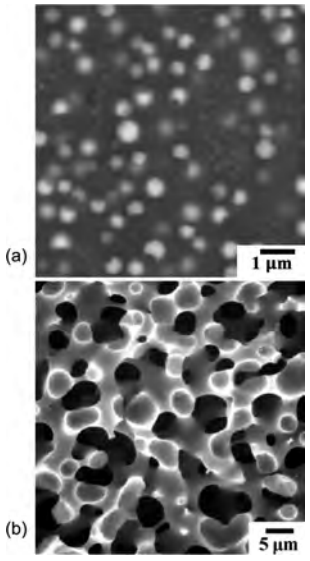

Figure 53. (a) SEM micrograph of liquid phases formed by nucleation and growth in a sodium borosilicate glass. Reprinted with permission from ref 417. Copyright 2017 EDP Sciences. (b) SEM micrograph of phases formed by spinodal decomposition. Panel b reprinted with permission from ref 415. Copyright 2010 Elsevier B.V.

On the other hand, in the spinodal region, LLPS outcomes strongly interconnected regions separated by diffuse interfaces (Figure 53b), which vary over time until they reach the binodal boundary (they overcome the spinodal boundaries, which are only effective for the initial stages of the decomposition). The morphology of the separated phases depends on the quenching rate and further thermal treatment schedule. Morphology provides only a qualitative indication of the mechanism class involved in phase separation. Analysis of the evolution of the phase compositions is necessary to determine which of these complex mechanisms is operating.

Spinodal decomposition takes place when a single phase spontaneously separates into two different phases, with no thermodynamic barrier. As already explained with schematic thermodynamic diagrams, this type of transformation occurs in the absence of nucleation because any infinitesimal compositional fluctuation in the system reduces the Gibbs free energy. As a result, spinodal transformation starts immediately and the only barrier is kinetic. The parent supercooled liquid thus separates into two coexisting phases, which are rich in one species and poor in the other, and it is all fluctuation-driven, from beginning to end. Hence, as opposed to nucleation, there is no time lag to initiate this process. The compositions of the liquid phases progress toward the respective binodal frontiers, their average size grows, and their kinetics only depend on the effective diffusivity. This phenomenon is observed in metallic, polymeric, and inorganic systems.

In most cases, the two phases emerge in approximately equal proportion and form intertwined structures that gradually coarsen. Spinodal decomposition is thus fundamentally different from nucleation and growth. In this mechanism, compositional fluctuations start the phase separation process everywhere, uniformly throughout the sample volume, whereas in the other mechanism, a nucleated phase forms at a discrete number of points.

The dynamics of spinodal decomposition are successfully modeled by the Cahn−Hilliard approach. To describe spinodal decomposition, Cahn and collaborators[416,425,426] modified the Gibbs free energy function proposed by Becker and Döring[427] by adding an interfacial energy term. The Cahn−Hilliard equation can be solved numerically by phase field models.[416,425,426,428] These models are capable of describing the evolution of separated phases by diffuse interfaces by taking into account the variation of the Gibbs free energy function characterized by a dual potential function. The variation of the concentration with time is used to model the composition and microstructure of the separated phases.

8.2. Effects of Liquid Phase Separation on Crystal Nucleation

Glass-forming ability is directly linked to the fluctuation-driven nucleation and crystallization tendency of a system; the faster the crystallization kinetics, the poorer the glass-forming ability. It has long been known that liquid−liquid phase separation can have a noticeable influence on the crystallization pathways and dynamics.[429] However, it is also known that LLPS is *not* essential to produce internal crystal nucleation in glasses; the stoichiometric glasses $BaO{\cdot}2SiO_2$ and $Li_2O{\cdot}2SiO_2$, for example, do not show LLPS and still copiously crystallize in the interior when enough energy is provided. Moreover, several alkali and alkaline earth silicates and alkali borates show extensive LLPS and still do not crystallize internally.

Theoretically, LLPS could influence crystal nucleation in several ways, but most of the possibilities fall into two main types:

(1) The *compositions* of the separated liquid phases. The crystal−liquid interfacial energy could be lower for crystals forming in one of the liquid phases than in the original liquid, or one of the liquid phases could have a higher atomic mobility than the parent glass.

(2) The *interfaces* between the separated liquid phases could promote heterogeneous crystal nucleation.

https://doi.org/10.1021/acs.chemrev.1c00974
Chem. Rev. XXXX, XXX, XXX−XXX

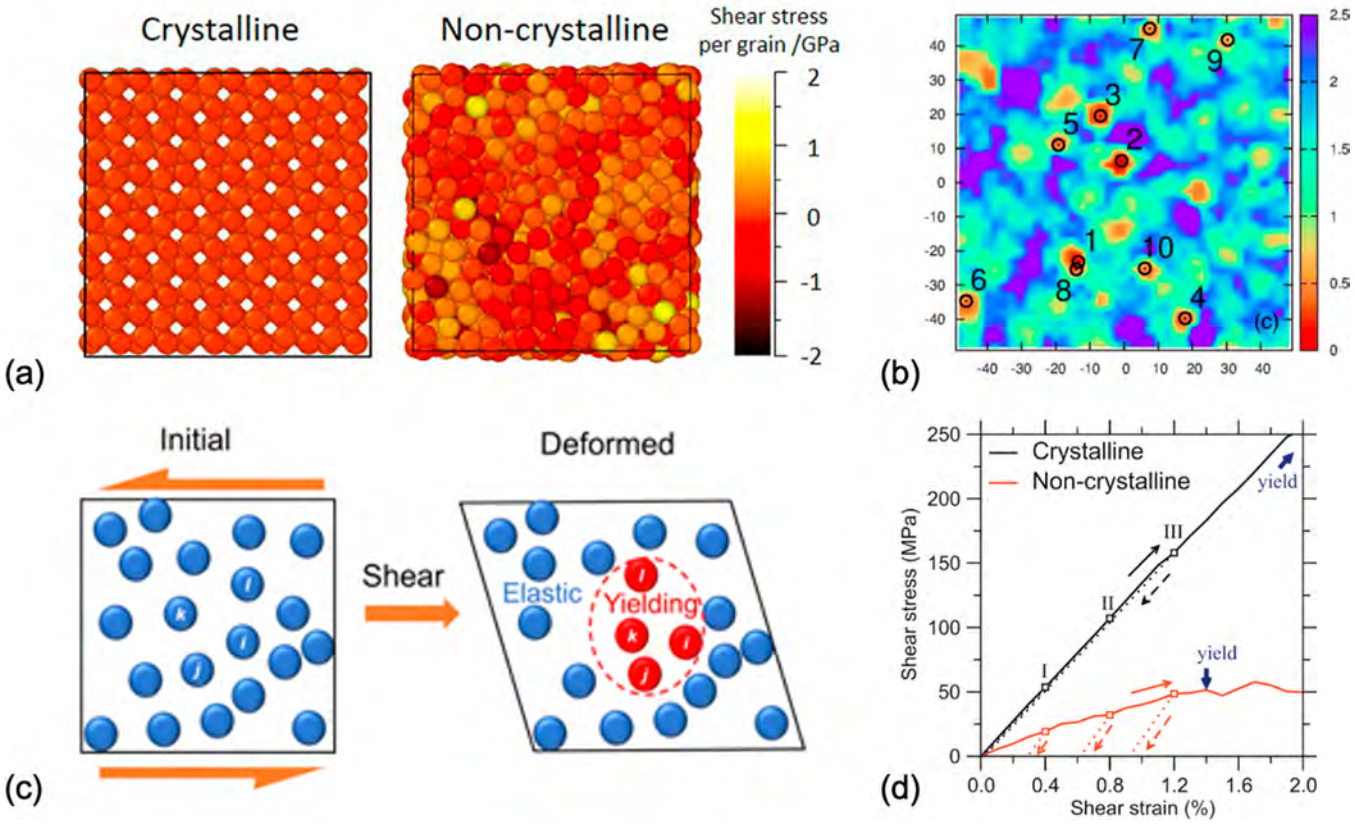

Figure 54. (a) Spatial distribution of the local shear stress per particle (in the absence of any external load) in a three-dimensional crystal and a disordered solid counterpart exhibiting a similar packing fraction (ref 445). (b) Spatial distribution of the local yield stress in a two-dimensional Lennard-Jones glass (ref 447). The locations of the first 10 plastic events upon loading are marked as open black circles. (c) Schematic illustration of nanoyielding, which manifests itself as a nonaffine rearrangement of the atoms *i*, *j*, *k*, and *l* upon loading. (d) Stress−strain relationship upon shear deformation in the three-dimensional crystals and disordered solids shown in panel a. The dashed lines represent the unloading process. Note that the nanoyielding behavior of a three-dimensional glass (e.g., panel a) can be different from that in a two-dimensional glass (e.g., panel b). Panels a and d are reprinted with permission from ref 445. Copyright 2019 Elsevier Ltd. Panel b is reprinted with permission from ref 447. Copyright 2018 American Physical Society.

These two points have been discussed by several authors. The main arguments were summarized by James[429,430] and Uhlmann and Kolbeck.[431] Recently, Zanotto[421] analyzed old and new evidence for the effect of LLPS on crystal nucleation in a comprehensive review. The subject of LLPS, including its effects on the crystallization of oxide glass-formers, was intensively pursued in the 1970s and 1980s[97,384,414,418,420,429,432−439] and resurfaced recently, motivated by the metallic and chalcogenide glass communities. Despite numerous works on the possible effects of LLPS on crystallization, they led to a confusing situation. Some authors advocated for a positive effect of the LLPS interfaces on crystal nucleation, while others defended compositional shifts, and various others detected no significant effect. A recent review[421] strongly supported the concept that the dominant effect of LLPS is to form one liquid phase with a composition quite close to that of the equilibrium crystal phase, which significantly increases the crystal nucleation rate.

9. MECHANICAL PROPERTIES

Currently humans mostly interact with information displays by touching a piece of glass, which has stimulated the development of novel scratch- and fracture-resistant glasses. Despite these developments, brittleness remains the main limitation of inorganic glasses. In that regard, fluctuations offer an additional degree of freedom (besides composition and thermal/pressure history) to enhance the mechanical properties of glasses. Indeed, although the mechanical properties of glasses (e.g., elasticity) are defined and measured at the macroscopic scale (i.e., the scale at which glass appears homogeneous), they are influenced by the structural fluctuations that emerge at a finer scale.[440,441] In the following, we focus on the effects of spatial fluctuations on elasticity, nanoductility, fracture, creep, and fatigue. Although the focus of this review paper is on oxide glasses, this section additionally touches on metallic glasses because comparisons between the two families of glasses offer useful insights.

9.1. Fluctuations in Local Elasticity

Structural heterogeneity is directly associated with the existence of fluctuations in the local elasticity of glasses,[440] which can result from the nonequilibrium nature of glasses or be induced by imposed macroscale elastic deformations.[442] Specifically, the extent of nanoscale elastic fluctuations was found to increase up to a factor of 3 upon elastic loading.[442] Due to the existence of such local structural fluctuations, the elasticity of glasses differs in nature from that of crystals. For example, the bulk modulus of a metallic glass is usually about 5−10% lower than that of its isochemical crystal counterpart, while the shear modulus of glasses is typically around 20−30% lower.[443,444]

https://doi.org/10.1021/acs.chemrev.1c00974
Chem. Rev. XXXX, XXX, XXX−XXX

Recent MD simulations have shown that the difference in elasticity between glasses and associated crystals is not solely a consequence of differing packing densities. Indeed, for the same packing density, the elasticity of a glass differs (by being less stiff) from that of a crystal.[445] The loss in stiffness in a disordered solid as compared to its crystalline counterpart has been shown to arise from the existence of some fluctuations in the local stress experienced within the network[445] (see Figure 54a). Such fluctuation in local stress is a manifestation of the nonequilibrium, noncrystalline, and nonergodic nature of glasses. Note that fluctuations in the local stress do not result in the formation of any macroscopic stress, since regions experiencing negative local stress (i.e., local compression) are counterbalanced by regions experiencing positive local stress (i.e., local tension).

In crystals, since such fluctuations are not observed, the local stress experienced by the atoms is initially zero, and then it homogeneously increases upon external loading so that the deformation remains fully elastic until the macroscopic yield stress is achieved. Once the macroscopic yield stress is reached, the crystal starts to exhibit irreversible ductile deformations or cracking. In contrast, in glasses, the stress that results from the application of an external load adds to the preexisting local stress. As such, due to preexisting stress fluctuations, the additional stress induced by the macroscopic deformation causes some positively prestressed regions to quickly reach their local yield stress and, thereby, to release their local stress through local plastic, irreversible reorganizations,[446] a behavior that has been referred to as "nanoyielding".[445] Note that the yield stress itself can also exhibit some heterogeneity[447,448] (also see Figure 54b). As illustrated in Figure 54, parts c and d, such nanoyielding is highly localized and, hence, does not result in the macroscopic yielding of the glass (i.e., it occurs during the macroscopic elastic regime). The loss of stress resulting from nanoyielding events, i.e., arising from the presence of some preexisting stress heterogeneity within glasses, explains their lower stiffness as compared to their crystalline counterparts (at constant composition and packing density).

In addition to the insights offered by simulations, nanoyielding has also been confirmed experimentally. On the basis of X-ray scattering and anisotropic pair distribution function analysis in metallic glasses, it has been shown that, even in the macroscopic elastic regime, a quarter of the glass (in volume fraction) tends to deform inelastically.[449] The existence of such elastic heterogeneity also manifests itself in the fact that vibrations in glasses are not well-described by classical homogeneous continuum elastic theories (e.g., Debye model), when the vibrational wavelengths are smaller than the typical scale of elastic heterogeneity.[450] In addition to static elasticity, the existence of some heterogeneity in viscoelasticity has also been observed at the nanoscale through both static and dynamic force microscopy.[451,452]

9.2. Intrinsic Nanoductility Induced by Topological Fluctuations

Glasses are often viewed as archetypical brittle materials at the macroscale, but the existence of ductility at the nanoscale (nanoductility) has been demonstrated by both experiments and simulations.[453−456] Recent results have shown that nanoductility arises from the existence of some spatial fluctuations in the topology/rigidity of glasses.[457] Figure 55a shows the spatial distribution of the number of constraints per atom (n_c, as described in section 5.4) in a $(Na_2O)_{20}(SiO_2)_{80}$ glass simulated by molecular dynamics simulations. Although this glass is, on average, isostatic ($\langle n_c \rangle = 3$), it exhibits some domains that are locally flexible ($n_c < 3$) and stressed-rigid ($n_c > 3$) with a typical size of 15 Å. The existence of such nanoscale topological fluctuations is important as, in turn, it results in some nanoductility during fracture. Figure 55a illustrates the role of topological fluctuations on crack propagation during fracture, wherein the crack gets deflected during propagation rather than propagating in a straight direction.[457] This has been explained by the fact that, thanks to local floppy modes of deformations, flexible domains are, upon loading, more prone to exhibit local nonreversible ductile deformations within the glass network (e.g., angular distortions or breaking of weak radial bonds, see Figure 55b) than stressed-rigid domains (which are unable to reorganize due to their high local connectivity).

Such topological fluctuations are driven by entropy and are only possible in glasses that exhibit some flexibility in their local topology, in other words, the ones with some spatial

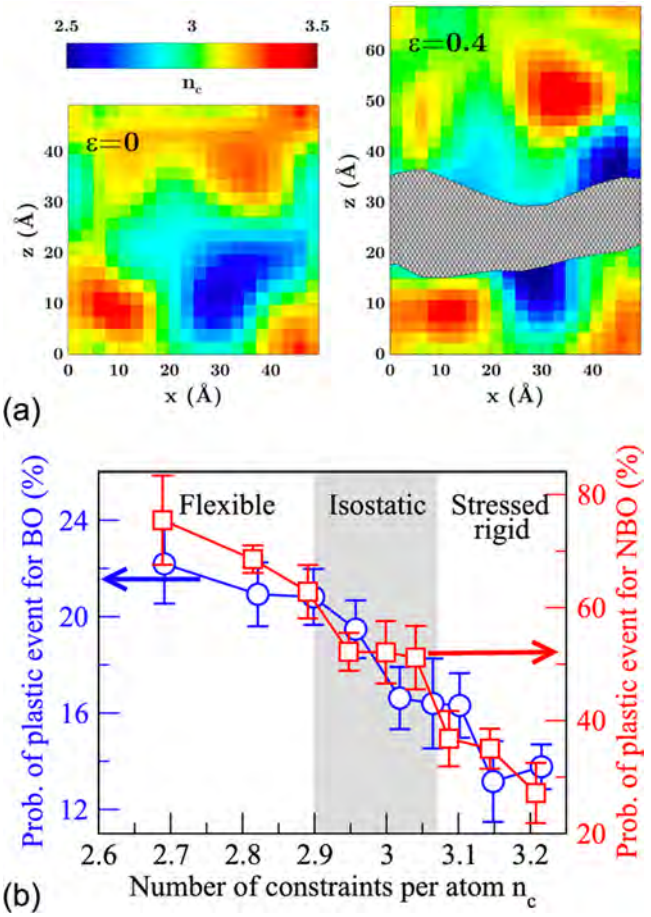

Figure 55. (a) Contour map showing the local number of constraints per atom (n_c) in a $(Na_2O)_{20}(SiO_2)_{80}$ glass (simulated by molecular dynamics) subjected to uniaxial tension (ref 457). The maps are obtained under zero (ϵ = 0, before fracture) and 40% (ϵ = 0.4, after fracture) normal strain. The gray area indicates the pathway followed by the final crack. (b) Probability of plastic events as a function of the local number of constraints n_c (ref 457). The gray area indicates the boundaries of the intermediate phase observed experimentally in $(Na_2O)_x(SiO_2)_{100-x}$ glasses by modulated differential scanning calorimetry (refs 458 and 459). Reprinted with permission from ref 457. Copyright 2016 American Physical Society.

https://doi.org/10.1021/acs.chemrev.1c00974
Chem. Rev. XXXX, XXX, XXX−XXX

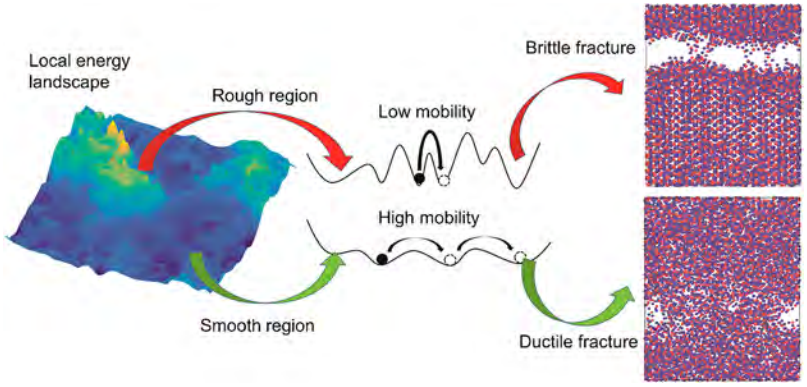

Figure 56. Schematic illustrating how local fluctuations in the potential energy landscape govern the propensity for disordered systems to break in a brittle vs ductile fashion. Adapted with permission from ref 461. Copyright 2021 Royal Society of Chemistry.

heterogeneity in their local rigidity. For instance, SiO_2 has a fixed local topology (all Si atoms are Q^4 units, i.e., surrounded by four bridging oxygen atoms), but $(Na_2O)_x(SiO_2)_{100-x}$ glasses feature some flexibility (i.e., the Na atoms can be distributed in different ways throughout the glass network and Si atoms can exhibit varying Q^n local environments). Although such topological fluctuations can spontaneously occur in some glasses, they can also be stimulated by extrinsic treatments. For instance, structural heterogeneity can be induced in pure SiO_2 through the application of an external pressure or irradiation.[460−462] High pressure has also been shown to affect structural fluctuations in bulk metallic glasses.[463] In addition to mechanical load, recent research has shown that thermal cycles can also introduce some structural heterogeneity in metallic glasses, which, in turn, can enhance their ductility.[464]

The extent of spatial, chemical, and/or topological fluctuations has also been found to dictate the brittle versus ductile nature of bulk metallic glasses.[465−472] Ultimately, it should be noted that topological fluctuations are associated with some heterogeneity in the underlying energy landscape, since topological constraints and floppy modes result in the formation of barriers and channels in the energy landscape, respectively. As such, the propensity for a large variety of disordered systems (oxide glasses, bulk metallic glasses, amorphous solids, colloidal gels, etc.) to break in a ductile (rather than brittle) fashion has been shown to be universally encoded in the low local roughness of their potential energy landscape (Figure 56).[461] The resistance of inorganic glasses to flaw initiation has also been shown to be governed by nanoscale fluctuations in the rigidity of their atomic network.[473]

9.3. Effect of Phase Separation on Fracture

Although spatial heterogeneity is limited to a few angstroms in homogeneous glasses, certain glasses (e.g., borate-based) can exhibit phase separation, which results in larger-scale heterogeneity (from 100 Å to 100 μm).[474−476] Such phase separation has been noted to affect fracture toughness.[477−481] For instance, phase separation has been noted to induce a 50% increase in the indentation fracture toughness of a sodium borosilicate glass.[482]

Recent peridynamic simulations have shown that phase separation can result in a 90% increase in the fracture energy of calcium aluminosilicate glasses (Figure 57).[483] Although phase separation was found to systematically result in an increase in fracture toughness, the extent of toughening was found to depend on the properties of the forming phases. Specifically,

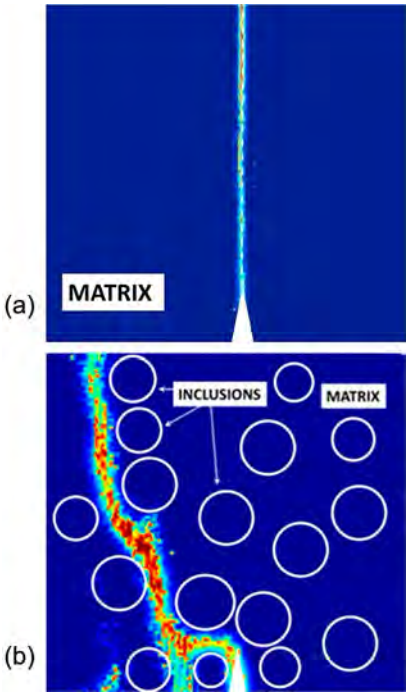

Figure 57. Visualization of the crack propagation path in a notched calcium aluminosilicate glass subjected to a tensile loading (a) without and (b) with compliant silica inclusions. Simulation details can be found in ref 483.

the increase in fracture energy was found to be governed by a balance between (i) the overall cohesion of the phase-separated glass and (ii) the propensity for crack deflection. For instance, the formation of weak (low surface energy) but stiff droplets tends to decrease the overall cohesion of the glass (i.e., its average surface energy) but increase its fracture toughness by inducing some crack deflections (since the crack tends to avoid the stiff phases). Similarly, the formation of tough and stiff droplets also induces significant crack deflections.

The maximum increase in fracture energy was observed in the case of the formation of soft (low modulus) but tough (high surface energy) droplets. In this ideal situation, the low stiffness of the droplets tends to attract the crack toward the tough droplets, which simultaneously induces some plastic energy dissipation (due to the change in crack direction) and forces the crack to propagate through the most cohesive

https://doi.org/10.1021/acs.chemrev.1c00974
Chem. Rev. XXXX, XXX, XXX−XXX

regions of the glass.[483] These behaviors have recently been confirmed in refs 484 and 485, wherein it was suggested that toughness can be enhanced upon implantation of soft metal nanoparticles.

9.4. Fluctuations Inducing Creep Viscoplastic Deformations

When subjected to a sustained load, certain glasses tend to exhibit delayed creep viscoplastic deformations.[486] Recent simulations conducted on a model Lennard-Jones disordered system and metallic glasses have shown that, at the atomic scale, creep is enabled by some localized, heterogeneous plastic reorganizations of the particles (Figure 58).[487,488] The heterogeneity of the particle local reorganizations was found to be encoded in the heterogeneity of the energy landscape, wherein particles having local access to a low energy barrier are more likely to exhibit a plastic reorganization. In turn, the heterogeneity of the reorganization (and of the energy landscape) was found to be encoded in the heterogeneity of the structure itself. The correlation between heterogeneous dynamical particle reorganization upon creep and structure was deciphered by using machine learning, wherein machine learning was used to construct a nonintuitive structural metric "softness" (see section 5.5) that exhibits a strong correlation with the particle dynamics.[487]

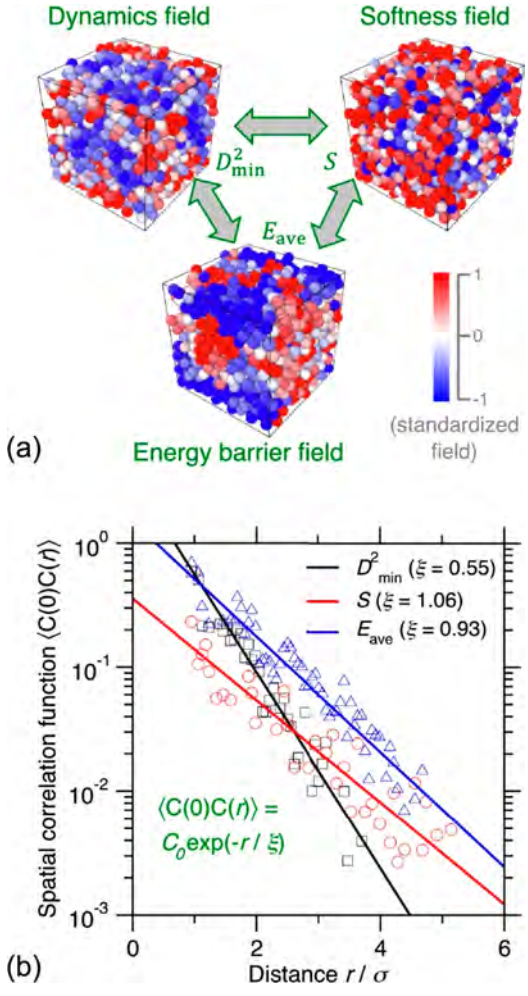

Figure 58. (a) Illustration of the spatial correlation between the heterogeneous fields of (i) particle dynamics upon creep (as captured by their nonaffine squared displacement D_{min}^2), (ii) the initial structure of the system (as captured by the "softness" machine-learned structural metric S), and (iii) the potential energy landscape (as captured by initial average energy barrier E_{ave} that is locally accessible to the particles). The particles are colored based on their standardized value in the corresponding field. (b) Spatial correlation function $\langle C(0)C(r)\rangle$ of the displacement (D_{min}^2, black), the softness (S, red), and the energy barrier fields (E_{ave}, blue) in the disordered system. Note that, in each case, the field value C (i.e., D_{min}^2, S, E_{ave}) is standardized for the calculation. The lines are exponential fits following $\exp(-r/\xi)$, where ξ is the characteristic correlation length. Reprinted with permission from ref 487. Copyright 2021 Acta Materialia Inc. Published by Elsevier Ltd.

9.5. Fluctuations Impact on Fatigue

As a result of fatigue, glasses can exhibit yielding far below their typical yield stress after a series of loading/unloading cycles.[490] Fatigue is especially pronounced (and problematic) in bulk metallic glasses. Results from molecular dynamics simulation have showed that, at the atomic scale, fatigue results from some heterogeneous nonaffine displacement of the atoms upon oscillatory stress.[491] Such atomic-scale reorganization is promoted in unstable glasses formed with a high cooling rate (i.e., with high fictive temperature). Recent molecular dynamics results have shown that the heterogeneity in fatigue-related atomic reorganization is encoded in the heterogeneity of the underlying potential energy landscape (Figure 59).[491] The evolution of such heterogeneous plastic regions upon loading/unloading cycles governs the fatigue failure process in disordered materials.[492,493] Moreover, the instability of glasses (i.e., their fictive temperature) also controls their propensity to exhibit fatigue. Indeed, in well-annealed glasses, yielding is triggered by the formation of sharp shear bands, whereas, in contrast, yielding results from diffusive shear bands in unstable glasses.[494]

10. OPTICAL PROPERTIES

Optical transparency is pivotal for many glass applications, including windows, telescopes, microscopes, and optical fibers, which are typically of silica or silicate compositions. The electron band gap in glasses can be manipulated by tuning the magnitude of the Rayleigh scattering, which is achieved by engineering the magnitude of the density fluctuations in the glass network or by introducing dopants. This section introduces the critical role of spatial fluctuations for manipulating the optical properties of glass. By suppressing or enhancing the magnitude of fluctuations, the performance of structural glass can be tuned for given applications. For example, for optical fibers and quantum communication, a minimum magnitude of spatial fluctuations such as density and void radius is required to minimize Rayleigh scattering and consequently improve power attenuation. On the other hand, maximizing the magnitude of spatial fluctuations leads to interesting nonlinear optical properties, which are pivotal for glass applications such as planar waveguides, optical data storage, and optical switches.[495,496]

https://doi.org/10.1021/acs.chemrev.1c00974
Chem. Rev. XXXX, XXX, XXX−XXX

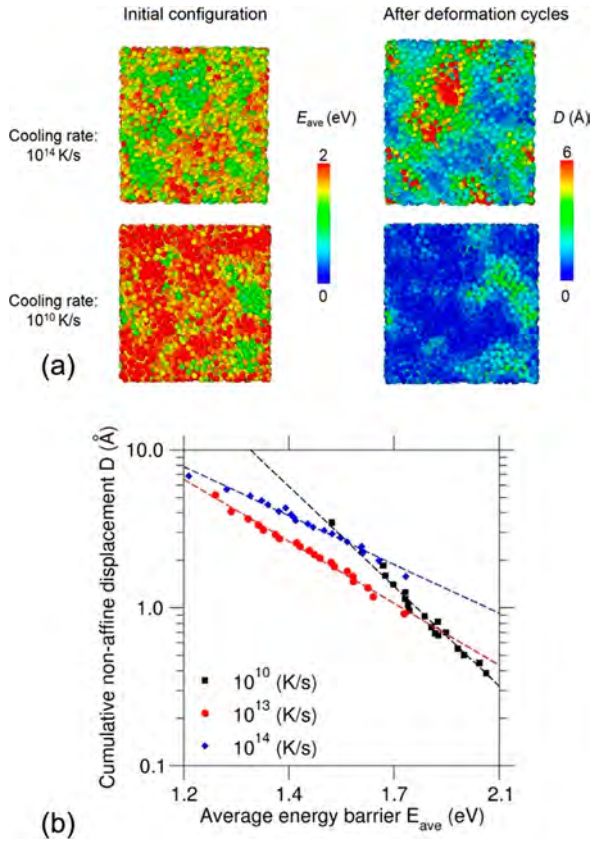

Figure 59. (a) Spatial maps of the cumulative nonaffine displacement (D) of the atoms upon fatigue of a $Cu_{64}Zr_{36}$ bulk metallic glass simulated by molecular dynamics for two select cooling rates. The maps are compared with those showing the average height of the energy barriers that are locally accessible to the atoms (E_{ave}) before any deformation. (b) Computed values of D as a function of E_{ave}. The lines are some power-law fits. Reprinted with permission from ref 491. Copyright 2020 American Chemical Society.

10.1. Suppression of Fluctuations to Optimize Glass Optical Properties

The field of optical communication is dominated by silica glasses, which require spatial fluctuations to be minimized. In pure vitreous silica, compositional fluctuations are nonexistent because the glass network has a single component, SiO_2; however, the magnitude of density fluctuations in silica can be large because the structural network of SiO_2 contains a high degree of porosity. These voids serve as centers for scattering of light, which is why Rayleigh scattering in silica glass is dominated by density fluctuations in the glass network.

Decreasing the magnitude of density fluctuations, and the resulting Rayleigh scattering, can be achieved by decreasing the void size using a pressurization treatment[497] or lowering the fictive temperature T_f through thermal annealing.[91,94] Positron annihilation lifetime spectroscopy (introduced in section 4.6) measurements on silica glass reveal that the void radius decreases continuously with increasing applied pressure during compression, as shown in Figure 60.[498] This work by Ono[498] also measured the Rayleigh scattering intensity using a 90° scattering measurement of compression and varying T_f. Figure 61 shows the Rayleigh scattering results versus the measured void radius, where the Rayleigh scattering loss is shown to be proportional to void radius for both the compression and varying T_f studies. Following the interpretation of voids as

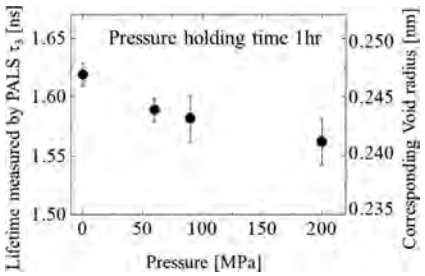

Figure 60. Third lifetime component, τ_3, and the corresponding void radius measured using PALS and plotted against the applied pressure. Adapted with permission from ref 498. Copyright 2021 IEEE.

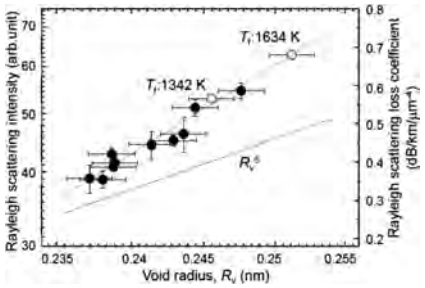

Figure 61. Rayleigh scattering intensity, measured using a 90° Rayleigh scattering measurement (left vertical axis). The absolute values of the Rayleigh scattering loss (right vertical axis) are calculated by comparison to the silica glass samples formed under ambient pressure at different T_f values. The x-axis is the void radius measured by PALS. The filled circles are for the samples synthesized with the hot isostatic pressure (HIP) machine, while the open circles show samples made without HIP. The broken line corresponds to the sixth power of the void radius, R_V. Adapted with permission from ref 498. Copyright 2021 IEEE.

light-scattering particles, the suppression of Rayleigh scattering can be explained both by the decrease of the void radius and a reduced number of voids. On the other hand, the decrease in Rayleigh scattering can also be attributed to a decrease in the magnitude of density fluctuations in the glass. This work concludes that the suppression of density fluctuations cannot be explained by a simple shrinkage of the entire glass network; instead, the applied pressure must have triggered preferential shrinkage of larger voids, which narrows the void distribution while keeping the SiO_2 tetrahedra intact.[498]

To gain a systematic understanding of the effect of pressure on the silica glass network in terms of homogeneity at the atomistic level, Yang et al.[137] used MD (see section 5.1) simulations to examine how the density fluctuations in SiO_2 glass change at various quench pressures P_Q, including conditions beyond those achievable in experiments. At lower quench pressures (P_Q < 4 GPa), the homogeneity of the silica glass is enhanced from pressurization owing to the reduction of the structural void size in the glass and narrowing of the void size distribution, as illustrated in Figure 62a. The change of the largest void radius from simulations at small quench pressure is consistent with the measurement from PALS, shown in Figure 62b.[497]

The densification of silica liquid has been described by Stixrude and Bukowinski from an increase of the characteristic −Si−O−Si−O− ring size (denoted as a "topological pruning" mechanism).[499] The same mechanism has been applied by Yang et al.[137] to account for the structural homogenization for the pressure-quenched silica glass, as shown in Figure 63a. At

https://doi.org/10.1021/acs.chemrev.1c00974
Chem. Rev. XXXX, XXX, XXX−XXX

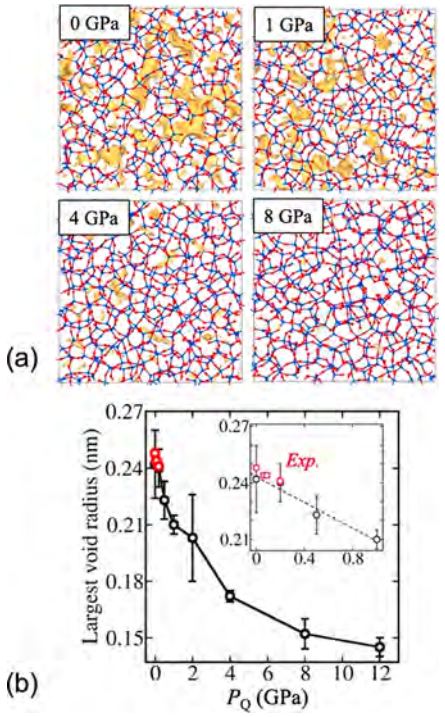

Figure 62. Pressure effects on voids in silica glass modeled using MD. (a) Morphologies of voids in four silica glass samples pressure-quenched at 0, 1, 4, and 8 GPa. The yellow regions are isosurfaces with a minimum distance of 0.1 nm from the surface of any atoms in the glass (i.e., voids with a radius <0.1 nm are not shown). The blue and red atoms are Si and O atoms, respectively. Only a slice of the glass (~10 Å thick) is visualized for figure clarity. (b) Variation of the largest void radius from both experiments (red, up to 0.2 GPa) and MD simulations (black). The inset is a close-up view of the pressure region from 0 to 1 GPa, where the dashed line is a guide for the eyes to show the consistent trends between the simulation results and the PALS experimental results. Reproduced with permission from ref 137. Copyright 2020 Yang et al. http://creativecommons.org/licenses/by/4.0/.

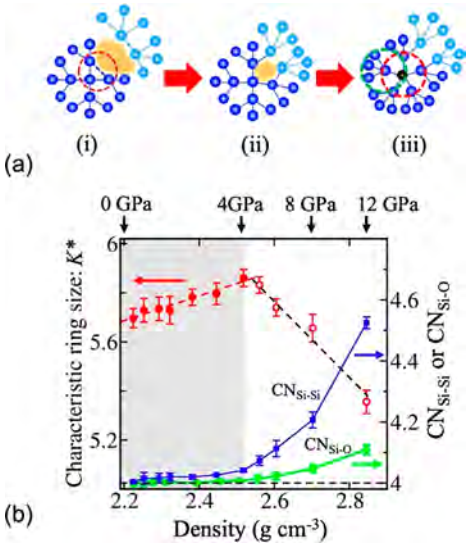

Figure 63. Homogenization mechanism of silica glass. (a) The configurational changes of the elimination of the three-membered ring (shown in red) and the introduction of different coordination number Si−Si at P_Q in SiO_2 glass. The yellow area denotes a void whose size decreases after the exemplary three-membered ring is eliminated. All spheres denote the Si atoms (the O atoms are not considered). (b) Characteristic ring size K^* (red) and coordination number (CN) for CN_{Si-Si} or CN_{Si-O} at different densities, where CN_{Si-Si} is the average number of first Si neighbor atoms to a central Si using a cutoff of 3.4 Å. The dashed red line and black dashed line are guides for the eyes. Reprinted with permission from ref 137. Copyright 2020 Yang et al. http://creativecommons.org/licenses/by/4.0/.

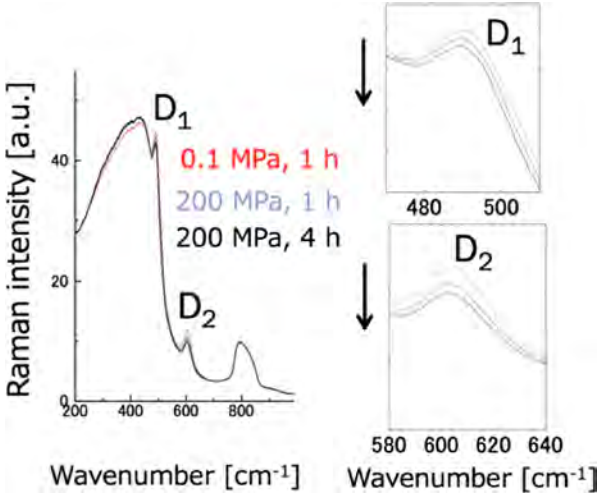

Figure 64. Raman spectrum of three pressure-quenched silica glass samples prepared at 0.1 MPa for 1 h, 0.2 GPa for 1 h, and 0.2 GPa for 4 h, all at 2073 K. The variations of the relative intensity of the D_1 and D_2 peaks as a function of time are enlarged for clarity on the right. Reproduced with permission from ref 137. Copyright 2020 Yang et al. http://creativecommons.org/licenses/by/4.0/.

lower pressures (≤4 GPa), they found that the population of small rings is lower, while the population of large rings increases with P_Q, thus reducing the free volume in the proximity of the rings and increasing the characteristic ring size, as shown in Figure 63b. The agreement between this result and Raman spectrum measurements of the D_1 and D_2 peaks arising from symmetric stretching of regular four-membered rings and three-membered rings is shown in Figure 64. Unlike elastic distortion of the ring structure under isostatic pressure, which will recover once the pressure is released, the change in ring structure due to moderate pressurization persists even after release of the pressure without heating.

The void interpretation fails when the quench pressure is above 4 GPa. Even though the voids become smaller at higher quench pressure, at high pressures the homogeneity of the silica glass deteriorates due to the appearance of Si atoms with higher Si−Si coordination, as shown by the blue curve in Figure 65. The trade-off between the change in voids and the change in Si coordination number leads to a maximum homogeneity of silica glass at some intermediate range of pressure (~4 GPa) based on MD simulations as shown by the calculated Rayleigh scattering coefficient from MD in Figure 65, with a value half that of conventional silica glass. Recall from section 1 that, to advance fields such as optical communication, Rayleigh scattering in optical fibers needs to be minimized. The work by Yang et al.[137] confirmed that manipulating the void radius distribution through pressure quenching has the potential to reduce Rayleigh scattering loss in silica glass by ~56%. If this result is realized, this processing would form the lowest loss optical fiber known in the optical communications industry, as of 2021.[500]

https://doi.org/10.1021/acs.chemrev.1c00974
Chem. Rev. XXXX, XXX, XXX−XXX

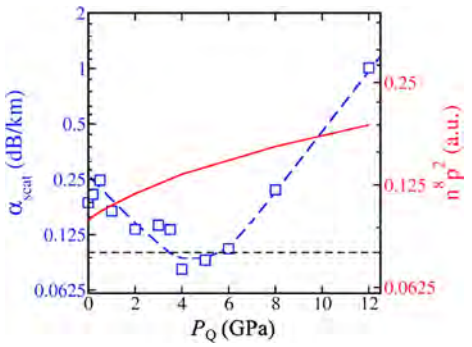

Figure 65. Calculated Rayleigh scattering coefficient (α_{scat}) and the term related to refractive index and photoelastic coefficient (n^8p^2) at different quench pressures using density fluctuations. The blue dashed line is an eye guide to show the trend of α_{scat}. The black dashed line corresponds to 0.1 dB km^{-1}. Reprinted with permission from ref 137. Copyright 2020 Yang et al. http://creativecommons.org/licenses/by/4.0/.

Yang et al.[501] demonstrated that the silica glasses hot-compressed up to 8 GPa are thermally stable at room temperature without a significant change in density. This is consistent with the findings of Onodera et al.,[502] where the densities of the silica glasses after hot compression at 7.7 GPa and various thermal treatments up to 1200 °C are stable over a time period of 1.5 years (permanently densified glass). On the other hand, the cold-compressed glass treated at 20 GPa is not permanently densified upon return to ambient pressure (although its initially pressure-treated density is identical to that of the hot-compressed glass recovered from treatment at 7.7 GPa/1200 °C). The higher homogeneity of the silica glass network structure was determined by Guerette et al.[503] using X-ray diffraction, Brillouin scattering, and MD simulations. The first sharp diffraction peak (FSDP) was observed to sharpen as the compressive pressure increases. Moreover, Masuno et al.[504] indicated that the hot-compression process up to 8 GPa under 1400 K induces the smaller wavelength dispersion of the refractive index even though the refractive index itself increases due to the compression. The smaller dispersion of the refractive index indicates sharpening of the distribution of the bipolar moments.

Besides the application of the hot compression, a recent study has found that adding fluorine to glassy SiO_2 has the potential to decrease these density fluctuations and further minimize Rayleigh scattering loss.[505] Suppression of density fluctuations can also be achieved by utilizing higher density glasses such as gallates, which tend to show a much lower loss. ZBLAN fibers are good examples to theoretically show much lower Rayleigh scattering loss.[506]

10.2. Enhancement of Fluctuations to Optimize Glass Optical Properties

While SiO_2 is a single-component glass, multicomponent glasses show increased optical loss due to concentration fluctuations. Such concentration fluctuations can be especially pronounced in heavy metal silicate and germanate glasses.[507,508] While optical loss is not desirable for optical communication applications, the increase in the magnitude of the fluctuations can be utilized to enhance nonlinear optical responses such as second-order harmonic generation (SHG) and third-order harmonic generation (THG).

Fluctuations impact the linear polarization P, which is given as

$$P = \varepsilon_0 \chi E \tag{93}$$

where E is an external electric field, ε_0 is the permittivity of free space, and χ is the linear susceptibility that is related to the refractive index n, with $\chi = n^2 - 1$. Glasses are isotropic in nature with macroscopic centrosymmetry which prohibits even-order nonlinear optical properties such as second-order nonlinearities (SONL), including SHG. However, it is possible to generate SONL in glass by enhancing spatial fluctuations through thermal gradients, laser irradiation, or by growing crystalline phases or introducing liquid−liquid phase separation.[495,496] These effects can be considered by replacing χ with $\chi(\mu + \sigma Z)$, where μ is the averaged shift from the fully centrosymmetric case, σ is the deviation due to the symmetry breaking, and Z is the input factor governing the breakdown of centrosymmetry. Here, Z can be related to T (if the fluctuation is triggered by temperature), E (if the fluctuation is trigger by electric field), or E^2 (if the fluctuation is attributed to the number of irradiated photons). The latter two effects correspond to SHG and THG, respectively, which are induced by fluctuations.

It remains difficult to distinguish the effects of fluctuations from the effects of induced ordering. Nevertheless, fiber sensors such as the optical time domain reflectometer, using Rayleigh, Raman, or Brillouin scattering, or a fiber-Bragg grating can be used to sense fluctuations induced by temperature, bending, water diffusion, oscillation. Glasses that have natively high nonlinear optical coefficients have an especially large potential to respond to such effects.[495,496] For example, studies on modified borophosphates show an increase in third-order nonlinearity when doped with Ti or Nb.[496,509] In addition, some chalcogenide glass families have been shown to exhibit a high degree of third-order susceptibility.[510] Glasses with a high sensitivity against poling are also good candidates.[511,512] SHG depends on the charge carrier concentration and mobility, but this spatial fluctuation is observable only before the cations recombine.[512] Therefore, nonlinearity is not always permanent as the glass relaxes over time.

11. CONCLUSIONS

This review article has addressed the current understanding of spatial and temporal fluctuations and their impact on key physical properties and processes of glass-forming systems. While, to date, most researchers evaluate glass performance based solely on an average description of structural features and properties, it is well-established that this simplification is often insufficient as glasses exhibit property values that fluctuate both spatially and temporally. Glass is spatially diverse due to its noncrystalline structure, which exhibits distributions in bond length, bond angle, coordination number, ring size, density, and rigidity across the dimensions of the sample. Glass is temporally evolving as a result of being a nonequilibrium material that continuously relaxes toward the metastable supercooled liquid state, a relaxation process that is dictated by local motions occurring on different time and length scales. This continuous relaxation evolves the glass structure and network topology over time, resulting in unstable local mechanical and optical behavior and a capricious propensity to crystallize and phase separate.

Studying spatiotemporal fluctuations provides fundamental insights into the nature of glassy materials, enabling improved design of next-generation glasses. The magnitude of fluctua-

https://doi.org/10.1021/acs.chemrev.1c00974
Chem. Rev. XXXX, XXX, XXX−XXX

tions is important because some applications require broad property distributions, such as promoting atomic rearrangement to enable shock absorption, while other applications require narrow property distributions such as limiting crack propagation for smart phone cover screens or minimizing Rayleigh scattering for optical data transmission. When tailoring a glass design with unusual properties or specific applications in mind, the overarching question is how fluctuations can be leveraged as an additional parameter to the composition and thermal/pressure history. In the pursuit of addressing these currently open questions, this article has reviewed how fluctuations are currently being quantified, characterized, and modeled for investigations of glass-forming systems, mainly commercially relevant oxide glasses. This review is a foundation which the authors hope the readers will build upon in future work and expand to understandings of fluctuations in other glass systems of both commerical and theoretical importance (e.g., superstable glasses, polymer glasses, molecular glasses, simulation glasses, spin glasses).

In section 3, discussions of kinetics and thermodynamics addressed why spatiotemporal fluctuations arise in glass-forming systems. The interplay of mathematical and physical understanding is used to relate fluctuations to kinetic and thermodynamic properties, which poses the question of how best to quantify fluctuations such as enthalpy and volume. Experimental and computational techniques, addressed in sections 4 and 5, respectively, for quantifying fluctuations are largely adapted from mean-field approaches but enable researchers to infer the nature of structural, topological, and dynamical fluctuations in glass. Characterization techniques such as nuclear magnetic resonance, X-ray, neutron, and electron diffraction, infrared and Raman vibrational spectroscopy, SAS, and positron annihilation spectroscopy reveal the broad distributions of structural and topological features in glasses, in contrast to their crystalline counterparts; however, a deeper understanding of what the broad distributions reveal about spatiotemporal fluctuations remains elusive. Characterization methods that more finely map the fluctuations in atomic positions and bonding characteristics could enable deeper experimental analysis of the physics of glass structure. Such work is within reach for future development.[130]

To compensate for the realistic limitations of experimental approaches (e.g., cost, time, equipment), it is becoming more common to design combined experimental−computational investigations. Computational means for exploring spatiotemporal fluctuations in glass-forming systems include molecular dynamics, Monte Carlo, statistical mechanical models, energy landscapes, topological constraint theory, and machine learning. As discussed for experimental limitations, the development and evolution of the computational toolset needs to be tailored for specific glass-forming systems. Often assumptions that apply to mean-field or crystalline systems are carried over into glass models. For example, to capture kinetic properties in glasses, molecular dynamics can be used to solve the Green−Kubo relations, which are derived from the fluctuation theorem for crystalline materials (introduced in section 3.1) by assuming a Gaussian time-averaged dissipative flux, even though dynamical heterogeneities in glass-forming systems manifest as nonmonatomic, non-Gaussian probability distributions. This dearth of methods to address the specific needs of glass systems calls for more astute derivations and appropriate simplifying assumptions tailored to represent fluctuations in glassy systems. Statistical mechanical methods to explore spatiotemporal fluctuations in glass-forming systems have grown dramatically in the recent years, but further expansion into medium-range phenomena (such as rings) is needed before the techniques can capture complex glass chemistries and thermal/pressure histories. Similarly, while energy landscapes are a promising methodology, their practical use often requires various input parameters and experimental validation to represent complex glass systems. A common limitation in computational materials science is the capabilities of the computational techniques themselves, not only seen with the growth of emerging fields such as machine learning but also in the development of more established fields. For example, DFT could theoretically be employed to explore spatiotemporal fluctuations by running numerous iterations of simulations with unique initial conditions, but considering the current computational cost limitations, this approach is often considered too inefficient.

Glass is a nonequilibrium material, meaning that its structure is continually relaxing through the movement of cooperatively rearranging regions. Though this relationship has been theorized, the relationship between the length scale of CRRs and dynamical heterogeneities has not yet been firmly established for glasses of practical interest. The movement of CRRs with time needs to be further elucidated as it directly impacts the propensity of a glass-forming system to crystallize or phase separate. Thermal and compositional fluctuations trigger crystal nucleation, and while significant progress in understanding and manipulating crystal nucleation and growth has been achieved in the past 70 years, further development of glass-ceramic materials is conditional on a deeper understanding of this process. Improved glass-forming ability (which favors high structural disorder) directly contradicts the appeal of lower magnitude fluctuations to limit crack propagation and Rayleigh scattering. A pressing open question remains to determine the minimum magnitude of fluctuations and disorder that can be reached without the system crystallizing or phase separating.

Conventionally, there are three overarching parameters manipulated during glass discovery: composition, thermal history, and pressure history. These three parameters are altered to optimize mechanical properties such as elasticity, intrinsic nanoductility, fracture, creep, and fatigue. The manipulation of these parameters impacts fluctuation formation and consequently material performance. By explicitly considering the magnitude of fluctuations with this list of parameters, glass applications with stringent requirements on mechanical and optical properties can be more finely tuned, especially in relation to newly developing large-scale manufacturing techniques such as additive manufacturing.[513−516] In sections 1, 4, and 10, density fluctuations have been shown to be critical for optimizing high-speed and high-bandwidth optical communication. Though an area of ongoing research, the benefits of this relationship have extended beyond theory and been implemented to induce sustained improvement of low-loss optical fibers. Density fluctuations are only one of a host of spatiotemporal fluctuations in glass. Additionally, nonlinear optical phenomena are influenced by localized fluctuations in glass. Studies into these phenomena are still in their nascent stage.

Throughout this article, we have discussed that glass is a *noncrystalline*, *nonergodic*, *nonequilibrium* material, which exhibits *nonlinear* and *nonexponential* relaxation with a *non-Arrhenius* temperature dependence, and as such, dynamical

https://doi.org/10.1021/acs.chemrev.1c00974
Chem. Rev. XXXX, XXX, XXX−XXX

heterogeneities manifest as *nonmonotonic* in time and with a *non-Gaussian* probability distribution. As can be inferred from the plethora of "non" words above, the traditional description of glass is based on what it is *not*, rather than what glass *is*. What is known about glasses is that they are composed of spatially and temporally fluctuating features, which impact properties and performance. Understanding the impact of fluctuations on properties and processes has improved fundamental knowledge of the chemistry and physics governing disordered systems and aided in the design of new structural glasses with optimized properties and performance. The authors of this review are confident that these studies will be useful for the glass research community that is still much focused on "average" structural features. With continued development of fluctuation studies, it will be exciting to see which industry will be revolutionized next by exploring glass structure−property−performance relationships beyond the average.

AUTHOR INFORMATION

Corresponding Author

John C. Mauro − *Department of Materials Science and Engineering, The Pennsylvania State University, University Park, Pennsylvania 16802, United States;* orcid.org/0000-0002-4319-3530; Email: jcm426@psu.edu

Authors

Katelyn A. Kirchner − *Department of Materials Science and Engineering, The Pennsylvania State University, University Park, Pennsylvania 16802, United States*

Daniel R. Cassar − *Department of Materials Engineering, Federal University of São Carlos, São Carlos, Sao Paulo 13565-905, Brazil; Ilum School of Science, Brazilian Center for Research in Energy and Materials, Campinas, Sao Paulo 13083-970, Brazil;* orcid.org/0000-0001-6472-2780

Edgar D. Zanotto − *Department of Materials Engineering, Federal University of São Carlos, São Carlos, Sao Paulo 13565-905, Brazil;* orcid.org/0000-0003-4931-4505

Madoka Ono − *Research Institute for Electronic Science, Hokkaido University, Sapporo, Hokkaido 001-0021, Japan; Materials Integration Laboratories, AGC Incorporated, Yokohama, Kanagawa 230-0045, Japan*

Seong H. Kim − *Department of Chemical Engineering, The Pennsylvania State University, University Park, Pennsylvania 16802, United States;* orcid.org/0000-0002-8575-7269

Karan Doss − *Department of Materials Science and Engineering, The Pennsylvania State University, University Park, Pennsylvania 16802, United States*

Mikkel L. Bødker − *Department of Chemistry and Bioscience, Aalborg University, Aalborg 9220, Denmark*

Morten M. Smedskjaer − *Department of Chemistry and Bioscience, Aalborg University, Aalborg 9220, Denmark;* orcid.org/0000-0003-0476-2021

Shinji Kohara − *Research Center for Advanced Measurement and Characterization National Institute for Materials Science, Tsukuba, Ibaraki 305-0047, Japan*

Longwen Tang − *Department of Civil and Environmental Engineering, University of California, Los Angeles, California 90095, United States*

Mathieu Bauchy − *Department of Civil and Environmental Engineering, University of California, Los Angeles, California 90095, United States;* orcid.org/0000-0003-4600-0631

Collin J. Wilkinson − *Department of Materials Science and Engineering, The Pennsylvania State University, University Park, Pennsylvania 16802, United States; Department of Research and Development, GlassWRX, Beaufort, South Carolina 29906, United States*

Yongjian Yang − *Department of Materials Science and Engineering, The Pennsylvania State University, University Park, Pennsylvania 16802, United States*

Rebecca S. Welch − *Department of Materials Science and Engineering, The Pennsylvania State University, University Park, Pennsylvania 16802, United States*

Matthew Mancini − *Department of Materials Science and Engineering, The Pennsylvania State University, University Park, Pennsylvania 16802, United States*

Complete contact information is available at: https://pubs.acs.org/10.1021/acs.chemrev.1c00974

Notes

The authors declare no competing financial interest.

Biographies

Katelyn A. Kirchner is a second-year Ph.D. candidate in the Department of Materials Science and Engineering at The Pennsylvania State University, U.S.A. Katelyn is a National Science Foundation Graduate Research Fellow and 2020 Alfred R. Cooper Young Scholar with six years of experience computationally investigating spatiotemporal fluctuations in structural glasses. In 2020, Katelyn earned a B.S. in Materials Science and Engineering from The Pennsylvania State University. The inspiration for the development of this comprehensive *Chemical Reviews* article discussing the field of spatial and temporal fluctuations in glass-forming systems was her undergraduate thesis ("A Statistical Investigation of Fluctuations in Glass-Forming Systems"), which was awarded first place in The Pennsylvania State University Library Outstanding Undergraduate Thesis Award and second place in the Society of Glass Technology Oldfield Award.

Daniel R. Cassar is a Professor at Ilum School of Science, part of the Brazilian Center for Research in Energy and Materials (CNPEM). He earned his Ph.D. in Materials Science and Engineering and his B.S. in Materials Engineering, both at the Federal University of Sao Carlos (UFSCar), Brazil. He worked as a postdoctoral researcher at the Center for Research, Technology, and Education in Vitreous Materials (CeRTEV), researching dynamic processes in glasses (crystallization and relaxation) and developing machine learning algorithms to predict glass properties. He has published journal articles and given seven invited talks. His research interest is in the interface between Materials and Data sciences, specifically in creating artificial intelligence tools for accelerating the development of new technological materials.

Edgar D. Zanotto is a Professor of Materials Science and Engineering and Director of the Center for Research, Technology and Education in Vitreous Materials (CeRTEV), both at the Federal University of São Carlos, Brazil, and an editor of the *Journal of Non-Crystalline Solids*. His main research interests include dynamic processes in inorganic glass-forming liquids (diffusion, viscous flow, relaxation, liquid−liquid phase separation, crystal nucleation and growth, crystallization, glass stability, and glass-forming ability) and properties of glasses and glass-ceramics. He has been working for 45 years in this field and has published over 350 scientific articles, three books, and five book prefaces, filled 30 patents, and delivered approximately 170 invited and plenary conference talks. He has supervised approximately 95 research students and postdocs and has been granted 52 research-

https://doi.org/10.1021/acs.chemrev.1c00974
Chem. Rev. XXXX, XXX, XXX−XXX

related prizes. Professor Zanotto is a member of both Brazilian and São Paulo State Academy of Sciences, National Academy of Engineering, The World Academy of Sciences, and World Academy of Ceramics, and Fellow of the Fulbright Foundation, Society of Glass Technology, the American Ceramic Society, and the Brazilian Ceramic Society.

Madoka Ono has double-assignment jobs at Hokkaido University as an assistant professor, and a principal researcher in AGC Inc. Her research interests are on the properties of glass, especially optical and mechanical, and the controllability by the structure and topology. She is a member of Japanese Society of Applied Physics, the American Ceramic Society, and the Japanese Ceramic Society. She has received the Outstanding Master Thesis Award, 43rd Encouragement Award of Laser Society of Japan, Japanese Optics Research of the Year 2018, and Promotion and Nurturing of Female Researchers Contribution Award.

Seong H. Kim is a Distinguished Professor and Associate Department Head of Chemical Engineering at the Pennsylvania State University. He earned B.S. and M.S. degrees in Chemistry from Yonsei University, Seoul, Korea, and a Ph.D. degree in Chemistry from Northwestern University, Evanston, Illinois. Prior to joining Pennsylvania State University in 2001, he was a postdoctoral researcher at University of California at Berkeley. His primary research interests are surface science of glass, tribology and tribochemistry, and cellulose in plant cell walls. He has authored more than 300 papers in peer-reviewed journals. He is a member of the editorial board of Friction, Colloids & Interfaces, and Lubricants, and a fellow of the Society of Tribologists and Lubrication Engineers (STLE).

Karan Doss is a Ph.D. candidate in the department of Materials Science and Engineering at Pennsylvania State University, U.S.A. He is also an engineering trainee in the Intelligent Systems division at NASA Ames research center where he received the division's spotlight award for implementing novel physics-based modeling methods to solve challenging problems in additive manufacturing. He graduated with distinction from Peoples Education Society (PES) University to earn his B.S. in Mechanical Engineering and subsequently received his M.S. in Materials Science and Engineering from Pennsylvania State University. His current research interests span relaxation kinetics in glass, viscosity of supercooled liquids and glasses, and data-driven modeling of complex dynamical systems.

Mikkel L. Bødker is currently a quantitative researcher at Norlys Energy Trading. He earned his Master of Science in Chemistry in 2019 and his Ph.D. in Physical Chemistry in 2021 from Aalborg University, Denmark, working with Professor Morten Smedskjaer. In his thesis work he applied statistical mechanical modeling and machine learning to capture composition–structure relations in common oxide glass families.

Morten M. Smedskjaer is a Professor of Materials Chemistry and Head of the Doctoral Program in Biotechnology, Chemistry, and Environmental Engineering, both at the Department of Chemistry and Bioscience, Aalborg University, Denmark. He received his Ph.D. degree from the same university in 2011 and worked as a research scientist at Corning Inc. from 2011 to 2012. His current research interests include the structure, topology, mechanical properties, and relaxation behavior of oxide and hybrid glasses, which are studied using a combination of experimental and computational methods. He has five granted patents, published over 180 journal articles, and given 28 invited and plenary conference talks. He has supervised more than 45 postdocs, graduate students, and research assistants. He is a fellow of the Danish Academy of Technical Sciences, and his awards include Vittorio Gottardi Prize, Sir Alastair Pilkington Award, W. H. Zachariasen Award, Grundfos Prize, Norbert J. Kreidl Award, and Best Ph.D. Award from the Danish Academy of Natural Science.

Shinji Kohara is a chief researcher at National Institute for Materials Science (NIMS). He received his Ph.D. degree in 1998 from Tokyo University of Science. In 1998, he was involved in the development of a dedicated high-energy X-ray diffractometer for disordered materials at the world's largest synchrotron radiation facility, SPring-8. From 2001 to 2015, he worked as a beamline scientist. Since 2015, he has been working at NIMS. His current research interests include the inorganic chemistry and materials science of glass, liquid, and amorphous materials.

Longwen Tang is a postdoctoral researcher in the PARIS research group at the University of California, Los Angeles. He received his Ph.D. degree from Wuhan University, China in 2019. His research focuses on the fracture behavior of disordered materials and the underlying physics that governs the dynamical behavior of disordered materials during the load. In particular, he is interested in understanding the structure–property relationship of disordered materials from the viewpoint of TCT and energy landscape approaches.

Mathieu Bauchy is an Associate Professor in the Civil and Engineering Department at the University of California, Los Angeles (UCLA), where he runs the Physics of AmoRphous and Inorganic Solids Laboratory (PARISlab). He received his undergraduate education in physics at Ecole Normale Supérieure (France) before pursuing a Ph.D. in condensed matter at Université Pierre et Marie Curie (France). He then joined the Massachusetts Institute of Technology (MIT) as a postdoctoral associate. His research revolves around simulations and machine learning applied to materials, with a special focus on the topology, mechanical properties, and relaxation of glasses. He has published over 180 journal articles and given over 40 invited talks. He received the Norbert J. Kreidl Award in Glass Science by the American Ceramics Society, the MDPI's Materials Young Investigator, and the Elsevier's Rising Star in Computational Materials Science Award.

Collin J. Wilkinson is the director of computational research and development at GlassWRX, LLC. At GlassWRX he uses machine learning and physical models to improve glass recycling in the United States. He earned his Ph.D. in 2020 from The Pennsylvania State University, U.S.A. Collin's research has largely focused on using a combination of machine learning and energy landscapes to understand key processing variables (specifically relaxation and crystallization) in glass-forming systems. He has recently been awarded the Norbert J. Kreidl Award for his work on understanding crystal nucleation through energy landscape descriptions.

Yongjian Yang is an Assistant Research Professor in the Department of Materials Science and Engineering at The Pennsylvania State University, U.S.A. He earned a Ph.D. degree from Rensselaer Polytechnic Institute and was awarded a Ferguson graduate student fellowship in 2017. He received the best student poster award (first place) with his intern research work at Corning Inc. on simulated crack initiation under indentation at the Glass & Optical Materials Division Annual Meeting in 2016. His research interests span across a diverse range of material chemistries (metallic glasses, silicate glasses, metal–organic frameworks), phases (glass, liquid, crystal), and types of material properties (structural, mechanical, optical, thermal, chemical) using molecular simulation and modeling methods.

Rebecca S. Welch is a Ph.D. student in the Department of Materials Science and Engineering under Dr. John Mauro at The Pennsylvania State University, U.S.A. She earned a B.A. in Physics at Coe College

https://doi.org/10.1021/acs.chemrev.1c00974
Chem. Rev. XXXX, XXX, XXX–XXX

and was awarded the National Science Foundation Graduate Research Fellowship. Her current graduate work includes investigating structure−property relationships in anomalous glass systems using a combination of molecular dynamics simulations and theoretical model development. She also studies methods in which to computationally model crystal nucleation in glass-forming liquids.

Matthew F. L. Mancini is a graduate student in Dr. John Mauro's research group at Pennsylvania State University where he focuses on synthesis and design of glassy materials for his Ph.D. Matthew focuses on the development of environmentally friendly commodity glasses, lightweight glass armors, and two-dimensional glass. Matthew earned his baccalaureate degree in Physics from the liberal arts honors institution New College of Florida in 2020 where his thesis was a compilation of three undergraduate publications that focused on thermal and spectroscopic characterization of glassy materials. Matthew is a Sigma Pi Sigma Physics Honors society member and a recipient of the Shively−Weyl optoelectronics research fellowship.

John C. Mauro is Dorothy Pate Enright Professor and Associate Head for Graduate Education in the Department of Materials Science and Engineering at The Pennsylvania State University. John earned a B.S. in Glass Engineering Science (2001), B.A. in Computer Science (2001), and Ph.D. in Glass Science (2006), all from Alfred University. He joined Corning Incorporated in 1999 and served in multiple roles there, including Senior Research Manager of the Glass Research department. John is the inventor or coinventor of several new glass compositions for Corning, including Corning Gorilla Glass products. John joined the faculty at Pennsylvania State University in 2017 and is currently a world-recognized expert in fundamental and applied glass science, statistical mechanics, computational and condensed matter physics, thermodynamics and kinetics, and the topology of disordered networks. John is the author of over 320 peer-reviewed publications and is Editor of the *Journal of the American Ceramic Society*. He is coauthor of *Fundamentals of Inorganic Glasses*, 3rd ed. (Elsevier, 2019), the definitive textbook on glass science and technology, and he is the author of the newly published textbook, *Materials Kinetics: Transport and Rate Phenomena* (Elsevier, 2021). John is a Fellow of the National Academy of Inventors, with 65 granted U.S. patents and another ∼20 additional patents pending. John is also a Fellow of the American Ceramic Society and the Society of Glass Technology. He is a Member of the National Academy of Engineering.

ACKNOWLEDGMENTS

Special thanks are given for helpful discussions with Sushmit Goyal of Corning Inc. The authors would also like to acknowledge support from various funding sources including AGC Inc., the National Science Foundation (NSF) Graduate Research Fellowship Program awarded to K.A.K., NSF (Grant Nos. 1928546 and 1762275) awarded to J.C.M., the São Paulo State Research Foundation (FAPESP) (Grant No. 2017/12491-0) awarded to D.R.C., the National Council for Scientific and Technological Development (CNPq) (Grant No. 15/13314-9) awarded to E.D.Z., FAPESP (Grant No. 2013/07793-6) awarded to E.D.Z., the Japan Society for the Promotion of Science (JSPS) (KAKENHI Grant Nos. 20H02428, 20H05880, 21H01835, and 21K19016) awarded to M.O., NSF (Grant No. DMR-2011410) awarded to S.H.K., the Independent Research Fund Denmark (Grant No. 7017-00019) awarded to M.M.S., the Japan Society for the Promotion of Science (JSPS) (KAKENHI Grant Nos. 20H05878 and 20H05881) awarded to S.K., and NSF (Grant Nos. CMMI-1762292, CMMI-1826420, CMMI-1922167, DMR-1928538, and DMR-1944510) awarded to M.B.

ABBREVIATIONS

ABED	angstrom-beam electron diffraction
BO	bridging oxygen
CN	coordination number
CNT	classical nucleation theory
CRDS	cavity ring down spectroscopy
CRR	cooperatively rearranging region
DFT	density functional theory
DIT	diffuse interface theory
FSDP	first sharp diffraction peak
GNN	graph neural network
HIP	hot isostatic pressure
kMC	kinetic Monte Carlo
LJ	Lennard-Jones
LLPS	liquid−liquid phase separation
MAS NMR	magnetic angle spinning nuclear magnetic resonance
MC	Monte Carlo
MD	molecular dynamics
MDSC	modulated differential scanning calorimetry
MMC	metropolis Monte Carlo
MSD	mean squared displacement
NBO	nonbridging oxygen
NMR	nuclear magnetic resonance
PALS	positron annihilation lifetime spectroscopy
PDF	pair distribution function
Ps	positronium
RMC	reverse Monte Carlo
SANS	small-angle neutron scattering
SAS	small-angle scattering
SAXS	small-angle X-ray scattering
SCL	supercooled liquid
SEM	scanning electron microscope
SHG	second-order harmonic generation
SR-IR	spectral reflectance infrared
STD	standard deviation
SVM	support vector machine
t-CAS	tectosilicate calcium aluminosilicate
TCT	topological constraint theory
TEM	transmission electron microscopy
THG	third-harmonic generation
TTT diagram	time−temperature−transformation diagram
V−T diagram	volume−temperature diagram
VFT	Vogel−Fulcher−Tammann (viscosity equation)

LIST OF KEY TERMS

glass = a noncrystalline, nonequilibrium, nonergodic state of matter that appears solid on a short time scale but continuously relaxes toward the liquid state (section 1.1)
bridging oxygen (BO) = an oxygen bonded to two or more network formers (section 1.1)
nonbridging oxygen (NBO) = an oxygen bonded to one network former (section 1.1)
network former = cations that form the covalent backbone of the glass network, e.g., Si, P, or B (section 1.1)
network modifier = cations that form ionic bonds and modify the connectivity of the glass network, e.g., Na, Li, K, Ca, Mg (section 1.1)

https://doi.org/10.1021/acs.chemrev.1c00974
Chem. Rev. XXXX, XXX, XXX−XXX

rigidity = a unitless scaling factor that ranges from 0 to 1 to define how easy or hard it is the break a constraint (section 1.1)
isostatic network = a state of rigidity wherein the number of atomic constraints equals the degrees of freedom (section 1.1)
constraint = a rigid bond or angle constraining the position of an atom (section 1.1)
Q-species = short-range structural units that define oxide glasses (section 1.1)
fluctuation = a deviation of a value from its mean value (section 2.1)
variance = second-order central moment (section 2.1)
ergodic = the time average equals the ensemble average of a given property or system (section 2.2)
spatial fluctuation = how properties and structure vary in different regions of the material which encompass fluctuations in structure and network topology (section 2.3)
temporal fluctuations = instantaneous changes in property values and structure with time (section 2.3)
spatiotemporal fluctuations = fluctuations in both space and time (section 2.3)
topological fluctuations = fluctuations in the network/interconnection of atoms within the system (section 2.3)
topology = the spatial relations defining the connectivity and atomic network (section 2.4)
glass transition = a continuous, kinetic transition between the liquid and glassy states (section 3)
fictive temperature = the temperature at which the glass departs from the supercooled liquid state and becomes out of equilibrium (section 3)
dynamical heterogeneity = atomic regions of slower or faster kinetics caused by chemical or structural fluctuations in condensed systems (section 3.1)
critical nucleus = an ordered crystalline-like arrangement of atoms, formed by fluctuations, that has an equal probability of growing or dissolving back into its matrix phase (section 7)
spinodal decomposition = a type of phase transformation that occurs when one phase separates into two interconnected phases spontaneously, without nucleation (section 7)

REFERENCES

(1) Varshneya, A. K.; Mauro, J. C. *Fundamentals of Inorganic Glasses*; Elsevier: Amsterdam, Netherlands, 2019.
(2) Mauro, J. C.; Tandia, A.; Vargheese, K. D.; Mauro, Y. Z.; Smedskjaer, M. M. Accelerating the Design of Functional Glasses through Modeling. *Chem. Mater.* **2016**, *28*, 4267−4277.
(3) Zanotto, E. D. A Bright Future for Glass-Ceramics. *Am. Ceram. Soc. Bull.* **2010**, *89*, 19−27.
(4) Main, D. Humankind's Most Important Material. *Atlantic*. April 7, **2018**.
(5) Mauro, J. C. Grand Challenges in Glass Science. *Front. Mater.* **2014**, *1*, 1−5.
(6) Fang, Z.; Chin, K.; Qu, R.; Cai, H. *Fundamentals of Optical Fiber Sensors*; John Wiley & Sons, Inc.: Hoboken, NJ, 2012.
(7) Mauro, J. C.; Uzun, S. S.; Bras, W.; Sen, S. Nonmonotonic Evolution of Density Fluctuations during Glass Relaxation. *Phys. Rev. Lett.* **2009**, *102*, 155506.
(8) Mauro, J. C. Effect of Fragility on Relaxation of Density Fluctuations in Glass. *J. Non-Cryst. Solids* **2011**, *357*, 3520−3523.
(9) Warren, B. E. X-Ray Determination of the Structure of Liquids and Glass. *J. Appl. Phys.* **1937**, *8*, 645−654.
(10) Evans, D. L. Glass Structure: The Bridge between the Molten and Crystalline States. *J. Non-Cryst. Solids* **1982**, *52*, 115−128.
(11) McMillan, P. F.; Piriou, B. Raman Spectroscopic Studies of Silicate and Related Glass Structure: A Review. *B. Mineral.* **1983**, *106*, 57−75.
(12) Greaves, G. N.; Sen, S. Inorganic Glasses, Glass-Forming Liquids and Amorphizing Solids. *Adv. Phys.* **2007**, *56*, 1−166.
(13) Micoulaut, M.; Phillips, J. C. Onset of Rigidity in Glasses: From Random to Self-Organized Networks. *J. Non-Cryst. Solids* **2007**, *353*, 1732−1740.
(14) Mauro, J. C.; Loucks, R. J.; Gupta, P. K. Fictive Temperature and the Glassy State. *J. Am. Ceram. Soc.* **2009**, *92*, 75−86.
(15) Parisi, G. Infinite Number of Order Parameters for Spin-Glasses. *Phys. Rev. Lett.* **1979**, *43*, 1754−1756.
(16) Altarelli, G.; Parisi, G. Asymptotic Freedom in Parton Language. *Nucl. Phys. B* **1977**, *126*, 298−318.
(17) Kardar, M.; Parisi, G.; Zhang, Y.-C. Dynamic Scaling of Growing Interfaces. *Phys. Rev. Lett.* **1986**, *56*, 889−892.
(18) Ozawa, M.; Berthier, L.; Biroli, G.; Tarjus, G. Role of Fluctuations in the Yielding Transition of Two-Dimensional Glasses. *Phys. Rev. Research* **2020**, *2*, 023203.
(19) Ikeda, A.; Berthier, L.; Sollich, P. Unified Study of Glass and Jamming Rheology in Soft Particle Systems. *Phys. Rev. Lett.* **2012**, *109*, 018301.
(20) Biroli, G.; Cammarota, C. Fluctuations and Shape of Cooperative Rearranging Regions in Glass-Forming Liquids. *Phys. Rev. X* **2017**, *7*, 011011.
(21) Berthier, L.; Biroli, G. Theoretical Perspective on the Glass Transition and Amorphous Materials. *Rev. Mod. Phys.* **2011**, *83*, 587−645.
(22) Sillescu, H. Heterogeneity at the Glass Transition: A Review. *J. Non-Cryst. Solids* **1999**, *243*, 81−108.
(23) Kirkpatrick, T. R.; Thirumalai, D. Colloquium: Random First Order Transition Theory Concepts in Biology and Physics. *Rev. Mod. Phys.* **2015**, *87*, 183−209.
(24) Charbonneau, P.; Kurchan, J.; Parisi, G.; Urbani, P.; Zamponi, F. Fractal Free Energy Landscapes in Structural Glasses. *Nat. Commun.* **2014**, *5*, 3725.
(25) Palmer, R. G.; Stein, D. L.; Abrahams, E.; Anderson, P. W. Models of Hierarchically Constrained Dynamics for Glassy Relaxation. *Phys. Rev. Lett.* **1984**, *53*, 958−961.
(26) Mandelstam, L.; Tamm, Ig. The Uncertainty Relation Between Energy and Time in Non-Relativistic Quantum Mechanics. In *Selected Papers*; Bolotovskii, B. M., Frenkel, V. Ya., Peierls, R., Eds.; Springer: Berlin, Heidelberg, Germany, 1991; pp 115−123.
(27) Das, A.; Chakrabarti, B. K. *Quantum Annealing and Related Optimization Methods*; Springer: Heidelberg, Germany, 2005.
(28) Varshneya, A. K.; Mauro, J. C. Comment on Misconceived ASTM Definition of "Glass" by A.C. Wright. *Glass Technol.: Eur. J. Glass Sci. Technol. A* **2010**, *51*, 28−30.
(29) Yadav, A. K.; Singh, P. A Review of the Structures of Oxide Glasses by Raman Spectroscopy. *RSC Adv.* **2015**, *5*, 67583−67609.
(30) Yano, T.; Kunimine, N.; Shibata, S.; Yamane, M. Structural Investigation of Sodium Borate Glasses and Melts by Raman Spectroscopy. *J. Non-Cryst. Solids* **2003**, *321*, 137−146.
(31) Zwanziger, J. W. Structure and Chemical Modification in Oxide Glasses. *Int. Rev. Phys. Chem.* **1998**, *17*, 65−90.
(32) Bauchy, M.; Micoulaut, M. Atomic Scale Foundation of Temperature-Dependent Bonding Constraints in Network Glasses and Liquids. *J. Non-Cryst. Solids* **2011**, *357*, 2530−2537.
(33) Oliveira, K.; Viana, M. *Foundations of Ergodic Theory*, 1st ed.; Cambridge University Press: Cambridge, U.K., 2016.
(34) Mauro, J. C. *Materials Kinetics: Transport and Rate Phenomena*; Elsevier: Amsterdam, Netherlands, 2020.
(35) Chaudhuri, P.; Berthier, L.; Kob, W. Universal Nature of Particle Displacements Close to Glass and Jamming Transitions. *Phys. Rev. Lett.* **2007**, *99*, 060604.

https://doi.org/10.1021/acs.chemrev.1c00974
Chem. Rev. XXXX, XXX, XXX−XXX

(36) Yan, L.; Wyart, M. Evolution of Covalent Networks under Cooling: Contrasting the Rigidity Window and Jamming Scenarios. *Phys. Rev. Lett.* **2014**, *113*, 215504.
(37) Palmer, R. G. Broken Ergodicity. *Adv. Phys.* **1982**, *31*, 669.
(38) Mauro, J. C.; Gupta, P. K.; Loucks, R. J. Continuously Broken Ergodicity. *J. Chem. Phys.* **2007**, *126*, 184511.
(39) Zanotto, E. D.; Mauro, J. C. The Glassy State of Matter: Its Definition and Ultimate Fate. *J. Non-Cryst. Solids* **2017**, *471*, 490−495.
(40) Badrinarayanan, P.; Zheng, W.; Li, Q.; Simon, S. L. The Glass Transition Temperature Versus the Fictive Temperature. *J. Non-Cryst. Solids* **2007**, *353*, 2603−2612.
(41) Yue, Y.-Z. Characteristic Temperatures of Enthalpy Relaxation in Glass. *J. Non-Cryst. Solids* **2008**, *354*, 1112−1118.
(42) Malek Mansour, M.; Baras, F. Fluctuation Theorem: A Critical Review. *Chaos* **2017**, *27*, 104609.
(43) Allen, M. P.; Tildesley, D. J. *Computer Simulation of Liquids*; Oxford University Press: Oxford, U.K., 2017.
(44) Frenkel, J. *Kinetic Theory of Liquids*; Oxford University Press: Oxford, U.K., 1946.
(45) McQuarrie, D. A. *Statistical Mechanics*; University Science Books: Sausalito, CA, 2000.
(46) Searles, D. J.; Evans, D. J. The Fluctuation Theorem and Green−Kubo Relations. *J. Chem. Phys.* **2000**, *112*, 9727−9735.
(47) Evans, D. J.; Searles, D. J.; Williams, S. R. *Fundamentals of Classical Statistical Thermodynamics: Dissipation, Relaxation, and Fluctuation Theorems*; John Wiley & Sons: Hoboken, NJ, 2016.
(48) Chen, L.-Q. *Thermodynamic Equilibrium and Stability of Materials*, 1st ed.; Springer: Singapore, 2022.
(49) Fabian, R.; Sidebottom, D. L. Dynamic Light Scattering in Network-Forming Sodium Ultraphosphate Liquids Near the Glass Transition. *Phys. Rev. B* **2009**, *80*, 064201.
(50) Pekin, T. C.; Ding, J.; Gammer, C.; Ozdol, B.; Ophus, C.; Asta, M.; Ritchie, R. O.; Minor, A. M. Direct Measurement of Nanostructural Change during in Situ Deformation of a Bulk Metallic Glass. *Nat. Commun.* **2019**, *10*, 2445.
(51) Eckert, H. Spying with Spins on Messy Materials: 60 Years of Glass Structure Elucidation by NMR Spectroscopy. *Int. J. Appl. Glass Sci.* **2018**, *9*, 167−187.
(52) Youngman, R. NMR Spectroscopy in Glass Science: A Review of the Elements. *Materials* **2018**, *11*, 476.
(53) Sen, S.; Youngman, R. E. NMR Study of Q-Speciation and Connectivity in K_2O-SiO_2 Glasses with High Silica Content. *J. Non-Cryst. Solids* **2003**, *331*, 100−107.
(54) Fischer, H. E.; Barnes, A. C.; Salmon, P. S. Neutron and X-Ray Diffraction Studies of Liquids and Glasses. *Rep. Prog. Phys.* **2006**, *69*, 233−299.
(55) Massiot, D.; Messinger, R. J.; Cadars, S.; Deschamps, M.; Montouillout, V.; Pellerin, N.; Veron, E.; Allix, M.; Florian, P.; Fayon, F. Topological, Geometric, and Chemical Order in Materials: Insights from Solid-State NMR. *Acc. Chem. Res.* **2013**, *46*, 1975−1984.
(56) Charpentier, T.; Menziani, M. C.; Pedone, A. Computational Simulations of Solid State NMR Spectra: A New Era in Structure Determination of Oxide Glasses. *RSC Adv.* **2013**, *3*, 10550.
(57) Florian, P.; Fayon, F.; Massiot, D. ^{2}J Si-O-Si Scalar Spin-Spin Coupling in the Solid State: Crystalline and Glassy Wollastonite $CaSiO_3$. *J. Phys. Chem. C* **2009**, *113*, 2562−2572.
(58) Dupree, R.; Holland, D.; McMillan, P. W.; Pettifer, R. F. The Structure of Soda-Silica Glasses: A Mas NMR Study. *J. Non-Cryst. Solids* **1984**, *68*, 399−410.
(59) De Jong, B. H. W. S.; Schramm, C. M.; Parziale, V. E. Silicon-29 Magic Angle Spinning NMR Study on Local Silicon Environments in Amorphous and Crystalline Lithium Silicates. *J. Am. Chem. Soc.* **1984**, *106*, 4396−4402.
(60) Eden, M. ^{27}Al NMR Studies of Aluminosilicate Glasses. In *Annual Reports NMR on Spectroscopy*; Webb, G., Ed.; Elsevier: San Diego, CA, 2015; Vol. *86*.
(61) Pahari, B.; Iftekhar, S.; Jaworski, A.; Okhotnikov, K.; Jansson, K.; Stevensson, B.; Grins, J.; Edén, M. Composition-Property-Structure Correlations of Scandium Aluminosilicate Glasses Revealed by Multinuclear ^{45}Sc, ^{27}Al, and ^{29}Si Solid-State NMR. *J. Am. Ceram. Soc.* **2012**, *95*, 2545−2553.
(62) Du, L.-S.; Stebbins, J. F. Solid-State NMR Study of Metastable Immiscibility in Alkali Borosilicate Glasses. *J. Non-Cryst. Solids* **2003**, *315*, 239−255.
(63) Chen, B.; Werner-Zwanziger, U.; Nascimento, M. L. F.; Ghussn, L.; Zanotto, E. D.; Zwanziger, J. W. Structural Similarity on Multiple Length Scales and Its Relation to Devitrification Mechanism: A Solid-State NMR Study of Alkali Diborate Glasses and Crystals. *J. Phys. Chem. C* **2009**, *113*, 20725−20732.
(64) Dubinsky, E. V.; Stebbins, J. F. Quench Rate and Temperature Effects on Framework Ordering in Aluminosilicate Melts. *Am. Mineral.* **2006**, *91*, 753−761.
(65) Trease, N. M.; Clark, T. M.; Grandinetti, P. J.; Stebbins, J. F.; Sen, S. Bond Length-Bond Angle Correlation in Densified Silica—Results from ^{17}O NMR Spectroscopy. *J. Chem. Phys.* **2017**, *146*, 184505.
(66) Ohara, K.; Onodera, Y.; Murakami, M.; Kohara, S. Structure of Disordered Materials under Ambient to Extreme Conditions Revealed by Synchrotron X-Ray Diffraction Techniques at SPring-8—Recent Instrumentation and Synergic Collaboration with Modelling and Topological Analyses. *J. Phys.: Condens. Matter* **2021**, *33*, 383001.
(67) Grimley, D. I.; Wright, A. C.; Sinclair, R. N. Neutron Scattering From Vitreous Silica IV. Time-of-Flight Diffraction. *J. Non-Cryst. Solids* **1990**, *119*, 49−64.
(68) Wright, A. C. Neutron Scattering from Vitreous Silica. V. The Structure of Vitreous Silica: What Have We Learned from 60 Years of Diffraction Studies? *J. Non-Cryst. Solids* **1994**, *179*, 84−115.
(69) Onodera, Y.; Takimoto, Y.; Hijiya, H.; Taniguchi, T.; Urata, S.; Inaba, S.; Fujita, S.; Obayashi, I.; Hiraoka, Y.; Kohara, S. Origin of the Mixed Alkali Effect in Silicate Glass. *NPG Asia Mater.* **2019**, *11*, 75.
(70) Proffen, T. Analysis of Disordered Materials Using Total Scattering and the Atomic Pair Distribution Function. *Rev. Mineral. Geochem.* **2006**, *63*, 255−274.
(71) Zhou, Q.; Shi, Y.; Deng, B.; Neuefeind, J.; Bauchy, M. Experimental Method to Quantify the Ring Size Distribution in Silicate Glasses and Simulation Validation Thereof. *Sci. Adv.* **2021**, *7*, 1−11.
(72) Shi, Y.; Neuefeind, J.; Ma, D.; Page, K.; Lamberson, L. A.; Smith, N. J.; Tandia, A.; Song, A. P. Ring Size Distribution in Silicate Glasses Revealed by Neutron Scattering First Sharp Diffraction Peak Analysis. *J. Non-Cryst. Solids* **2019**, *516*, 71−81.
(73) Hirata, A.; Guan, P.; Fujita, T.; Hirotsu, Y.; Inoue, A.; Yavari, A. R.; Sakurai, T.; Chen, M. Direct Observation of Local Atomic Order in a Metallic Glass. *Nat. Mater.* **2011**, *10*, 28−33.
(74) Hirata, A.; Kang, L. J.; Fujita, T.; Klumov, B.; Matsue, K.; Kotani, M.; Yavari, A. R.; Chen, M. W. Geometric Frustration of Icosahedron in Metallic Glasses. *Science* **2013**, *341*, 376−379.
(75) Hirata, A.; Kohara, S.; Asada, T.; Arao, M.; Yogi, C.; Imai, H.; Tan, Y.; Fujita, T.; Chen, M. Atomic-Scale Disproportionation in Amorphous Silicon Monoxide. *Nat. Commun.* **2016**, *7*, 11591.
(76) Yasaitis, J. A.; Kaplow, R. Structure of Amorphous Silicon Monoxide. *J. Appl. Phys.* **1972**, *43*, 995−1000.
(77) Sharma, S. K.; Mammone, J. F.; Nicol, M. F. Raman Investigation of Ring Configurations in Vitreous Silica. *Nature* **1981**, *292*, 140−141.
(78) Brawer, S. A.; White, W. B. Raman Spectroscopic Investigation of the Structure of Silicate Glasses. I. The Binary Alkali Silicates. *J. Chem. Phys.* **1975**, *63*, 2421−2432.
(79) Sharma, S. K.; Yoder, H. S.; Matson, D. W. Raman Study of Some Melilites in Crystalline and Glassy States. *Geochim. Cosmochim. Ac.* **1988**, *52*, 1961−1967.
(80) Matson, D. W.; Sharma, S. K.; Philpotts, J. A. The Structure of High-Silica Alkali-Silicate Glasses. A Raman Spectroscopic Investigation. *J. Non-Cryst. Solids* **1983**, *58*, 323−352.
(81) Liu, H.; Hahn, S. H.; Ren, M.; Thiruvillamalai, M.; Gross, T. M.; Du, J.; Duin, A. C. T.; Kim, S. H. Searching for Correlations

https://doi.org/10.1021/acs.chemrev.1c00974
Chem. Rev. XXXX, XXX, XXX−XXX

between Vibrational Spectral Features and Structural Parameters of Silicate Glass Network. *J. Am. Ceram. Soc.* **2020**, *103*, 3575−3589.
(82) Luo, J.; Zhou, Y.; Milner, S. T.; Pantano, C. G.; Kim, S. H. Molecular Dynamics Study of Correlations between IR Peak Position and Bond Parameters of Silica and Silicate Glasses: Effects of Temperature and Stress. *J. Am. Ceram. Soc.* **2018**, *101*, 178−188.
(83) Luo, J.; Zhou, Y.; Pantano, C. G.; Kim, S. H. Correlation Between IR Peak Position and Bond Parameter of Silica Glass: Molecular Dynamics Study on Fictive Temperature (Cooling Rate) Effect. *J. Am. Ceram. Soc.* **2018**, *101*, 5419−5427.
(84) He, H.; Chen, Z.; Lin, Y.-T.; Hahn, S. H.; Yu, J.; van Duin, A. C. T.; Gokus, T. D.; Rotkin, S. V.; Kim, S. H. Subsurface Structural Change of Silica upon Nanoscale Physical Contact: Chemical Plasticity beyond Topographic Elasticity. *Acta Mater.* **2021**, *208*, 116694.
(85) He, H.; Qiao, Q.; Yu, J.; Kim, S. H. Synergy between Surface Mechanochemistry and Subsurface Dissolution on Wear of Soda Lime Silica Glass in Basic Solution. *J. Am. Ceram. Soc.* **2021**, *104*, 428−436.
(86) He, H.; Hahn, S. H.; Yu, J.; Qiao, Q.; van Duin, A. C. T.; Kim, S. H. Friction-Induced Subsurface Densification of Glass at Contact Stress Far below Indentation Damage Threshold. *Acta Mater.* **2020**, *189*, 166−173.
(87) Luo, J.; Huynh, H.; Pantano, C. G.; Kim, S. H. Hydrothermal Reactions of Soda Lime Silica Glass - Revealing Subsurface Damage and Alteration of Mechanical Properties and Chemical Structure of Glass Surfaces. *J. Non-Cryst. Solids* **2016**, *452*, 93−101.
(88) Galeener, F. L. Planar Rings in Vitreous Silica. *J. Non-Cryst. Solids* **1982**, *49*, 53−62.
(89) Huang, P. Y.; Kurasch, S.; Srivastava, A.; Skakalova, V.; Kotakoski, J.; Krasheninnikov, A. V.; Hovden, R.; Mao, Q.; Meyer, J. C.; Smet, J.; Muller, D. A.; Kaiser, U. Direct Imaging of a Two-Dimensional Silica Glass on Graphene. *Nano Lett.* **2012**, *12*, 1081−1086.
(90) Liu, H.; Kaya, H.; Lin, Y. T.; Ogrinc, A.; Kim, S. H. Vibrational Spectroscopy Analysis of Silica and Silicate Glass Networks. *J. Am. Ceram. Soc.* **2022**, *105*, 2355−2384.
(91) Lines, M. E. Oxide Glasses for Fast Photonic Switching: A Comparative Study. *J. Appl. Phys.* **1991**, *69*, 6876−6884.
(92) Wandel, M. *Attenuation in Silica-Based Optical Fibers*; Technical University of Denmark: Kongens Lyngby, Denmark, 2006.
(93) Pinheiro, M.; Martin, R. L.; Rycroft, C. H.; Jones, A.; Iglesia, E.; Haranczyk, M. Characterization and Comparison of Pore Landscapes in Crystalline Porous Materials. *J. Mol. Graph. Model.* **2013**, *44*, 208−219.
(94) Watanabe, T.; Saito, K.; Ikushima, A. J. Fictive Temperature Dependence of Density Fluctuation in SiO_2 Glass. *J. Appl. Phys.* **2003**, *94*, 4824−4827.
(95) Shannon, R. D. Revised Effective Ionic Radii and Systematic Studies of Interatomic Distances in Halides and Chalcogenides. *Acta Cryst. A* **1976**, *32*, 751−767.
(96) Dannefaer, S.; Bretagnon, T.; Kerr, D. Vacancy-type Defects in Crystalline and Amorphous SiO_2. *J. Appl. Phys.* **1993**, *74*, 884−890.
(97) Uedono, A.; Tanigawa, S. Positron Annihilation in Vitreous Silica Glasses. *Jpn. J. Appl. Phys.* **1993**, *32*, 2687−2691.
(98) Ito, K.; Nakanishi, H.; Ujihira, Y. Extension of the Equation for the Annihilation Lifetime of *Ortho* -Positronium at a Cavity Larger than 1 Nm in Radius. *J. Phys. Chem. B* **1999**, *103*, 4555−4558.
(99) Ono, M.; Hara, K.; Fujinami, M.; Ito, S. Void Structure in Silica Glass with Different Fictive Temperatures Observed with Positron Annihilation Lifetime Spectroscopy. *Appl. Phys. Lett.* **2012**, *101*, 164103.
(100) Pandey, A.; Biswas, P.; Drabold, D. A. Inversion of Diffraction Data for Amorphous Materials. *Sci. Rep.* **2016**, *6*, 33731.
(101) Biswas, P.; Atta-Fynn, R.; Drabold, D. A. Reverse Monte Carlo Modeling of Amorphous Silicon. *Phys. Rev. B* **2004**, *69*, 195207.
(102) Mauro, J. C.; Loucks, R. J. Impact of Fragility on Enthalpy Relaxation in Glass. *Phys. Rev. E* **2008**, *78*, 021502.
(103) Massobrio, C.; Du, J.; Bernasconi, M.; Salmon, P. S. *Molecular Dynamics Simulations of Disordered Materials*; Springer: Cham, Switzerland, 2015.
(104) Zwanzig, R. *Nonequlibrium Statistical Mechanics*; Oxford University Press: Oxford, U.K., 2001.
(105) Mauro, J. C.; Smedskjaer, M. M. Statistical Mechanics of Glass. *J. Non-Cryst. Solids* **2014**, *396−397*, 41−53.
(106) Mauro, J. C. Topological Constraint Theory of Glass. *Am. Ceram. Soc. Bull.* **2011**, *90*, 31−37.
(107) Sosso, G. C.; Chen, J.; Cox, S. J.; Fitzner, M.; Pedevilla, P.; Zen, A.; Michaelides, A. Crystal Nucleation in Liquids: Open Questions and Future Challenges in Molecular Dynamics Simulations. *Chem. Rev.* **2016**, *116*, 7078−7116.
(108) Naumis, G. G. Energy Landscape and Rigidity. *Phys. Rev. E* **2005**, *71*, 026114.
(109) Mauro, J. C.; Loucks, R. J. Selenium Glass Transition: A Model Based on the Enthalpy Landscape Approach and Non-equilibrium Statistical Mechanics. *Phys. Rev. B* **2007**, *76*, 174202.
(110) Micoulaut, M.; Massobrio, C. Improving the Structural Description of High-Temperature Liquid $GeSe_2$ from Ab Initio Molecular Dynamics Simulations. *J. Optoelectron. Adv. Mater.* **2009**, *11*, 1907−1914.
(111) Micoulaut, M.; Vuilleumier, R.; Massobrio, C. Improved Modeling of Liquid $GeSe_2$: Impact of the exchange-correlation functional. *Phys. Rev. B* **2009**, *79*, 214205.
(112) Massobrio, C.; Celino, M.; Salmon, P. S.; Martin, R. A.; Micoulaut, M.; Pasquarello, A. Atomic Structure of the Two Intermediate Phase Glasses $SiSe_4$ and $GeSe_4$. *Phys. Rev. B* **2009**, *79*, 174201.
(113) Le Roux, S.; Zeidler, A.; Salmon, P. S.; Boero, M.; Micoulaut, M.; Massobrio, C. Structural Properties of Liquid Ge_2Se_3: A First-Principles Study. *Phys. Rev. B* **2011**, *84*, 134203.
(114) Cobb, M.; Drabold, D. A.; Cappelletti, R. L. Ab Initio Molecular-Dynamics Study of the Structural, Vibrational, and Electronic Properties of Glassy $GeSe_2$. *Phys. Rev. B* **1996**, *54*, 12162−12171.
(115) Kirchner, K. A.; Kim, S. H.; Mauro, J. C. Statistical Mechanics of Topological Fluctuations in Glass-Forming Liquids. *Physica A* **2018**, *510*, 787−801.
(116) Koziatek, P.; Barrat, J. L.; Rodney, D. Short- and Medium-Range Orders in as-Quenched and Deformed SiO_2 Glasses: An Atomistic Study. *J. Non-Cryst. Solids* **2015**, *414*, 7−15.
(117) Trave, A.; Tangney, P.; Scandolo, S.; Pasquarello, A.; Car, R. Pressure-Induced Structural Changes in Liquid SiO_2 from Ab Initio Simulations. *Phys. Rev. Lett.* **2002**, *89*, 245504.
(118) Yang, Y.; Shin, Y. K.; Li, S.; Bennett, T. D.; van Duin, A. C. T.; Mauro, J. C. Enabling Computational Design of ZIFs Using ReaxFF. *J. Phys. Chem. B* **2018**, *122*, 9616−9624.
(119) Kirchner, K. A.; Bødker, M. S.; Smedskjaer, M. M.; Kim, S. H.; Mauro, J. C. Statistical Mechanical Model of Topological Fluctuations and the Intermediate Phase in Binary Phosphate Glasses. *J. Phys. Chem. B* **2019**, *123*, 7640−7648.
(120) Neuefeind, J.; Liss, K.-D. Bond Angle Distribution in Amorphous Germania and Silica. *Ber. Bunsenges. Phys. Chem.* **1996**, *100*, 1341−1349.
(121) Wang, B.; Yu, Y.; Wang, M.; Mauro, J. C.; Bauchy, M. Nanoductility in Silicate Glasses Is Driven by Topological Heterogeneity. *Phys. Rev. B* **2016**, *93*, 064202.
(122) Le Roux, S.; Jund, P. Ring Statistics Analysis of Topological Networks: New Approach and Application to Amorphous GeS_2 and SiO_2 Systems. *Comput. Mater. Sci.* **2010**, *49*, 70−83.
(123) Micoulaut, M.; Phillips, J. C. Rings and Rigidity Transitions in Network Glasses. *Phys. Rev. B* **2003**, *67*, 104204.
(124) Yuan, X.; Cormack, A. N. Efficient Algorithm for Primitive Ring Statistics in Topological Networks. *Comput. Mater. Sci.* **2002**, *24*, 343−360.
(125) Kerner, R. A Model for Formation and Structural Properties of Alkali Borate Glasses. *J. Non-Cryst. Solids* **1991**, *135*, 155−170.

https://doi.org/10.1021/acs.chemrev.1c00974
Chem. Rev. XXXX, XXX, XXX−XXX

(126) Guttman, L. Ring Structure of the Crystalline and Amorphous Forms of Silicon Dioxide. *J. Non-Cryst. Solids* **1990**, *116*, 145−147.
(127) King, S. V. Ring Configurations in a Random Network Model of Vitreous Silica. *Nature* **1967**, *213*, 1112−1113.
(128) Franzblau, D. S. Computation of Ring Statistics for Network Models of Solids. *Phys. Rev. B* **1991**, *44*, 4925−4930.
(129) Goetzke, K.; Klein, H.-J. Properties and Efficient Algorithmic Determination of Different Classes of Rings in Finite and Infinite Polyhedral Networks. *J. Non-Cryst. Solids* **1991**, *127*, 215−220.
(130) Yang, Y.; Zhou, J.; Zhu, F.; Yuan, Y.; Chang, D. J.; Kim, D. S.; Pham, M.; Rana, A.; Tian, X.; Yao, Y.; et al. Determining the Three-Dimensional Atomic Structure of an Amorphous Solid. *Nature* **2021**, *592*, 60−64.
(131) Heimbach, I.; Rhiem, F.; Beule, F.; Knodt, D.; Heinen, J.; Jones, R. O. PyMolDyn: Identification, Structure, and Properties of Cavities/Vacancies in Condensed Matter and Molecules. *J. Comput. Chem.* **2017**, *38*, 389−394.
(132) Wiles, N. T.; Goyal, S.; Baker, S. P. Geometric Configuration of Five-Coordinated Al and Si in Tectosilicate Calcium Aluminosilicate Glasses and its Effect on Plastic Flow. *J. Non-Cryst. Solids* **2020**, *543*, 120129.
(133) Xiang, Y.; Du, J.; Smedskjaer, M. M.; Mauro, J. C. Structure and Properties of Sodium Aluminosilicate Glasses from Molecular Dynamics Simulations. *J. Chem. Phys.* **2013**, *139*, 044507.
(134) Onodera, Y.; Kohara, S.; Tahara, S.; Masuno, A.; Inoue, H.; Shiga, M.; Hirata, A.; Tsuchiya, K.; Hiraoka, Y.; Obayashi, I.; et al. Understanding Diffraction Patterns of Glassy, Liquid and Amorphous Materials via Persistent Homology Analyses. *J. Ceram. Soc. Japan* **2019**, *127*, 853−863.
(135) Du, T.; Li, H.; Zhou, Q.; Wang, Z.; Sant, G.; Ryan, J. V.; Bauchy, M. Atomistic Origin of the Passivation Effect in Hydrated Silicate Glasses. *npj Mater. Degrad.* **2019**, *3*, 7.
(136) Sheng, H. W.; Luo, W. K.; Alamgir, F. M.; Bai, J. M.; Ma, E. Atomic Packing and Short-to-Medium-Range Order in Metallic Glasses. *Nature* **2006**, *439*, 419−425.
(137) Yang, Y.; Homma, O.; Urata, S.; Ono, M.; Mauro, J. C. Topological Pruning Enables Ultra-Low Rayleigh Scattering in Pressure-Quenched Silica Glass. *npj Comput. Mater.* **2020**, *6*, 139.
(138) Widmer-Cooper, A.; Harrowell, P.; Fynewever, H. How Reproducible Are Dynamic Heterogeneities in a Supercooled Liquid? *Phys. Rev. Lett.* **2004**, *93*, 135701.
(139) Widmer-Cooper, A.; Harrowell, P. On the Study of Collective Dynamics in Supercooled Liquids through the Statistics of the Isoconfigurational Ensemble. *J. Chem. Phys.* **2007**, *126*, 154503.
(140) Kim, D.; Jeong, D.; Jung, Y. Dynamic Propensity as an Indicator of Heterogeneity in Room-Temperature Ionic Liquids. *Phys. Chem. Chem. Phys.* **2014**, *16*, 19712−19719.
(141) Vargheese, K. D.; Tandia, A.; Mauro, J. C. Origin of Dynamical Heterogeneities in Calcium Aluminosilicate Liquids. *J. Chem. Phys.* **2010**, *132*, 194501.
(142) Manjunatha, L.; Takamatsu, H.; Cannon, J. J. Atomic-Level Breakdown of Green−Kubo Relations Provides New Insight into the Mechanisms of Thermal Conduction. *Sci. Rep.* **2021**, *11*, 5597.
(143) Mauro, J. C.; Varshneya, A. K. Modeling of Rigidity Percolation and Incipient Plasticity in Germanium Selenium Glasses. *J. Am. Ceram. Soc.* **2007**, *90*, 192−198.
(144) Mauro, J. C.; Varshneya, A. K. Multiscale Modeling of Arsenic Selenide Glass. *J. Non-Cryst. Solids* **2007**, *353*, 1226−1231.
(145) Mauro, J. C.; Varshneya, A. K. Model Interaction Potentials for Selenium from *Ab Initio* Molecular Simulations. *Phys. Rev. B* **2005**, *71*, 214105.
(146) Mauro, J. C.; Varshneya, A. K. Monte Carlo Simulation of Se_xTe_{1-x} Glass Structure with *Ab Initio* Potentials. *Phys. Rev. B* **2005**, *72*, 024212.
(147) Sørensen, S. S.; To, T.; Christensen, J. F. S.; Johra, H.; Smedskjaer, M. M. Impact of Network Topology on the Thermal and Mechanical Properties of Lithium Germanate Glasses. *J. Am. Ceram. Soc.* **2022**, *105*, 977.
(148) Bødker, M. L.; Pedersen, J. B.; Muñoz, F.; Mauro, J. C.; Smedskjaer, M. M. Statistical Mechanical Model for the Formation of Octahedral Silicon in Phosphosilicate Glasses. *J. Am. Ceram. Soc.* **2022**, *105*, 1031.
(149) Micoulaut, M. Concepts and Applications of Rigidity in Non-Crystalline Solids: A Review on New Developments and Directions. *Adv. Phys.-X* **2016**, *1*, 147−175.
(150) Goyal, S.; Mauro, J. C. Statistical Mechanical Model of Bonding in Mixed Modifier Glasses. *J. Am. Ceram. Soc.* **2018**, *101*, 1906−1915.
(151) Mauro, J. C. Statistics of Modifier Distributions in Mixed Network Glasses. *J. Chem. Phys.* **2013**, *138*, 12A522.
(152) Kirchner, K. A.; Mauro, J. C. Statistical Mechanical Model of the Self-Organized Intermediate Phase in Glass-Forming Systems with Adaptable Network Topologies. *Front. Mater.* **2019**, *6*, 11.
(153) Kirchner, K. A.; Goyal, S.; McKenzie, M. E.; Harris, J. T.; Mauro, J. C. Statistical Description of the Thermodynamics of Glass-Forming Liquids. *Physica A* **2020**, *559*, 125059.
(154) Bødker, M. S.; Mauro, J. C.; Goyal, S.; Youngman, R. E.; Smedskjaer, M. M. Predicting Q-Speciation in Binary Phosphate Glasses Using Statistical Mechanics. *J. Phys. Chem. B* **2018**, *122*, 7609−7615.
(155) Curado, F.; Tsallis, C. Generalized Statistical Mechanics: Connection with Thermodynamics. *J. Phys. A-Math. Gen.* **1991**, *24*, L69−L72.
(156) Gupta, P. K.; Mauro, J. C. The Laboratory Glass Transition. *J. Chem. Phys.* **2007**, *126*, 224504.
(157) Mauro, J. C.; Loucks, R. J.; Sen, S. Heat Capacity, Enthalpy Fluctuations, and Configurational Entropy in Broken Ergodic Systems. *J. Chem. Phys.* **2010**, *133*, 164503.
(158) Gupta, P. K.; Mauro, J. C. Comment on: "On the Reality of Residual Entropies of Glasses and Disordered Crystals" [J. Chem. Phys. 128, 154510 (2008)]. *J. Chem. Phys.* **2008**, *129*, 067101.
(159) Mauro, J. C.; Loucks, R. J.; Sen, S. Response to "Comment on 'Heat Capacity, Enthalpy Fluctuations, and Configurational Entropy in Broken Ergodic Systems' [J. Chem. Phys. 134, 147101 (2011)]. *J. Chem. Phys.* **2011**, *134*, 147102.
(160) Phillips, J. C. Topology of Covalent Non-Crystalline Solids I: Short-Range Order in Chalcogenide Alloys. *J. Non-Cryst. Solids* **1979**, *34*, 153−181.
(161) Kerner, R.; Phillips, J. C. Quantitative Principles of Silicate Glass Chemistry. *Solid State Commun.* **2000**, *117*, 47−51.
(162) Micoulaut, M. Rigidity Transitions and Constraint Counting in Amorphous Networks: Beyond the Mean-Field Approach. *Europhys. Lett.* **2002**, *58*, 830−836.
(163) Boolchand, P.; Lucovsky, G.; Phillips, J. C.; Thorpe, M. F. Self-Organization and the Physics of Glassy Networks. *Philos. Mag.* **2005**, *85*, 3823−3838.
(164) Naumis, G. G. Variation of the Glass Transition Temperature with Rigidity and Chemical Composition. *Phys. Rev. B* **2006**, *73*, 172202.
(165) Micoulaut, M. Rigidity and Intermediate Phases in Glasses Driven by Speciation. *Phys. Rev. B* **2006**, *74*, 184208.
(166) Gupta, P. K.; Mauro, J. C. Composition Dependence of Glass Transition Temperature and Fragility. I. A Topological Model Incorporating Temperature-Dependent Constraints. *J. Chem. Phys.* **2009**, *130*, 094503.
(167) Gupta, P. K.; Miracle, D. B. A Topological Basis for Bulk Glass Formation. *Acta Mater.* **2007**, *55*, 4507−4515.
(168) Smedskjaer, M. M.; Mauro, J. C.; Sen, S.; Deubener, J.; Yue, Y. Impact of Network Topology on Cationic Diffusion and Hardness of Borate Glass Surfaces. *J. Chem. Phys.* **2010**, *133*, 154509.
(169) Fu, A. I.; Mauro, J. C. Topology of Alkali Phosphate Glass Networks. *J. Non-Cryst. Solids* **2013**, *361*, 57−62.
(170) Soules, T. F. A Molecular Dynamic Calculation of the Structure of Sodium Silicate Glasses. *J. Chem. Phys.* **1979**, *71*, 4570−4578.
(171) Du, J.; Benmore, C. J.; Corrales, R.; Hart, R. T.; Weber, J. K. R. A Molecular Dynamics Simulation Interpretation of Neutron and

https://doi.org/10.1021/acs.chemrev.1c00974
Chem. Rev. XXXX, XXX, XXX−XXX

X-Ray Diffraction Measurements on Single Phase Y_2O_3-Al_2O_3 Glasses. *J. Phys.: Condens. Matter* **2009**, *21*, 205102.
(172) Cormack, A.N.; Cao, Y. Molecular Dynamics Simulation of Silicate Glasses. *Mol. Eng.* **1996**, *6*, 183−227.
(173) Micoulaut, M.; Raty, J.-Y.; Otjacques, C.; Bichara, C. Understanding Amorphous Phase-Change Materials from the Viewpoint of Maxwell Rigidity. *Phys. Rev. B* **2010**, *81*, 174206.
(174) Bauchy, M.; Micoulaut, M.; Celino, M.; Le Roux, S.; Boero, M.; Massobrio, C. Angular Rigidity in Tetrahedral Network Glasses with Changing Composition. *Phys. Rev. B* **2011**, *84*, 054201.
(175) Mauro, J. C.; Smedskjaer, M. M. Distinguishability of Particles in Glass-Forming Systems. *Physica A* **2012**, *391*, 5392−5403.
(176) Okabe, I.; Tanaka, H.; Nakanishi, K. Structures and Phase Transitions of Amorphous Ices. *Phys. Rev. E* **1996**, *53*, 2638−2647.
(177) Micoulaut, M.; Naumis, G. G. Glass Transition Temperature Variation, Cross-Linking and Structure in Network Glasses: A Stochastic Approach. *Europhys. Lett.* **1999**, *47*, 568−574.
(178) Dargaud, O.; Cormier, L.; Menguy, N.; Patriarche, G. Multi-Scale Structuration of Glasses: Observations of Phase Separation and Nanoscale Heterogeneities in Glasses by Z-Contrast Scanning Electron Transmission Microscopy. *J. Non-Cryst. Solids* **2012**, *358*, 1257−1262.
(179) Rajbhandari, P.; Chen, Y.; Doumert, B.; Montagne, L.; Tricot, G. Investigation of Zinc Alkali Pyrophosphate Glasses. Part II: Local and Medium Range Orders Analysed by 1D/2D NMR. *Mater. Chem. Phys.* **2015**, *155*, 23−29.
(180) Brow, R. K.; Tallant, D. R.; Myers, S. T.; Phifer, C. C. The Short-Range Structure of Zinc Polyphosphate Glass. *J. Non-Cryst. Solids* **1995**, *191*, 45−55.
(181) Meyer, K. Characterization of the Structure of Binary Zinc Ultraphosphate Glasses by Infrared and Raman Spectroscopy. *J. Non-Cryst. Solids* **1997**, *209*, 227−239.
(182) Ellison, A.; Cornejo, I. A. Glass Substrates for Liquid Crystal Displays. *Int. J. Appl. Glass Sci.* **2010**, *1*, 87−103.
(183) Wilkinson, C. J.; Mauro, J. C. Explorer. Py: Mapping the Energy Landscapes of Complex Materials. *SoftwareX* **2021**, *14*, 100683.
(184) Angelani, L.; Parisi, G.; Ruocco, G.; Viliani, G. Connected Network of Minima as a Model Glass: Long Time Dynamics. *Phys. Rev. Lett.* **1998**, *81*, 4648−4651.
(185) Angelani, L.; Parisi, G.; Ruocco, G.; Viliani, G. Potential Energy Landscape and Long-Time Dynamics in a Simple Model Glass. *Phys. Rev. E* **2000**, *61*, 1681−1691.
(186) Miller, M. A.; Doye, J. P. K.; Wales, D. J. Structural Relaxation in Atomic Clusters: Master Equation Dynamics. *Phys. Rev. E* **1999**, *60*, 3701−3718.
(187) Mauro, J. C.; Varshneya, A. K. A Nonequilibrium Statistical Mechanical Model of Structural Relaxation in Glass. *J. Am. Ceram. Soc.* **2006**, *89*, 1091−1094.
(188) Mauro, J. C.; Loucks, R. J.; Gupta, P. K. Metabasin Approach for Computing the Master Equation Dynamics of Systems with Broken Ergodicity. *J. Phys. Chem. A* **2007**, *111*, 7957−7965.
(189) Henkelman, G.; Uberuaga, B. P.; Jónsson, H. Climbing Image Nudged Elastic Band Method for Finding Saddle Points and Minimum Energy Paths. *J. Chem. Phys.* **2000**, *113*, 9901−9904.
(190) Henkelman, G.; Jónsson, H. Improved Tangent Estimate in the Nudged Elastic Band Method for Finding Minimum Energy Paths and Saddle Points. *J. Chem. Phys.* **2000**, *113*, 9978−9985.
(191) Sheppard, D.; Xiao, P.; Chemelewski, W.; Johnson, D. D.; Henkelman, G. A Generalized Solid-State Nudged Elastic Band Method. *J. Chem. Phys.* **2012**, *136*, 074103.
(192) Li, L.; Li, X.; Duan, Z.; Meyer, R. J.; Carr, R.; Raman, S.; Koziol, L.; Henkelman, G. Adaptive Kinetic Monte Carlo Simulations of Surface Segregation in PdAu Nanoparticles. *Nanoscale* **2019**, *11*, 10524−10535.
(193) Wilkinson, C. J.; Cassar, D. R.; DeCeanne, A.; Kirchner, K. A.; McKenzie, M. E.; Zanotto, E. D.; Mauro, J. C. Energy Landscape Modeling of Crystal Nucleation. *Acta Mater.* **2021**, *217*, 117163.
(194) Grosse, R.; Krause, P.; Meissner, M.; Tausend, A. The Coefficients of Thermal Expansion and the Gruneisen Functions of Trigonal and Amorphous Selenium in the Temperature Range between 10K and 300K. *J. Phys. C: Solid State Phys.* **1978**, *11*, 45−53.
(195) Smedskjaer, M. M.; Mauro, J. C.; Yue, Y. Prediction of Glass Hardness Using Temperature-Dependent Constraint Theory. *Phys. Rev. Lett.* **2010**, *105*, 115503.
(196) Mauro, J. C.; Gupta, P. K.; Loucks, R. J. Composition Dependence of Glass Transition Temperature and Fragility. II. A Topological Model of Alkali Borate Liquids. *J. Chem. Phys.* **2009**, *130*, 234503.
(197) Jiang, Q.; Zeng, H.; Liu, Z.; Ren, J.; Chen, G.; Wang, Z.; Sun, L.; Zhao, D. Glass Transition Temperature and Topological Constraints of Sodium Borophosphate Glass-Forming Liquids. *J. Chem. Phys.* **2013**, *139*, 124502.
(198) Swiler, D. R.; Varshneya, A. K.; Callahan, R. M. Microhardness, Surface Toughness and Average Coordination Number in Chalcogenide Glasses. *J. Non-Cryst. Solids* **1990**, *125*, 250−257.
(199) Trachenko, K.; Dove, M. T.; Brazhkin, V.; El'kin, F. S. Network Rigidity and Properties of SiO_2 and GeO_2 Glasses under Pressure. *Phys. Rev. Lett.* **2004**, *93*, 135502.
(200) Varshneya, A. K. Some Comments on Physical Properties of Chalcogenide Glasses. *J. Non-Cryst. Solids* **2000**, *273*, 1−7.
(201) Hermansen, C.; Youngman, R. E.; Wang, J.; Yue, Y. Structural and Topological Aspects of Borophosphate Glasses and Their Relation to Physical Properties. *J. Chem. Phys.* **2015**, *142*, 184503.
(202) Smedskjaer, M. M. Topological Model for Boroaluminosilicate Glass Hardness. *Front. Mater.* **2014**, *1*, 1−6.
(203) Sreeram, A. N.; Varshneya, A. K.; Swiler, D. R. Molar Volume and Elastic Properties of Multicomponent Chalcogenide Glasses. *J. Non-Cryst. Solids* **1991**, *128*, 294−309.
(204) Senapati, U.; Varshneya, A. K. Configurational Arrangements in Chalcogenide Glasses: A New Perspective on Phillips' Constraint Theory. *J. Non-Cryst. Solids* **1995**, *185*, 289−296.
(205) Senapati, U.; Varshneya, A. K. Viscosity of Chalcogenide Glass-Forming Liquids: An Anomaly in the 'Strong' and 'Fragile' Classification. *J. Non-Cryst. Solids* **1996**, *197*, 210−218.
(206) Senapati, U.; Firstenberg, K.; Varshneya, A. K. Structure-Property Inter-Relations in Chalcogenide Glasses and Their Practical Implications. *J. Non-Cryst. Solids* **1997**, *222*, 153−159.
(207) Grothaus, J.; Boolchand, P. Molecular Phase Separation in Stoichiometric Chalcogenide Glasses. *J. Non-Cryst. Solids* **1985**, *72*, 1−22.
(208) Halfpap, B. L.; Lindsay, S. M. Rigidity Percolation in the Germanium-Arsenic-Selenium Alloy System. *Phys. Rev. Lett.* **1986**, *57*, 847−849.
(209) Bresser, W.; Boolchand, P.; Suranyi, P. Rigidity Percolation and Molecular Clustering in Network Glasses. *Phys. Rev. Lett.* **1986**, *56*, 2493−2496.
(210) Norban, B.; Pershing, D.; Enzweiler, R. N.; Boolchand, P.; Griffiths, J. E.; Phillips, J. C. Coordination-Number-Induced Morphological Structural Transition in a Network Glass. *Phys. Rev. B* **1987**, *36*, 8109−8114.
(211) Yang, Y.; Wilkinson, C. J.; Lee, K.-H.; Doss, K.; Bennett, T. D.; Shin, Y. K.; van Duin, A. C. T.; Mauro, J. C. Prediction of the Glass Transition Temperatures of Zeolitic Imidazolate Glasses through Topological Constraint Theory. *J. Phys. Chem. Lett.* **2018**, *9*, 6985−6990.
(212) Zitkovsky, I.; Boolchand, P. Molecular Structure of As_2S_3 Glass. *J. Non-Cryst. Solids* **1989**, *114*, 70−72.
(213) He, H.; Thorpe, M. F. Elastic Properties of Glasses. *Phys. Rev. Lett.* **1985**, *54*, 2107−2110.
(214) Nemilov, S. V. Structural Aspect of Possible Interrelation between Fragility (Length) of Glass Forming Melts and Poisson's Ratio of Glasses. *J. Non-Cryst. Solids* **2007**, *353*, 4613−4632.
(215) Stolyar, S. V.; Klyuev, V. P.; Bulaeva, A. V. Viscosity and Thermal Expansion of Na Borate Glasses in the Tg Range. *Fiz. Khim. Stekla* **1984**, *10*, 447−454.

https://doi.org/10.1021/acs.chemrev.1c00974
Chem. Rev. XXXX, XXX, XXX−XXX

(216) Moynihan, C. T. Correlation between the Width of the Glass Transition Region and the Temperature Dependence of the Viscosity of High-Tg Glasses. *J. Am. Ceram. Soc.* **1993**, *76*, 1081−1087.
(217) Suzuki, S.; Kobayashi, T.; Takahashi, M.; Imaoka, M. Viscosity of Some Oxide Glasses in the Glass Transition Range. *J. Ceram. Soc. Jpn.* **1981**, *89*, 252−259.
(218) Chryssikos, G. D.; Duffy, J. A.; Hutchinson, J. M.; Ingram, M. D.; Kamitsos, E. I.; Pappin, A. J. Lithium Borate Glasses: A Quantitative Study of Strength and Fragility. *J. Non-Cryst. Solids* **1994**, *174*, 378−383.
(219) Phillips, J. C.; Thorpe, M. F. Constraint Theory, Vector Percolation and Glass Formation. *Solid State Commun.* **1985**, *53*, 699−702.
(220) Cai, Y.; Thorpe, M. F. Floppy Modes in Network Glasses. *Phys. Rev. B* **1989**, *40*, 10535−10542.
(221) Thorpe, M. F. Bulk and Surface Floppy Modes. *J. Non-Cryst. Solids* **1995**, *182*, 135−142.
(222) Gupta, P. K.; Cooper, A. R. Topologically Disordered Networks of Rigid Polytopes. *J. Non-Cryst. Solids* **1990**, *123*, 14−21.
(223) Gupta, P. K. Rigidity, Connectivity, and Glass-Forming Ability. *J. Am. Ceram. Soc.* **1993**, *76*, 1088−1095.
(224) Cooper, A. R. Zachariasen's Rules, Madelung Constant, and Network Topology. *Phys. Chem. Glasses* **1978**, *19*, 60−68.
(225) Thorpe, M. F. Continuous Deformations in Random Networks. *J. Non-Cryst. Solids* **1983**, *57*, 355−370.
(226) Mohanty, C.; Mandal, A.; Gogi, V. K.; Chen, P.; Novita, D.; Chbeir, R.; Bauchy, M.; Micoulaut, M.; Boolchand, P. Linking Melt Dynamics With Topological Phases and Molecular Structure of Sodium Phosphate Glasses From Calorimetry, Raman Scattering, and Infrared Reflectance. *Front. Mater.* **2019**, *6*, 69.
(227) Smedskjaer, M. M.; Mauro, J. C.; Sen, S.; Yue, Y. Quantitative Design of Glassy Materials Using Temperature-Dependent Constraint Theory. *Chem. Mater.* **2010**, *22*, 5358−5365.
(228) Smedskjaer, M. M.; Mauro, J. C.; Youngman, R. E.; Hogue, C. L.; Potuzak, M.; Yue, Y. Topological Principles of Borosilicate Glass Chemistry. *J. Phys. Chem. B* **2011**, *115*, 12930−12946.
(229) Hu, Y.; Liu, Z.; Yang, K.; Krishnan, N. M. A.; Smedskjaer, M. M.; Sant, G.; Bauchy, M. Rigidity Theory of Glass: Determining the Onset Temperature of Topological Constraints by Molecular Dynamics. *J. Non-Cryst. Solids* **2021**, *554*, 120614.
(230) Hermansen, C.; Mauro, J. C.; Yue, Y. A Model for Phosphate Glass Topology Considering the Modifying Ion Sub-Network. *J. Chem. Phys.* **2014**, *140*, 154501.
(231) Laurent, O.; Mantisi, B.; Micoulaut, M. Structure and Topology of Soda-Lime Silicate Glasses: Implications for Window Glass. *J. Phys. Chem. B* **2014**, *118*, 12750−12762.
(232) Potter, A. R.; Wilkinson, C. J.; Kim, S. H.; Mauro, J. C. Effect of Water on Topological Constraints in Silica Glass. *Scripta Mater.* **2019**, *160*, 48−52.
(233) Hermansen, C.; Rodrigues, B. P.; Wondraczek, L.; Yue, Y. An Extended Topological Model for Binary Phosphate Glasses. *J. Chem. Phys.* **2014**, *141*, 244502.
(234) Welch, R. S.; Wilkinson, C. J.; Shih, Y.; Bødker, M. S.; DeCeanne, A. V.; Smedskjaer, M. M.; Huang, L.; Affatigato, M.; Feller, S. A.; Mauro, J. C. Topological Model of Alkali Germanate Glasses and Exploration of the Germanate Anomaly. *J. Am. Ceram. Soc.* **2020**, *103*, 4224−4233.
(235) Wilkinson, C. J.; Pakhomenko, E.; Jesuit, M. R.; DeCeanne, A.; Hauke, B.; Packard, M.; Feller, S. A.; Mauro, J. C. Topological Constraint Model of Alkali Tellurite Glasses. *J. Non-Cryst. Solids* **2018**, *502*, 172−175.
(236) Yang, K.; Hu, Y.; Li, Z.; Krishnan, N. M. A.; Smedskjaer, M. M.; Hoover, C. G.; Mauro, J. C.; Sant, G.; Bauchy, M. Analytical Model of the Network Topology and Rigidity of Calcium Aluminosilicate Glasses. *J. Am. Ceram. Soc.* **2021**, *104*, 3947−3962.
(237) Zeng, H.; Jiang, Q.; Liu, Z.; Li, X.; Ren, J.; Chen, G.; Liu, F.; Peng, S. Unique Sodium Phosphosilicate Glasses Designed Through Extended Topological Constraint Theory. *J. Phys. Chem. B* **2014**, *118*, 5177−5183.
(238) Hermansen, C.; Guo, X.; Youngman, R. E.; Mauro, J. C.; Smedskjaer, M. M.; Yue, Y. Structure-Topology-Property Correlations of Sodium Phosphosilicate Glasses. *J. Chem. Phys.* **2015**, *143*, 064510.
(239) Trachenko, K.; Dove, M. T. Intermediate State in Pressurized Silica Glass: Reversibility Window Analogue. *Phys. Rev. B* **2003**, *67*, 212203.
(240) Bauchy, M.; Micoulaut, M. Transport Anomalies and Adaptative Pressure-Dependent Topological Constraints in Tetrahedral Liquids: Evidence for a Reversibility Window Analogue. *Phys. Rev. Lett.* **2013**, *110*, 095501.
(241) Bauchy, M. Structural, Vibrational, and Thermal Properties of Densified Silicates: Insights from Molecular Dynamics. *J. Chem. Phys.* **2012**, *137*, 044510.
(242) Zhao, C.; Zhou, W.; Zhou, Q.; Wang, Z.; Sant, G.; Guo, L.; Bauchy, M. Topological Origin of Phase Separation in Hydrated Gels. *J. Colloid Interface Sci.* **2021**, *590*, 199−209.
(243) Feng, X.; Bresser, W. J.; Boolchand, P. Direct Evidence for Stiffness Threshold in Chalcogenide Glasses. *Phys. Rev. Lett.* **1997**, *78*, 4422−4425.
(244) Selvanathan, D.; Bresser, W. J.; Boolchand, P.; Goodman, B. Thermally Reversing Window and Stiffness Transitions in Chalcogenide Glasses. *Solid State Commun.* **1999**, *111*, 619−924.
(245) Boolchand, P.; Georgiev, D. G.; Goodman, B. Discovery of the Intermediate Phase in Chalcogenide Glasses. *J. Optoelectron. Adv. Mater.* **2001**, *3*, 703−720.
(246) Bhosle, S.; Gunasekera, K.; Boolchand, P.; Micoulaut, M. Melt Homogenization and Self-Organization in Chalcogenides-Part II. *Int. J. Appl. Glass Sci.* **2012**, *3*, 205−220.
(247) Bauchy, M.; Micoulaut, M. Densified Network Glasses and Liquids with Thermodynamically Reversible and Structurally Adaptive Behaviour. *Nat. Commun.* **2015**, *6*, 1−8.
(248) Thorpe, M. F.; Jacobs, D. J.; Chubynsky, M. V.; Phillips, J. C. Self-Organization in Network Glasses. *J. Non-Cryst. Solids* **2000**, *266*, 859−866.
(249) Novita, D. I.; Boolchand, P.; Malki, M.; Micoulaut, M. Fast-Ion Conduction and Flexibility of Glassy Networks. *Phys. Rev. Lett.* **2007**, *98*, 195501.
(250) Selvanathan, D.; Bresser, W. J.; Boolchand, P. Stiffness Transitions in Si_xSe_{1-x} Glasses from Raman Scattering and Temperature-Modulated Differential Scanning Calorimetry. *Phys. Rev. B* **2000**, *61*, 15061−15076.
(251) Boolchand, P.; Feng, X.; Bresser, W. J. Rigidity Transitions in Binary Ge-Se Glasses and the Intermediate Phase. *J. Non-Cryst. Solids* **2001**, *293*, 348−356.
(252) Wang, Y.; Wells, J.; Georgiev, D. G.; Boolchand, P.; Jackson, K.; Micoulaut, M. Sharp Rigid to Floppy Phase Transition Induced by Dangling Ends in a Network Glass. *Phys. Rev. Lett.* **2001**, *87*, 185503.
(253) Golovchak, R.; Jain, H.; Shpotyuk, O.; Kozdras, A.; Saiter, A.; Saiter, J.-M. Experimental Verification of the Reversibility Window Concept in Binary As-Se Glasses Subjected to a Long-Term Physical Aging. *Phys. Rev. B* **2008**, *78*, 014202.
(254) Lucas, P.; King, E. A.; Gulbiten, O.; Yarger, J. L.; Soignard, E.; Bureau, B. Bimodal Phase Percolation Model for the Structure of Ge-Se Glasses and the Existence of the Intermediate Phase. *Phys. Rev. B* **2009**, *80*, 214114.
(255) Shpotyuk, O.; Golovchak, R. Pseudo-self-organized Topological Phases in Glassy Selenides for IR Photonics. *Phys. Status Solidi C* **2011**, *8*, 2572−2576.
(256) Golovchak, R.; Kozdras, A.; Shpotyuk, O.; Gorecki, C.; Kovalskiy, A.; Jain, H. Temperature-Dependent Structural Relaxation in $As_{40}Se_{60}$ Glass. *Phys. Lett. A* **2011**, *375*, 3032−3036.
(257) King, E. A.; Sen, S.; Takeda, W.; Boussard-Pledel, C.; Bureau, B.; Guin, J.-P.; Lucas, P. Extended Aging of Ge-Se Glasses below the Glass Transition Temperature. *J. Chem. Phys.* **2021**, *154*, 164502.
(258) Chubynsky, M. V.; Brière, M.-A.; Mousseau, N. Self-Organization with Equilibration: A Model for the Intermediate Phase in Rigidity Percolation. *Phys. Rev. E* **2006**, *74*, 016116.

https://doi.org/10.1021/acs.chemrev.1c00974
Chem. Rev. XXXX, XXX, XXX−XXX

(259) Brière, M.-A.; Chubynsky, M. V.; Mousseau, N. Self-Organized Criticality in the Intermediate Phase of Rigidity Percolation. *Phys. Rev. E* **2007**, *75*, 056108.
(260) Barré, J.; Bishop, A. R.; Lookman, T.; Saxena, A. Adaptability and "Intermediate Phase" in Randomly Connected Networks. *Phys. Rev. Lett.* **2005**, *94*, 208701.
(261) Yan, L. Entropy Favors Heterogeneous Structures of Networks near the Rigidity Threshold. *Nat. Commun.* **2018**, *9*, 1359.
(262) Berthier, L.; Biroli, G. Theoretical Perspective on the Glass Transition and Amorphous Materials. *Rev. Mod. Phys.* **2011**, *83*, 587−645.
(263) Nayar, D.; Chakravarty, C. Water and Water-like Liquids: Relationships between Structure, Entropy and Mobility. *Phys. Chem. Chem. Phys.* **2013**, *15*, 14162−14177.
(264) Starr, F. W.; Sastry, S.; Douglas, J. F.; Glotzer, S. C. What Do We Learn from the Local Geometry of Glass-Forming Liquids? *Phys. Rev. Lett.* **2002**, *89*, 125501.
(265) Hu, Y. C.; Li, F. X.; Li, M. Z.; Bai, H. Y.; Wang, W. H. Five-Fold Symmetry as Indicator of Dynamic Arrest in Metallic Glass-Forming Liquids. *Nat. Commun.* **2015**, *6*, 8310.
(266) Tanaka, H.; Kawasaki, T.; Shintani, H.; Watanabe, K. Critical-like Behaviour of Glass-Forming Liquids. *Nat. Mater.* **2010**, *9*, 324−331.
(267) Tanaka, H.; Tong, H.; Shi, R.; Russo, J. Revealing Key Structural Features Hidden in Liquids and Glasses. *Nat. Rev. Phys.* **2019**, *1*, 333−348.
(268) Cubuk, E. D.; Schoenholz, S. S.; Rieser, J. M.; Malone, B. D.; Rottler, J.; Durian, D. J.; Kaxiras, E.; Liu, A. J. Identifying Structural Flow Defects in Disordered Solids Using Machine-Learning Methods. *Phys. Rev. Lett.* **2015**, *114*, 108001.
(269) Schoenholz, S. S.; Cubuk, E. D.; Sussman, D. M.; Kaxiras, E.; Liu, A. J. A Structural Approach to Relaxation in Glassy Liquids. *Nat. Phys.* **2016**, *12*, 469−471.
(270) Fan, Z.; Ding, J.; Ma, E. Machine Learning Bridges Local Static Structure with Multiple Properties in Metallic Glasses. *Mater. Today* **2020**, *40*, 48−62.
(271) Liu, H.; Xiao, S.; Tang, L.; Bao, E.; Li, E.; Yang, C.; Zhao, Z.; Sant, G.; Smedskjaer, M. M.; Guo, L.; et al. Predicting the Early-Stage Creep Dynamics of Gels from Their Static Structure by Machine Learning. *Acta Mater.* **2021**, *210*, 116817.
(272) Freitas, R.; Reed, E. J. Uncovering the Effects of Interface-Induced Ordering of Liquid on Crystal Growth Using Machine Learning. *Nat. Commun.* **2020**, *11*, 3260.
(273) Cubuk, E. D.; Ivancic, R. J. S.; Schoenholz, S. S.; Strickland, D. J.; Basu, A.; Davidson, Z. S.; Fontaine, J.; Hor, J. L.; Huang, Y.-R.; Jiang, Y.; et al. Structure-Property Relationships from Universal Signatures of Plasticity in Disordered Solids. *Science* **2017**, *358*, 1033−1037.
(274) Cubuk, E. D.; Schoenholz, S. S.; Rieser, J. M.; Malone, B. D.; Rottler, J.; Durian, D. J.; Kaxiras, E.; Liu, A. J. Identifying Structural Flow Defects in Disordered Solids Using Machine-Learning Methods. *Phys. Rev. Lett.* **2015**, *114*, 108001.
(275) Wang, Q.; Ding, J.; Zhang, L.; Podryabinkin, E.; Shapeev, A.; Ma, E. Predicting the Propensity for Thermally Activated β Events in Metallic Glasses via Interpretable Machine Learning. *npj Comput. Mater.* **2020**, *6*, 194.
(276) Cortes, C.; Vapnik, V. Support-Vector Networks. *Mach. Learn.* **1995**, *20*, 273−297.
(277) Chen, T.; Guestrin, C. XGBoost: A Scalable Tree Boosting System. In *KDD '16: Proceedings of the 22nd ACM SIGKDD International Conference on Knowledge Discovery and Data Mining*, San Francisco, CA, August 13−17, 2016; Association for Computing Machinery: New York; pp 785−794.
(278) Dreiseitl, S.; Ohno-Machado, L. Logistic Regression and Artificial Neural Network Classification Models: A Methodology Review. *J. Biomed. Inform.* **2002**, *35*, 352−359.
(279) Cubuk, E. D.; Schoenholz, S. S.; Kaxiras, E.; Liu, A. J. Structural Properties of Defects in Glassy Liquids. *J. Phys. Chem. B* **2016**, *120*, 6139−6146.
(280) Wang, Q.; Jain, A. A Transferable Machine-Learning Framework Linking Interstice Distribution and Plastic Heterogeneity in Metallic Glasses. *Nat. Commun.* **2019**, *10*, 5537.
(281) Bapst, V.; Keck, T.; Grabska-Barwińska, A.; Donner, C.; Cubuk, E. D.; Schoenholz, S. S.; Obika, A.; Nelson, A. W. R.; Back, T.; Hassabis, D.; et al. Unveiling the Predictive Power of Static Structure in Glassy Systems. *Nat. Phys.* **2020**, *16*, 448−454.
(282) Scarselli, F.; Gori, M.; Tsoi, A. C.; Hagenbuchner, M.; Monfardini, G. The Graph Neural Network Model. *IEEE Trans. Neural Netw.* **2009**, *20*, 61−80.
(283) Rasmussen, C. E. Gaussian Processes in Machine Learning. In *Advanced Lectures on Machine Learning: ML Summer Schools 2003, Canberra, Australia, February 2−14, 2003, Tübingen, Germany, August 4−16, 2003, Revised Lectures*; Bousquet, O., von Luxburg, U., Rätsch, G., Eds.; Lecture Notes in Computer Science *3176*; Springer: Berlin, Heidelberg, 2004; pp 63−71.
(284) Boattini, E.; Marín-Aguilar, S.; Mitra, S.; Foffi, G.; Smallenburg, F.; Filion, L. Autonomously Revealing Hidden Local Structure in Supercooled Liquids. *Nat. Commun.* **2020**, *11*, 1−9.
(285) Freitas, R.; Reed, E. J. Uncovering the Effects of Interface-Induced Ordering of Liquid on Crystal Growth Using Machine Learning. *Nature Commun.* **2020**, *11*, 1−10.
(286) Liu, X.; Li, F.; Yang, Y. Softness" as the Structural Origin of Plasticity in Disordered Solids: A Quantitative Insight from Machine Learning. *Sci. China Mater.* **2019**, *62*, 154−160.
(287) Battaglia, P. W.; Pascanu, R.; Lai, M.; Rezende, D.; Kavukcuoglu, K. Interaction Networks for Learning about Objects, Relations and Physics. *arXiv (Computer Science.Artificial Intelligence)*, December 1, **2016**, 1612.00222, ver. 1. https://doi.org/10.48550/arXiv.1612.00222, accessed October 20, 2021.
(288) Battaglia, P. W.; Hamrick, J. B.; Bapst, V.; Sanchez-Gonzalez, A.; Zambaldi, V.; Malinowski, M.; Tacchetti, A.; Raposo, D.; Santoro, A.; Faulkner, R.; et al. Relational Inductive Biases, Deep Learning, and Graph Networks. *arXiv (Computer Science.Artificial Intelligence)*, June 4, **2018**, 1806.01261, ver. 3. https://doi.org/10.48550/arXiv.1806.01261, accessed October 20, 2021.
(289) Santoro, A.; Raposo, D.; Barrett, D. G. T.; Malinowski, M.; Pascanu, R.; Battaglia, P.; Lillicrap, T. A Simple Neural Network Module for Relational Reasoning. *arXiv (Computer Science.Artificial Intelligence)*, June 5, **2017**, 1706.01427, ver. 1. https://doi.org/10.48550/arXiv.1706.01427, accessed October 20, 2021.
(290) Goodfellow, I.; Bengio, Y.; Courville, A. *Deep Learning*; The MIT Press: Cambridge, MA, 2016.
(291) Anderson, P. W. Through the Glass Lightly. *Science* **1995**, *267*, 1615.
(292) Ediger, M. D.; Angell, C. A.; Nagel, S. R. Supercooled Liquids and Glasses. *J. Phys. Chem.* **1996**, *100*, 13200−13212.
(293) Angell, C. A.; Ngai, K. L.; McKenna, G. B.; McMillan, P. F.; Martin, S. W. Relaxation in Glassforming Liquids and Amorphous Solids. *J. Appl. Phys.* **2000**, *88*, 3113−3157.
(294) Debenedetti, P. G.; Stillinger, F. H. Supercooled Liquids and the Glass Transition. *Nature* **2001**, *410*, 259−267.
(295) Sabelko, J.; Ervin, J.; Gruebele, M. Observation of Strange Kinetics in Protein Folding. *P. Natl. Acad. Sci. USA* **1999**, *96*, 6031−6036.
(296) Bredenbeck, J.; Helbing, J.; Kumita, J. R.; Woolley, G. A.; Hamm, P. α-Helix Formation in a Photoswitchable Peptide Tracked from Picoseconds to Microseconds by Time-Resolved IR Spectroscopy. *P. Natl. Acad. Sci. USA* **2005**, *102*, 2379−2384.
(297) Krzaékała, F.; Montanari, A.; Ricci-Tersenghi, F.; Semerjian, G.; Zdeborová, L. Gibbs States and the Set of Solutions of Random Constraint Satisfaction Problems. *P. Natl. Acad. Sci. USA* **2007**, *104*, 10318−10323.
(298) Bouchaud, J.-P.; Mézard, M.; Dalibard, J. *Complex Systems: Lecture Notes of the Les Houches Summer School 2006*; Elsevier: Amsterdam, Netherlands, 2011.
(299) Ihalainen, J. A.; Bredenbeck, J.; Pfister, R.; Helbing, J.; Chi, L.; Van Stokkum, I. H. M.; Woolley, G. A.; Hamm, P. Folding and

Unfolding of a Photoswitchable Peptide from Picoseconds to Microseconds. *P. Natl. Acad. Sci. USA* **2007**, *104*, 5383−5388.
(300) Xi, H.; Gao, K. Z.; Ouyang, J.; Shi, Y.; Yang, Y. Slow Magnetization Relaxation and Reversal in Magnetic Thin Films. *J. Phys.-Condens. Mater.* **2008**, *20*, 295220.
(301) Mauro, J. C.; Tandia, A.; Vargheese, K. D.; Mauro, Y. Z.; Smedskjaer, M. M. Accelerating the Design of Functional Glasses through Modeling. *Chem. Mater.* **2016**, *28*, 4267−4277.
(302) Zanotto, E. D.; Mauro, J. C. The Glassy State of Matter: Its Definition and Ultimate Fate. *J. Non-Cryst. Solids* **2017**, *471*, 490−495.
(303) Ding, L.; Thieme, M.; Demouchy, S.; Kunisch, C.; Kaus, B. J. P. Effect of Pressure and Temperature on Viscosity of a Borosilicate Glass. *J. Am. Ceram. Soc.* **2018**, *101*, 3936−3946.
(304) Ding, L.; Buhre, S.; Kunisch, C.; Kaus, B. Pressure Dependence of Density and Structural Relaxation of Glass near the Glass Transition Region. *J. Am. Ceram. Soc.* **2018**, *101*, 1149−1158.
(305) Ding, L.; Doss, K.; Yang, Y.; Lee, K. H.; Bockowski, M.; Demouchy, S.; Thieme, M.; Ziebarth, B.; Wang, Q.; Smedskjaer, M. M.; et al. Volume Relaxation in a Borosilicate Glass Hot Compressed by Three Different Methods. *J. Am. Ceram. Soc.* **2021**, *104*, 816−823.
(306) Ellison, A.; Cornejo, I. A. Glass Substrates for Liquid Crystal Displays. *Int. J. Appl. Glass Sci.* **2010**, *1*, 87−103.
(307) Zheng, Q.; Mauro, J. C. Variability in the Relaxation Behavior of Glass: Impact of Thermal History Fluctuations and Fragility. *J. Chem. Phys.* **2017**, *146*, 074504.
(308) Tsujikawa, K.; Tajima, K.; Zhou, J. Intrinsic Loss of Optical Fibers. *Opt. Fiber Technol.* **2005**, *11*, 319−331.
(309) Ediger, M. D. Spatially Heterogenous Dynamics in Supercooled Liquids. *Annu. Rev. Phys. Chem.* **2000**, *51*, 99−128.
(310) Kohlrausch, R. Theorie Des Elektrischen Rückstandes in Der Leidener Flasche. *Ann. Phys. Chem.* **1854**, *167*, 179−214.
(311) Scherer, G. W. *Relaxation in Glass and Composites*; John Wiley & Sons, Inc.: New York, 1986.
(312) Böhmer, R.; Chamberlin, R. V.; Diezemann, G.; Geil, B.; Heuer, A.; Hinze, G.; Kuebler, S. C.; Richert, R.; Schiener, B.; Sillescu, H.; et al. Nature of the Non-Exponential Primary Relaxation in Structural Glass-Formers Probed by Dynamically Selective Experiments. *J. Non-Cryst. Solids* **1998**, *235*−*237*, 1−9.
(313) Williams, G.; Watts, D. C. Non-Symmetrical Dielectric Relaxation Behaviour Arising from a Simple Empirical Decay Function. *T. Faraday Soc.* **1970**, *66*, 80−85.
(314) Stickel, F.; Fischer, E. W.; Richert, R. Dynamics of Glass-Forming Liquids. I. Temperature-Derivative Analysis of Dielectric Relaxation Data. *J. Chem. Phys.* **1995**, *102*, 6251−6257.
(315) Niss, K.; Dalle-Ferrier, C.; Tarjus, G.; Alba-Simionesco, C. On the Correlation between Fragility and Stretching in Glass-Forming Liquids. *J. Phys.: Condens. Matter* **2012**, *24*, 059501.
(316) Moynihan, C. T.; Macedo, P. B.; Montrose, C. J.; Montrose, C. J.; Gupta, P. K.; DeBolt, M. A.; Dill, J. F.; Dom, B. E.; Drake, P. W.; Easteal, A. J.; et al. Structural Relaxation in Vitreous Materials. *Ann. N.Y. Acad. Sci.* **2006**, *279*, 15−35.
(317) Comez, L.; Masciovecchio, C.; Monaco, G.; Fioretto, D. Progress in Liquid and Glass Physics by Brillouin Scattering Spectroscopy. *Solid State Phys.* **2012**, *63*, 1−77.
(318) Birge, N. O.; Nagel, S. R. Specific-Heat Spectroscopy of the Glass Transition. *Phys. Rev. Lett.* **1985**, *54*, 2674−2677.
(319) Jakobsen, B.; Hecksher, T.; Christensen, T.; Olsen, N. B.; Dyre, J. C.; Niss, K. Communication: Identical Temperature Dependence of the Time Scales of Several Linear-Response Functions of Two Glass-Forming Liquids. *J. Chem. Phys.* **2012**, *136*, 081102.
(320) Olsen, N. B.; Dyre, J. C.; Christensen, T. Structural Relaxation Monitored by Instantaneous Shear Modulus. *Phys. Rev. Lett.* **1998**, *81*, 1031−1033.
(321) Montroll, E. W.; Bendler, J. T. On Lévy (or Stable) Distributions and the Williams-Watts Model of Dielectric Relaxation. *J. Stat. Phys.* **1984**, *34*, 129−162.
(322) Angell, C. A. Formation of Glasses from Liquids and Biopolymers. *Science* **1995**, *267*, 1924−1935.
(323) Böhmer, R.; Ngai, K. L.; Angell, C. A.; Plazek, D. J. Nonexponential Relaxations in Strong and Fragile Glass Formers. *J. Chem. Phys.* **1993**, *99*, 4201−4209.
(324) Guo, X.; Smedskjaer, M. M.; Mauro, J. C. Linking Equilibrium and Nonequilibrium Dynamics in Glass-Forming Systems. *J. Phys. Chem. B* **2016**, *120*, 3226−3231.
(325) Zheng, Q.; Mauro, J. C. Viscosity of Glass-Forming Systems. *J. Am. Ceram. Soc.* **2017**, *100*, 6−25.
(326) Ngai, K. L. Temperature Dependence of the Stretched Exponent in Structural Relaxation of Fragile Glass-Forming Molecular Liquids. *J. Non-Cryst. Solids* **1991**, *131*−*133*, 80−83.
(327) Ngai, K. L.; Rendell, R. W.; Plazek, D. J. Couplings between the Cooperatively Rearranging Regions of the Adam-Gibbs Theory of Relaxations in Glass-Forming Liquids. *J. Chem. Phys.* **1991**, *94*, 3018−3029.
(328) Dyre, J. C. Ten Themes of Viscous Liquid Dynamics. *J. Phys.-Condens. Mater.* **2007**, *19*, 205105.
(329) Gupta, P. K.; Mauro, J. C. Two Factors Governing Fragility: Stretching Exponent and Configurational Entropy. *Phys. Rev. E* **2008**, *78*, 1−3.
(330) Wilkinson, C. J.; Doss, K.; Gulbiten, O.; Allan, D. C.; Mauro, J. C. Fragility and Temperature Dependence of Stretched Exponential Relaxation in Glass-Forming Systems. *J. Am. Ceram. Soc.* **2021**, *104*, 4559−4567.
(331) Phillips, J. C. Stretched Exponential Relaxation in Molecular and Electronic Glasses. *Rep. Prog. Phys.* **1996**, *59*, 1133.
(332) Grassberger, P.; Procaccia, I. The Long Time Properties of Diffusion in a Medium with Static Traps. *J. Chem. Phys.* **1982**, *77*, 6281−6284.
(333) Potuzak, M.; Welch, R. C.; Mauro, J. C. Topological Origin of Stretched Exponential Relaxation in Glass. *J. Chem. Phys.* **2011**, *135*, 214502.
(334) Welch, R. C.; Smith, J. R.; Potuzak, M.; Guo, X.; Bowden, B. F.; Kiczenski, T. J.; Allan, D. C.; King, E. A.; Ellison, A. J.; Mauro, J. C. Dynamics of Glass Relaxation at Room Temperature. *Phys. Rev. Lett.* **2013**, *110*, 265901.
(335) Richert, R. Heterogeneous Dynamics in Liquids: Fluctuations in Space and Time. *J. Phys.: Condens. Matter* **2002**, *14*, R703.
(336) Mauro, J. C.; Uzun, S. S.; Bras, W.; Sen, S. Nonmonotonic Evolution of Density Fluctuations during Glass Relaxation. *Phys. Rev. Lett.* **2009**, *102*, 155506.
(337) Gulbiten, O.; Mauro, J. C.; Lucas, P. Relaxation of Enthalpy Fluctuations during Sub-Tg Annealing of Glassy Selenium. *J. Chem. Phys.* **2013**, *138*, 244504.
(338) Mauro, J. C. Effect of Fragility on Relaxation of Density Fluctuations in Glass. *J. Non-Cryst. Solids* **2011**, *357*, 3520−3523.
(339) Richert, R. Origin of Dispersion in Dipolar Relaxations of Glasses. *Chem. Phys. Lett.* **1993**, *216*, 223−227.
(340) Richert, R.; Richert, M. Dynamic Heterogeneity, Spatially Distributed Stretched-Exponential Patterns, and Transient Dispersions in Solvation Dynamics. *Phys. Rev. E* **1998**, *58*, 779−784.
(341) Böhmer, R.; Chamberlin, R. V.; Diezemann, G.; Geil, B.; Heuer, A.; Hinze, G.; Kuebler, S. C.; Richert, R.; Schiener, B.; Sillescu, H.; et al. Nature of the Non-Exponential Primary Relaxation in Structural Glass-Formers Probed by Dynamically Selective Experiments. *J. Non-Cryst. Solids* **1998**, *235*, 1−9.
(342) Heuer, A.; Tracht, U.; Kuebler, S. C.; Spiess, H. W. The Orientational Memory from Three-Time Correlations in Multidimensional NMR Experiments. *J. Mol. Struct.* **1999**, *479*, 251−259.
(343) Chamberlin, R. V.; Schiener, B.; Boehmer, R. Slow Dielectric Relaxation of Supercooled Liquids Investigated by Nonresonant Spectral Hole Burning. *Mater. Res. Soc. Symp. P.* **1996**, *455*, 117−125.
(344) Wendt, H.; Richert, R. Heterogeneous Relaxation Patterns in Supercooled Liquids Studied by Solvation Dynamics. *Phys. Rev. E* **2000**, *61*, 1722−1728.
(345) Lévy, P. *Théorie de l'addition Des Variables Aléatoires*; Gauthier-Villars: Paris, 1937.

https://doi.org/10.1021/acs.chemrev.1c00974
Chem. Rev. XXXX, XXX, XXX−XXX

(346) Doss, K.; Mauro, J. C. Theory of Structural Relaxation in Glass from the Thermodynamics of Irreversible Processes. *Phys. Rev. B* **2021**, *103*, 062606.
(347) Jurlewicz, A.; Weron, K. A Relationship between Asymmetric Lévy-Stable Distributions and the Dielectric Susceptibility. *J. Stat. Phys.* **1993**, *73*, 69−81.
(348) Förster, T. Experimentelle Und Theoretische Untersuchung Des Zwischenmolekularen Übergangs von Elektronenanregungsenergie. *Z. Naturforsch. A* **1949**, *4*, 321−327.
(349) Palmer, R. G.; Stein, D. L.; Abrahams, E.; Anderson, P. W. Models of Hierarchically Constrained Dynamics for Glassy Relaxation. *Phys. Rev. Lett.* **1984**, *53*, 958−961.
(350) Glarum, S. H. Dielectric Relaxation of Polar Liquids. *J. Chem. Phys.* **1960**, *33*, 1371−1375.
(351) Klafter, J.; Shlesinger, M. F. On the Relationship among Three Theories of Relaxation in Disordered Systems. *P. Natl. A. Sci.* **1986**, *83*, 848−851.
(352) Sillescu, H. Heterogeneity at the Glass Transition: A Review. *J. Non-Cryst. Solids* **1999**, *243*, 81−108.
(353) Stevenson, J. D.; Schmalian, J.; Wolynes, P. G. The Shapes of Cooperatively Rearranging Regions in Glass-Forming Liquids. *Nat. Phys.* **2006**, *2*, 268−274.
(354) Reinsberg, S. A.; Heuer, A.; Doliwa, B.; Zimmermann, H.; Spiess, H. W. Comparative Study of the NMR Length Scale of Dynamic Heterogeneities of Three Different Glass Formers. *J. Non-Cryst. Solids* **2002**, *307*, 208−214.
(355) Weeks, E. R.; Crocker, J. C.; Levitt, A. C.; Schofield, A.; Weitz, D. A. Three-Dimensional Direct Imaging of Structural Relaxation near the Colloidal Glass Transition. *Science* **2000**, *287*, 627−631.
(356) Kegel, W. K.; van Blaaderen, A. Direct Observation of Dynamical Heterogeneities in Colloidal Hard-Sphere Suspensions. *Science* **2000**, *287*, 290−293.
(357) Vargheese, K. D.; Tandia, A.; Mauro, J. C. Origin of Dynamical Heterogeneities in Calcium Aluminosilicate Liquids. *J. Chem. Phys.* **2010**, *132*, 194501.
(358) Sen, S. Differential Mobility and Spatially Heterogeneous Dynamics of Oxygen Atoms in a Supercooled Glass-Forming Network Liquid. *Phys. Rev. B* **2008**, *78*, 1−4.
(359) Kob, W.; Donati, C.; Plimpton, S. J.; Poole, P. H.; Glotzer, S. C. Dynamical Heterogeneities in a Supercooled Lennard-Jones Liquid Walter. *Phys. Rev. Lett.* **1997**, *79*, 2827−2830.
(360) Donati, C.; Douglas, J. F.; Kob, W.; Plimpton, S. J.; Poole, P. H.; Glotzer, S. C. Stringlike Cooperative Motion in a Supercooled Liquid. *Phys. Rev. Lett.* **1998**, *80*, 2338−2341.
(361) Fris, J. A. R.; Alarcón, L. M.; Appignanesi, G. A. Time Evolution of Dynamic Propensity in a Model Glass Former: The Interplay between Structure and Dynamics. *J. Chem. Phys.* **2009**, *130*, 024108.
(362) Lačević, N.; Glotzer, S. C. Dynamical Heterogeneity and Jamming in Glass-Forming Liquids. *J. Phys. Chem. B* **2004**, *108*, 19623−19633.
(363) Appignanesi, G. A.; Rodríguez Fris, J. A.; Frechero, M. A. Reproducibility of Dynamical Heterogeneities and Metabasin Dynamics in Glass Forming Liquids: The Influence of Structure on Dynamics. *Phys. Rev. Lett.* **2006**, *96*, 1−4.
(364) Berthier, L.; Biroli, G.; Bouchaud, J. P.; Kob, W.; Miyazaki, K.; Reichman, D. R. Spontaneous and Induced Dynamic Correlations in Glass Formers. II. Model Calculations and Comparison to Numerical Simulations. *J. Chem. Phys.* **2007**, *126*, 184504.
(365) Berthier, L.; Biroli, G.; Bouchaud, J. P.; Kob, W.; Miyazaki, K.; Reichman, D. R. Spontaneous and Induced Dynamic Fluctuations in Glass Formers. I. General Results and Dependence on Ensemble and Dynamics. *J. Chem. Phys.* **2007**, *126*, 184503.
(366) Giovambattista, N.; Buldyrev, S. V.; Starr, F. W.; Stanley, H. E. Dynamic Heterogeneities in Liquid Water. *J. Phys. Chem. B* **2003**, *708*, 483−490.
(367) Mazza, M. G.; Giovambattista, N.; Starr, F. W.; Stanley, H. E. Relation between Rotational and Translational Dynamic Heterogeneities in Water. *Phys. Rev. Lett.* **2006**, *96*, 057803.
(368) Vogel, M.; Glotzer, S. C. Temperature Dependence of Spatially Heterogeneous Dynamics in a Model of Viscous Silica. *Phys. Rev. E* **2004**, *70*, 061504.
(369) Hong, N. V.; Lan, M. T.; Nhan, N. T.; Hung, P. K. Polyamorphism and Origin of Spatially Heterogeneous Dynamics in Network-Forming Liquids under Compression: Insight from Visualization of Molecular Dynamics Data. *Appl. Phys. Lett.* **2013**, *102*, 191908.
(370) Holand, W.; Beall, G. H. *Glass Ceramic Technology*; John Wiley & Sons: Hoboken, NJ, 2012.
(371) Gutzow, I. S.; Schmelzer, J. W. P. *The Vitreous State: Thermodynamics, Structure, Rheology, and Crystallization*; Springer: London, 2013.
(372) Neuville, D. R. *From Glass to Crystal: Nucleation, Growth and Phase Separation: From Research to Applications*; EDP Sciences: Les Ulis, France, 2017.
(373) Gibbs, J. W. *The Collected Works of J. Willard Gibbs in Two Vol.s. Vol. 1: Thermodynamics*; Longmans, Green and Co.: New York, 1931; Vol. *1*.
(374) Gibbs, J. W. On the Equilibrium of Heterogeneous Substances. *Transactions of the Connecticut Academy of Arts and Sciences* **1876**, 3.
(375) Schmelzer, J. W. P. *Nucleation Theory and Applications*; Wiley-VCH: Weinheim, Germany, 2005.
(376) Gránásy, L. Diffuse Interface Theory of Nucleation. *J. Non-Cryst. Solids* **1993**, *162*, 301−303.
(377) Gránásy, L.; Herlach, D. M. Diffuse Interface Approach to Crystal Nucleation in Glasses. *J. Non-Cryst. Solids* **1995**, *192*, 470−473.
(378) Gránásy, L.; James, P. F. Nucleation in Oxide Glasses: Comparison of Theory and Experiment. *P. R. Soc. London A Mater.* **1998**, *454*, 1745−1766.
(379) Evteev, A. V.; Kosilov, A. T.; Levchenko, E. V.; Logachev, O. B. Kinetics of Isothermal Nucleation in a Supercooled Iron Melt. *Phys. Solid State* **2006**, *48*, 815−820.
(380) Separdar, L.; Rino, J. P.; Zanotto, E. D. Molecular Dynamics Simulations of Spontaneous and Seeded Nucleation and Theoretical Calculations for Zinc Selenide. *Comput. Mater. Sci.* **2021**, *187*, 110124.
(381) Tipeev, A. O.; Zanotto, E. D.; Rino, J. P. Crystal Nucleation Kinetics in Supercooled Germanium: MD Simulations versus Experimental Data. *J. Phys. Chem. B* **2020**, *124*, 7979−7988.
(382) Xia, X.; Dutta, I.; Mauro, J. C.; Aitken, B. G.; Kelton, K. F. Temperature Dependence of Crystal Nucleation in $BaO{\cdot}2SiO_2$ and $5BaO{\cdot}8SiO_2$ Glasses Using Differential Thermal Analysis. *J. Non-Cryst. Solids* **2017**, *459*, 45−50.
(383) Rodrigues, A. M. *Diffusional Processes in Barium Disilicate Glass: Crystallization, Viscous Flow, and Relaxation*. Ph.D. Thesis, Universidade Federal de São Carlos, São Carlos, Brazil, 2014.
(384) Zanotto, E. D. *The Effects of Amorphous Phase Separation on Crystal Nucleation in Baria-Silica and Lithia-Silica Glasses*. Ph.D. Thesis, The University of Sheffield, Sheffield, U.K., 1982.
(385) Schmelzer, J. W. P.; Tropin, T. V.; Fokin, V. M.; Abyzov, A. S.; Zanotto, E. D. Effects of Glass Transition and Structural Relaxation on Crystal Nucleation: Theoretical Description and Model Analysis. *Entropy* **2020**, *22*, 1098.
(386) Fokin, V. M.; Abyzov, A. S.; Yuritsyn, N. S.; Schmelzer, J. W. P.; Zanotto, E. D. Effect of Structural Relaxation on Crystal Nucleation in Glasses. *Acta Mater.* **2021**, *203*, 116472.
(387) Cassar, D. R.; Serra, A. H.; Peitl, O.; Zanotto, E. D. Critical Assessment of the Alleged Failure of the Classical Nucleation Theory at Low Temperatures. *J. Non-Cryst. Solids* **2020**, *547*, 120297.
(388) Xia, X.; Van Hoesen, D. C.; McKenzie, M. E.; Youngman, R. E.; Kelton, K. F. Low-Temperature Nucleation Anomaly in Silicate Glasses Shown to Be Artifact in a 5BaO·8SiO2 Glass. *Nat. Commun.* **2021**, *12*, 2026.
(389) Berthier, L.; Biroli, G.; Bouchaud, J.-P.; Cipelletti, L.; Masri, D. E.; L'Hôte, D.; Ladieu, F.; Pierno, M. Direct Experimental

https://doi.org/10.1021/acs.chemrev.1c00974
Chem. Rev. XXXX, XXX, XXX−XXX

Evidence of a Growing Length Scale Accompanying the Glass Transition. *Science* **2005**, *310*, 1797−1800.
(390) Flenner, E.; Szamel, G. Dynamic Heterogeneity in a Glass Forming Fluid: Susceptibility, Structure Factor, and Correlation Length. *Phys. Rev. Lett.* **2010**, *105*, 217801.
(391) Ediger, M. D. Spatially Heterogeneous Dynamics in Supercooled Liquids. *Annu. Rev. Phys. Chem.* **2000**, *51*, 99−128.
(392) Henritzi, P.; Bormuth, A.; Klameth, F.; Vogel, M. A Molecular Dynamics Simulations Study on the Relations between Dynamical Heterogeneity, Structural Relaxation, and Self-Diffusion in Viscous Liquids. *J. Chem. Phys.* **2015**, *143*, 164502.
(393) Wang, L.; Xu, N.; Wang, W.; Guan, P. Revealing the Link between Structural Relaxation and Dynamic Heterogeneity in Glass-Forming Liquids. *Phys. Rev. Lett.* **2018**, *120*, 125502.
(394) Morris, D. G. Crystallisation of the Metglas 2826 Amorphous Alloy. *Acta Metall. Mater.* **1981**, *29*, 1213−1220.
(395) Stevenson, J. D.; Wolynes, P. G. The Ultimate Fate of Supercooled Liquids. *J. Phys. Chem. A* **2011**, *115*, 3713−3719.
(396) Fitzner, M.; Sosso, G. C.; Cox, S. J.; Michaelides, A. Ice Is Born in Low-Mobility Regions of Supercooled Liquid Water. *Proc. Natl. Acad. Sci. U.S.A.* **2019**, *116*, 2009−2014.
(397) Puosi, F.; Pasturel, A. Nucleation Kinetics in a Supercooled Metallic Glass Former. *Acta Mater.* **2019**, *174*, 387−397.
(398) Sellberg, J. A.; Huang, C.; McQueen, T. A.; Loh, N. D.; Laksmono, H.; Schlesinger, D.; Sierra, R. G.; Nordlund, D.; Hampton, C. Y.; Starodub, D.; et al. Ultrafast X-Ray Probing of Water Structure below the Homogeneous Ice Nucleation Temperature. *Nature* **2014**, *510*, 381−384.
(399) Sciortino, F.; Geiger, A.; Stanley, H. E. Effect of Defects on Molecular Mobility in Liquid Water. *Nature* **1991**, *354*, 218−221.
(400) Russo, J.; Tanaka, H. Understanding Water's Anomalies with Locally Favoured Structures. *Nat. Commun.* **2014**, *5*, 3556.
(401) Kelton, K.; Greer, A. L. *Nucleation in Condensed Matter: Applications in Materials and Biology*; Elsevier: Amsterdam, Netherlands, 2010.
(402) Kelton, K. F.; Greer, A. L. Interpretation of Experimental Measurements of Transient Nucleation. In *Rapidly Quenched Metals*; Steeb, S., Warlimont, H., Eds.; Elsevier: Amsterdam, Netherlands, 1985; pp 223−226. DOI: 10.1016/B978-0-444-86939-5.50056-7
(403) Kelton, K. F.; Greer, A. L. Transient Nucleation Effects in Glass Formation. *J. Non-Cryst. Solids* **1986**, *79*, 295−309.
(404) Alexandrov, D. V.; Malygin, A. P. Nucleation Kinetics and Crystal Growth with Fluctuating Rates at the Intermediate Stage of Phase Transitions. *Modelling Simul. Mater. Sci. Eng.* **2014**, *22*, 015003.
(405) Bording, J. K.; Taftø, J. Molecular-Dynamics Simulation of Growth of Nanocrystals in an Amorphous Matrix. *Phys. Rev. B* **2000**, *62*, 8098−8103.
(406) Alvarez, I.; Cooper, A. R. The Effect of Heat Transfer on Linear Crystallization Kinetics in One Dimension. *J. Cryst. Growth* **1976**, *33*, 136−144.
(407) Herron, L. W.; Bergeron, C. G. Measurement of Melt-Crystal Interface Temperature during Crystallization in Melts of Binary Borate Glasses. *Phys. Chem. Glasses: Eur. J. Glass Sci. Technol., Part B* **1978**, *19*, 89−94.
(408) Herron, L. W.; Bergeron, C. G. Heat-Flow-Controlled Growth During Li2B4O7 Crystallization. *J. Am. Ceram. Soc.* **1979**, *62*, 110.
(409) Christian, J. W. *The Theory of Transformations in Metals and Alloys (Part I + II)*; Pergamon: Amsterdam, Netherlands, 2002.
(410) Crank, J. *The Mathematics of Diffusion*; Oxford University Press: Oxford, U.K., 1975.
(411) Carruthers, J. R.; Peterson, G. E.; Grasso, M.; Bridenbaugh, P. M. Nonstoichiometry and Crystal Growth of Lithium Niobate. *J. Appl. Phys.* **1971**, *42*, 1846−1851.
(412) Zanotto, E. D.; Tsuchida, J. E.; Schneider, J. F.; Eckert, H. Thirty-Year Quest for Structure-Nucleation Relationships in Oxide Glasses. *Int. Mater. Rev.* **2015**, *60*, 376−391.
(413) Gupta, P. K.; Cassar, D. R.; Zanotto, E. D. Role of Dynamic Heterogeneities in Crystal Nucleation Kinetics in an Oxide Supercooled Liquid. *J. Chem. Phys.* **2016**, *145*, 211920.
(414) Mazurin, O. V.; Porai-Koshits, E. A. *Phase Separation in Glass*; Elsevier: Amsterdam, Netherlands, 1984.
(415) Kukizaki, M. Large-Scale Production of Alkali-Resistant Shirasu Porous Glass (SPG) Membranes: Influence of ZrO_2 Addition on Crystallization and Phase Separation in Na2O-CaO-Al_2O_3-B_2O3-SiO_2 Glasses; and Alkali Durability and Pore Morphology of the Membranes. *J. Membr. Sci.* **2010**, *360*, 426−435.
(416) Cahn, J. W. On Spinodal Decomposition. *Acta Metall.* **1961**, *9*, 795−801.
(417) Schuller, S. Phase Separation in Glass. In *From Glass to Crystal - Nucleation, Growth and Phase Separation: From Research to Applications*; Neuville, D., Cormier, L., Caurant, D., Montagne, L., Eds.; EDP Sciences: Les Ulis, France, 2017; pp 125−153.
(418) Lan, S.; Wu, Z. D.; Lau, M. T.; Kui, H. W. Crystallization in Homogeneous and Phase-Separated Pd41.25Ni41.25P17.5 Bulk Metallic Glasses. *J. Non-Cryst. Solids* **2013**, *373*, 5−12.
(419) Seward, T. P., III; Uhlmann, D. R.; Turnbull, D. Development of Two-Phase Structure in Glasses, with Special Reference to the System BaO-SiO_2. *J. Am. Ceram. Soc.* **1968**, *51*, 634−642.
(420) Ramsden, A. H. *Crystal Nucleation and Growth in Baria-Silica Glasses*. Ph.D. Dissertation, University of Sheffield, Sheffield, U.K., 1978.
(421) Zanotto, E. D. Effect of Liquid Phase Separation on Crystal Nucleation in Glass-Formers. Case Closed. *Ceram. Int.* **2020**, *46*, 24779−24791.
(422) Volmer, M.; Weber, A. Keimbildung in Übersättigten Gebilden. *Z. Phys. Chem.* **1926**, *119U*, 277−301.
(423) Borelius, G. Zur Theorie Der Urnwandlungen Uom RnetattJschem Hiechphasen. V Schwankwngen Und Kernbitdung Dn Vnterkahttem Phasen. *Ann. Phys.* **1938**, *425*, 517−531.
(424) Greig, J. W. Immiscibility in Silicate Melts; Part 1. *Am. J. Sci.* **1927**, *73*, 1−44.
(425) Cahn, J. W.; Hilliard, J. E. Free Energy of a Nonuniform System. III. Nucleation in a Two-Component Incompressible Fluid. *J. Chem. Phys.* **1959**, *31*, 688−699.
(426) Cahn, J. W.; Charles, R. J. Initial Stages of Phase Separation in Glasses. *Phys. Chem. Glasses* **1965**, *6*, 181−191.
(427) Becker, R.; Döring, W. Kinetische Behandlung Der Keimbildung in Übersättigten Dämpfen. *Ann. Phys.* **1935**, *416*, 719−752.
(428) Qin, R. S.; Bhadeshia, H. K. Phase Field Method. *Mater. Sci. Technol.* **2010**, *26*, 803−811.
(429) James, P. F. Nucleation in Glass-Forming Systems. A Review. In *Nucleation and Crystallization in Glasses*; Simmons, J. H., Beau, G. H., Eds.; Advances in Ceramics *4*; American Ceramic Society: Columbus, OH, 1982; pp 14−48.
(430) James, P. F. Liquid-Phase Separation in Glass-Forming Systems. *J. Mater. Sci.* **1975**, *10*, 1802−1825.
(431) Uhlmann, D. R.; Kolbeck, A. G. Phase Separation and the Revolution in Concept of Glass Structure. *Phys. Chem. Glasses* **1976**, *17*, 146−158.
(432) Tashiro, M. Nucleation and Crystal Growth in Glasses. In *Proceedings of the 8th International Congress on Glass, London*; Society of Glass Technology: Sheffield, U.K., 1968; p 113.
(433) Zarzycki, J. Phase-Separated Systems. *Discuss. Faraday Soc.* **1970**, *50*, 122.
(434) Tomozawa, M. Liquid Phase Separation and Crystal Nucleation in Li_2O-SiO_2 Glasses. *Phys. Chem. Glasses* **1972**, 161.
(435) Zanotto, E. D.; James, P. F.; Craievich, A. F. The Effects of Amorphous Phase Separation on Crystal Nucleation Kinetics in BaO-SiO_2 Glasses; Part 3 Isothermal Treatments at 718 to 760C; Small-Angle X-Ray Scattering Results. *J. Mater. Sci.* **1986**, *21*, 3050−3064.
(436) Craievich, A. F.; Zanotto, E.; James, P. Kinetics of Sub-Liquidus Phase Separation in Silicate and Borate Glasses. A Review. *B. Mineral.* **1983**, *106*, 169−184.
(437) Zanotto, E. D.; Craievich, A. F.; James, P. F. SAXS and TEM Studies of Phase Separation in BaO-SiO_2 Glasses. *J. Phys. Colloques* **1982**, *43*, C9-107−C9−110.

https://doi.org/10.1021/acs.chemrev.1c00974
Chem. Rev. XXXX, XXX, XXX−XXX

(438) Zanotto, E. D.; James, P. F. The Compositional Dependence of Crystal Nucleation in Li2O-SiO_2 Glasses. *Glastech. Ber.* **1983**, *56*, 794−799.
(439) Hammel, J. Phase Separation in Na_2O-CaO-SiO_2 Glasses. In *Nucleation*; Zettlemoyer, A., Ed.; Marcel Dekker: New York, 1969.
(440) Liu, C.; Maaß, R. Elastic Fluctuations and Structural Heterogeneities in Metallic Glasses. *Adv. Funct. Mater.* **2018**, *28*, 1800388.
(441) Goldenberg, C.; Tanguy, A.; Barrat, J.-L. Particle Displacements in the Elastic Deformation of Amorphous Materials: Local Fluctuations vs. Non-Affine Field. *EPL* **2007**, *80*, 16003.
(442) Ross, P.; Küchemann, S.; Derlet, P. M.; Yu, H.; Arnold, W.; Liaw, P.; Samwer, K.; Maaß, R. Linking Macroscopic Rejuvenation to Nano-Elastic Fluctuations in a Metallic Glass. *Acta Mater.* **2017**, *138*, 111−118.
(443) Cheng, Y. Q.; Ma, E. Atomic-Level Structure and Structure-Property Relationship in Metallic Glasses. *Prog. Mater. Sci.* **2011**, *56*, 379−473.
(444) Hufnagel, T. C.; Schuh, C. A.; Falk, M. L. Deformation of Metallic Glasses: Recent Developments in Theory, Simulations, and Experiments. *Acta Mater.* **2016**, *109*, 375−393.
(445) Liu, H.; Dong, S.; Tang, L.; Krishnan, N. M. A.; Sant, G.; Bauchy, M. Effects of Polydispersity and Disorder on the Mechanical Properties of Hydrated Silicate Gels. *J. Mech. Phys. Solids* **2019**, *122*, 555−565.
(446) Falk, M. L.; Langer, J. S. Dynamics of Viscoplastic Deformation in Amorphous Solids. *Phys. Rev. E* **1998**, *57*, 7192−7205.
(447) Barbot, A.; Lerbinger, M.; Hernandez-Garcia, A.; García-García, R.; Falk, M. L.; Vandembroucq, D.; Patinet, S. Local Yield Stress Statistics in Model Amorphous Solids. *Phys. Rev. E* **2018**, *97*, 033001.
(448) Patinet, S.; Vandembroucq, D.; Falk, M. L. Connecting Local Yield Stresses with Plastic Activity in Amorphous Solids. *Phys. Rev. Lett.* **2016**, *117*, 045501.
(449) Dmowski, W.; Iwashita, T.; Chuang, C.-P.; Almer, J.; Egami, T. Elastic Heterogeneity in Metallic Glasses. *Phys. Rev. Lett.* **2010**, *105*, 205502.
(450) Léonforte, F.; Tanguy, A.; Wittmer, J. P.; Barrat, J.-L. Inhomogeneous Elastic Response of Silica Glass. *Phys. Rev. Lett.* **2006**, *97*, 055501.
(451) Liu, Y. H.; Wang, D.; Nakajima, K.; Zhang, W.; Hirata, A.; Nishi, T.; Inoue, A.; Chen, M. W. Characterization of Nanoscale Mechanical Heterogeneity in a Metallic Glass by Dynamic Force Microscopy. *Phys. Rev. Lett.* **2011**, *106*, 125504.
(452) Gao, M.; Perepezko, J. H. Mapping the Viscoelastic Heterogeneity at the Nanoscale in Metallic Glasses by Static Force Spectroscopy. *Nano Lett.* **2020**, *20*, 7558−7565.
(453) Celarie, F.; Prades, S.; Bonamy, D.; Ferrero, L.; Bouchaud, E.; Guillot, C.; Marlière, C. Glass Breaks like Metal, but at the Nanometer Scale. *Phys. Rev. Lett.* **2003**, *90*, 075504.
(454) Chen, Y.-C.; Lu, Z.; Nomura, K.; Wang, W.; Kalia, R. K.; Nakano, A.; Vashishta, P. Interaction of Voids and Nanoductility in Silica Glass. *Phys. Rev. Lett.* **2007**, *99*, 155506.
(455) Shi, Y.; Luo, J.; Yuan, F.; Huang, L. Intrinsic Ductility of Glassy Solids. *J. Appl. Phys.* **2014**, *115*, 043528.
(456) Wang, B.; Yu, Y.; Lee, Y. J.; Bauchy, M. Intrinsic Nano-Ductility of Glasses: The Critical Role of Composition. *Front. Mater.* **2015**, *2*, 1−9.
(457) Wang, B.; Yu, Y.; Wang, M.; Mauro, J. C.; Bauchy, M. Nanoductility in Silicate Glasses Is Driven by Topological Heterogeneity. *Phys. Rev. B* **2016**, *93*, 064202.
(458) Vaills, Y.; Qu, T.; Micoulaut, M.; Chaimbault, F.; Boolchand, P. Direct Evidence of Rigidity Loss and Self-Organization in Silicate Glasses. *J. Phys.-Condes. Matter* **2005**, *17*, 4889−4896.
(459) Micoulaut, M. Constrained Interactions, Rigidity, Adaptative Networks, and Their Role for the Description of Silicates. *Am. Mineral.* **2008**, *93*, 1732−1748.
(460) Yuan, F.; Huang, L. Brittle to Ductile Transition in Densified Silica Glass. *Sci. Rep.* **2015**, *4*, 1−8.
(461) Tang, L.; Liu, H.; Ma, G.; Du, T.; Mousseau, N.; Zhou, W.; Bauchy, M. The Energy Landscape Governs Ductility in Disordered Materials. *Mater. Horiz.* **2021**, *8*, 1242−1252.
(462) Ravinder, R.; Kumar, A.; Kumar, R.; Vangla, P.; Krishnan, N. M. A. Irradiation-Induced Brittle-to-Ductile Transition in α-Quartz. *J. Am. Ceram. Soc.* **2020**, *103*, 3962−3970.
(463) Bian, X. L.; Zhao, D.; Kim, J. T.; Şopu, D.; Wang, G.; Pippan, R.; Eckert, J. Controlling the Distribution of Structural Heterogeneities in Severely Deformed Metallic Glass. *Mater. Sci. Eng. A-Struct.* **2019**, *752*, 36−42.
(464) Ketov, S. V.; Sun, Y. H.; Nachum, S.; Lu, Z.; Checchi, A.; Beraldin, A. R.; Bai, H. Y.; Wang, W. H.; Louzguine-Luzgin, D. V.; Carpenter, M. A.; Greer, A. L. Rejuvenation of Metallic Glasses by Non-Affine Thermal Strain. *Nature* **2015**, *524*, 200−203.
(465) Murali, P.; Guo, T. F.; Zhang, Y. W.; Narasimhan, R.; Li, Y.; Gao, H. J. Atomic Scale Fluctuations Govern Brittle Fracture and Cavitation Behavior in Metallic Glasses. *Phys. Rev. Lett.* **2011**, *107*, 215501.
(466) Singh, I.; Guo, T. F.; Murali, P.; Narasimhan, R.; Zhang, Y. W.; Gao, H. J. Cavitation in Materials with Distributed Weak Zones: Implications on the Origin of Brittle Fracture in Metallic Glasses. *J. Mech. Phys. Solids* **2013**, *61*, 1047−1064.
(467) Yuan, X.; Şopu, D.; Moitzi, F.; Song, K. K.; Eckert, J. Intrinsic and Extrinsic Effects on the Brittle-to-Ductile Transition in Metallic Glasses. *J. Appl. Phys.* **2020**, *128*, 125102.
(468) Raghavan, R.; Murali, P.; Ramamurty, U. On Factors Influencing the Ductile-to-Brittle Transition in a Bulk Metallic Glass. *Acta Mater.* **2009**, *57*, 3332−3340.
(469) Li, W.; Gao, Y.; Bei, H. On the Correlation between Microscopic Structural Heterogeneity and Embrittlement Behavior in Metallic Glasses. *Sci. Rep.* **2015**, *5*, 14786.
(470) Wang, N.; Ding, J.; Yan, F.; Asta, M.; Ritchie, R. O.; Li, L. Spatial Correlation of Elastic Heterogeneity Tunes the Deformation Behavior of Metallic Glasses. *npj Comput. Mater.* **2018**, *4*, 1−10.
(471) Zhao, P.; Li, J.; Hwang, J.; Wang, Y. Influence of Nanoscale Structural Heterogeneity on Shear Banding in Metallic Glasses. *Acta Mater.* **2017**, *134*, 104−115.
(472) An, Q.; Samwer, K.; Demetriou, M. D.; Floyd, M. C.; Duggins, D. O.; Johnson, W. L.; Goddard, W. A. How the Toughness in Metallic Glasses Depends on Topological and Chemical Heterogeneity. *Proc. Natl. Acad. Sci. U.S.A.* **2016**, *113*, 7053−7058.
(473) Benzine, O.; Bruns, S.; Pan, Z.; Durst, K.; Wondraczek, L. Local Deformation of Glasses Is Mediated by Rigidity Fluctuation on Nanometer Scale. *Adv. Sci.* **2018**, *5*, 1800916.
(474) Varshneya, A. K. *Fundamentals of Inorganic Glasses*; Academic Press Inc.: Boston, MA, 1993.
(475) James, P. F. Liquid-Phase Separation in Glass-Forming Systems. *J. Mater. Sci.* **1975**, *10*, 1802−1825.
(476) Kreidl, N. Phase Separation in Glasses. *J. Non-Cryst. Solids* **1991**, *129*, 1−11.
(477) Rouxel, T.; Yoshida, S. The Fracture Toughness of Inorganic Glasses. *J. Am. Ceram. Soc.* **2017**, *100*, 4374−4396.
(478) Miyata, N.; Jinno, H. Use of Vickers Indentation Method for Evaluation of Fracture Toughness of Phase-Separated Glasses. *J. Non-Cryst. Solids* **1980**, *38*−*39*, 391−396.
(479) Shaw, R. R.; Uhlmann, D. R. Effect of Phase Separation on the Properties of Simple Glasses II. Elastic Properties. *J. Non-Cryst. Solids* **1971**, *5*, 237−263.
(480) Cheng, S.; Song, C.; Ercius, P.; Cionea, C.; Hosemann, P. Indentation Cracking Behaviour and Structures of Nanophase Separation of Glasses. *hys. Chem. Glasses: Eur. J. Glass Sci. Technol. B* **2017**, *58*, 237−242.
(481) Soga, N. Elastic Moduli and Fracture Toughness of Glass. *J. Non-Cryst. Solids* **1985**, *73*, 305−313.
(482) Seal, A. K.; Chakraborti, P.; Roy, N. R.; Mukherjee, S.; Mitra, M. K.; Das, G. C. Effect of Phase Separation on the Fracture

https://doi.org/10.1021/acs.chemrev.1c00974
Chem. Rev. XXXX, XXX, XXX−XXX

Toughness of SiO_2-B_2O_3-Na_2O Glass. *Bull. Mater. Sci.* **2005**, *28*, 457−460.
(483) Tang, L.; Krishnan, N. M. A.; Berjikian, J.; Rivera, J.; Smedskjaer, M. M.; Mauro, J. C.; Zhou, W.; Bauchy, M. Effect of Nanoscale Phase Separation on the Fracture Behavior of Glasses: Toward Tough, yet Transparent Glasses. *Phys. Rev. Materials* **2018**, *2*, 113602.
(484) Ono, M.; Miyasaka, S.; Takato, Y.; Urata, S.; Yoshino, H.; Ando, R.; Hayashi, Y. Higher Toughness of Metal-Nanoparticle-Implanted Sodalime Silicate Glass with Increased Ductility. *Sci. Rep.* **2019**, *9*, 15387.
(485) Ono, M.; Miyasaka, S.; Takato, Y.; Urata, S.; Hayashi, Y. Tuning the Mechanical Toughness of the Metal Nanoparticle-Implanted Glass: The Effect of Nanoparticle Growth Conditions. *J. Am. Ceram. Soc.* **2021**, *104*, 5341−5353.
(486) Dysthe, D.; Podladchikov, Y.; Renard, F.; Feder, J.; Jamtveit, B. Universal Scaling in Transient Creep. *Phys. Rev. Lett.* **2002**, *89*, 246102.
(487) Liu, H.; Xiao, S.; Tang, L.; Bao, E.; Li, E.; Yang, C.; Zhao, Z.; Sant, G.; Smedskjaer, M. M.; Guo, L.; Bauchy, M. Predicting the Early-Stage Creep Dynamics of Gels from Their Static Structure by Machine Learning. *Acta Mater.* **2021**, *210*, 116817.
(488) Cao, P.; Short, M. P.; Yip, S. Understanding the Mechanisms of Amorphous Creep through Molecular Simulation. *Proc. Natl. Acad. Sci. U.S.A.* **2017**, *114*, 13631−13636.
(489) Spaepen, F. A Microscopic Mechanism for Steady State Inhomogeneous Flow in Metallic Glasses. *Acta Metall.* **1977**, *25*, 407−415.
(490) Orowan, E. The Fatigue of Glass Under Stress. *Nature* **1944**, *154*, 341−343.
(491) Tang, L.; Ma, G.; Liu, H.; Zhou, W.; Bauchy, M. Bulk Metallic Glasses' Response to Oscillatory Stress Is Governed by the Topography of the Energy Landscape. *J. Phys. Chem. B* **2020**, *124*, 11294−11298.
(492) Sha, Z. D.; Qu, S. X.; Liu, Z. S.; Wang, T. J.; Gao, H. Cyclic Deformation in Metallic Glasses. *Nano Lett.* **2015**, *15*, 7010−7015.
(493) van Doorn, J. M.; Verweij, J. E.; Sprakel, J.; van der Gucht, J. Strand Plasticity Governs Fatigue in Colloidal Gels. *Phys. Rev. Lett.* **2018**, *120*, 208005.
(494) Yeh, W.-T.; Ozawa, M.; Miyazaki, K.; Kawasaki, T.; Berthier, L. Glass Stability Changes the Nature of Yielding under Oscillatory Shear. *Phys. Rev. Lett.* **2020**, *124*, 225502.
(495) Richardson, K.; Krol, D.; Hirao, K. Glasses for Photonic Applications. *Int. J. Appl. Glass Sci.* **2010**, *1*, 74−86.
(496) Bengisu, M. Borate Glasses for Scientific and Industrial Applications: A Review. *J. Mater. Sci.* **2016**, *51*, 2199−2242.
(497) Ono, M.; Aoyama, S.; Fujinami, M.; Ito, S. Significant Suppression of Rayleigh Scattering Loss in Silica Glass Formed by the Compression of Its Melted Phase. *Opt. Exp.* **2018**, *26*, 7942.
(498) Ono, M. Void Engineering in Silica Glass for Ultralow Optical Scattering Loss. *J. Lightwave Technol.* **2021**, *39*, 5258−5262.
(499) Yang, Y.; Tokunaga, H.; Ono, M.; Hayashi, K.; Mauro, J. C. Thermal Expansion of Silicate Glass-forming Systems at High Temperatures from Topological Pruning of Ring Structures. *J. Am. Ceram. Soc.* **2020**, *103*, 4256−4265.
(500) Tamura, Y.; Sakuma, H.; Morita, K.; Suzuki, M.; Yamamoto, Y.; Shimada, K.; Honma, Y.; Sohma, K.; Fuji, T.; Hasegawa, T. Lowest-Ever 0.1419-DB/Km Loss Optical Fiber. In *Optical Fiber Communication Conference Postdeadline Papers*; Optica Publishing Group: Washington, DC, 2017.
(501) Yang, Y.; Tokunaga, H.; Hayashi, K.; Ono, M.; Mauro, J. C. Understanding Thermal Expansion of Pressurized Silica Glass Using Topological Pruning of Ring Structures. *J. Am. Ceram. Soc.* **2021**, *104*, 114−127.
(502) Onodera, Y.; Kohara, S.; Salmon, P. S.; Hirata, A.; Nishiyama, N.; Kitani, S.; Zeidler, A.; Shiga, M.; Masuno, A.; Inoue, H.; et al. Structure and Properties of Densified Silica Glass: Characterizing the Order within Disorder. *NPG Asia Mater.* **2020**, *12*, 85.
(503) Guerette, M.; Ackerson, M. R.; Thomas, J.; Yuan, F.; Bruce Watson, E.; Walker, D.; Huang, L. Structure and Properties of Silica Glass Densified in Cold Compression and Hot Compression. *Sci. Rep.* **2015**, *5*, 15343.
(504) Masuno, A.; Nishiyama, N.; Sato, F.; Kitamura, N.; Taniguchi, T.; Inoue, H. Higher Refractive Index and Lower Wavelength Dispersion of SiO_2 Glass by Structural Ordering Evolution via Densification at a Higher Temperature. *RSC Adv.* **2016**, *6*, 19144−19149.
(505) Urata, S.; Nakamura, N.; Aiba, K.; Tada, T.; Hosono, H. How Fluorine Minimizes Density Fluctuations of Silica Glass: Molecular Dynamics Study with Machine-Learning Assisted Force-Matching Potential. *Mater. Des.* **2021**, *197*, 109210.
(506) Cozmuta, I.; Cozic, S.; Poulain, M.; Poulain, S.; Martini, J. R. Breaking the Silica Ceiling: ZBLAN-Based Opportunities for Photonics Applications. *SPIE* **2020**, *11276*, 112760R.
(507) Eschler, H.; Weidinger, F. Acousto-optic Properties of Dense Flint Glasses. *J. Appl. Phys.* **1975**, *46*, 65−70.
(508) Morinaga, K.; Nakashima, K. Phase Separation in Germanate Glasses. *J. Non-Cryst. Solids* **1988**, *103*, 108−116.
(509) Nazabal, V.; Fargin, E.; Ferreira, B.; Le Flem, G.; Desbat, B.; Buffeteau, T.; Couzi, M.; Rodriguez, V.; Santran, S.; Canioni, L.; et al. Thermally Poled New Borate Glasses for Second Harmonic Generation. *J. Non-Cryst. Solids* **2001**, *290*, 73−85.
(510) Ogusu, K.; Yamasaki, J.; Maeda, S.; Kitao, M.; Minakata, M. Linear and Nonlinear Optical Properties of Ag-As-Se Chalcogenide Glasses for All-Optical Switching. *Opt. Lett.* **2004**, *29*, 265.
(511) Alley, T. G.; Brueck, S. R. J.; Wiedenbeck, M. Secondary Ion Mass Spectrometry Study of Space-Charge Formation in Thermally Poled Fused Silica. *J. Appl. Phys.* **1999**, *86*, 6634−6640.
(512) Dussauze, M.; Cremoux, T.; Adamietz, F.; Rodriguez, V.; Fargin, E.; Yang, G.; Cardinal, T. Thermal Poling of Optical Glasses: Mechanisms and Second-Order Optical Properties. *Int. J. Appl. Glass Sci.* **2012**, *3*, 309−320.
(513) DebRoy, T.; Wei, H. L.; Zuback, J. S.; Mukherjee, T.; Elmer, J. W.; Milewski, J. O.; Beese, A. M.; Wilson-Heid, A.; De, A.; Zhang, W. Additive Manufacturing of Metallic Components - Process, Structure and Properties. *Prog. Mater. Sci.* **2018**, *92*, 112−224.
(514) Luo, J.; Pan, H.; Kinzel, E. C. Additive Manufacturing of Glass. *J. Manuf. Sci. E* **2014**, *136*, 061024.
(515) Klein, J.; Stern, M.; Franchin, G.; Kayser, M.; Inamura, C.; Dave, S.; Weaver, J. C.; Houk, P.; Colombo, P.; Yang, M.; et al. Additive Manufacturing of Optically Transparent Glass. *3D Print. Addit. Manuf.* **2015**, *2*, 92−105.
(516) Luo, J.; Gilbert, L. J.; Bristow, D. A.; Landers, R. G.; Goldstein, J. T.; Urbas, A. M.; Kinzel, E. C. Additive Manufacturing of Glass for Optical Applicaitons. *Proc. SPIE* **2016**, *9738*, 97380Y.

https://doi.org/10.1021/acs.chemrev.1c00974
Chem. Rev. XXXX, XXX, XXX−XXX